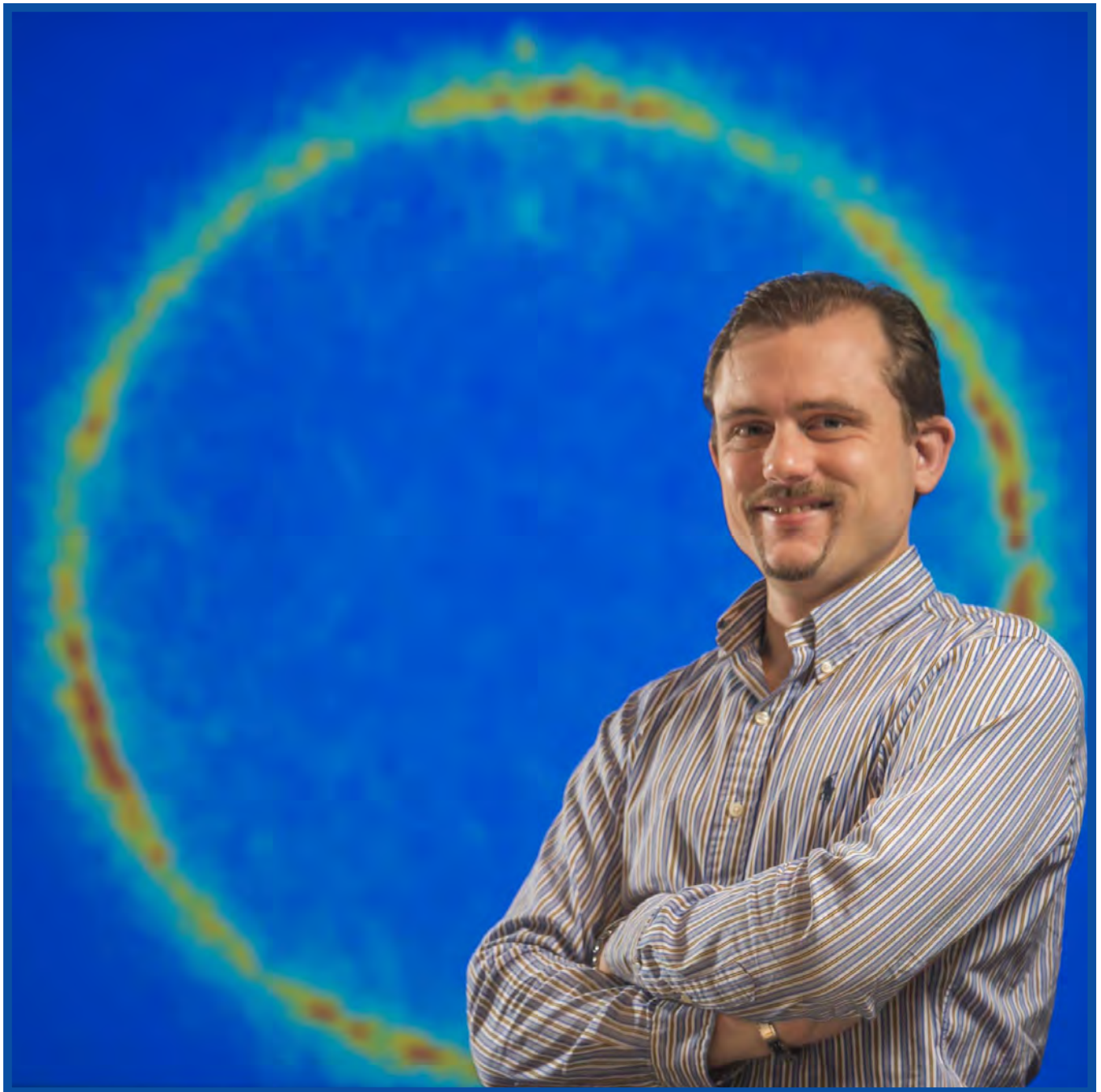# LLE Review

Quarterly Report

UR
LLE
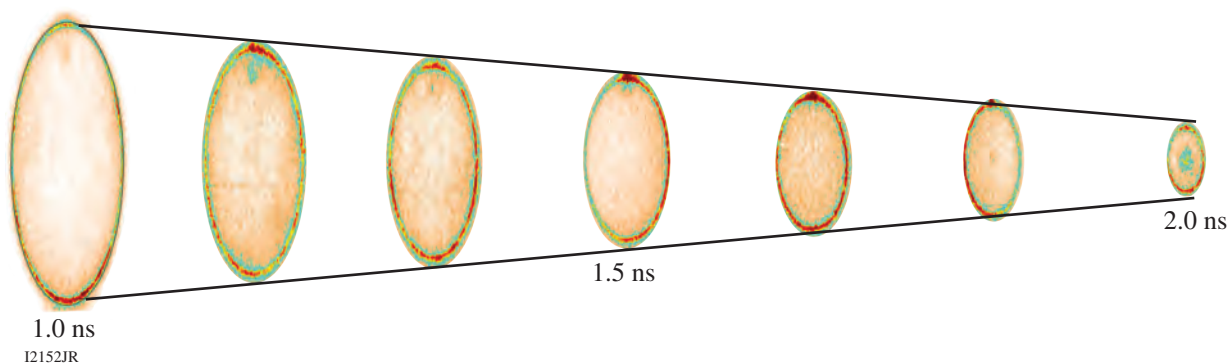
About the Cover:

The photograph on the cover highlights scientist Dr. Tomline Michel and a soft x-ray image of a direct-drive implosion on OMEGA. The image is produced by "self"-backlighting the imploding target using the soft x rays produced by the coronal plasma opposing a gated pinhole camera. The sharp inner edge observed in the self-emission images provides an accurate measurement of the position of the ablation surface. The steep edge was created by the combination of the limb effect and the absorption of the x rays in the cold dense shell. The absorption steepens the gradient by reducing the emission by a factor of 2 over a few microns in the gradient direction.

The image below shows a series of self-emission images used to measure the implosion trajectory on OMEGA. The accurate radial and laser absorption measurements as a function of time were used to determine the conversion of absorbed laser energy into kinetic energy of the shell (rocket efficiency) for different ablator materials. The measurements are consistent with predicted increases in the rocket efficiency of 28% for Be and 5% for C compared to a CH ablator.

1.0 ns

1.5 ns

2.0 ns

I2152JR

LLE Review

Quarterly Report

UR
LLE

Contents

In Brief

This volume of the LLE Review, covering July–September 2013, features "Demonstration of the Improved Rocket Efficiency in Direct-Drive Implosions by Using Different Ablator Materials" by D. T. Michel, V. N. Goncharov, I. V. Igumenshchev, W. Seka, and D. H. Froula. This article (p. 199) reports on the first experimental study of rocket efficiency where different ablators were used to vary the ratio of the atomic number over the atomic mass. Success of direct-drive implosions critically depends on the ability to create high ablation pressures ($\sim$100 MBar) and accelerating the imploding shell to ignition-relevant velocities ($>3.7 \times 10^7$ cm/s) by using direct laser illumination. It is demonstrated that the implosion velocity of Be shells is increased by 20% compared to C and CH shells in direct-drive implosions. These measurements are consistent with the predicted increase in the hydrodynamic efficiency of 18% for Be and 7% for C compared to a CH ablator.

Additional highlights of research presented in this issue include the following:

- M. Storm, P. Schiebel, R. R. Freeman, and K. U. Akli (The Ohio State University Department of Physics); B. Eichman, W. Theobald, C. Mileham, C. Stoeckl, I. A. Begishev, and G. Fiksel (LLE); Z. Zhong (The National Synchrotron Light Source, Brookhaven National Laboratory); and R. B. Stephens (General Atomics) present the results of characterization of a high-proton-energy x-ray image (p. 205). The Bragg angle, rocking curve, and reflection efficiency of a quartz crystal x-ray imager (Miller indices 234) were measured at photon energy of 15.6909 keV, corresponding to the $K_{\alpha 2}$ line of Zr, using the X15A beamline at the National Synchrotron Light Source at Brookhaven National Laboratory. Using one of the curved crystals, the Zr $K_{\alpha 2}$ emission was imaged from a hot Zr plasma generated by LLE's 10-J, Multi-Terawatt laser. Estimates of the reflectivity obtained by comparing the spatially integrated signal from the images to the direct x-ray emissivity of the source were, within experimental error, in agreement with values obtained at the X15A beamline.

- J. B. Oliver, J. Bromage, C. Smith, D. Sadowski, C. Dorrer, and A. L. Rigatti demonstrate a process for producing ultra-broadband coatings with high reflectivity, high-laser-damage thresholds, and controlled dispersion (p. 212). Large-aperture deposition of high-laser-damage-threshold, low-dispersion optical coatings for 15-fs pulses has been developed using plasma-ion−assisted electron-beam evaporation. Coatings are demonstrated over 10-in.-aperture substrates.

- C. Dorrer presents the results of the optical signals generated by multiple sinusoidal temporal phase modulations (multi-FM) of a monochromatic field (p. 222). Statistical analysis based on the central limit theorem shows that the signals' optical spectrum converges to a normal distribution as a number of modulations increases, making it possible to predict the frequency range containing a given fraction of the total energy with the associated cumulative density function. Analysis and simulation of frequency-modulation-to-amplitude-modulation conversion of arbitrary multi-FM signals are performed. These developments are of theoretical and practical importance for high-energy laser systems, where optical pulses are phase modulated in the front end to smooth out the on-target beam profile and prevent potentially catastrophic damage to optical components.

- R. D. Petrasso reports on the Fifth Omega Laser Users Group Workshop on p. 237.

- This volume concludes with a summary of LLE's Summer High School Research Program (p. 243), the FY13 Laser Facility Report (p. 245), and the National Laser Users' Facility and External Users' Programs (p. 247).

Alexei Kozlov
Editor

Demonstration of the Improved Rocket Efficiency in Direct-Drive Implosions by Using Different Ablator Materials

In direct-drive inertial confinement fusion (ICF), laser beams directly illuminate a fusion capsule.[1] The laser beams ablate the target surface and, through the rocket effect,[2] drive the capsule to velocities required for thermonuclear ignition. To achieve ignition conditions, the imploding shell must reach kinetic energy larger than a threshold value (E_{min}) that depends strongly on the implosion velocity (maximum mass-averaged shell velocity), $E_{min} \propto V_{imp}^{-6}$ (Ref. 3). To maximize the implosion velocity, the conversion of laser energy into kinetic energy of the shell (hydrodynamic efficiency) can be optimized by an appropriate choice of ablator material. By changing the ablator material, the rocket efficiency can be optimized (conversion of absorbed laser energy into kinetic energy of the shell). This article reports on the experimental investigation of the material dependence of the rocket efficiency in direct-drive implosions using the OMEGA laser.[4]

The rocket efficiency of ICF implosions depends on the drive pressure and mass ablation rate. To gain physical insight into the material dependence of these quantities, a stationary laser ablation model was used.[5–7] The sound speed at the ablation region $\left[c_s \sim \left(I_L / \rho_A \right)^{1/3} \right]$ is given by balancing the energy flux of the laser (laser intensity I_L) with the energy flux of the plasma flow $\rho_A c_s^3$, where ρ_A is the mass density at the maximum laser absorption and c_s is the sound speed. Since the laser deposition region is given by the critical electron density, the mass density at the deposition region is given by $\rho_c = \left(\langle A \rangle / \langle Z \rangle \right) n_c m_p$, where ρ_c is the mass density at the critical density, n_c is the electron critical density, m_p is the mass of a proton, and $\langle A \rangle / \langle Z \rangle$ is the average atomic number over the average atomic mass. This shows that both the ablation pressure $\left(p_a \sim \rho_c c_s^2 \sim \rho_c^{1/3} \right)$ and mass ablation rate $\left(m_a \sim \rho_c c_s \sim \rho_c^{2/3} \right)$ increase with the ratio of $\langle A \rangle / \langle Z \rangle$. Although the model does not take into account some key physics of laser coupling, including the temperature dependence of laser deposition or cross-beam energy transfer (CBET),[8,9] it predicts an increased rocket efficiency with increasing $\langle A \rangle / \langle Z \rangle$ in the ablator material.

Experimentally, the rocket efficiency is typically inferred by measuring the velocity of the target and using numerical simulations to obtain the unablated target mass. Different techniques have been employed to measure the velocity of the shell in ICF experiments. Early planar experiments investigated the rocket efficiency using shadowgraphy and the peak x-ray emission from the coronal plasma.[10–12] In more-recent studies, time-averaged velocities were inferred from neutron bang-time measurements[13,14] and time-resolved velocities have been determined using x-ray backlighting.[15–18] In the direct-drive experiments, the absorbed energy has been varied by changing the intensity of the laser, the wavelength of the laser, the aspect ratio (thickness over the diameter of the shell) of the target, and the diameter of the laser beams relative to the target diameter.[8,12–15] An extensive indirect-drive study of the implosion velocity was conducted at the National Ignition Facility, where the dopant material and dopant concentration were varied while maintaining a nearly constant $\langle A \rangle / \langle Z \rangle$ (Ref. 18).

This article describes the first demonstration of the effects of $\langle A \rangle / \langle Z \rangle$ on the hydrodynamic efficiency by measuring the implosion velocities for Be $\left(\langle A \rangle / \langle Z \rangle = 2.25 \right)$, C $\left(\langle A \rangle / \langle Z \rangle = 2 \right)$, and CH $\left(\langle A \rangle / \langle Z \rangle = 1.85 \right)$ ablators. A 20% increase in the velocity of the shell is measured for a Be ablator compared to CH and C ablators when maintaining a constant initial target mass. The hydrodynamic simulations of the time-resolved radius, velocity of the shell, and unabsorbed laser energy are in good agreement with the measurements. These results show an increase in hydrodynamic efficiency of 7% for C and 18% for Be over the CH ablator.

The experiments employed 60 OMEGA ultraviolet ($\lambda_0 = 351$ nm) laser beams that uniformly illuminated the target and were smoothed by polarization smoothing,[19] smoothing by spectral dispersion,[20] and distributed phase plates [fourth-order super-Gaussian with a 650-μm full width at half maximum (FWHM)].[21] Three 100-ps-long pickets were used to set the target implosion onto a low adiabat[22] followed by a 1.2-ns square pulse that drove the target to its final velocity. The laser energy during the main drive was 22.9±0.2 kJ, which resulted in an on-target overlapped intensity of 7×10^{14} W/cm^2. Three ablators (CH, C, and Be) were used with various mass densities

of 1.03 mg/cm^3, 3.35 mg/cm^3, and 1.83 mg/cm^3 corresponding to CH, C, and Be, respectively. Their thicknesses were varied to maintain the total ablator mass to be equivalent to 27-μm-thick CH. The outer radius was 447±10 μm and the total mass was 64±2 μg.

The total unabsorbed laser energy was measured with an uncertainty of 5% using several calorimeters located around the target chamber. The scattered light was time resolved at four locations by multiplexing the signal into a 1.5-m spectrometer using a high-dynamic-range streak camera.[23] The system had a 100-ps (FWHM) temporal resolution.

The soft x rays (1 keV) emitted by the imploding target were imaged with a pinhole array (10-μm-diam holes) onto a four-strip x-ray framing camera (XRFC) with a magnification of 12 (Ref. 24). This resulted in 16 time-resolved images (four per strip). Each image was time integrated over 40 ps. The relative timing between images (Δt) was known to $\sigma(\Delta r) \sim$ 5 ps after off-line calibration using 10-ps x-ray bursts produced by the Multi-Terawatt laser.[25] The relative timing of the XRFC between shots was determined by measuring the electric pulse at the output of the microchannel plate relative to the laser fiducial. The absolute timing was determined by measuring the rise in x-ray emission relative to the laser fiducial. A 4-mm-diam gold target was irradiated with five

spatially distinct square laser beam pulses that rose over 100 ps to a 1-ns-long flattop [Fig. 136.1(a)]. An accuracy of 30 ps was determined from the standard deviation of several absolute timing measurements.

An accurate measurement of the position of the ablation surface was made using the steep inner edge [Fig. 136.1(b)] observed in the self-emission images [Fig. 136.1(c)]. This edge is created by the combination of the limb effect from the coronal soft x-ray emission and the absorption of the x rays, from the opposite side of the target, in the cold dense shell.[24] The absorption steepens the gradient by reducing the emission by a factor of 2 over a few microns in its direction. The position of the half-intensity point of this edge follows the radius, where the plasma temperature approaches zero (ablation surface) and provides an accurate measure of the radius of the shell. Since the peak-to-valley intensity is much larger than the noise, the position of the half-intensity point is not sensitive to it. The measurement accuracy of the position of the half-intensity point in the inner emission gradient for a single lineout is given by (MTF/2) × [1/(S/N)] ≈ 1 μm, where MTF = 10 μm is the modulation transfer function of the diagnostic and S/N ~ 5 is the signal-to-noise ratio, where the signal is given by the difference in the peak-to-valley. This accuracy is supported by the 3-μm standard deviation of the radius from the best-fit circle using a χ^2 analysis [insert in Fig. 136.1(b)]. The radius of

E22219JR
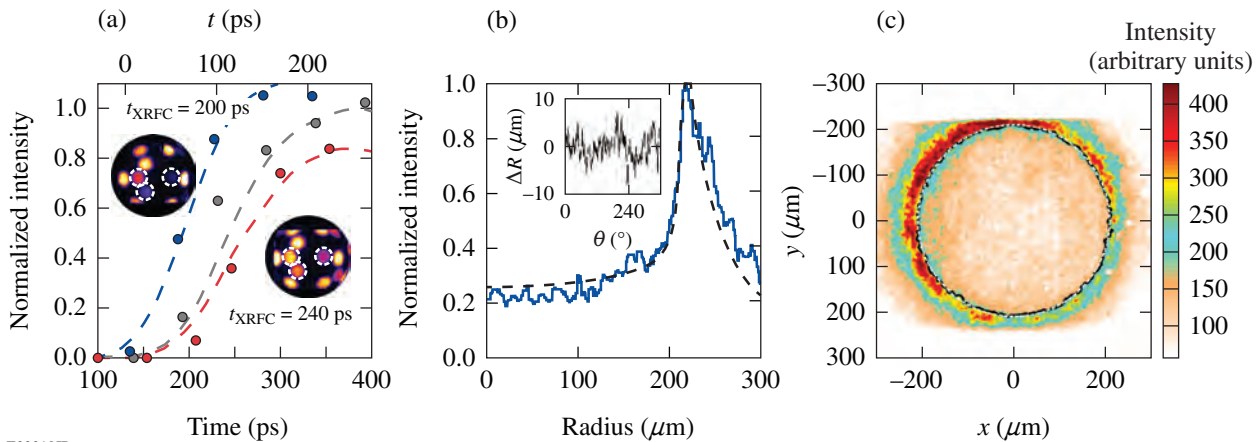
Figure 136.1

(a) A gold sphere is illuminated by several laser beams that are delayed with successive 50-ps intervals. To absolutely calibrate the timing of the x-ray framing camera (XRFC) to the laser, the x-ray emission measured by the XRFC, in the time reference (bottom axis) of the XRFC (symbols), is compared to the measured laser pulse, in the time reference (top axis) of the laser (curves). The two images (insets) correspond to the XRFC measurements at t_{XRFC} = 200 ps and t_{XRFC} = 240 ps. The dashed white circles correspond to the three beams used in the plot. (b) A single radial lineout (solid curve) of the self-emission image is compared with a lineout obtained from post-processing the hydrodynamic simulation (dashed curve). The variation of the difference between the half-intensity point and the radius of the best circle is plotted (inset). (c) The self-emission image at t = 2.5 ns was obtained from a CH target. The black curve corresponds to the location of the half-intensity point; the dashed white circle corresponds to the best-fit circle.

the shell, at each time, was obtained by averaging the position of the inner gradient over angle. This improved the accuracy by a factor of $\sqrt{N} \approx 10$, where $N = 2\pi R/\text{MTF}$ is the number of independent measurements and R is the radius from the χ^2 analysis. This results in a radial measurement accuracy of $\sigma(R) < 0.4$ μm. The accuracy in the measurement of the averaged ($\Delta t = 200$ ps) velocity is given by

$$\frac{\sigma(V)}{V} = \sqrt{\left[\frac{\sigma(\Delta t)}{\Delta t}\right]^2 + \left[\frac{\sigma(\Delta R)}{\Delta R}\right]^2} \approx 4\%, \qquad (1)$$

where, for a velocity of 200 km/s, $\Delta R = 40$ μm and $\sigma(\Delta R) = \sqrt{2}\sigma(R) = 0.6$ μm.

Figure 136.2 shows that, for all times, the velocity of the shell is higher in the Be ablator than in the CH and C ablators. The velocity increases in time to ~240 km/s for the CH, ~230 km/s for the C, and ~290 km/s for the Be ablator. A 20% increase in the velocity of the shell was measured at the end of the laser pulse when a Be ablator was used rather than the standard CH or C ablator. This increase is a result of the increase in $\langle A \rangle / \langle Z \rangle$ for Be compared to C and CH.
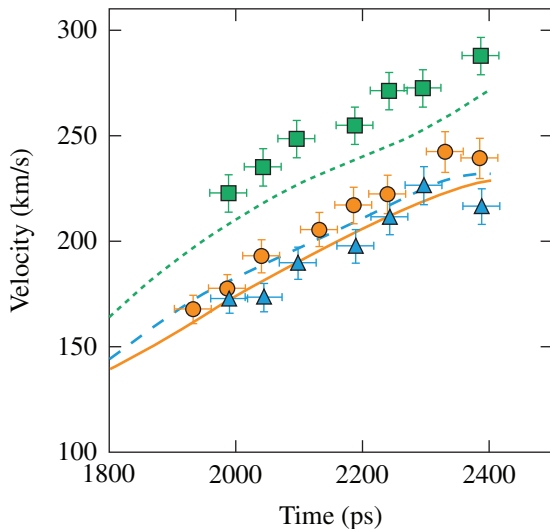
E22220JR

Figure 136.2
Comparison of the calculated (curves) and measured velocities of the shells averaged over 200 ps (symbols) in CH (orange solid line and circles), C (blue dashed line and triangles), and Be (green dotted line and squares) ablators. Timing error bars correspond to the absolute timing; the relative timing between points is smaller (5 ps).

Figures 136.3(a)–136.3(c) show the time-resolved radii of the imploding shell for the three ablators. An excellent reproduc-

ibility in trajectory measurements was observed by repeating the shots (two times for C and three times for Be). A decoupling between the position of the shell and the measured radius from the self-emission images occurred at the end of the laser pulse when the plasma was no longer being heated. This reduced the plasma expansion velocity, increasing the plasma density on the outside of the shell.

Simulations of the trajectories [Figs. 136.3(a)–136.3(c)] and velocities (Fig. 136.2) of the shells are in good agreement with measurements, indicating that the ablation pressure P_a and the mass M of the shell are well modeled:

$$\left(\frac{P_a}{M} = \frac{1}{4\pi R^2}\frac{dV}{dt}\right). \qquad (2)$$

This suggests that the coupling of the absorbed laser energy to the shell motion is well modeled. The 80-ps delay observed in the C trajectories [Fig. 136.3(b)] and velocities (Fig. 136.2) may be caused by a delay in the arrival of the shock at the inner interface of the shell, leading to a delay in the initial target motion and indicating an error in the equation of state for C.

The measured shell trajectories were compared with hydrodynamic simulations by post-processing simulations with *Spect3D*[26] and extracting the position of the half-intensity point at each time in the calculated self-emission profile. Simulations included both nonlocal heat transport[27] and CBET models[9] developed in the 1-D hydrodynamic code *LILAC*.[28] Simulated images were integrated over 40 ps and convolved by the MTF of the diagnostic. The comparison of the measured and calculated emission profiles displayed in Fig. 136.1(b) shows that the gradients of the inner edge are in excellent agreement. The position of the inner surface is insensitive to the models used since it is dominated by the point where the temperature approaches zero (a well-defined point in the simulations) and does not require Abel inversion for comparison with the simulations. The half-intensity point follows the ablation front with a constant difference of 3.5 μm caused by the widening of the inner edge by the convolution with the MTF of the diagnostic.

Figures 136.3(d)–136.3(f) show the time-resolved unabsorbed laser light measurements for the three ablators. The total absorption was measured to be 69% for Be and CH, increasing to 72% for C. This indicates that the increase in implosion velocity for the Be ablator is a result of increased conversion efficiency of the absorbed energy into kinetic energy, not an increase in the absorption. There is excellent agree-
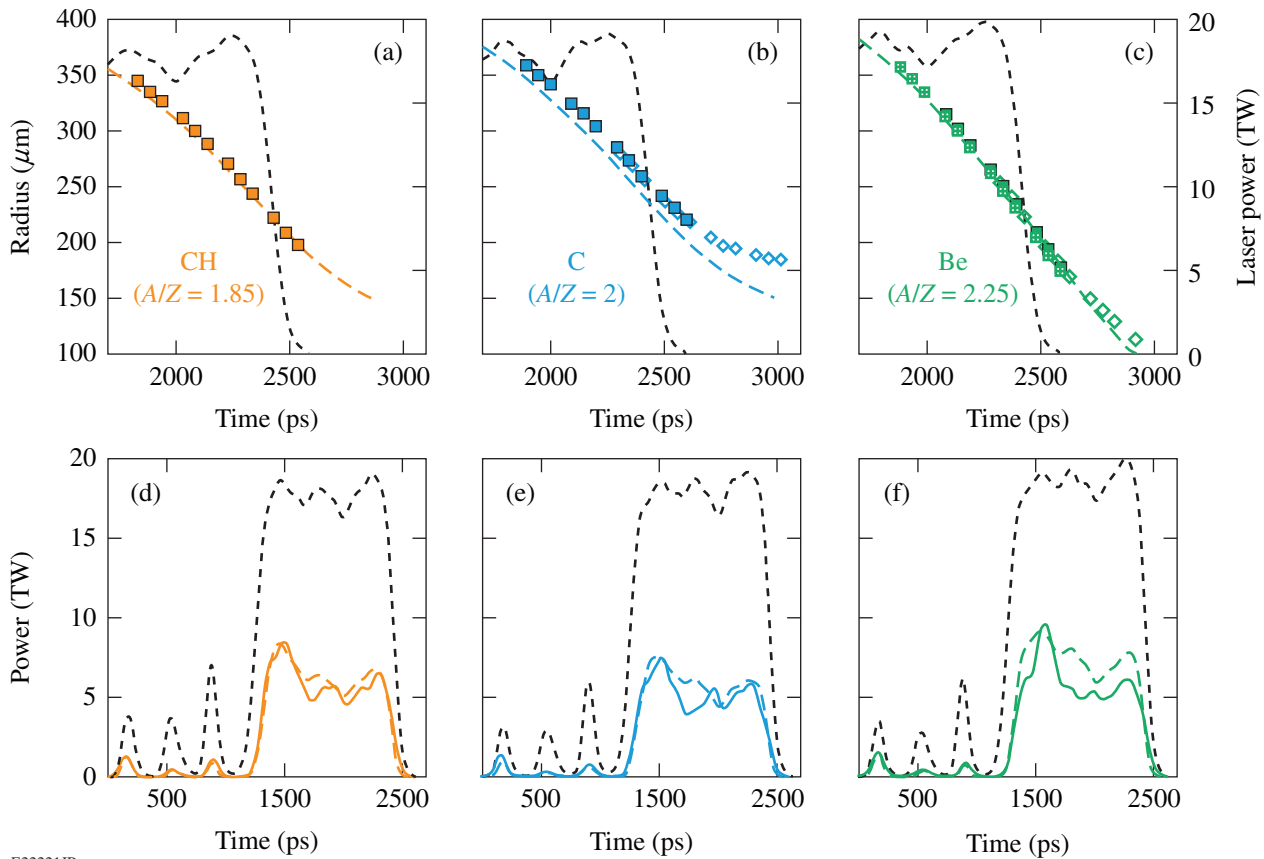
E22221JR

Figure 136.3
[(a)–(c)] Comparison of the calculated (curves) and measured (symbols) shell trajectories (the different symbols represent different shots). [(d)–(f)] Comparison of the measured (solid curve) and calculated (dashed curve) unabsorbed scattered light. The results are presented for [(a) and (d)] CH, [(b) and (e)] C, and [(c) and (f)] Be ablators. The laser power is plotted on each figure (dashed black curve) and corresponds to an on-target overlapped intensity of 7×10^{14} W/cm^2.

ment between the simulated and measured unabsorbed laser powers for C and CH ablators, which is consistent with the good agreement in shell velocities (Fig. 136.2). This indicates that when both nonlocal heat transport and CBET are included, the simulations correctly account for the absorption of the laser energy. For the Be ablator, the calculated total absorption is slightly smaller (60%) than in the experiments, which is consistent with the slightly lower (6% lower) calculated velocities.

Figure 136.4 shows the results from simulations where the ablation pressure increases and the percentage of remaining mass decreases with increasing $\langle A \rangle / \langle Z \rangle$. This produces a higher acceleration of the shell, at a given radius, leading to a higher implosion velocity for Be. In higher-energy designs, the longer acceleration phase will likely increase the velocity of the shell in Be more than what is measured in these experiments.

The increased ablation pressure, combined with the higher mass ablation rate, leads to a higher kinetic energy and hydro-

dynamic efficiency [Fig. 136.4(c)]. The hydrodynamic efficiency was calculated to be increased by 18% for Be and 7% for C compared to the CH ablator. In these experiments, the simulation slightly underestimates the hydrodynamic efficiency for Be since the laser absorption [Fig. 136.3(f)] and the shell velocity (Fig. 136.2) were measured to be slightly higher than calculated by the simulations. The transfer of absorbed laser energy into the kinetic energy (rocket efficiency) of the shell was calculated to increase by 28% for Be and 5% for C ablators compared to the CH ablator.

In summary, a 20%-higher implosion velocity was obtained when using a Be ablator compared to a C or CH ablator. Simulations that include nonlocal heat transport and CBET models accurately reproduce shell trajectories, velocities, and unabsorbed laser power for the three materials. They show that the increase in velocity is a result of increasing $\langle A \rangle / \langle Z \rangle$ and that the hydrodynamic efficiency is increased by 18% for Be and 7% for C ablators over a CH ablator.
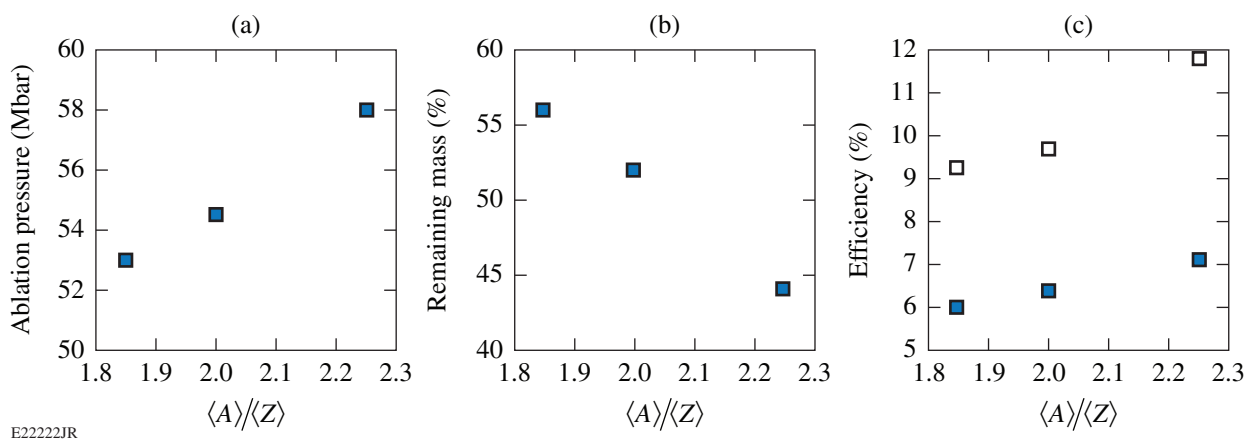
Figure 136.4

Comparison of the calculated (a) ablation pressure and (b) percentage of remaining mass at $t = 2.3$ ns for the CH ablator $\left(\langle A\rangle/\langle Z\rangle = 1.85\right)$, C ablator $\left(\langle A\rangle/\langle Z\rangle = 2\right)$, and Be ablator $\left(\langle A\rangle/\langle Z\rangle = 2.25\right)$. (c) Comparison of the hydrodynamic efficiency (solid squares) and the efficiency of the transfer of the absorbed laser into the kinetic energy of the shell (open squares) for the three ablators.

REFERENCES

1. J. Nuckolls *et al.*, Nature **239**, 139 (1972).

2. M. Murakami and K. Nishihara, Jpn. J. Appl. Phys. **26**, 1132 (1987).

3. M. C. Herrmann, M. Tabak, and J. D. Lindl, Nucl. Fusion **41**, 99 (2001).

4. T. R. Boehly, D. L. Brown, R. S. Craxton, R. L. Keck, J. P. Knauer, J. H. Kelly, T. J. Kessler, S. A. Kumpan, S. J. Loucks, S. A. Letzring, F. J. Marshall, R. L. McCrory, S. F. B. Morse, W. Seka, J. M. Soures, and C. P. Verdon, Opt. Commun. **133**, 495 (1997).

5. W. M. Manheimer, D. G. Colombant, and J. H. Gardner, Phys. Fluids **25**, 1644 (1982).

6. P. Mora, Phys. Fluids **25**, 1051 (1982).

7. C. E. Max, C. F. McKee, and W. C. Mead, Phys. Fluids **23**, 1620 (1980).

8. D. H. Froula, I. V. Igumenshchev, D. T. Michel, D. H. Edgell, R. Follett, V. Yu. Glebov, V. N. Goncharov, J. Kwiatkowski, F. J. Marshall, P. B. Radha, W. Seka, C. Sorce, S. Stagnitto, C. Stoeckl, and T. C. Sangster, Phys. Rev. Lett. **108**, 125003 (2012).

9. I. V. Igumenshchev, W. Seka, D. H. Edgell, D. T. Michel, D. H. Froula, V. N. Goncharov, R. S. Craxton, L. Divol, R. Epstein, R. Follett, J. H. Kelly, T. Z. Kosc, A. V. Maximov, R. L. McCrory, D. D. Meyerhofer, P. Michel, J. F. Myatt, T. C. Sangster, A. Shvydky, S. Skupsky, and C. Stoeckl, Phys. Plasmas **19**, 056314 (2012).

10. R. Decoste *et al.*, Phys. Rev. Lett. **42**, 1673 (1979).

11. B. H. Ripin *et al.*, Phys. Plasmas **23**, 1012 (1980).

12. D. T. Attwood *et al.*, Phys. Rev. Lett. **38**, 282 (1977).

13. T. H. Tan *et al.*, Phys. Fluids **24**, 754 (1981).

14. P. B. Radha, C. Stoeckl, V. N. Goncharov, J. A. Delettrez, D. H. Edgell, J. A. Frenje, I. V. Igumenshchev, J. P. Knauer, J. A. Marozas, R. L. McCrory, D. D. Meyerhofer, R. D. Petrasso, S. P. Regan, T. C. Sangster, W. Seka, and S. Skupsky, Phys. Plasmas **18**, 012705 (2011).

15. M. H. Key *et al.*, Opt. Commun. **44**, 343 (1983).

16. B. A. Hammel *et al.*, Phys. Fluids B **5**, 2259 (1993).

17. D. G. Hicks, B. K. Spears, D. G. Braun, R. E. Olson, C. M. Sorce, P. M. Celliers, G. W. Collins, and O. L. Landen, Phys. Plasmas **17**, 102703 (2010).

18. D. G. Hicks *et al.*, Phys. Plasmas **19**, 122702 (2012).

19. T. R. Boehly, V. A. Smalyuk, D. D. Meyerhofer, J. P. Knauer, D. K. Bradley, R. S. Craxton, M. J. Guardalben, S. Skupsky, and T. J. Kessler, J. Appl. Phys. **85**, 3444 (1999).

20. S. Skupsky, R. W. Short, T. Kessler, R. S. Craxton, S. Letzring, and J. M. Soures, J. Appl. Phys. **66**, 3456 (1989).

21. T. J. Kessler, Y. Lin, J. J. Armstrong, and B. Velazquez, in *Laser Coherence Control: Technology and Applications*, edited by H. T. Powell and T. J. Kessler (SPIE, Bellingham, WA, 1993), Vol. 1870, pp. 95–104.

22. V. N. Goncharov, T. C. Sangster, T. R. Boehly, S. X. Hu, I. V. Igumenshchev, F. J. Marshall, R. L. McCrory, D. D. Meyerhofer, P. B. Radha, W. Seka, S. Skupsky, C. Stoeckl, D. T. Casey, J. A. Frenje, and R. D. Petrasso, Phys. Rev. Lett. **104**, 165001 (2010).

23. W. R. Donaldson, R. Boni, R. L. Keck, and P. A. Jaanimagi, Rev. Sci. Instrum. **73**, 2606 (2002).

24. D. T. Michel, C. Sorce, R. Epstein, N. Whiting, I. V. Igumenshchev, R. Jungquist, and D. H. Froula, Rev. Sci. Instrum. **83**, 10E530 (2012).

25. V. Bagnoud, I. A. Begishev, M. J. Guardalben, J. Puth, and J. D. Zuegel, Opt. Lett. **30**, 1843 (2005).

26. J. J. MacFarlane *et al.*, High Energy Density Phys. **3**, 181 (2007).

27. V. N. Goncharov, T. C. Sangster, P. B. Radha, R. Betti, T. R. Boehly, T. J. B. Collins, R. S. Craxton, J. A. Delettrez, R. Epstein, V. Yu. Glebov, S. X. Hu, I. V. Igumenshchev, J. P. Knauer, S. J. Loucks, J. A. Marozas, F. J. Marshall, R. L. McCrory, P. W. McKenty, D. D. Meyerhofer, S. P. Regan, W. Seka, S. Skupsky, V. A. Smalyuk, J. M. Soures, C. Stoeckl, D. Shvarts, J. A. Frenje, R. D. Petrasso, C. K. Li, F. Séguin, W. Manheimer, and D. G. Colombant, Phys. Plasmas **15**, 056310 (2008).

28. J. Delettrez, Can. J. Phys. **64**, 932 (1986).

Characterization of a High-Photon-Energy X-Ray Imager

Introduction

In the *fast-ignition* (FI) approach to inertial confinement fusion (ICF), a compressed deuterium–tritium (DT) fuel capsule is ignited by injecting high-energy particles just prior to peak compression.[1] In the cone-in-shell concept, the particles are energetic (*fast*) electrons that are accelerated from the tip of a cone by a high-energy, short-pulse laser with a power of several petawatts. The hollow cone is embedded in a capsule that is imploded by a high-energy nanosecond laser with energies of several hundred kilojoules. The cone-in-shell concept reduces the distance over which the electrons must propagate to reach the compressed part of the fuel while maintaining a plasma-free path for the short-pulse ignitor laser. Experiments that determine the fast-electron penetration efficiency into FI fuel capsules are essential. Surrogate integrated experiments[2] were performed on the 60-beam OMEGA Laser System[3] to assess the fast-electron coupling from a measurement of the neutron-yield enhancement from compressed deuterated plastic shells. Those experiments allow only a global coupling efficiency to be inferred. They did not show where the fast electrons deposited their energy in the compressed plastic. Imaging K_α emission generated by fast electrons while propagating through a buried fluorescent layer is a powerful technique to determine local energy deposition.[4] In integrated experiments, this technique has been further developed by imaging the K_α x rays emitted from fluorescent materials that are doped into the fuel.[5,6] Figure 136.5 illustrates this concept. Electrons accelerated from the cone tip propagate into the compressed capsule where they stimulate the emission of K_α, which propagates out of the capsule. A spherically bent crystal, oriented at the Bragg angle, collects and focuses the K_α photons to an x-ray detector [charge-coupled device (CCD) or imaging plate)]. The resulting image shows the spatial distribution of the K_α photons from which the spatial distribution of the fast electrons can be inferred.

The use of K_α emission in ICF studies is well established, with most applications employing the $K_{\alpha1}$ of Cu at ~8.048 keV. The fast-electron spreading angle in flat-foil targets, irradiated with a high-intensity laser, is routinely inferred by imaging the
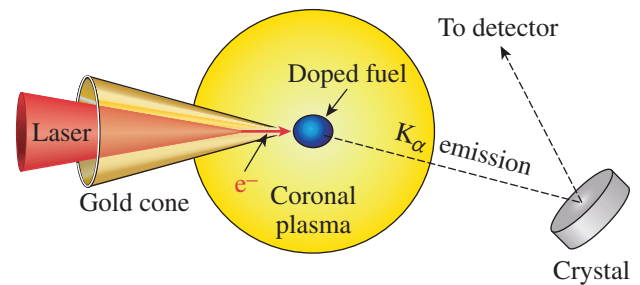
E21813JR

Figure 136.5

Fast electrons, originating from the tip of a gold cone inserted into an ICF capsule, propagate into the doped fuel, where they stimulate the emission of K_α x rays. The x rays, which are imaged to a detector using a spherically bent crystal, are used to infer the fast-electron spatial distribution.

$K_{\alpha1}$ emitted from Cu layers buried at different depths inside the foil.[4] Another application involves backlighting the ICF fuel assembly with Cu $K_{\alpha1}$ to generate radiographic information about the fuel density.[7] The use of Cu $K_{\alpha1}$ to diagnose the penetration efficiency of fast electrons in hot dense ICF fuel capsules is limited, however, by the K_α line shift that accompanies high-temperature–induced ionization in the background fuel.[5] As the K_α lines shift in energy, they move outside the acceptance bandwidth of the imaging crystals; consequently, the detection efficiency drops. For Cu $K_{\alpha1}$, a background temperature of ~35 eV is sufficient for the center wavelength to shift beyond the acceptance bandwidth of a typical quartz crystal reflector cut with Miller indices (211) (Ref. 8). One-dimensional hydrodynamic calculations performed to estimate the temperature of a 870-μm-diam fuel capsule with a 40-μm-thick shell, imploded using 20 kJ from the OMEGA laser, indicated a shell temperature in excess of 200 eV (Ref. 9).

The issue of line shifting may be mitigated by using K_α radiation from higher-Z materials, such as Zr, that are more robust against temperature-induced shifts. Promising results with a novel quartz-crystal imager working at a photon energy of 15.6909 keV, corresponding to the Zr $K_{\alpha2}$ line, were recently reported.[10] Calculations described in Ref. 10 suggest that the center wavelength of the Zr $K_{\alpha2}$ line remains inside

the acceptance band of a quartz reflector up to a temperature of at least 200 eV. There is very little experimental work reporting on crystal imaging systems at such high photon energies. This article reports on the performance of a spherically curved quartz-crystal imager designed to reflect photons with an energy of 15.6909 keV. Since the design of the imaging system relies on an accurate knowledge of the crystal, which is cut with Miller indices (234), measurements were taken to determine the Bragg angle, rocking curve, peak reflectivity, and integrated reflectivity. Several curved crystals and a flat sample were characterized using a narrow-bandwidth x-ray source tuned to 15.6909 keV. The imager was successfully tested using a Zr plasma source generated with a 10-J, 1-ps laser system. The measured peak reflectivity from the laser experiment is in agreement with the results from a synchrotron facility.

Quartz-Crystal Imager

Figure 136.6 shows the configuration in which the K_α imager is aligned for use in laser–solid experiments. In the first stage of alignment, a continuous-wave (cw) alignment laser is propagated through target chamber center (TCC), indicated by the position of the imaging fiducial in Fig. 136.6, and onto the center of the crystal. To enhance its reflectivity in the visible, the crystal is coated with 30 nm of Al. The crystal is oriented to reflect the laser light back along its own path. This arrangement defines the origin of the angular coordinate system. The crystal is then rotated through an angle $\theta_{1/2}$, where $\theta_{1/2}$ is $90°- \theta_B$ and θ_B is the Bragg angle for the K_α diffraction. The laser light is then reflected through a full angle $\theta_F = 2\theta_{1/2}$.
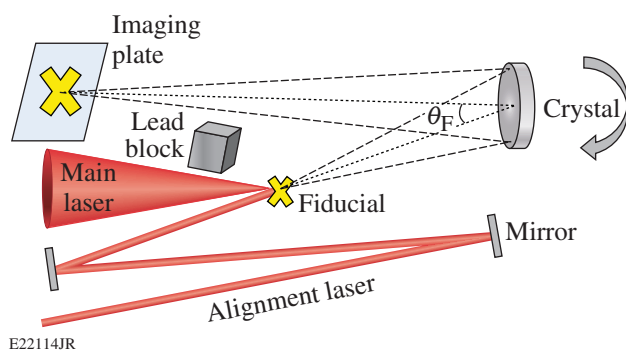

E22114JR

Figure 136.6
Schematic representation of a K_α x-ray imager simultaneously demonstrating the alignment and experimental configurations. For the experiment with the main laser, the curved crystal is rotated to satisfy the Bragg condition for K_α x rays that are diffracted and focused onto the imaging plate.

The fiducial is then positioned at TCC and imaged to an imaging plate (or CCD camera) with a magnification m that is determined by the crystal focal length f and the fiducial–crystal

separation distance s_0 by $m = f/(s_0-f)$. The position of the visible image is recorded. In the experiment, with the fiducial and alignment laser removed, the main laser irradiates a target placed at TCC and the K_α emission is imaged onto the imaging plate with the same magnification. The imaging plate is wrapped in Al foil to prevent exposure to room and laser light. A lead block placed between the target and the imaging plate prevents the direct line-of-sight x-ray irradiation of the imaging plate. The alignment technique relies on the visible and K_α images being close to coincident. If the visible image forms at an angle that is outside the crystal's rocking-curve range of angles, the Bragg condition will not be satisfied for the K_α emission and no K_α image will form. Such a discrepancy arises from misalignment of the crystal planes and the crystal surface. In the laser–solid experiments described below, a fiducial was imaged by the crystal designated Sph3 using visible light from the alignment laser before being rotated to the correct position for K_α diffraction with an accuracy of 0.01°. The displacement between the visible and the K_α images along the dispersion direction 1.85 m away at the imaging plate was ~2 mm, corresponding to an angular offset of ~0.06°. In this case, the offset was within the measured rocking-curve width of 0.12° full width at half maximum (FWHM) of this crystal. In general, the visible image can be offset by a predetermined angle to ensure the Bragg condition is satisfied for the K_α emission.

Determination of the Crystal Bragg Angle, Rocking Curve, and Reflectivity

Measurements were made to determine the Bragg angle, rocking curve, and reflection efficiency of three curved (25-cm focal length) and one flat sample of a quartz crystal (Miller indices 234) for a photon energy of 15.6909 keV corresponding to the $K_{\alpha 2}$ line of Zr. The measurements were made with the X15A x-ray beamline at the National Synchrotron Light Source at Brookhaven National Laboratory. Figure 136.7 shows the experimental configuration. The X15A beamline provides x rays from around $E_\nu = 5$ keV to $E_\nu = 28$ keV. A slit ensures that the x rays are collimated. A quartz-crystal monochromator selects the energy, providing a beam with a bandwidth $\Delta E/E \sim 10^{-4}$. The monochromator crystals are cut perpendicular to the axis with Miller indices (111) corresponding to a lattice spacing of 3.136 Å. The crystal surfaces are set to be parallel and are rotated together to select a specific energy. The monochromator was first calibrated using the K edge of Zr at $E = 17.998$ keV, corresponding to an x-ray angle of incidence from the storage ring of 6.3057°. The monochromator crystals were then rotated to select the desired x-ray energy of $E = 15.6909$ keV corresponding to Zr $K_{\alpha 2}$. In addition to the selected energy, the monochromator passes x rays whose energy corresponds
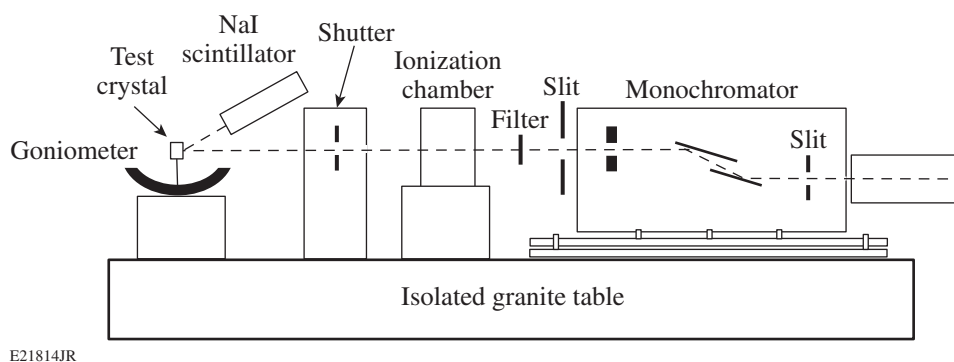
Figure 136.7
Experimental configuration. A monochromator selects x rays with a bandwidth of $\Delta E/E = 10^{-4}$. The beam is apertured to 1.6 mm (horizontally) by 100 μm (vertically). An ionization chamber measures the flux. The crystal is mounted on a motorized goniometer that rotates the crystal in the vertical direction. A shutter, synchronized with the goniometer, releases the beam when the crystal is stationary. Photons reflected from the crystal are detected using a NaI scintillator.

to the third, fourth, and fifth higher harmonic orders.[11] The flux of these x rays is sequentially weaker. At 15.6909 keV, the fundamental carries 99.7% of the x-ray energy while the third, fourth, and fifth orders contribute 0.28%, 0.013%, and 0.0003% of the energy, respectively. Filtering of the x-ray beam, a necessity for the experiment described here, increases the relative amount of higher-order x rays through differential attenuation. To suppress the propagation of higher orders of the fundamental x-ray energy, the monochromator was slightly detuned from the peak transmission angle of its rocking curve to the 50% transmission angle. With such a configuration, the third-order component is reduced by a factor of ~100, while the higher-order components are suppressed even more.

To limit the overall flux, a second lead slit apertured the x-ray beam to 1.6 mm × 100 μm in the horizontal and vertical directions, respectively. Mo filter foils can be placed in front of the slit to further attenuate the beam where necessary. An ionization chamber measures the x-ray flux after the slit. The x-ray flux at the ionization chamber is directly proportional to the electron current in the main storage ring. A computer-controlled shutter sets the x-ray exposure time. Typical exposure times were 1 s with an absolute error of ~20 ms. The test crystal is mounted on a computer-controlled goniometer with a 90° full range of motion. X rays reflected from the crystal were measured using a NaI scintillator positioned to intercept the x rays at the focus of the curved crystal. The test crystal was positioned to intercept the x-ray beam at its center. To obtain the rocking curve, the goniometer rotated the test crystal about its center in 0.0025° steps in the vertical direction. For each step, the rotation paused and the shutter opened for 1.0 s. The large NaI detector with a radius of 2.54 cm ensured that all the reflected x-ray photons were collected over the entire angular

range. The same procedure was used for all four samples. Three crystals (flat, Sph1, and Sph2) were provided by Inrad Optics and were fabricated from the same batch, while the curved crystal Sph3 was provided by Eco Pulse. The Inrad crystals had a thickness of 71±1 μm and a diameter of 30 mm, while the Eco Pulse crystal had a thickness of 125 μm and a diameter of 25 mm. To determine the energy incident on the crystal, the scintillator was placed in front of the crystal to directly intercept the x-ray beam at normal incidence. To reduce the x-ray signal below the scintillator saturation level, a 225-μm-thick Mo filter was placed (as indicated in Fig. 136.7) to attenuate the beam.

Prior to obtaining its efficiency with the NaI scintillator, the Bragg angle of Sph3 was measured using a Fuji SR imaging-plate detector. The imaging plate was oriented in the vertical direction and positioned in place of the scintillator. To prevent room-light illumination of the imaging plates, they were wrapped in a 25-μm-thick sheet of Al foil. The crystal was first aligned in its mount on an optical table and oriented such that a horizontally propagating cw laser, with normal incidence on the crystal, was back-reflected along its own path. The crystal and mount were then transferred to the goniometer and swept through an angular range of 4°. The Bragg angle is computed by determining the vertical position of the peak of the rocking curve, recorded on the imaging plate, relative to the x-ray beam and the distance of the peak position to the center of the crystal. Averaging over four sweeps, the peak was observed to occur at an incidence angle of $\theta_{1/2} = 2.80°$ with a standard deviation of 0.06°. The variation arises from the finite repeatability of repositioning the imaging plate between measurements. A further error associated with the finite precision with which the relevant distances could be measured was evaluated to be

~$\pm 0.25°$. The Bragg angle was therefore measured to be $\theta_B = 87.2 \pm 0.3)°$ for the Zr $K_{\alpha 2}$ line (15.6909 keV), which results in an inferred crystal $2d$ spacing of $2d = 1.5822(4)$ Å using Bragg's law ($n\lambda = 2d\sin\theta_B$) in the second order. In addition, Inrad provided rocking-curve measurements for their samples using the Cu $K_{\alpha 1}$ line at 8.0478 keV and measured a Bragg peak at $(76.75 \pm 0.10)°$ in the first order, from which $2d = 1.5827(7)$ Å is inferred. The corresponding Bragg angle in the second order for the Zr $K_{\alpha 2}$ line is $(86.8 \pm 0.5)°$. Both inferred $2d$ values agree within the measurement uncertainty and are close to the calculated value of $2d_{cal} = 1.5825$ Å (Ref. 6).

The rocking curves and reflection efficiencies for all four crystals are shown in Fig. 136.8. The results show that the spherical crystal Sph1 had the highest reflectivity of the curved crystals at around $(3.6 \pm 0.7) \times 10^{-4}$ with a curve FWHM of ~$0.09°$. The primary errors in the reflectivity measurement arise from jitter in the scintillator exposure time as a result of the shutter response and from the uncertainty in the thickness of the Mo stack used to filter the direct beam. For the exposure time employed, the shutter error is estimated to be ~2%. The stack thickness was calculated from the total weight, measured using a Scientech analytical balance, and the stack transverse size, measured with digital calipers. The associated error in the transmission was determined to be around ~17%. Errors associated with uncertainties in the storage ring current, the
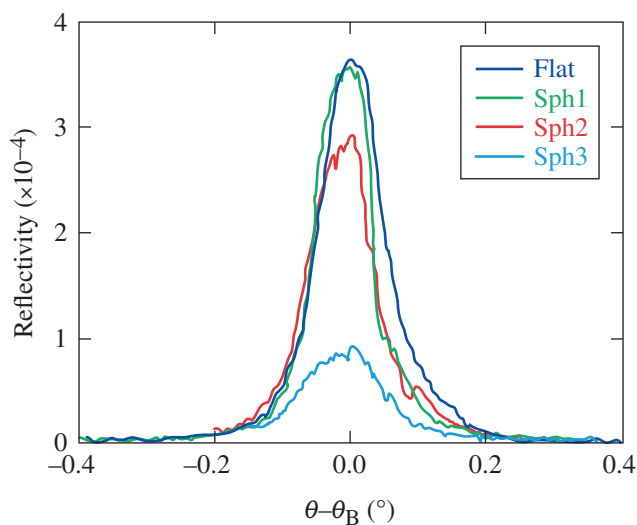

E21815JR

Figure 136.8
Measured rocking curves of four quartz crystals (234) at 15.6909 keV. The spherical crystal Sph1 had a peak reflectivity of $(3.6 \pm 0.7) \times 10^{-4}$ and a rocking-curve full width at half maximum of $0.09°$. Also shown are the rocking curves for another spherical crystal (Sph2) and a flat crystal, all from the same production batch, and a third spherical crystal (Sph3) obtained from a different vendor.

free-space x-ray propagation distances, and photon-counting statistics in the scintillator are negligible. A flat crystal from the same production batch produced a very similar result, showing that the crystal bending had a minor effect on the rocking curve. A lower reflectivity was measured for Sph2 from the same production batch, while the sample Sph3 had an ~4×-lower peak reflectivity. The results are summarized in Table 136.I. As a check, the measurements were repeated with Fujifilm SR imaging-plate detectors, instead of the NaI scintillator, producing similar results, albeit with larger errors. The SR imaging-plate detectors were also used to determine the homogeneity of the reflectivity of crystal Sph3 over a region of its surface. The crystal was translated to positions ±5 mm above, below, and to the side of the center position, and the measurements were repeated with no significant variation in the performance at the different sites.

Table 136.I: Rocking-curve width, peak reflectivity, and integrated reflectivity of a flat and various curved quartz (234) crystals at the Zr $K_{\alpha 2}$ line (15.6909 keV).

Crystal	FWHM ($\theta°$)	Peak reflectivity	Integrated reflectivity (mrad)
Flat	0.11	$(3.7 \pm 0.7) \times 10^{-4}$	$(8.8 \pm 1.8) \times 10^{-4}$
Sph1	0.09	$(3.6 \pm 0.7) \times 10^{-4}$	$(7.7 \pm 1.8) \times 10^{-4}$
Sph2	0.14	$(2.9 \pm 0.6) \times 10^{-4}$	$(7.0 \pm 1.4) \times 10^{-4}$
Sph3	0.12	$(9.0 \pm 1.8) \times 10^{-5}$	$(2.5 \pm 0.6) \times 10^{-4}$

The theoretical value of reflectivity for each crystal was calculated using the x-ray oriented programs (XOP) code.[12] The XOP code uses the DEBAX database of atomic and molecular properties and photon-interaction cross sections and scattering factors for a wide range of crystal materials. The crystal type was selected to be α quartz with the Miller indices set to (468), indicating that the calculation was performed for the second-order diffraction. The photon energy was set to 15.69 keV, the Poisson ratio to 0.17, and the polarization to sigma. The asymmetry angle was set to $0°$, signifying perfect parallelism between the diffracting planes and the crystal surface. The diffraction geometry was set to Bragg and, to account for the crystal curvature, the calculation theory was set to Multilamellar. The final input parameter was the Debye–Waller temperature parameter that took into account the thermal motion of the crystal lattice. The precise value of the temperature parameter is difficult to determine for triagonal crystalline structures such as quartz. Approximate formulas exist in XOP for cubic crystal structures such as pure silicon. In that case, the temperature parameter is close to unity for the lowest-order diffraction but is reduced for higher orders. In the current calculation, the tem-

perature factor was a free parameter that was adjusted until the calculated width of the rocking curve matched the experimentally observed value. The corresponding reflectivity values were then recorded. The temperature parameter and the calculated peak and integrated reflectivity for spherical crystals Sph1 and Sph3 are displayed in Table 136.II. The calculated values of the integrated reflectivity for the two crystals are a factor of ~3 and ~8 higher than the measured values, respectively.

It is not clear why the measured reflectivity is lower than the predicted values. Measurements of the crystal thickness of Sph1 indicated that the thickness was within 2% of the stated value. The calculations include x-ray absorption in quartz, which for a 71-μm thickness decreases the calculated reflectivity by ~9% compared to the case where absorption is not included. Absorption by impurities is not accounted for but is an unlikely explanation; although moderate- to high-Z impurities could have a significant effect on absorption, the most-common impurities in quartz crystals are low-Z materials such as Li and Al, and since the crystal is visibly transparent, we can assume that the crystal is reasonably pure. Another possibility is that the reflectivity was suppressed by defects introduced in the crystal during the manufacturing process. We also cannot eliminate the possibility that imperfections on the substrate surface might have been transferred to the crystal or that the bonding mechanism introduced stress and dislocations to the diffracting structures. There is no indication that the additional bending of the crystal led to any further degradation since the reflectivity of the flat sample was similar in magnitude to the curved crystals. Finally, the application of models that are strictly derived for cubic crystal geometry provides uncertainty and another potential source of disagreement between the measured and calculated values.

Imaging Capability and Reflectivity
**Using a Plasma-Based Source**

Laser experiments were performed with LLE's Multi-Terawatt (MTW) laser[13] to test the imaging capability of a spherical crystal using Zr $K_{\alpha2}$ x rays. This test was performed with the sample Sph3. The crystal imaged the emission from the rear surface of a Zr foil target irradiated with a p-polarized laser pulse with a 10-J energy incident at a 45° angle. The laser energy is absorbed by electrons at the critical-density surface of a plasma that forms in front of the target at the beginning of the laser interaction. The electrons are driven into the target where they stimulate the emission of K_α radiation. The K_α yield from such a target is proportional to the laser energy, while background noise caused by bremsstrahlung as the electrons lose energy in collisions is proportional to the laser intensity. To reduce the background, the pulse duration was lengthened to 10 ps and the laser spot was defocused to ~30 μm (FWHM) corresponding to a mean intensity of ~1 × 10^{17} W/cm^2. The crystal was oriented to reflect the $K_{\alpha2}$ emission on a Fujifilm TR imaging plate. To further reduce the background signal and enhance the signal-to-background ratio, a 17-μm-thick Zr filter and a 25-μm-thick Al filter were placed in front of the imaging plate while a 3-mm-thick lead collimator obstructed the direct line of sight to the target. The target dimensions were 1 mm × 1 mm × 17 μm. The distance from the target to the center of the crystal was 28.9 cm, providing a magnification of 6.6. The crystal diameter was 2.5 cm, corresponding to a solid angle from the target of 5.9 × 10^{-3} sr. The extreme rays that diffract at the edge range of the crystal subtend angles of 2.2° and 4.4°. The corresponding energies were 15.679 keV and 15.711 keV, respectively, giving an energy acceptance bandwidth for the crystal of 32 eV. The $K_{\alpha2}$ line broadening and shifting that accompany target heating are not expected to be significant for the current case of moderate laser energy and a large-mass target, and the $K_{\alpha2}$ line is expected to remain fully within the bandwidth.

Figure 136.9 shows an image corrected for magnification along with a horizontal and a vertical lineout through the peak intensity pixel. The FWHM of the horizontal and vertical lineouts is 32 and 38 μm, respectively. The image exhibits a signal-to-background ratio of better than 40:1 with an x-ray signal that peaks at around 0.18 PSL. A single-photon–counting spectrometer[14] determined the total number of radiated K_α photons to be (10+7/–2) × 10^{10} corresponding to a laser-to-K_α energy conversion efficiency of ~3 × 10^{-5}. Taking into

Table 136.II: The peak and integrated reflectivity for each crystal calculated using the x-ray oriented programs (*XOP*) software.[12]

Crystal	Radius of curvature (cm)	Thickness (μm)	Temperature parameter	Peak reflectivity	Integrated reflectivity (mrad)
Sph1	50	71	0.45	1.4×10^{-3}	2.2×10^{-3}
Sph3	50	125	0.35	1.0×10^{-3}	2.1×10^{-3}
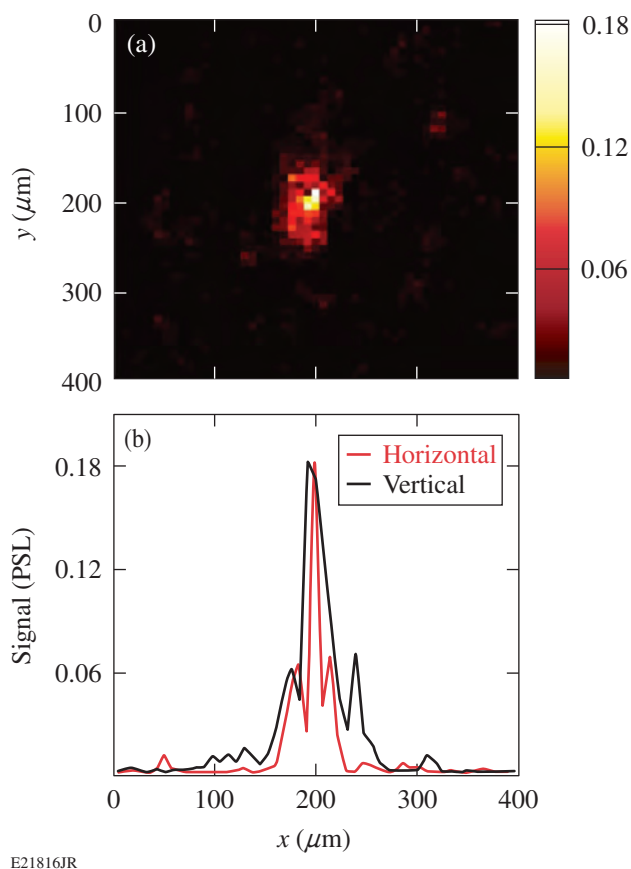
E21816JR

Figure 136.9

(a) An image of the Zr $K_{\alpha 2}$ emission through the rear surface of a 17-μm-thick laser-irradiated Zr foil (the color scheme refers to the measured signal in PSL) and (b) horizontal and vertical lineouts through the peak of the emission.

account the relative solid angle between the single-photon–counting spectrometer and the crystal, the total number of K_α photons incident on the quartz crystal was ~5×10^7. The quartz crystal reflects only the $K_{\alpha 2}$ line on the detector, which contains one third (~1.6×10^7) of the total number of K_α photons. Accounting for the 17-μm-thick Zr filter and the 25-μm-thick Al filter (~77% total transmission) and assuming an imaging plate sensitivity of (2.5±0.5) mPSL/photon at 15.7 keV (Ref. 15), a perfectly reflecting crystal is estimated to produce a total signal of $(3.0 + 3.4/–1.1) \times 10^4$ PSL. Comparing this with the experimentally measured value of (5.5±1.1) PSL, which is the spatially integrated value from Fig. 136.9, implies a peak reflectivity of $(1.8 + 1.4/–1.0) \times 10^{-4}$ at 15.7 keV. The peak reflectivity inferred from the laser experiment is a factor of ~2 higher, but it is within the experimental uncertainties in reasonable agreement with the peak reflectivity obtained from the rocking curve measurement of Sph3 (see Table 136.I).

Conclusion

A high-energy x-ray-photon imager has been developed to image the x-ray emission from laser-generated Zr plasmas. The imager's optic consists of a spherically bent quartz crystal with Miller indices (234) and a focal length of 25 cm. The Bragg angle, rocking curve, and reflectivity were determined for three spherically bent samples. A flat crystal was tested as a control to determine the impact of the bending procedure. The experiments were carried out at The National Synchrotron Light Source using photons with an energy of 15.6909 keV, corresponding to the Zr $K_{\alpha 2}$ line. The lattice $2d$ spacing for two of the curved samples was determined by the supplier to be $2d = 1.5827(7)$ Å, corresponding to Bragg and incidence angles, for Zr $K_{\alpha 2}$ x rays of $(86.8\pm0.5)°$ and $(3.2\pm0.5)°$, respectively. The incident angle of the third curved sample was directly measured to be $(2.8\pm0.3)°$, resulting in a Bragg angle of $(87.2\pm0.3)°$ and inferred $2d = 1.5822(4)$ Å. The peak reflectivity and rocking curve width for the best-performing sample were determined to be ~4×10^{-4} and ~$0.1°$, respectively. An image of the Zr line emission was obtained using a laser-generated Zr plasma produced by the 10-J Multi-Terawatt laser. The measurement confirmed the peak reflectivity of the crystal for the Zr $K_{\alpha 2}$ line by using the emitted K_α photon number measured with an absolutely calibrated single-photon–counting spectrometer.[14]

REFERENCES

1. M. Tabak *et al.*, Phys. Plasmas **1**, 1626 (1994).

2. W. Theobald, A. A. Solodov, C. Stoeckl, K. S. Anderson, R. Betti, T. R. Boehly, R. S. Craxton, J. A. Delettrez, C. Dorrer, J. A. Frenje, V. Yu. Glebov, H. Habara, K. A. Tanaka, J. P. Knauer, R. Lauck, F. J. Marshall, K. L. Marshall, D. D. Meyerhofer, P. M. Nilson, P. K. Patel, H. Chen, T. C. Sangster, W. Seka, N. Sinenian, T. Ma, F. N. Beg, E. Giraldez, and R. B. Stephens, Phys. Plasmas **18**, 056305 (2011).

3. T. R. Boehly, D. L. Brown, R. S. Craxton, R. L. Keck, J. P. Knauer, J. H. Kelly, T. J. Kessler, S. A. Kumpan, S. J. Loucks, S. A. Letzring, F. J. Marshall, R. L. McCrory, S. F. B. Morse, W. Seka, J. M. Soures, and C. P. Verdon, Opt. Commun. **133**, 495 (1997).

4. R. B. Stephens *et al.*, Phys. Rev. E **69**, 066414 (2004).

5. M. H. Key, J. C. Adam, K. U. Akli, M. Borghesi, M. H. Chen, R. G. Evans, R. R. Freeman, H. Habara, S. P. Hatchett, J. M. Hill, A. Heron, J. A. King, R. Kodama, K. L. Lancaster, A. J. MacKinnon, P. Patel, T. Phillips, L. Romagnani, R. A. Snavely, R. Stephens, C. Stoeckl, R. Town, Y. Toyama, B. Zhang, M. Zepf, and P. A. Norreys, Phys. Plasmas **15**, 022701 (2008).

6. L. Jarrott, M. S. Wei, H. Sawada, W. Theobald, A. A. Solodov, C. McGuffey, R. B. Stephens, C. Stoeckl, C. Mileham, F. Marshall, J. Delettrez, R. Betti, P. K. Patel, H. McLean, C. Chen, M. H. Key, T. Doeppner, T. Yabuuchi, T. Iwawaki, H. Habara, A. Greenwood, N. Alfonso, D. Hoover, E. Giraldez, and F. N. Beg, Bull. Am. Phys. Soc. **57**, 115 (2012).

7. W. Theobald, A. A. Solodov, C. Stoeckl, V. Yu. Glebov, S. Ivancic, F. J. Marshall, G. McKiernan, C. Mileham, T. C. Sangster, F. N. Beg, C. Jarrott, E. Giraldez, R. B. Stephens, M. S. Wei, M. H. Key, H. McLean, and J. Santos, Bull. Am. Phys. Soc. **57**, 115 (2012).

8. U. K. Akli, "Fast Ignition Experimental and Theoretical Studies," Ph.D. thesis, University of California at Davis, 2006.

9. J. Delettrez, R. Epstein, M. C. Richardson, P. A. Jaanimagi, and B. L. Henke, Phys. Rev. A **36**, 3926 (1987).

10. K. U. Akli, M. S. del Rio, S. Jiang, M. S. Storm, A. Krygier, R. B. Stephens, N. R. Pereira, E. O. Baronova, W. Theobald, Y. Ping, H. S. McLean, P. K. Patel, M. H. Key, and R. R. Freeman, Rev. Sci. Instrum. **82**, 123503 (2011).

11. Z. Zhong *et al.*, Nucl. Instrum. Methods Phys. Res. A **450**, 556 (2000).

12. M. Sanchez del Rio and R. J. Dejus, in *Advances in Computational Methods for X-Ray and Neutron Optics*, edited by M. Sanchez del Rio (SPIE, Bellingham, WA, 2004), Vol. 5536, pp. 171–174.

13. V. Bagnoud, I. A. Begishev, M. J. Guardalben, J. Puth, and J. D. Zuegel, Opt. Lett. **30**, 1843 (2005).

14. B. R. Maddox *et al.*, Rev. Sci. Instrum. **79**, 10E924 (2008).

15. A. L. Meadowcroft, C. D. Bentley, and E. N. Stott, Rev. Sci. Instrum. **79**, 113102 (2008).

Plasma-Ion–Assisted Coatings for 15-fs Laser Systems

Introduction

Interest in femtosecond (fs)-pulsed, high-intensity laser facilities continues to grow as evidenced by numerous large laser projects, including the Astra Gemini and Vulcan 10PW lasers at the Rutherford Appleton Laboratory, the Scarlet laser at Ohio State, the planned construction of the Apollon Laser Facility, the Extreme Light Infrastructure (ELI) project, and the planned construction of the Multi-Terawatt Optical Parametric Amplifier Line (MTW-OPAL) laser at the University of Rochester.[1–5] These laser facilities are designed to explore matter interactions with ultra-intense laser sources, necessitating the construction of high-energy, short-pulse lasers with ever-higher peak powers. Optical coatings capable of withstanding such high incident laser intensity must be developed and deposited on substrates at the beam size of these lasers, making it possible to create such laser facilities and achieve the desired laser intensities.

Electron-beam evaporation remains the primary optical coating technology for large-scale lasers, such as those used for inertial confinement fusion (ICF), although most coatings have been used for nanosecond (ns)- and picosecond (ps)-pulse durations.[6–11] The addition of plasma-ion–assisted deposition (PIAD) has also been successfully demonstrated for fabricating coatings for high-power lasers.[12,13] Since these technologies are readily available and have been proven successful in the production of meter-scale, high-laser-damage-threshold coatings, plasma-assisted evaporation has been selected for this development effort of large-aperture optical coatings for 15-fs applications.

Coatings for laser systems that must deliver compressed pulses of less-than-1-ps duration require more-stringent performance criteria than those for longer pulses, based on the wavelength-dependent group delay (GD), the group-delay dispersion (GDD), and higher-order dispersion terms resulting from the reflected phase from the coated surface. Spatial variations in the reflected phase over the optic aperture are particularly challenging since such variations cannot generally be compensated by other components in the laser system. Optical coatings for femtosecond applications require not only a controlled, smooth

GDD over the required bandwidth to maintain the temporal profile of the pulse but also a smooth phase across the optic aperture to provide consistent performance over the beam, so any coating technology pursued must be able to provide such performance over the desired substrate aperture.

This work describes the development of high-laser-damage-threshold coatings for a 15-fs optical parametric chirped-pulse–amplification (OPCPA) laser system having a spectral bandwidth of 810 to 1010 nm using plasma-ion–assisted electron-beam evaporation.[5] The high degree of sensitivity of controlled-phase coating designs requires that the coating performance be independent of relative humidity, thereby creating a need for a densified coating process producing low-porosity films. The use of optical coatings with high-peak-power laser systems necessitates high laser-damage thresholds, limiting potential coating materials and electric-field distributions within the coating structure. In addition, spatial control of phase-on reflection for the entire bandwidth is critical to preserving pulse length; coating deposition must be quite uniform, without high-spatial-frequency changes in the reflected phase of the coating. Coating requirements are demonstrated on 10-in. substrates, although the deposition process was designed to be scalable for use on meter-class laser system components, such as those in use at the National Ignition Facility, the Laser MégaJoule Facility, the OMEGA EP Laser System, and other fusion-class lasers.[6–11]

Background

The primary challenge when depositing coatings for femtosecond pulses is to preserve the compressibility of the temporal pulse. The consequence of a 15-fs temporal pulse is that its physical length is of the order of the thickness of an optical interference coating; in this case, the physical length of a 15-fs pulse would be 4.5 μm, or approximately five wavelengths of light. Each wavelength in the spectral bandwidth has a relative GD when reflecting from a multilayer optical coating, corresponding to the time that particular spectral region remains in the coating, since the interference effects of the coating may occur at different depths in the multilayer for

different wavelengths. In the case of a 15-fs pulse, differences in the delay will lead to a temporal broadening of the pulse since some wavelengths will be reflected from the outer layers of the coating while others will be reflected from farther within the mirror. Through proper design of the coating, adjustments to the delay for different wavelengths may be made, for example, by the use of Gires–Tournois interferometer structure(s), resulting in coatings with positive, negative, or neutral dispersion.[14] Any significant delays incorporated in the optical coating, however, are typically the result of resonant cavities, leading to the amplification of the electric field intensity and likely resulting in a significant reduction in the laser-damage threshold of the coating.[15–18] By properly selecting the coating materials and minimizing the electric-field intensity in the lower-bandgap layers, one can achieve significant improvements in the laser-damage threshold of the coating.[15–20]

The shape of the wavelength-dependent GDD is also an important consideration for pulse compression since low-order phase profiles may be able to be compensated by tuning the combination of the stretcher and compressor in an OPCPA system.[21] Furthermore, GDD ripple of one mirror may be reduced by using another compensating mirror with the inverse ripple in the GDD.[22–24] This requires a systems-level approach for optical coating design since a given GDD magnitude or profile may or may not be acceptable, depending on the other components in the system, and whether the dispersion is purely additive or if there are coatings that cancel accumulated dispersion. Such components, if they contain higher electric-field intensities as a result of resonant cavities, may be placed in positions of low electric-field intensity prior to pulse amplification to offset the dispersive properties of coatings in high-fluence regions of the system.

A primary challenge for the production of coatings for femtosecond applications remains the deposition of such coatings for large-aperture applications, given that most femtosecond coatings are produced by ion-beam or magnetron sputtering.[16,25–27] Precision deposition for large-area coatings is generally performed by electron-beam evaporation as a result of the relative ease of scaling the coating process; while some femtosecond coatings have been demonstrated using evaporation processes, low-dispersion, high-damage-threshold coatings suitable for use in a meter-class laser system have not been thoroughly investigated.[28,29] To maintain acceptable wavefront performance and dispersion characteristics of the coatings, thickness uniformity and thin-film stress must be controlled over the aperture of interest while limiting film defects that may lead to reduced laser-damage thresholds.[13,30–32]

To meet the spectral bandwidth of a coating, a quarter-wave reflector is typically constructed of alternating high- and low-index materials; the width of the reflector at normal incidence is given by

$$\Delta g = \frac{2}{\pi} \sin^{-1}\left(\frac{n_H - n_L}{n_H + n_L}\right), \tag{1}$$

where Δg is the half-width of the reflector in normalized frequency, n_H is the refractive index of the high-index material, and n_L is the refractive index of the low-index material.[33] The upper and lower normalized frequency bounds of the reflector are then given by

$$g_{edge} = 1 \pm \Delta g \tag{2}$$

with the corresponding wavelengths of the reflector edges given by

$$\lambda_{edge} = \lambda_0 / g_{edge}. \tag{3}$$

Using coating materials suitable for the visible spectrum and a center wavelength of 910 nm, the width of a reflector using $n_H = 2.2$ and $n_L = 1.45$ is insufficient to maintain high reflectance and low GDD for the spectral extent of a 15-fs pulse. At near-normal incidence, the design complexity must become much greater by using multiple reflectors or a geometric stack in order to achieve the desired bandwidth, leading to greater difficulties in obtaining the desired group delay for one spectral region relative to another. To achieve the desired bandwidth, a larger difference in refractive index (which is not available) must be used or the coating must be used in s-polarization at oblique incidence since the width of the reflector increases as the incidence angle increases. The use of a greater Δn for the layers of the reflector coating, where Δn is defined as $n_H - n_L$, leads to a broader reflectance band for a quarter-wave reflector as does the use of s-polarization at higher angles of incidence. As shown in Fig. 136.10, the use of a niobia $(n_H = 2.20)$/silica $(n_L = 1.45)$ reflector provides a significantly broader reflectance band than if hafnia $(n = 2.05)$ is used as the high-index material, although based on the work of Mangote et al., the expected laser-damage resistance is less than half that of hafnia.[20,33]

Experiment

An initial series of dielectric coatings were prepared in a cryo-pumped, 54-in. coating chamber equipped with quartz heater lamps, dual electron-beam guns, multipoint quartz crystal monitoring, and planetary substrate rotation. Granular
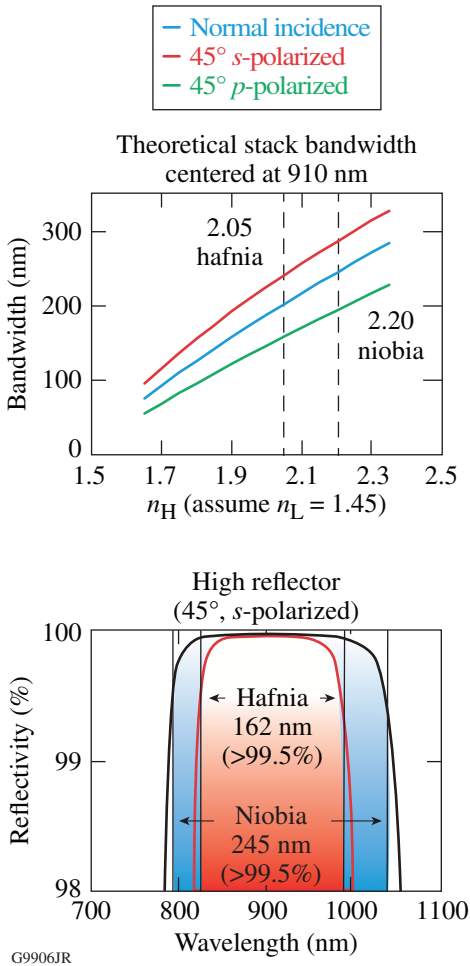
Figure 136.10

(a) Dependence of a high-reflector stack width on n_H, assuming $n_L = 1.45$, for normal and 45°-incidence use. (b) Theoretical width of an *s*-polarized reflector at 45° incidence is significantly broader for a niobia/silica coating than for a hafnia/silica coating. Using the reflector in *s*-polarization at high incidence angles broadens the reflectance band, while using *p*-polarization narrows the usable spectral bandwidth.

To meet the required spectral bandwidth using a traditional quarter-wave reflector, different material combinations, angles of incidence, and polarizations were evaluated. For an all-dielectric solution, it was determined that a 45°-incidence, *s*-polarized quarter-wave reflector fabricated with refractive indices of 2.20 (Nb_2O_5) and 1.45 (SiO_2) would be sufficient to meet the 810- to 1010-nm bandwidth with relatively low dispersion effects. Using a high-index material with a refractive index of less than 2.20 would require a greater angle of incidence with a corresponding larger substrate or a more-complex design to broaden the reflectivity while controlling the dispersion properties, typically resulting in higher electric-field intensities and an associated reduction in damage thresholds. To provide broader bandwidths, *p*-polarized reflectors, and lower-incidence angles, more-complex dielectric coatings with potentially higher GD, GDD, and electric-field intensity may be considered, or it will become necessary to use coatings based on a metal reflector.

Coating deposition for the all-dielectric coatings was performed at a substrate temperature of 120°C to stabilize the deposition temperature in the presence of heating from the electron-beam guns and plasma source. Niobia and hafnia were deposited at a deposition rate of 0.12 nm/s, silica at 0.4 nm/s, and alumina at 0.2 nm/s. Metal coatings were deposited at ambient temperature, with the only substrate heating resulting from the deposition and plasma sources. Copper was deposited at 1 nm/s, while silver was deposited as quickly as possible for maximum reflectance without ejection of defects from the source, which was determined to be ~1.8 nm/s.

The positions of the electron-beam guns and planetary rotation geometry were configured for uniform deposition over the substrate aperture without the use of uniformity masks; the goal was to limit phase discontinuities in the coating resulting from disruptions in the vapor plume caused by uniformity masking.[30,34] A custom planetary rotation was designed and fabricated with three 13-in. planets alternating with three 4-in. planets designed for through-planet optical monitoring as shown in Fig. 136.11. All components were fabricated with precise manufacturing tolerances to ensure minimal thickness errors from differences in planet height or angular tilt with respect to the planet axis of rotation. The smaller-diameter rotation system makes higher revolution speeds possible, ensuring greater averaging of the deposition and a more-uniform coating. Comparable performance could also be achieved by reducing the deposition rate of the dielectric materials if it became necessary to coat larger substrates that could not practically be rotated at such high speeds.

silicon dioxide was evaporated from a continuously rotating pan, while niobium, hafnium, silver, copper, and aluminum oxide were deposited from a six-pocket electron-beam gun. A Thin Film Solutions plasma source was installed in the chamber to provide densification and more-complete oxidation of the niobium and hafnium. The plasma source was operated with a beam voltage of 160 V with a 35-A discharge current for deposition of dielectric coatings with an oxygen flow of 55 sccm introduced through the process gas ring above the plasma source. The plasma source was reduced to a 5-A discharge current with no oxygen flow for deposition of metal layers as well as the first 15 nm of alumina deposited over the silver to minimize oxidation of the silver surface.

Coating designs of alternating niobia and silica layers were selected to flatten GDD, minimize the standing-wave electric-field intensity, and achieve a compromise between the two goals. The influence of film nonuniformity was also evaluated by theoretically propagating a pulse through a system containing 25 identical mirrors with 1% uniformity errors. The theoretical performance of the coating designs is shown in Figs. 136.12(a)–136.12(c). Adjustments to the stretcher/compressor angles and distances provide for up to third-order phase-error compensation; consequently, coating designs that
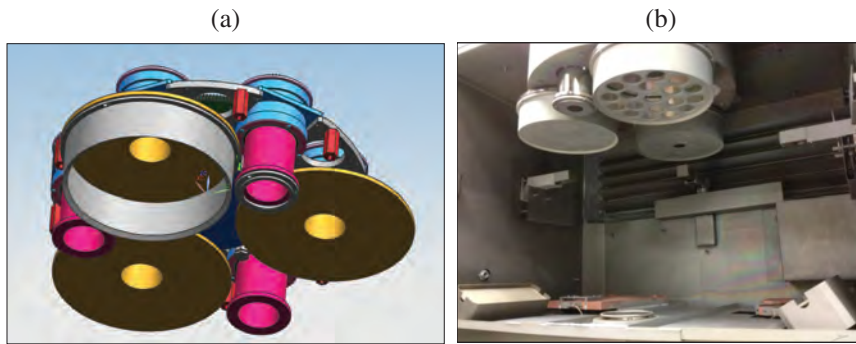
Figure 136.11
(a) Design of a precision planetary rotation system for high-speed rotation of substrates up to 310 mm in diameter, as well as the (b) fabricated rotation installed in a 54-in. coating diameter. Substrate planets alternate with 100-mm planets, making through-planet optical monitoring possible. System geometry is configured for uniform deposition over the substrate aperture without the use of shadow masks.

G9899JR
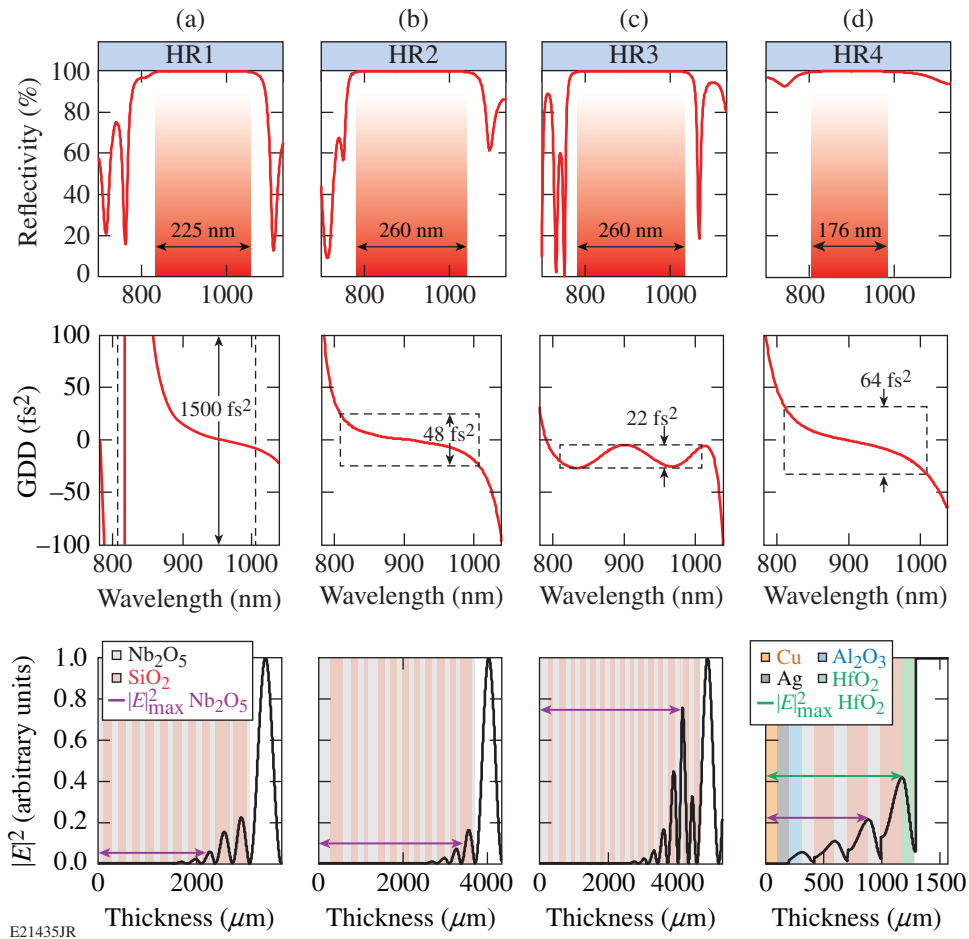
E21435JR

Figure 136.12
Theoretical reflectance, group-delay dispersion, and standing-wave electric-field intensity within the coating structure for HR1–HR4. Note that HR1–HR3 are for *s*-polarization, while HR4 is for *p*-polarized usage. Reflectance bandwidth is indicated for $R > 99.5\%$.

provide a phase-on reflection that closely fits a third-order polynomial are preferred to designs with less dispersion containing higher-order phase terms.[21]

While the all-dielectric design meets the specifications for an *s*-polarized reflector, a *p*-polarized reflector is also required. No low-GDD, all-dielectric design has been identified that is expected to maintain high laser-damage thresholds, owing to the enhanced electric-field intensities within the coating structure required for dispersion control. Instead, an enhanced silver coating was developed, as shown in Fig. 136.12(d). A copper underlayer was incorporated between the substrate and the silver layer to improve environmental durability; the dielectric enhancement layers consist of alumina (adhesion to the silver), niobia/silica (maximum Δn for reflectivity and spectral bandwidth), and hafnia (laser-damage resistance in the highest electric-field intensity).[35] The design for this coating can be expressed as

$$\text{substrate}/\text{Cu Ag A}\left(\text{NS}\right)^3\text{H}/\text{air}, \qquad (4)$$

where A, N, S, and H represent nominally one quarter-wave optical thickness of alumina, niobia, silica, and hafnia, respectively, and the superscript "3" denotes a repetition of the included layers. The theoretical performance of such a coating meets reflectivity and dispersion requirements, with laser-damage thresholds remaining as the primary concern. For comparison, a protected silver mirror with a nominal half-wave optical thickness of alumina as well as an enhanced silver mirror with two hafnia/silica pairs of enhancement layers were also deposited.

These coatings are being developed for use with a 15-fs pulse having a spectral bandwidth of 810 to 1010 nm; however, a laser-damage test facility with this capability has not been identified. As a result, laser-damage thresholds have been evaluated with a number of different systems, with different center wavelengths, temporal pulse lengths, use environment, and evaluation criteria. The primary testing for femtosecond-coating performance was performed by Lidaris (formerly VULRC, Vilnius University) with an 800-nm laser and a 59-fs pulse. Damage testing was also performed at LLE by systems at 1053 nm with 1-ns, 10-ps, and 0.6-ps pulse durations, with testing at the nanosecond- and picosecond-pulse durations in accordance with the protocols described by Papernov and Howard, respectively.[36,37] In all cases, coating designs were adjusted from a nominal 910-nm center wavelength to center the coating performance at the wavelength being tested. All laser-damage thresholds are reported as the fluence of the incident beam; i.e., as the coating surface is adjusted to a greater angle of incidence relative to the incident laser, the beam fluence remains constant while the fluence on the surface is decreased by the cosine of the angle of incidence.

Accurate dispersion measurement was also not available at LLE. Sample coatings were evaluated with a beta version of a KMLabs *Chromatis* white-light interferometer for characterizing GDD. Measurements were compared to expected theoretical performance using this system, and further characterization will be pursued as possible. Initial results showed that HR2 and HR3 performed consistent with the theoretical GDD shown in Fig. 136.12, with an estimated measurement accuracy of ± 10 fs^2.

Results

Source positions for niobium and silicon dioxide were optimized individually to provide uniform deposition over the substrate aperture by adjusting the radial distance from the chamber center and the source height, with multilayer uniformity evaluated based on the performance of a modified Grezes–Besset stack as described by Baumeister.[38] Optimal source positions were found to be 520 mm from center for niobium with a source-to-substrate distance of 606 mm, while the silica source was located 509 mm from chamber center with a source-to-substrate distance of 584 mm. The slight difference in optimal source position can be attributed to differences in the vapor plume shape of the two materials, as well as the extended size of the silica source relative to the small spot evaporation of the niobium. The multilayer thickness uniformity based on measurements of five samples distributed over a 254-mm aperture was determined to be $\pm 0.04\%$ by characterizing a best fit of the spectral data in OptiRE shown in Fig. 136.13 (Ref. 39). The uniformity was found to be sensitive to changes in source height of the order of 1 to 2 mm, requiring significant care in the loading of sources particularly for silicon dioxide granules, which were ~3 mm in size.

Samples of HR1–HR4 as described in Fig. 136.12 were deposited on 50.8-mm-diam fused-silica substrates. Analysis of the coating performance included simulations of the effects of the coating on a theoretical system containing 25 mirrors, assuming second- and third-order dispersion effects could be compensated by tuning the stretcher/compressor combination. Figure 136.14 shows the impact on the temporal pulse shape assuming a system of 25 identical mirrors for each of the coating designs. HR2 has a moderate amplitude with a low-order dispersion that can be compensated through stretcher/compressor adjustments.
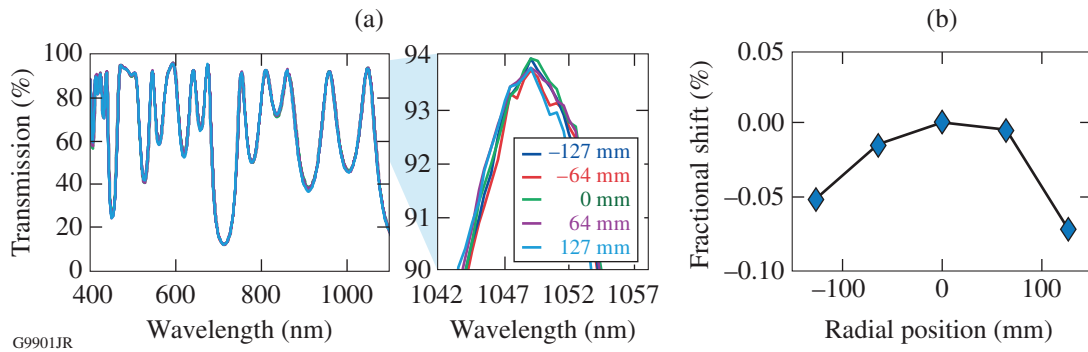
G9901JR

Figure 136.13
Measured thin-film uniformity over a 254-mm aperture based on system geometry. (a) Overlay of the spectral transmittance shows a negligible variation in coating performance among the samples. (b) Curve fitting and normalization of film thickness indicate film nonuniformity is of the order of ±0.04%. Thickness variations are slowly varying, with minimal phase errors since the film deposition is continuous with no shadow masks between the source and substrate.
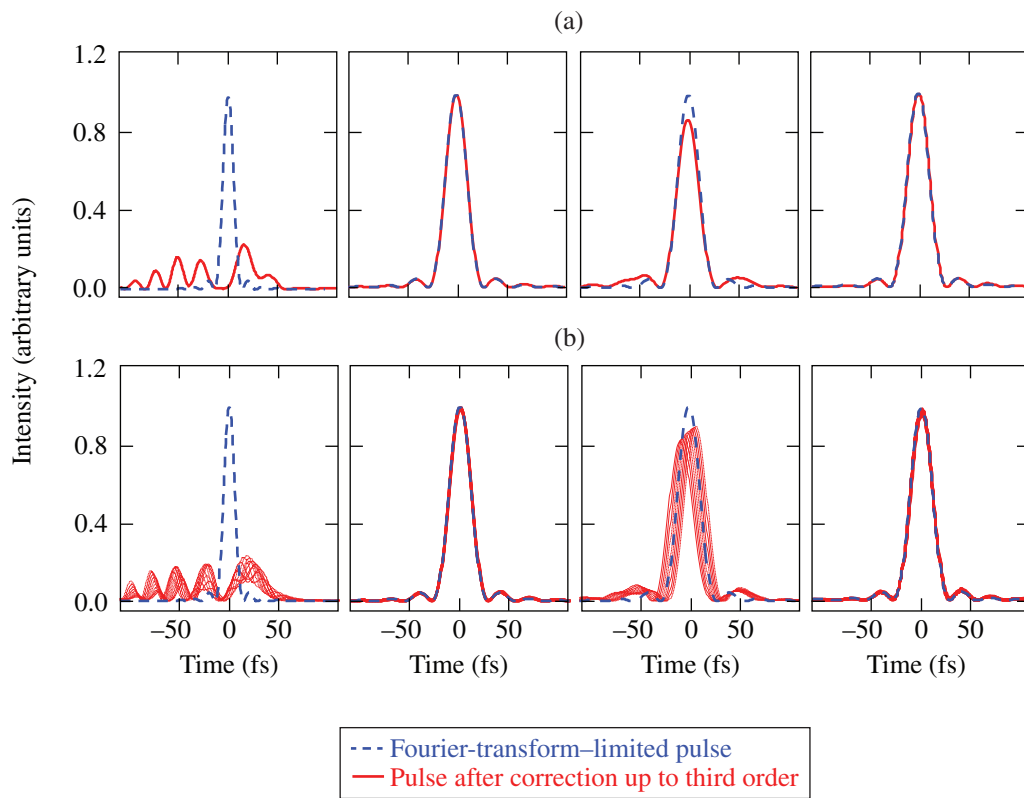

E21439JR

Figure 13.14
Impact on the temporal pulse shape for a theoretical system containing 25 mirrors of HR1, HR2, HR3, and HR4. The second- and third-order phase error resulting from dispersion is removed, based on the assumption that such error can be compensated by stretcher/compressor tuning. The performance in (a) is based strictly on the dispersion of the mirrors, while (b) assesses the impact of 1% film thickness nonuniformity over the mirror aperture.

Laser-damage testing by Lidaris at 59 fs required deposited coatings that were spectrally centered at an 800-nm wavelength to align with the test capability. The nominal S:1 laser-damage thresholds (beam fluence) of HR1, HR2, and HR3 were measured to be 1.64 J/cm^2, 1.16 J/cm^2, and 0.12 J/cm^2, respectively,

indicating a strong correlation with the maximum electric-field intensity in the niobia layers, as shown in Fig. 136.15. Based on the work of Mero *et al.*, it is expected that use with a 15-fs pulse will result in a reduction of the damage threshold of approximately 1/3, using a $\tau^{0.3}$ scaling law.[40]

The laser-damage threshold of the enhanced silver coating HR4 is also shown in Fig. 136.15, with its performance at 0.69 J/cm^2 remaining consistent with that of HR1–HR3 based on the electric-field intensity in the outer high-index layers. Note that the damage threshold of HR4 is higher than expected [above the dashed line in Fig. 136.15(b)] based on the electric-field intensity in the outermost layer, which is hafnia, but this would correspond to the larger bandgap of hafnia relative to that of niobia in HR1–HR3, in agreement with the findings of Mangote *et al.*[20]
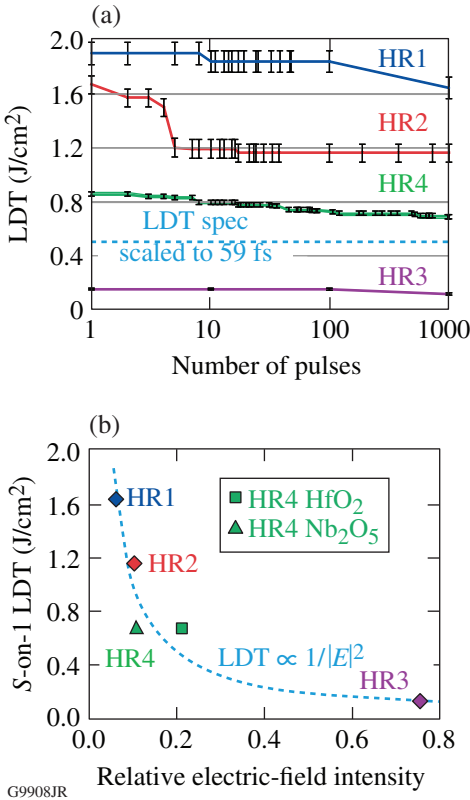

Figure 136.15
(a) Laser-damage thresholds (LDT's) of HR1–HR4 as tested by Lidaris using a 59-fs pulse with a center wavelength of 800 nm. (b) The performance of each coating is consistent with its relative electric-field intensity in the air-side high-index layer, indicating the damage is driven by the low electronic bandgap of the high-index material. Manipulation of the relative intensity of the electric field provides higher damage thresholds in HR1 and HR2.

Based on the performance of HR4 as a *p*-polarized reflector and the inherent broad reflectance and low GDD, two additional silver-based coatings were evaluated. Evaporated Cu/Ag metallic coatings were overcoated with a half-wave optical thickness of alumina (substrate/Cu Ag 2A/air) as well as enhanced with two dielectric pairs of layers (substrate/Cu Ag AHSH/air),

where A, H, and S are as defined previously. As the number of layer pairs in the dielectric overcoat is reduced, the reflectivity, in general, is decreased but the GDD is improved, approaching 0 fs^2 for a layer of bare silver. As shown in Fig. 136.16, the laser-damage performance of the silver mirrors remains similar, with HR4 shown to have the lowest average damage threshold of the three mirror designs. As additional dielectric enhancement layers are added, the electric-field intensity at the silver layer is reduced, with an expected improvement in laser-damage threshold; since the hafnia-overcoated metal mirrors consistently have the highest laser-damage threshold, it appears the damage threshold remains a function of the bandgap of the high-index dielectric layer and not the metallic layers beneath.
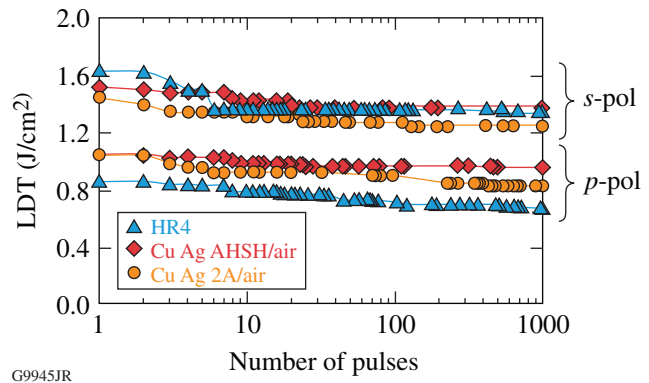

Figure 136.16
Laser-damage thresholds of silver-based mirrors as tested by Lidaris using a 59-fs pulse with a center wavelength of 800 nm. Damage thresholds for *s*-polarization remain consistently higher than those for *p*-polarization.

This work is intended for use over large apertures, with initial coating requirements for a 254-mm aperture, and ultimate potential needs of the order of a 1-m aperture. Based on the results above concerning temporal pulse shape and laser-damage threshold, HR2 was selected for demonstration on a larger-aperture substrate. The coating was deposited on a 310-mm-diam by 14-mm-thick fused-silica substrate, with a surface deviation of less than $\lambda/10$ from flat. The primary concerns for scale-up include spatial irregularities in the reflected phase leading to variations in GDD and surface flatness, with minimal variation in reflectivity assured, given the measured film-thickness nonuniformity. The HR2 coating was deposited and the reflected wavefront performance was measured on an 18-in. phase-shifting Zygo interferometer operating at 1064 nm. The wavefront performance is shown in Fig. 136.17.

The optical power of 1.76 waves at 1064 nm, as measured in Fig. 136.17(b), corresponds to a thin-film stress of the order of 150 MPa based on Stoney's equation. A flatter coated surface
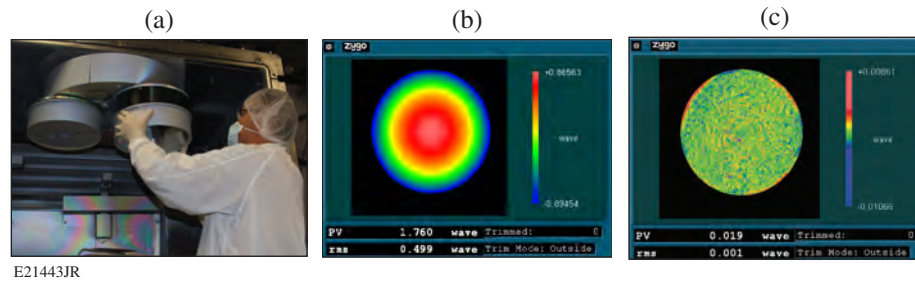
Figure 136.17
(a) The deposition process was demonstrated on a 310-mm-diam substrate, with (b) the flatness of the coated substrate in ~150 MPa of thin-film stress. (c) Removal of the stress-induced surface deformation results in a remaining spatial phase error of a random speckle pattern below the resolution of the interferometer.

may be realized by increasing the substrate thickness or depositing a compensating coating on the rear surface of the optic. As shown in Fig. 136.17(c), removing the stress-induced power and astigmatism from the wavefront map leads to a wavefront error indistinguishable from the noise of the interferometer resolution, with no discernible pattern indicative of spatial phase error from the substrate rotation, shadows, or other irregularities in the coating process. This shows that the deposition process provides a smooth optical phase-on reflection suitable for use with femtosecond optical pulses.

Future Work

Development of improved high-reflector coating designs is continuing, based on minimizing the electric-field intensity in high-refractive-index layers, maximizing the electronic band-gap of all coating materials in regions of high electric-field intensity, and controlling GDD as possible with metallic layers. Magnetron sputtering of metallic coatings will be evaluated as a means of limiting film defects for silver and copper deposition.

Remaining optical-coating challenges to be demonstrated for construction of the MTW-OPAL laser include a beam combiner/separator for the pump and signal beams as they enter and exit the nonlinear crystals for amplification of the signal pulse. To minimize the impact on GDD, a configuration transmitting the signal and reflecting the 527-nm pump laser has been selected for this dichroic filter. Operating at Brewster's angle for a p-polarized signal beam and an s-polarized pump beam eliminates the need for a second-surface antireflection coating. In addition, a filter is also required to reject the idler beam (1100 to 1505 nm) resulting from the parametric amplification process. Since the signal must again be propagated without negatively impacting the spectral phase, a transmissive coating design was selected for this application, with the idler being reflected at 56° incidence in s-polarization, in order to provide a sufficiently broad spectral width of the reflectance

band and to reject the full spectrum of the idler beam. Measured performance of current demonstrations of these coatings is shown in Fig. 136.18, with both coating designs having a
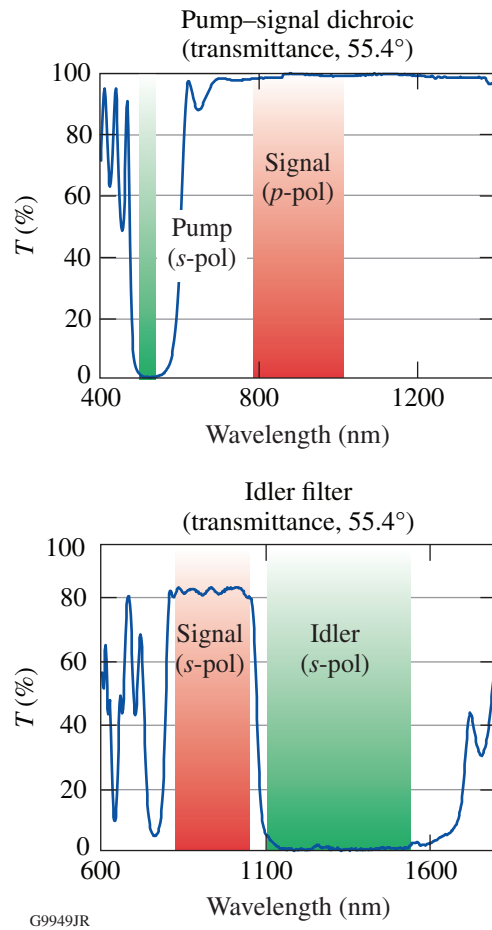

Figure 136.18
(a) Filters for the pump–signal combiner/separator and (b) removal of the idler from the co-propagating signal beam. Performance of both filter types has been successfully demonstrated for small apertures.

negligible impact on the theoretical GDD of the signal beam in transmission.

A final challenge is the deposition of a reflective coating for the final focusing optic. As the pulse is focused onto target, the beam will be full fluence with a compressed, 15-fs pulse. Dispersion and nonlinear refractive index of optical glasses necessitates the use of a reflective focusing optic, although a radially dependent GD and GDD resulting from coating nonuniformity over the curved substrate surface may lead to broadening of the temporal pulse at the focus if a dielectric interference coating is used. Metallic coatings may not possess a sufficiently high laser-damage threshold for the highest-fluence region of the optical system. At this time, modifying the radial source position within the overall system geometry is being pursued to match the coating-thickness distribution over the curvature of the substrate surface. Current models indicate adjustments in source position relative to chamber center are sufficient to compensate expected film nonuniformity caused by substrate curvature. This will be pursued further once an optical system design has been completed for MTW-OPAL, specifying the dimensions and curvature of the final focusing optic.

Conclusions

A process for producing plasma-assisted evaporated coatings with high reflectivity, high laser-damage thresholds, and controlled dispersion over large apertures has been developed. Demonstrated performance of an all-dielectric solution for a 45°-incidence, *s*-polarized reflector over a range of 810 to 1010 nm includes $R > 99.5\%$, a laser-damage threshold of >1.1 J/cm^2 (coating design shifted to be centered at 800 nm and tested with a 59-fs pulse), and a low-order (correctable) GDD < 50 fs^2. It has been shown that laser-damage performance depends on the maximum electric-field intensity in the high-refractive-index layers, with improved performance for larger-bandgap high-index materials, such as hafnia. Film-thickness nonuniformity is less than 0.1% over a 254-mm aperture, with spatial phase errors remaining well controlled, successfully limiting the spatial-dependent mirror dispersion. Such a coating is suitable for the propagation of 15-fs pulses with negligible degradation of the transform-limited pulse shape, based on temporal modeling with stretcher/compressor compensation.

Near-normal incidence and 45°-incidence, *p*-polarized reflectors have been demonstrated using protected and enhanced silver coatings. The dispersion performance of an enhanced silver coating is much better than that of the all-dielectric solution, with comparable reflectivity; while *p*-polarized damage thresholds are lower, *s*-polarized performance of the metallic coatings is comparable or better than that shown by the all-dielectric films. The performance achieved is readily scaled from the 254-mm aperture demonstrated to larger optics, using plasma-assisted evaporation coating systems.

REFERENCES

1. O. Chekhlov *et al.*, in *High Power Lasers for Fusion Research II*, edited by A. A. S. Awwal (SPIE, Bellingham, WA, 2007), Vol. 6735, Paper 67350J.

2. J. P. Chambaret *et al.*, in *Solid State Lasers and Amplifiers IV, and High-Power Lasers*, edited by T. Graf *et al.* (SPIE, Bellingham, WA, 2010), Vol. 7721, Paper 77211D.

3. G. Overton, Laser Focus World **48**, 15 (2012).

4. G. A. Mourou *et al.*, Plasma Phys. Control. Fusion **49**, B667 (2007).

5. J. Bromage, C. Dorrer, M. Millecchia, J. Bunkenburg, R. Jungquist, and J. D. Zuegel, in *Conference on Lasers and Electro-Optics 2012*, OSA Technical Digest (online) (Optical Society of America, 2012), Paper CTh1N.7.

6. J. H. Campbell *et al.*, in *Optical Engineering at the Lawrence Livermore National Laboratory II: The National Ignition Facility*, edited by M. A. Lane and C. R. Wuest (SPIE, Bellingham, WA, 2004), Vol. 5341, pp. 84–101.

7. J. B. Oliver, J. Howe, A. Rigatti, D. J. Smith, and C. Stolz, in *Optical Interference Coatings*, OSA Technical Digest Series (Optical Society of America, Washington, DC, 2001), Paper ThD2.

8. B. Pinot *et al.*, in *Laser-Induced Damage in Optical Materials 2001*, edited by G. J. Exarhos *et al.* (SPIE, Bellingham, WA, 2002), Vol. 4679, pp. 234–241.

9. E. Lavastre *et al.*, in *Optical Interference Coatings*, OSA Technical Digest Series (Optical Society of America, Washington, DC, 2004), Paper TuF3.

10. J. B. Oliver, T. J. Kessler, H. Huang, J. Keck, A. L. Rigatti, A. W. Schmid, A. Kozlov, and T. Z. Kosc, in *Laser-Induced Damage in Optical Materials: 2005*, edited by G. J. Exarhos *et al.* (SPIE, Bellingham, WA, 2005), Vol. 5991, Paper 59911A.

11. J. Bellum *et al.*, in *Laser-Induced Damage in Optical Materials: 2009*, edited by G. J. Exarhos *et al.* (SPIE, Bellingham, WA, 2009), Vol. 7504, Paper 75040C.

12. R. Thielsch *et al.*, Thin Solid Films **410**, 86 (2002).

13. J. B. Oliver, P. Kupinski, A. L. Rigatti, A. W. Schmid, J. C. Lambropoulos, S. Papernov, A. Kozlov, J. Spaulding, D. Sadowski,

Z. R. Chrzan, R. D. Hand, D. R. Gibson, I. Brinkley, and F. Placido, Appl. Opt. **50**, C19 (2011).

14. R. Szipöcs *et al.*, Opt. Lett. **19**, 201 (1994).

15. C. K. Carniglia *et al.*, in *Laser Induced Damage in Optical Materials: 1983*, edited by H. E. Bennett *et al.*, Natl. Bur. Stand. (U.S.), Spec. Publ. 688 (U.S. Government Printing Office, Washington, DC, 1985), pp. 347–353.

16. K. Starke, T. Groß, and D. Ristau, in *Laser-Induced Damage in Optical Materials: 2000*, edited by G. J. Exarhos *et al.* (SPIE, Bellingham, WA, 2001), Vol. 4347, pp. 528–534.

17. S. Chen *et al.*, Appl. Opt. **51**, 6188 (2012).

18. J. H. Apfel, Appl. Opt. **16**, 1880 (1977).

19. J. B. Oliver, S. Papernov, A. W. Schmid, and J. C. Lambropoulos, in *Laser-Induced Damage in Optical Materials: 2008*, edited by G. J. Exarhos *et al.* (SPIE, Bellingham, WA, 2008), Vol. 7132, Paper 71320J.

20. B. Mangote *et al.*, Rev. Sci. Instrum. **83**, 013109 (2012).

21. S. Kane and J. Squier, J. Opt. Soc. Am. B **14**, 1237 (1997).

22. F. X. Kärtner *et al.*, J. Opt. Soc. Am. B **18**, 882 (2001).

23. F. X. Kärtner *et al.*, U.S. Patent No. US6,590,925 B1 (8 July 2003).

24. V. Pervak *et al.*, Opt. Express **17**, 7943 (2009).

25. F. X. Kärtner *et al.*, Opt. Lett. **22**, 831 (1997).

26. V. Pervak *et al.*, Opt. Express **16**, 10220 (2008).

27. V. Pervak *et al.*, in *Advances in Optical Thin Films II*, edited by C. Amra, N. Kaiser, and H. A. Macleod (SPIE, Bellingham, WA, 2005), Vol. 5963, Paper 59631P.

28. M. Bischoff *et al.*, in *Advances in Optical Thin Films II*, edited by C. Amra, N. Kaiser, and H. A. Macleod (SPIE, Bellingham, WA, 2005), Vol. 5963, Paper 59631N.

29. Z. Jinlong *et al.*, Appl. Opt. **50**, C388 (2011).

30. J. B. Oliver and D. Talbot, Appl. Opt. **45**, 3097 (2006).

31. C. J. Stolz *et al.*, in *27th Annual Boulder Damage Symposium: Laser-Induced Damage in Optical Materials: 1995*, edited by H. E. Bennett *et al.* (SPIE, Bellingham, WA, 1996), Vol. 2714, pp. 374–382.

32. C. J. Stolz, M. D. Feit, and T. V. Pistor, Appl. Opt. **45**, 1594 (2006).

33. H. A. Macleod, *Thin-Film Optical Filters*, 4th ed., Series in Optics and Optoelectronics, edited by E. R. Pike and R. G. W. Brown (CRC Press, Boca Raton, FL, 2010), pp. 222–223.

34. S. K. Yao, J. Appl. Phys. **50**, 3390 (1979).

35. D.-Y. Song *et al.*, Appl. Opt. **24**, 1164 (1985).

36. S. Papernov and A. W. Schmid, J. Appl. Phys. **82**, 5422 (1997).

37. H. P. Howard, A. F. Aiello, J. G. Dressler, N. R. Edwards, T. J. Kessler, A. A. Kozlov, I. R. T. Manwaring, K. L. Marshall, J. B. Oliver, S. Papernov, A. L. Rigatti, A. N. Roux, A. W. Schmid, N. P. Slaney, C. C. Smith, B. N. Taylor, and S. D. Jacobs, Appl. Opt. **52**, 1682 (2013).

38. P. Baumeister, *Optical Coating Technology* (SPIE Optical Engineering Press, Bellingham, WA, 2004), pp. 9-56–9-57.

39. A. V. Tikhonravov and M. K. Trubetskov, OptiLayer Thin Film Software, Optilayer Ltd., http://www.optilayer.com (9 June 2005).

40. M. Mero *et al.*, Phys. Rev. B **71**, 115109 (2005).

Spectral and Temporal Properties of Optical Signals with Multiple Sinusoidal Phase Modulations

Introduction

High-energy laser systems have been developed for exploring regimes of high-intensity interaction of light with matter, e.g., plasma physics, astrophysics, and the generation of particles. One application of these lasers is inertial confinement fusion (ICF)—a strategy for producing energy by compressing and heating capsules filled with hydrogen isotopes and igniting fusion reactions that release a large number of energetic neutrons.[1,2] Laser systems developed for ICF are large-scale complex optical systems that must produce temporally shaped optical pulses containing megajoules of energy in the ultraviolet (UV).[3,4] The laser–target interaction is an intensity-dependent process that requires the time-dependent power of the optical pulses to be precisely shaped. Temporal phase modulation must be added to prevent damage to the laser system and smooth out intensity variations at the surface of the target. High-intensity narrowband optical waves lead to stimulated Brillouin scattering (SBS) in optical components with potentially catastrophic consequences.[5] The growth of SBS waves is inhibited by increasing the bandwidth of the optical wave, typically by phase modulation in the low-energy front end to generate multiple sidebands. Phase modulation at a few GHz's with index modulation sufficient to create approximately ten sidebands is used on systems like the National Ignition Facility (NIF) and the Laser Mégajoule Facility (LMJ).[5–7] Uniform compression of the target is required to reach the conditions for fusion in the target core, but such compression is hindered by instabilities.[8] Smoothing by spectral dispersion (SSD) reduces the fluence variations of individual beams to produce a target irradiation that is spatially uniform on a time-averaged basis.[9–11] SSD uses temporal phase modulation to induce a time-dependent instantaneous frequency on the optical pulse. A phase plate placed before the focusing component at the end of the laser system creates a highly modulated far field composed of speckles.[12] A diffractive component in the laser system ensures that the far-field position depends on the optical frequency. The combination of time-varying instantaneous frequency, frequency-dependent far-field position, and highly modulated far field is used to obtain a uniform target illumination when averaged over the duration of the optical pulse. The NIF and the LMJ were built for indirect drive—an approach to ICF where the target is compressed by x rays generated when the optical pulses interact with the walls of a hohlraum.[1] In this approach, phase modulation at a single frequency with a modulation index of a few radians is sufficient for SSD when implemented with angular dispersion in only one direction. In the direct-drive approach to ICF, the optical pulses directly compress the target.[2] If SSD is implemented in only one direction, modulation at multiple frequencies is required, at least during the low-energy portion of the pulse shape.[11,13] Theoretical studies and experimental demonstration of a system combining pulses with three high-frequency phase modulations and pulses with SBSS (SBS suppression) and single-frequency SSD have been performed.[14–16] Optical pulses with multiple temporal phase modulations are routinely used on these high-energy laser facilities for reducing the threat of SBS and optimizing the target illumination by SSD.

A known issue when using phase-modulated optical pulses is the conversion of frequency modulation to amplitude modulation (FM-to-AM conversion).[7,17–19] A pulse of constant power with a single sinusoidal temporal phase modulation at frequency f has spectral sidebands at frequencies separated by f with spectral density given by Bessel functions of the first kind and precise phase relations.[20] When the spectral amplitude and/or phase of these sidebands are modified, the power becomes time dependent, e.g., it has a sinusoidal modulation at frequency f. A modification of the time-varying power of the shaped pulse might be detrimental to the interaction of the pulse with the target. It can also lead to optical damage in the laser system by increasing the peak power beyond the damage threshold of optical components. Sources of FM-to-AM conversion include chromatic dispersion, wavelength-dependent gain of laser amplifiers, generation of low-energy replicas interfering with the main signal, and spectral clipping. Studies of FM-to-AM conversion in pulses with a single phase modulation are available in the literature. Examples of FM-to-AM conversion of signals with SBSS at 2 GHz and SSD at 14.25 GHz have been presented in the context of the LMJ,[7] but no general study for pulses with multiple phase modulation (multi-FM) has been published. This study is highly relevant to the operation of cur-

rent systems and engineering of future systems because these systems typically use phase modulation at multiple frequencies.

This article first presents a statistical study of the optical spectrum of multi-FM signals. The optical spectrum of these signals is shown to converge to a normal distribution using an analogy with the statistical properties of the probability density function of the sum of independently distributed variables, which allows one to use the central limit theorem. Convergence of the frequency integral of the spectral density to the cumulative density function of the normal distribution makes it possible to predict the frequency range containing a given fraction of the total energy. The statistical study is followed by general derivations of FM-to-AM conversion in optical signals with multiple phase modulations from linear and quadratic spectral amplitude modulation, for example, resulting from spectral filters and optical amplifiers and from quadratic and cubic spectral phase modulations, for example, caused by chromatic dispersion in optical fibers in the front end. These impairments are inherently present in high-energy laser systems because of their architecture and component availability. Compensation subsystems must be developed so that the transfer function of the entire laser system does not lead to FM-to-AM conversion. These compensators are, for example, Lyot-type filters that compensate for the gain narrowing in a Nd:glass amplifier and a grating compressor that compensates for chromatic dispersion.[6,16] The design and performance of these subsystems are intrinsically linked to understanding the modulation magnitude in critical parts of the system where optical damage might occur. FM-to-AM conversion caused by the nonlinear frequency conversion from the infrared to the ultraviolet is not treated but could be the subject of further studies based on what is already known for single-frequency modulation.[7,18,19,21] FM-to-AM conversion from free-space propagation close to image planes of the diffraction grating used for SSD is described by a quadratic spectral phase[7,14] and can be treated with the same formalism. Another source of FM-to-AM conversion in high-energy laser systems is the interference of multiple replicas of the main pulse generated during amplification in the fiber front end.[17,22] This is inherent to the propagation of polarized signals in polarization-maintaining optical fibers having a finite extinction ratio, but the associated AM can be significantly reduced via engineering, in particular using optical fibers that transmit light along only one well-defined polarization[17] or alternating the orientation of the fast and slow axes of the optical fibers.[22]

For the impairments considered in this article, the amplitude modulation is evaluated by two metrics without frequency resolution: peak-to-valley (PV) and root-mean-square (rms) modulation on the temporal pulse, and by the PV modulation at specific frequencies. The specific frequencies are the individual modulation frequencies f_n in the case of linear amplitude modulation and quadratic phase modulation. They are the sums and differences of modulation frequencies $f_i \pm f_j$ for quadratic amplitude modulation and cubic phase modulation. Evaluating the amplitude modulation on the temporal pulse is crucial to setting allowable limits for individual impairments. Evaluating the modulation at specific frequencies helps to interpret time-resolved measurements provided by high-bandwidth diagnostics. Bandwidth-limited measurements of the instantaneous power can be interpolated at high frequencies not measured by the diagnostic. It is conceivable that limiting impairments can be identified from the spectral signature of the measured relative modulations at different frequencies.

The following sections (1) present general notations and definitions; (2) present a statistical approach to predicting the spectrum of signals with multiple sinusoidal phase modulations and frequency intervals containing a given fraction of the total energy; (3) describe FM-to-AM conversion in the presence of linear amplitude modulation and quadratic phase modulation, which leads to amplitude modulation at the phase-modulation frequencies; (4) detail FM-to-AM conversion in the presence of quadratic amplitude modulation and cubic phase modulation, which leads to amplitude modulation at combinations of the phase-modulation frequencies; and (5) present additional considerations and conclusions.

General Considerations

1. Definitions

An initially monochromatic field at the frequency ω_0 is modulated at multiple microwave frequencies $f_j = \Omega_j / 2\pi$ with respective modulation index m_j. For simplification, the oscillating term resulting from ω_0, present in all the temporal fields, is not written, and spectral fields are consistently plotted after translation by ω_0; i.e., with a zero carrier frequency. The phase modulations are co-phased at $t = 0$ for the derivation of FM-to-AM conversion. One reason for doing so is that for a small number of modulation frequencies, one can identify a time around which the sinusoidal modulations are co-phased, i.e., reach a maximum. This is justified by the absence of correlation for the values of sinusoidal modulations at non-commensurate frequencies. As such, the probability that one reaches a maximum around a given time is uncorrelated to the probability that the others reach a maximum around the same time, and the probability that they are all within some range of their maximal value at a given time is the product of the

individual probability, which is nonzero. Various simulations with co-phasing and with random relative phases on monochromatic fields have led to similar results, and the relative phase of the uncorrelated sinusoidal modulations generally does not play a significant role when calculating the overall amplitude modulation in a PV and rms sense. When using a pulse of finite duration, the relative phases of the temporal phase modulations and their timing relative to the power of the pulse play a role, e.g., the maximum PV modulation might not be reached over the finite time interval where the pulse power is nonzero. The derivations presented here correspond to a worst-case scenario, where the amplitude modulations are considered over a very large temporal range. With these conventions, the temporal field is simply written as

$$E(t) = \exp\left[i \sum_j m_j \cos(\Omega_j t)\right]. \qquad (1)$$

2. Parameters for Derivations and Simulations

The analytical derivations are performed for an arbitrary number of noncommensurate microwave frequencies of arbitrary modulation index with impairments leading to a small change in the electric field of the optical pulse, i.e., inducing a small amplitude modulation. This is the useful range for application to high-energy lasers since the impairments and amplitude modulation must be minimized. Signals with commensurate frequencies have been studied in the context of providing a uniform spectral density over a given bandwidth, but the resulting on-target smoothing might be impacted by resonances.[23] These signals should be the subject of a separate study if they find an application for beam smoothing. Simulations have been performed with the parameters defined in Ref. 16 for the so-called picket channel. The corresponding frequencies and modulation indices are given in Table 136.III and a detail of the phase modulations is shown in Fig. 136.19(a). The optical signal obtained by phase modulation with these parameters is called the "test signal" for the remainder of this

article. These parameters were determined by simulations to optimize the on-target smoothing, including the engineering constraints related to potential implementation on the NIF.[13] Small relative changes to these frequencies would not affect the smoothing, but they have been chosen as multiples of a reference clock available at the Omega Laser Facility because this allows them to be temporally synchronized to the optical pulse. The microwave frequencies are commensurate, but the integer multiples linking them are so large that no effect of commensurability has been observed in simulations. The resulting optical spectrum is shown in Fig. 136.19(b). A Gaussian spectral density with an identical rms bandwidth (50 GHz) has been plotted, as discussed in the next section.
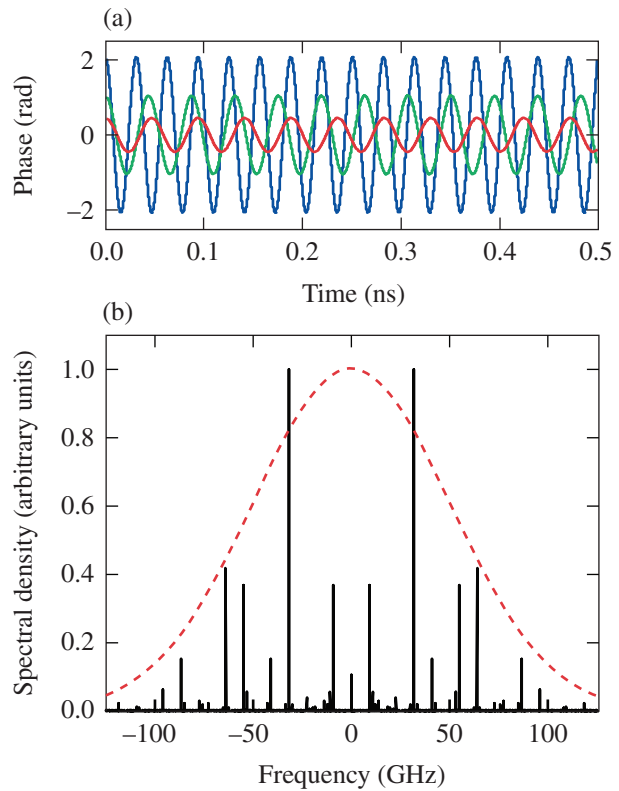
Figure 136.19
(a) Phase modulations used for simulations with parameters given in Table 136.III (f_1, f_2, and f_3 plotted in red, green, and blue, respectively). (b) Optical spectrum resulting from these phase modulations applied to a monochromatic field (black solid line) and Gaussian spectrum with identical root mean square (rms) bandwidth (red dashed line).

The considered spectral impairments are linear amplitude modulation (parameter l), quadratic amplitude modulation (parameter q), quadratic phase modulation (parameter φ_2), and cubic phase modulation (parameter φ_3), with transfer function given, respectively, by

Table 136.III: Characteristics of the phase modulations used for simulations. All frequencies are multiples of the reference frequency f_{ref} = 37.998935 MHz.

Modulation	Frequency (GHz)	Multiple of f_{ref}	Modulation index (rad)
Multi-FM-1	f_1 = 21.165	557	0.45
Multi-FM-2	f_2 = 22.837	601	1.04
Multi-FM-3	f_3 = 31.881	839	2.07

$$\tau(\omega) = \sqrt{1 + l\omega}, \tag{2}$$

$$\tau(\omega) = \sqrt{1 + q\omega^2}, \tag{3}$$

$$\tau(\omega) = \exp\left(i\varphi_2\omega^2/2\right), \tag{4}$$

$$\tau(\omega) = \exp\left(i\varphi_3\omega^3/6\right). \tag{5}$$

The range of impairment parameters for simulations was arbitrarily chosen between 0 and a maximal value calculated so that for amplitude impairments, the magnitude of the transfer function reaches the value 1.2 at $f = 100$ GHz and for phase impairments, the phase of the transfer function reaches the value 0.2 rad at $f = 100$ GHz. The parameters l, q, φ_2, and φ_3 are chosen positive to simplify the equations.

Spectrum and Bandwidth of Signals
with Multiple Phase Modulations
1. Spectrum and Bandwidth of Signal
    with Single Phase Modulation
    Signals with a single temporal phase modulation are widely used in telecommunications and their spectral properties are well documented.[20] The optical spectrum of a signal with phase modulation at frequency Ω with index m is composed of discrete sidebands at the frequencies $n\Omega$ and power given by the Bessel function of the first kind $\left| J_n(m) \right|^2$. According to Carson's rule, 98% of the energy is contained in the bandwidth

$$\mathrm{BW}_{98\%} = 2(m+1)\Omega. \tag{6}$$

Knowledge of the spectral properties of signals with multiple phase modulations can be obtained using statistical arguments, as shown in this section. One approach for obtaining an operational definition of the bandwidth of these signals is to use the bandwidth of the spectrum $S(\omega,m,\Omega) = \left| \tilde{E}(\omega,m,\Omega) \right|^2$ in the rms sense,

$$\mathrm{BW}_{\mathrm{rms}}(m,\Omega) = \sqrt{\int \omega^2 S(\omega,m,\Omega)\,\mathrm{d}\omega \Big/ \int S(\omega,m,\Omega)\,\mathrm{d}\omega}, \tag{7}$$

which can be expressed using the properties of the Fourier transform as

$$\mathrm{BW}_{\mathrm{rms}}(m,\Omega) = \sqrt{\int \left| \frac{\partial E}{\partial t}(t) \right|^2 \mathrm{d}t \Big/ \int \left| E(t) \right|^2 \mathrm{d}t}. \tag{8}$$

Equation (8) is straightforward to calculate, resulting in

$$\mathrm{BW}_{\mathrm{rms}}(m,\Omega) = m\Omega/\sqrt{2}. \tag{9}$$

2. Bandwidth of Signals with Multiple Phase Modulations
    Equation (8) can be extended to a signal with multiple phase modulations given by Eq. (1):

$$\mathrm{BW}_{\mathrm{rms}}\left(\{m_j,\Omega_j\}\right) = \sqrt{\int \left[\sum_j m_j \Omega_j \sin\left(\Omega_j t\right) \right]^2 \mathrm{d}t}, \tag{10}$$

where the square can be expanded to give

$$\mathrm{BW}_{\mathrm{rms}}\left(\{m_j,\Omega_j\}\right) =$$

$$\sqrt{\sum_{j,k} m_j m_k \Omega_j \Omega_k \int \sin\left(\Omega_j t\right) \sin\left(\Omega_k t\right) \mathrm{d}t}. \tag{11}$$

For noncommensurate frequencies (Ω_j, Ω_k), the integral in Eq. (11) is 0, while for $j = k$, the integral is equal to 1/2, leading to the expression

$$\mathrm{BW}_{\mathrm{rms}}\left(\{m_j,\Omega_j\}\right) = \sqrt{\sum_j m_j^2 \Omega_j^2/2}. \tag{12}$$

The rms bandwidth of a signal with multiple noncommensurate phase modulations is the root mean square of the individual rms bandwidths.

An alternate way to obtain this result is to consider that the temporal electric field of a signal with multiple phase modulations is the product of the fields corresponding to individual phase modulations. In the spectral domain, this implies that the resulting field is the convolution of the individual fields. Because the modulation frequencies are not commensurate, the optical frequency of each sideband in the resulting spectrum is obtained by a unique linear combination of the optical frequencies of the sidebands of the individual fields. The amplitude of that sideband in the convolved field is given by a product of the amplitudes in each individual field. As a result, the power of that sideband is given by a product of the corresponding powers. The optical spectrum of the signal with multiple phase modulations is the convolution of the spectra corresponding to the individual modulations only when the modulation frequencies are non-commensurate. This general result was used in Ref. 7 for the two particular frequencies corresponding to SBSS and

SSD on the LMJ. From the general properties of the Fourier transform, it is known that the rms width of a convolution of multiple functions is equal to the rms of the individual rms widths, which confirms Eq. (12).

3. Spectrum of Signals with Multiple Phase Modulations

Obtaining an approximation of the spectrum of a signal with multiple phase modulations is important to quantify the energy present in a particular frequency interval. A comparison of Eqs. (6) and (9) indicates that the rms width and the Carson's rule bandwidth are loosely connected for arbitrary values of the modulation index. The rms width is computationally easy to use but it is not a precise indicator of the energy fraction present in a given frequency interval. One possible strategy to obtain useful information about the spectral density of a signal given by Eq. (1) is to formally reconsider the property that the resulting spectrum is the convolution of the individual spectra for modulation parameters (m_j, Ω_j) in light of the probability theory.

One considers N independent random variables $\{\omega_j\}$, where each random variable ω_j has a probability density function (pdf) given by $S(\omega, m_j, \Omega_j)$. Since the modulation frequencies are different, the probability density functions are different and the variables are not identically distributed. The convolution of these spectra, $S(\omega, \{m_j, \Omega_j\})$ is the pdf of the sum of the N random variables

$$S_N = \sum_j \omega_j$$

because of the probabilistic independence. The sum of a large number of independent and identically distributed variables with zero mean is probabilistically described by the central limit theorem, which states that the probability density function of the sum converges to a normal distribution with variance equal to N times the individual variance. This result is true in some conditions for the sum of N random variables that are independent but not identically distributed: the probability density function of the sum also converges to a normal distribution with variance given by the sum of the individual variances.[24] The sum cumulative distribution function (cdf) converges to the cdf of that normal distribution. A sufficient condition for convergence is that the third-order moment of the absolute value of each individual variable is finite. It is straightforward to simulate this quantity for Bessel spectra and conclude that this is the case. This makes it possible to conclude that the spectrum of the field given by Eq. (1) converges to a Gaussian function with standard deviation given by Eq. (12) for a large number of modulation frequencies. The normal distribution and its cdf are well documented. For a normally distributed random variable x with unity standard deviation, the probit function, i.e., the quantile function (inverse of the cdf) of the normal distribution, yields the quantity x_p, defining the interval $]-\infty, x_p]$, corresponding to a statistical probability p (Ref. 25). For a Gaussian spectral density of standard deviation σ, the probit function gives the multiple x_p, defining the interval $]-\infty, \sigma x_p]$, containing the fraction p of the signal energy. Symmetric intervals $[-f_p, f_p]$ containing 98% of the energy, are considered in this article to be consistent with Carson's rule for a single modulation frequency. Considering the symmetry of the normal distribution, the frequency f_p is the product of the standard deviation by the probit function applied to $p = 0.99$, i.e., $f_p = 2.326\,\sigma$.

4. Simulations

The optical spectrum of signals with multiple phase modulations has been simulated for a variety of situations. The cumulative distribution function for the test-signal spectrum shown in Fig. 136.19(b) is displayed in Fig. 136.20. The cdf of a normal distribution with identical rms bandwidth (50 GHz) is also plotted for comparison. The agreement between these two curves is good. The cdf calculated from the spectrum reaches 99% at ~99 GHz, indicating that 98% of the energy is contained in the frequency interval 2×99 GHz = 198 GHz (note that the cdf is by definition an integral starting at $-\infty$, while the bandwidth of interest is defined as a symmetric interval centered at the
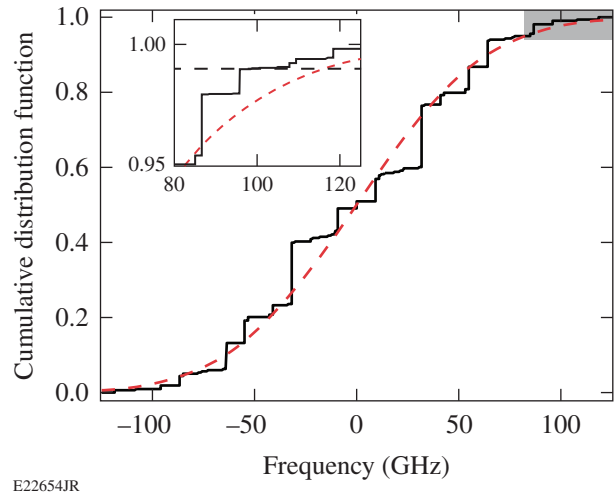

E22654JR

Figure 136.20
Cumulative density function of the spectrum shown in Fig. 136.19(b) (black solid line) and the Gaussian function with identical rms bandwidth (red dashed line). The inset is a close-up of the tail of the cumulative density functions at high frequencies, where a horizontal dashed line has been added to show the frequency values at which the two functions reach 0.99.

zero frequency). The 98% bandwidth of the Gaussian spectral density with rms bandwidth equal to 50 GHz is $2 \times 2.326 \times 50$ GHz = 233 GHz. The ratio of the actual 98% bandwidth to the 98% bandwidth predicted by the normal distribution is $\rho = 0.85$. The inset in Fig. 136.20 displays a close-up of the two cumulative density functions at high frequencies, confirming the discrepancy for the predicted 98% bandwidth. It is clear from this inset that the spectrum of the test signal is more concentrated and expands less toward high frequencies. The 17% overestimate predicted by the normal distribution is consistent with the more-general results obtained below.

Statistical simulations were performed to quantify the convergence of the spectrum of a multi-FM signal to its Gaussian approximation and of the corresponding cdf's. Figure 136.21 shows simulation results for the ratio ρ of the bandwidth containing 98% of the energy calculated from the spectral density to the bandwidth containing 98% of the energy assuming that the spectrum is Gaussian with standard deviation given by Eq. (12). For each number of modulation frequencies N (horizontal axis, from 1 to 10 on the left plots and 10 to 100 on the right plots) the standard deviation of the modulation index σ_m was allowed to vary between 1 and 5 (vertical axis). For each combination of N and σ_m, 1000 random draws of the modulation indices and modulation frequencies were made. For each draw, the modulation index is normally distributed with standard deviation σ_m and the modulation frequencies are initially normally distributed with standard deviation equal to 1 but are rescaled so that the rms bandwidth of the resulting signal is 100 GHz, following Eq. (12). This rescaling allows one to standardize the simulation results and necessary sampling in the time and frequency domain. Because it would be, in practice, difficult to co-phase a large number of sinusoidal modulations, the relative phase of the N modulations was chosen as a random variable uniformly distributed between 0 and 2π. This procedure allows one to map a wide range of multi-FM signals. The results displayed in the first row of Fig. 136.21 are the average values of the ratio ρ as a function of σ_m and N. For example, $\langle \rho \rangle = 1$ means that the 98% bandwidth of the calculated spectrum and Gaussian approximation are on average the same; values lower than 1 indicate that the Gaussian function overestimates the 98% bandwidth. The second row of Fig. 136.21 represents the standard deviation of the ratio ρ calculated over the 1000 random draws performed for the N modulation frequencies and modulation indices of standard deviation σ_m.

The optical spectrum of the phase-modulated fields effectively converged to a Gaussian distribution, and the cumulative
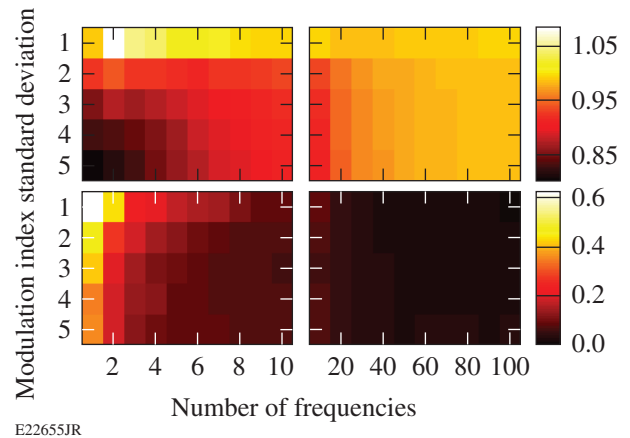

E22655JR

Figure 136.21
Statistics for the ratio ρ of the bandwidths containing 98% of the energy calculated from the spectral density of a multi-FM spectrum and directly calculated from the modulation parameters (frequencies and indices) assuming a normal spectral density. The upper and lower rows correspond to the average value and standard deviation, respectively, determined as a function of the number of modulation frequencies and standard deviation of the modulation index. The statistics are calculated over 1000 random draws of the modulation parameters.

distribution function of the spectrum converged to the corresponding cdf as the number of frequencies was increased. A strong correlation between the convergence of the cdf and the convergence of $\langle \rho \rangle$ toward 1 was observed, making it possible to discuss the following general spectral properties in light of the bandwidth results presented in Fig. 136.21:

• The spectrum approximation by a normal distribution gets better as the number of modulation frequencies increases. The average value of the ratio ρ converges to 1 and the standard deviation around the average value decreases as N increases. This is expected because the central limit theorem applies to the sum of a large number of independent variables.

• The ratio ρ is in most cases smaller than 1, meaning that the calculated spectrum is more concentrated toward lower frequencies than its normal approximation. This can be explained by the squarish shape of the spectrum of phase-modulated signals, which leads to more energy concentration for a given standard deviation. Predicting the spectral extent of a multi-FM signal using its rms bandwidth and the normal approximation leads to an overestimate.

• Small phase-modulation indices lead to a better approximation than large modulation indices; in particular for $\sigma_m = 1$, the normal approximation is good in an average sense even

for a small number of modulation frequencies. This is caused by the general shape of the spectrum of sinusoidally modulated signals: for a single phase modulation with low modulation index, the spectrum is close to a bell-shaped curve multiplied by a frequency comb at the modulation frequencies. Since the individual probability density functions are closer to normal distribution, the convergence of the probability density function of the sum of the variables to a normal distribution is faster.

• The spread of the simulated ρ relative to the average value is smaller as the number of frequencies increases (consequence of the central limit theorem) and as the modulation index increases for a given number of frequencies. The latter is attributed to the larger number of spectral modes resulting from larger modulation indices, leading to a smoother cdf because the spectral density of individual modes is on average smaller.

**Impairments Leading to FM-to-AM Conversion
at the Modulation Frequencies**

1. Linear Spectral Amplitude

A linear spectral modulation corresponds, for example, to amplification at a frequency detuned from the maximum of an amplifier gain. The corresponding transfer function over the bandwidth of the pulse is

$$\tau\left(\omega\right)=\sqrt{1+l\omega}\approx1+\frac{l}{2}\,\omega. \tag{13}$$

The temporal field after this transfer function is

$$E'=E+\frac{il}{2}\,\frac{\partial E}{\partial t}. \tag{14}$$

With the expression of the initial electric field given by Eq. (1), the modulated field is

$$E'\left(t\right)=E\left(t\right)\left[1+\frac{l}{2}\sum_{j}m_{j}\,\Omega_{j}\,\sin\left(\Omega_{j}t\right)\right], \tag{15}$$

and the modulated power at first order in l is

$$P'\left(t\right)=1+l\sum_{j}m_{j}\,\Omega_{j}\,\sin\left(\Omega_{j}t\right). \tag{16}$$

Equation (16) shows that the modulation on the output pulse is at the modulation frequencies Ω_{j} with PV amplitude

$$\mathrm{PV}\left(\Omega_{j}\right)=2lm_{j}\,\Omega_{j}. \tag{17}$$

The highest modulation is observed at the frequency for which the associated bandwidth $m_{j}\Omega_{j}$ is maximal. With noncommensurate modulation frequencies, there are times when the modulations in Eq. (16) are simultaneously close to a maximum and other times at which they are simultaneously close to a minimum. The PV modulation is given by

$$\mathrm{PV}=2l\sum_{j}m_{j}\,\Omega_{j}, \tag{18}$$

and the rms modulation for these uncorrelated sinusoidal modulations is given by

$$\mathrm{rms}=l\,\sqrt{\sum_{j}m_{j}^{2}\,\Omega_{j}^{2}\Big/2}\,. \tag{19}$$

Simulation results for the test signal are shown in Figs. 136.22 and 136.23. Figure 136.22 displays the modulated temporal power corresponding to a linear spectral amplitude modulation $l = 0.44/(100\ \mathrm{GHz})$: it is dominated by the modulation at the highest frequency f_3 but the influence of other frequencies can be seen as the slight modulation of the local power extrema. Figure 136.23 compares simulated and analytical results for the modulations determined without frequency resolution (PV and rms AM) [Eqs. (18) and (19)] and at the three modulation frequencies [Eq. (17)]. An excellent agreement is obtained. The highest modulation is observed at the frequency f_3 since that frequency corresponds to the highest product $m_j\Omega_j$.
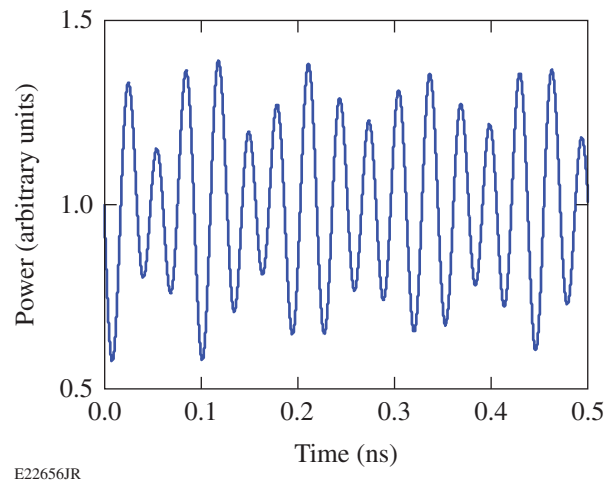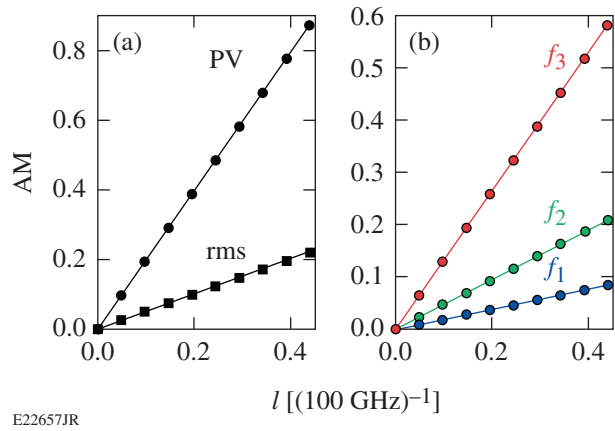

E22656JR

Figure 136.22
Temporal power after linear spectral amplitude modulation corresponding to $l = 0.44/(100\ \mathrm{GHz})$.

E22657JR

Figure 136.23
(a) Peak-to-valley and rms amplitude modulation (AM) versus magnitude of the linear spectral amplitude modulation. (b) Peak-to-valley AM at the frequencies f_j versus magnitude of the linear spectral amplitude modulation. The lines correspond to the simulations and the markers correspond to the analytical derivation.

2. Quadratic Spectral Phase

A quadratic spectral phase is the dominant phase term due to the chromatic dispersion of materials, e.g., laser glass and optical fibers, as well as the dominant term when propagating in a grating compressor. This impairment is represented in the spectral domain by the transfer function

$$\tau(\omega) = \exp\left(i\varphi_2\omega^2/2\right) \approx 1 + i\varphi_2\omega^2/2, \tag{20}$$

which leads to the temporal field

$$E' = E - i\frac{\varphi_2}{2}\frac{\partial^2 E}{\partial t^2}. \tag{21}$$

With the expression of the initial field given by Eq. (1), the resulting field is

$$E'(t) = E(t)\left\{1 - \frac{\varphi_2}{2}\sum_j m_j\Omega_j^2\cos\left(\Omega_j t\right)\right.$$

$$\left. + i\frac{\varphi_2}{2}\left[\sum_j m_j\Omega_j\sin\left(\Omega_j t\right)\right]^2\right\}. \tag{22}$$

When calculating the power (i.e., the modulus squared of the field), the imaginary component in Eq. (22) leads to a second-order term in φ_2. The power is given at first order by

$$P'(t) = 1 - \varphi_2\sum_j m_j\Omega_j^2\cos\left(\Omega_j t\right). \tag{23}$$

A quadratic spectral phase leads to amplitude modulation at the frequencies Ω_j with respective peak-to-valley amplitude

$$PV\left(\Omega_j\right) = 2\varphi_2 m_j\Omega_j^2. \tag{24}$$

Temporal modulations are observed at the modulation frequencies Ω_j, as for linear amplitude modulation, but the largest modulation corresponds to the frequency having the largest product $m_j\Omega_j^2$. An argument similar to that made about Eq. (16) shows that the overall peak-to-valley AM is

$$PV = 2\varphi_2\sum_j m_j\Omega_j^2, \tag{25}$$

while the rms AM is given by

$$rms = \varphi_2\sqrt{\sum_j m_j^2\Omega_j^4/2}. \tag{26}$$

Simulation results for quadratic spectral phase modulation are shown in Figs. 136.24 and 136.25. Figure 136.24 shows the modulated power after second-order dispersion $\varphi_2 = 1.01$ ps². Features similar to those of Fig. 136.22 are observed. Figure 136.25 shows the excellent agreement between the simulated and analytical results [Eqs. (25) and (26) for the peak-to-valley and rms AM, and Eq. (24) for the peak-to-valley AM at
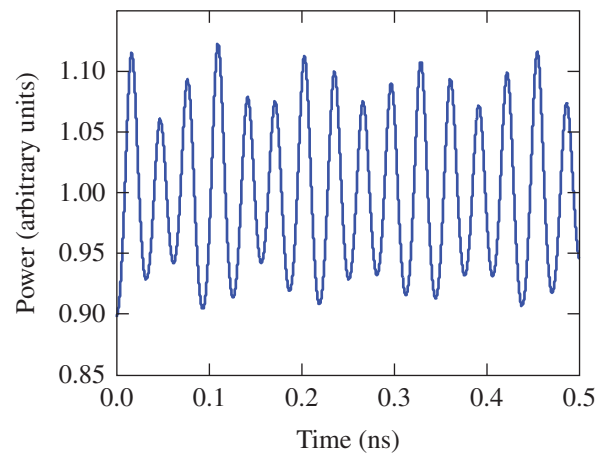
E22658JR

Figure 136.24
Temporal power after quadratic spectral phase corresponding to $\varphi_2 = 1.01$ ps².
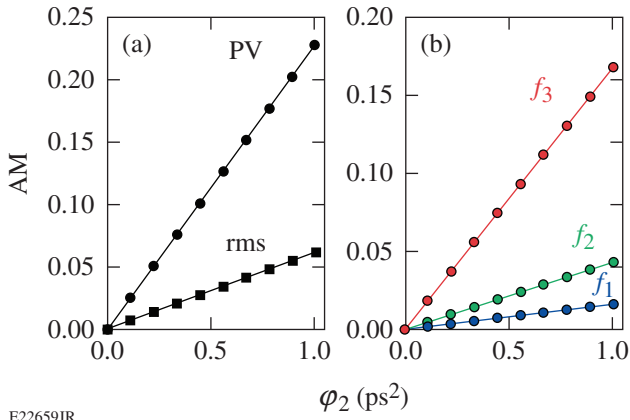
E22659JR

Figure 136.25
(a) Peak-to-valley and rms AM versus magnitude of the quadratic spectral phase modulation. (b) Peak-to-valley AM at the frequencies f_j versus magnitude of the quadratic spectral phase modulation. The lines correspond to the simulations and the markers correspond to the analytical derivation.

each frequency f_j] when the magnitude of the phase modulation is modified. The highest temporal modulation is observed at the frequency f_3 because that frequency corresponds to the largest quantity $m_j \Omega_j^2$, considering the parameters in Table 136.III.

3. Combination of Linear Spectral Amplitude and Quadratic Spectral Phase

Linear amplitude modulation and quadratic temporal phase modulation lead to temporal modulation at the frequencies Ω_j. Inspection of Eqs. (16) and (23) shows that the corresponding modulations occur in quadrature, each of them being either a sine or a cosine of the argument $\Omega_j t$. It is straightforward to show that the peak-to-valley AM at frequency Ω_j resulting from the in-quadrature modulations with respective PV amplitudes $2lm_j \Omega_j$ and $2\varphi_2 m_j \Omega_j^2$ is

$$\sqrt{\left(2\varphi_2 m_j \Omega_j^2\right)^2 + \left(2lm_j \Omega_j\right)^2},$$

i.e.,

$$PV\left(\Omega_j\right) = 2m_j \Omega_j \sqrt{\left(\varphi_2 \Omega_j\right)^2 + l^2}. \tag{27}$$

Since the modulation frequencies are not commensurate, there are times at which the extrema of the individual modulations are simultaneously reached, leading to the peak-to-valley AM

$$PV = 2 \sum_j m_j \Omega_j \sqrt{\left(\varphi_2 \Omega_j\right)^2 + l^2}. \tag{28}$$

The rms AM is obtained by considering that the resulting temporal power is the sum of uncorrelated sinusoidal functions oscillating at Ω_j with amplitude given by half the PV modulation expressed by Eq. (27). This leads to

$$rms = \sqrt{\sum_j m_j^2 \Omega_j^2 \left[\left(\varphi_2 \Omega_j\right)^2 + l^2\right] \bigg/ 2}. \tag{29}$$

Figure 136.26 compares simulated and analytical results when the second-order dispersion is $\varphi_2 = 1.01$ ps^2 and the linear spectral amplitude modulation is modified. Excellent agreement is obtained, confirming the fact that Eqs. (27)–(29) accurately predict the influence of the combined phase and amplitude modulations. Similar agreement was observed when scanning the magnitude of the phase modulation for a given amplitude modulation.
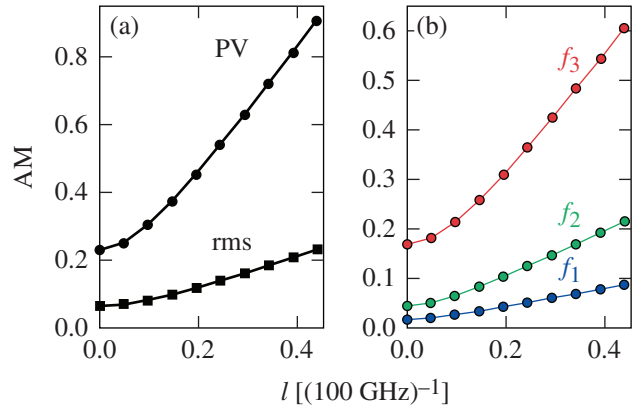
E22660JR

Figure 136.26
(a) Peak-to-valley and rms AM versus magnitude of the linear spectral amplitude for $\varphi_2 = 1.01$ ps^2. (b) Peak-to-valley AM at the frequencies f_j versus magnitude of the linear spectral amplitude for $\varphi_2 = 1.01$ ps^2. The lines correspond to the simulations and the markers correspond to the analytical derivation.

Impairments Leading to FM-to-AM Conversion at Intermodulation Frequencies
1. Quadratic Spectral Amplitude

Quadratic amplitude modulation occurs after propagation in a component at a frequency corresponding to an amplitude externum of the component's transfer function; for example, amplification at the peak of the gain of an amplifier. The corresponding transfer function is

$$\tau\left(\omega\right) = \sqrt{1 + q\omega^2} \approx 1 + \frac{q}{2}\omega^2, \tag{30}$$

leading to the temporal field

$$E' = E - \frac{q}{2}\frac{\partial^2 E}{\partial t^2}. \tag{31}$$

The resulting field is

$$E'(t) = E(t)\left\{1 + \frac{q}{2}\left[\sum_j m_j \Omega_j \sin\left(\Omega_j t\right)\right]^2\right.$$

$$\left. + i\frac{q}{2}\sum_j m_j \Omega_j^2 \cos\left(\Omega_j t\right)\right\}, \tag{32}$$

where the real component proportional to q between the curled brackets will be the main modulation source since the complex quantity in the same brackets is squared when calculating the optical power. The resulting power, at first order in q, is

$$P'(t) = 1 + q\left[\sum_j m_j \Omega_j \sin\left(\Omega_j t\right)\right]^2. \tag{33}$$

When $q > 0$, the modulated power in Eq. (33) is higher than the average power of the signal in the absence of impairment at all times. This is explained by the fact that the transfer function [Eq. (30)] does not conserve the signal energy. Since one is interested in the temporal modulation of the power around its average value, and not around its value without impairment, AM determinations are scaled by the average power of the signal of Eq. (33),

$$1 + \frac{q}{2}\sum_j m_j^2 \Omega_j^2.$$

The minimum value of Eq. (33) is 1. The maximum value is obtained when all the modulations reach an extremum, and the resulting peak-to-valley AM is

$$PV = q\left(\sum_j m_j \Omega_j\right)^2 \bigg/ \left(1 + \frac{q}{2}\sum_j m_j^2 \Omega_j^2\right). \tag{34}$$

The rms AM on the resulting power is calculated from Eq. (33), leading to

$$rms = \frac{q\sqrt{\sum_j m_j^4 \Omega_j^4 \bigg/ 8 + \sum_{j,k} m_j^2 m_k^2 \Omega_j^2 \Omega_k^2}}{\left(1 + \frac{q}{2}\sum_j m_j^2 \Omega_j^2\right)}. \tag{35}$$

Equation (33) can be developed into a sum of terms proportional to $\sin\left(\Omega_j t\right)\sin\left(\Omega_k t\right)$. The choice of $j = k$ leads to a term oscillating at the frequency $2\Omega_j$ with PV amplitude $qm_j^2 \Omega_j^2$. The two terms corresponding to the choice (j,k) and (k,j) with $j \neq k$ lead to modulations at $\Omega_j + \Omega_k$ and $\Omega_j - \Omega_k$, each of them with a PV amplitude $2qm_j m_k \Omega_j \Omega_k$. The resulting AM's at these frequencies are

$$PV\left(2\Omega_j\right) = qm_j^2 \Omega_j^2 \bigg/ \left(1 + \frac{q}{2}\sum_j m_j^2 \Omega_j^2\right) \tag{36}$$

and

$$PV\left(\Omega_j \pm \Omega_k\right) = 2qm_j m_k \Omega_j \Omega_k \bigg/ \left(1 + \frac{q}{2}\sum_j m_j^2 \Omega_j^2\right). \tag{37}$$

The modulation amplitudes at the frequencies $\Omega_j + \Omega_k$ and $\Omega_j - \Omega_k$ are identical. Simulation and analytical results for quadratic spectral amplitude modulation are displayed in Figs. 136.27 and 136.28. Figure 136.27 shows the complex behavior of the amplitude modulation, in particular the clear presence of modulations at multiple frequencies. Figure 136.28
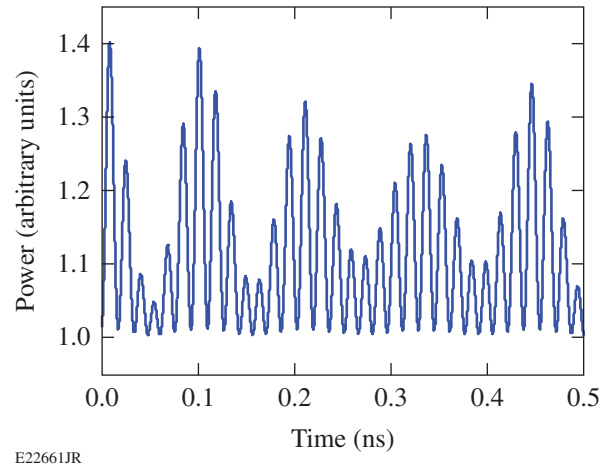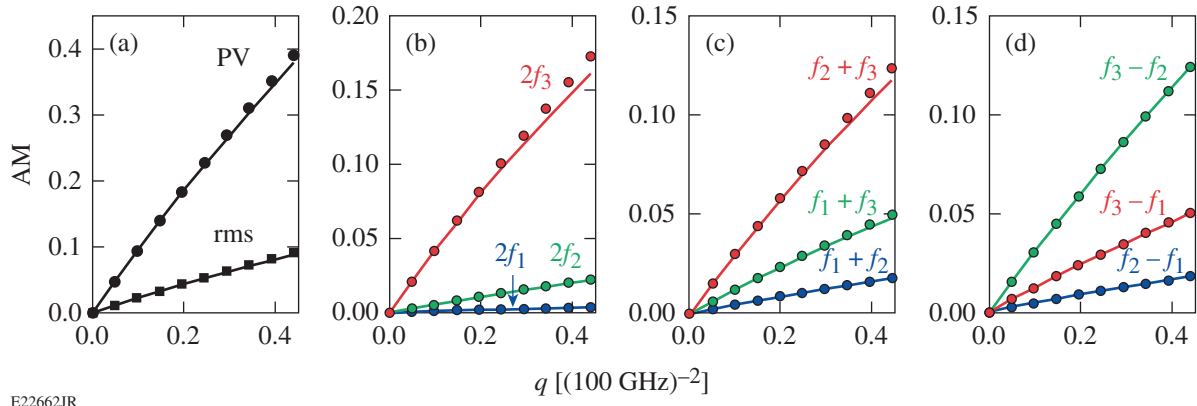

E22661JR

Figure 136.27
Temporal power after quadratic spectral amplitude modulation corresponding to $q = 0.44/(100 \text{ GHz})^2$.

E22662JR

Figure 136.28
(a) Peak-to-valley and rms AM versus magnitude of the quadratic spectral amplitude modulation. [(b)–(d)] Peak-to-valley AM at the frequencies $2f_j, f_j + f_k$, and $f_j - f_k$ versus magnitude of the quadratic spectral amplitude modulation. The lines correspond to the simulations and the markers correspond to the analytical derivation.

details the PV and rms AM for the temporal power as well as the frequency-resolved peak-to-valley AM. The simulation results are in excellent agreement with the analytical results from Eqs. (34)–(37). The highest modulations are observed at the frequencies $2f_3, f_2 + f_3$, and $f_3 - f_2$, which contribute most of the PV modulation observed in the time domain. The first two of these frequencies are larger than 50 GHz, while the third is approximately 10 GHz. Bandwidth limitation in a temporal diagnostic might hinder the ability to accurately characterize the temporal modulation. Detection of a modulation at a low frequency (e.g., $\Omega_j - \Omega_k$) indicates the presence of modulation at a higher frequency (e.g., $\Omega_j + \Omega_k$) with identical amplitude.

2. Cubic Spectral Phase

A cubic spectral phase is typically the leading phase impairment once the quadratic spectral phase has been compensated over the bandwidth of the source. Because the relative signs of the second-order and third-order dispersions for propagation in materials and in a grating compressor are different, a cubic spectral phase is induced when a grating compressor is used to compensate the chromatic dispersion of optical fibers. The transfer function is represented by

$$\tau(\omega) = \exp\left(i\varphi_3 \omega^3 / 6\right) \approx 1 + i\varphi_3 \omega^3 / 6. \quad (38)$$

This leads to the output temporal field

$$E' = E + \frac{\varphi_3}{6} \frac{\partial^3 E}{\partial t^3}. \quad (39)$$

The expression for the third-order derivative of Eq. (1) is lengthy, but only the real terms should be kept since they are the ones leading to an approximation of the modulated power at first order in φ_3 when inserted into Eq. (39). The modulated power is given by

$$P'(t) = 1 - \varphi_3 \sum_j m_j \Omega_j \sin\left(\Omega_j t\right) \sum_j m_j \Omega_j^2 \cos\left(\Omega_j t\right). \quad (40)$$

For this impairment, the spectrally resolved amplitude modulation is calculated first. The product of the two summation terms in Eq. (40) gives modulations at the frequencies $2\Omega_j$ and at the intermodulation frequencies $\Omega_j \pm \Omega_k$. The term at $2\Omega_j$ corresponds to

$$\varphi_3 m_j \Omega_j \sin\left(\Omega_j t\right) m_j \Omega_j^2 \cos\left(\Omega_j t\right) =$$
$$\varphi_3 m_j^2 \Omega_j^3 \sin\left(2\Omega_j t\right) / 2. \quad (41)$$

The peak-to-valley AM at $2\Omega_j$ is

$$\text{PV}\left(2\Omega_j\right) = \varphi_3 m_j^2 \Omega_j^3. \quad (42)$$

The terms corresponding to $j \neq k$ are

$$\varphi_3 m_j m_k \Omega_j \Omega_k \left[\Omega_k \sin\left(\Omega_j t\right) \cos\left(\Omega_k t\right)\right.$$
$$\left. + \Omega_j \sin\left(\Omega_k t\right) \cos\left(\Omega_j t\right)\right], \quad (43)$$

which can be expressed using a trigonometric identity for the product of a sine and cosine as

$$\varphi_3 m_j m_k \Omega_j \Omega_k \left\{ \left(\Omega_j + \Omega_k\right) \sin\left[\left(\Omega_j + \Omega_k\right)t\right] \right.$$
$$\left. + \left(\Omega_k - \Omega_j\right) \sin\left[\left(\Omega_j - \Omega_k\right)\right] \right\} \Big/ 2. \qquad (44)$$

The peak-to-valley AM for these sum/difference frequencies is therefore

$$PV\left(\Omega_j \pm \Omega_k\right) = \varphi_3 m_j m_k \Omega_j \Omega_k \left(\Omega_j \pm \Omega_k\right), \qquad (45)$$

where it has been assumed that $\Omega_j > \Omega_k$.

The rms AM is obtained by noting that the average temporal value of Eq. (40) is equal to 1 because the spectral field is phase modulated but not amplitude modulated. One can then write

$$\mathrm{rms}^2 = \varphi_3^2 \int \left[\sum_j m_j \Omega_j \sin\left(\Omega_j t\right)\right]^2$$
$$\times \left[\sum_j m_j \Omega_j^2 \cos\left(\Omega_j t\right)\right]^2 dt. \qquad (46)$$

Each square in the previous equation can be developed, and considering that the integral of a product of sinusoidal functions with noncommensurate frequencies is zero if it contains odd powers of a sinusoidal function (either sine or cosine) at a particular frequency, Eq. (46) can be rewritten as

$$\mathrm{rms}^2 = \varphi_3^2 \int \sum_j m_j^2 \Omega_j^2 \sin^2\left(\Omega_j t\right) \sum_j m_j^2 \Omega_j^4 \cos^2\left(\Omega_j t\right) dt \qquad (47)$$

and as

$$\mathrm{rms}^2 = \varphi_3^2 \int \left[\sum_j m_j^4 \Omega_j^6 \sin^2\left(\Omega_j t\right)\cos^2\left(\Omega_j t\right) \right.$$
$$\left. + \sum_{j \neq k} m_j^2 m_k^2 \Omega_j^2 \Omega_k^4 \sin^2\left(\Omega_j t\right)\cos^2\left(\Omega_k t\right) \right] dt. \qquad (48)$$

Equation (48) can be calculated to obtain the rms AM in the presence of third-order dispersion,

$$\mathrm{rms} = \frac{\varphi_3}{2} \sqrt{\sum_j m_j^4 \Omega_j^6 \Big/ 2 + \sum_{j \neq k} m_j^2 m_k^2 \Omega_j^2 \Omega_k^4}. \qquad (49)$$

The peak-to-valley AM is difficult to obtain in the general case because the different sinusoidal components in Eq. (40) have different frequencies and reach their maxima at different times, but a minimal and maximal bound for that quantity can be obtained. A minimal bound $PV_{\min}$ is obtained by considering that the peak-to-valley modulation must be larger than the modulation amplitude obtained considering any two different temporal arguments in Eq. (40). One can consider a time value for which each sine and cosine in that equation is equal to $\pm 1\big/\sqrt{2}$, leading to the inequality

$$PV \geq PV_{\min} = \varphi_3 \sum_j m_j \Omega_j \sum_j m_j \Omega_j^2. \qquad (50)$$

A maximal bound $PV_{\max}$ is obtained by considering that, at this approximation order, only the modulations at all the frequencies $2\Omega_j$ and $\Omega_j + \Omega_k$ contribute to the temporal modulation. The resulting peak-to-valley AM is smaller than the sum of individual peak-to-valley AM (the equality is reached only if a time exists when all the individual modulations reach their maximum and another time when they all reach their minimum). The maximal bound is the sum of Eqs. (42) and (45), leading to the inequality

$$PV \leq PV_{\max} = PV_{\min} + \varphi_3 \sum_{j > k} m_j m_k \Omega_j \Omega_k \left(\Omega_j - \Omega_k\right). \qquad (51)$$

The span of the interval $PV_{\max} - PV_{\min}$ is small compared to the predicted range of peak-to-valley modulation values since the summation in Eq. (51) contains terms that are small, because either some of the modulation indices are small or the frequency differences are smaller than the frequency sums. In particular, one has $PV_{\min} = PV_{\max} = \varphi_3 m_1^2 \Omega_1^3$ for a single modulation frequency.

Figures 136.29 and 136.30 display results pertaining to temporal AM in the presence of a cubic spectral phase. The existence of multiple modulation frequencies is clearly visible in Fig. 136.29. Figure 136.30(a) shows the analytical and simulation results for the peak-to-valley and rms modulation on the test signal as a function of the cubic spectral modulation magnitude. Excellent agreement is obtained for the rms AM. The peak-to-valley AM obtained by simulation is correctly bracketed by the AM calculated with Eqs. (50) and (51). The frequency-resolved peak-to-valley AM reveals that the AM is dominated by contributions at the frequencies $2f_3$ and $f_2 + f_3$. Contrary to the case of quadratic gain modulation, AM at
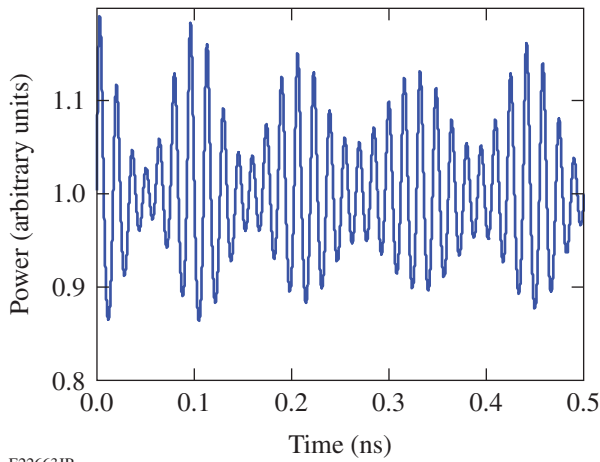
E22663JR

Figure 136.29
Temporal power after cubic spectral phase modulation corresponding to $\varphi_3 = 4.8$ ps^3.
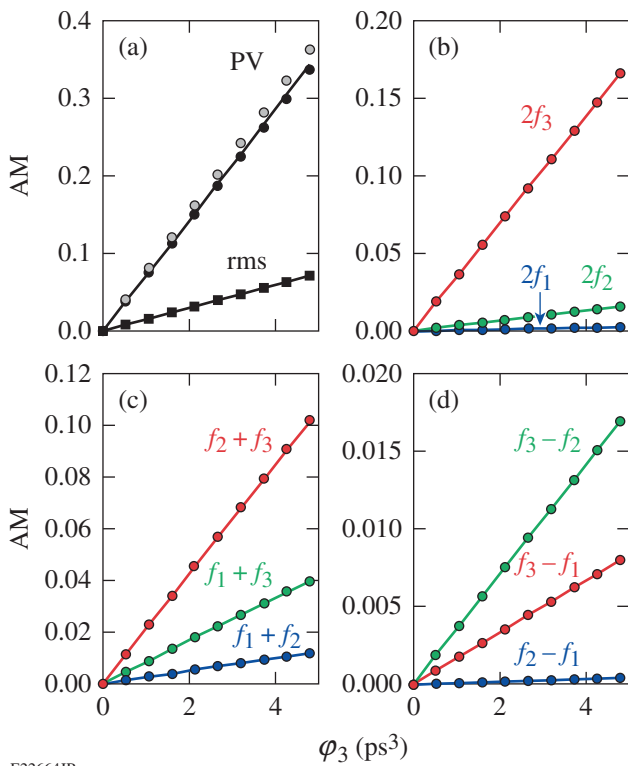

E22664JR

Figure 136.30
(a) Peak-to-valley and rms AM versus magnitude of the cubic spectral phase modulation. The lower and higher bounds for the peak-to-valley AM are shown with black and gray markers, respectively. [(b)–(d)] Peak-to-valley AM at the frequencies $2f_j$, $f_j + f_k$, and $f_j - f_k$ versus magnitude of the cubic spectral phase modulation. The lines correspond to the simulations and the markers correspond to the analytical derivation.

the low frequency $f_3 - f_2$ is much smaller than the AM at $f_2 + f_3$. A signal impaired by third-order dispersion detected by a low-bandwidth temporal diagnostic might seem of much better quality than it actually is.

Additional Considerations

At first order in the modulation resulting from each impairment, the power of an impaired signal is

$$P'(t) = 1 + l \sum_j m_j \Omega_j \sin\left(\Omega_j t\right) - \varphi_2 \sum_j m_j \Omega_j^2 \cos\left(\Omega_j t\right)$$

$$+ q \left[\sum_j m_j \Omega_j \sin\left(\Omega_j t\right)\right]^2 - \varphi_3 \sum_j m_j \Omega_j \sin\left(\Omega_j t\right)$$

$$\times \sum_j m_j \Omega_j^2 \cos\left(\Omega_j t\right), \qquad (52)$$

where the summations correspond to linear amplitude modulation, quadratic phase modulation, quadratic amplitude modulation, and cubic phase modulation. Because the Fourier transform is a linear operator, the frequency signature of the modulated power can partially reveal the origin of the impairments: temporal modulations at some of the phase-modulation frequencies indicate that the signal is impaired by a linear amplitude modulation or quadratic phase modulation, while temporal modulations at some of the sum or difference frequencies indicate that the signal is impaired by a quadratic amplitude modulation or cubic phase modulation.

The ratio of the AM at different frequencies can be used in some cases to identify the source of impairment. For example, this ratio for frequencies f_j and f_k is $m_j f_j / m_k f_k$ when the main impairment is linear amplitude modulation [Eq. (17)] and $m_j f_j^2 / m_k f_k^2$ when the main impairment is quadratic phase modulation [Eq. (24)]. Since the modulation indices and frequencies are known, such quantitative analysis can reveal the origin of the temporal modulation. When these two impairments are present, a more-precise study of the ratio of the AM at different frequencies is likely to reveal their respective contributions—Eq. (27) contains only two unknowns: the coefficient for linear amplitude modulation l and the coefficient for quadratic phase modulation φ_2. These unknowns can be determined if at least two modulation frequencies are present in the signal. With more than two frequencies, the best set of coefficients can be determined in the least-squares sense. Similar considerations can be applied to modulations observed

at intermodulation frequencies when quadratic amplitude modulation and cubic phase modulation are present.

Analytical expressions for the amplitude modulation resulting from impairments of a phase-modulated signal are the necessary starting points for understanding the requirements of temporal diagnostics used to characterize the resulting signals. In practical situations, a diagnostic with a flat response up to a frequency as high as twice the highest phase-modulation frequency in the system is necessary and sufficient to capture the time-domain signal, provided that the impairments are limited to those treated in this article. Insufficient bandwidth leads to an underestimate of the amplitude modulation present on the signal. For signals corresponding to the parameters in Table 136.III, intermodulation frequencies can be at frequencies difficult to reach with the current state-of-the-art single-shot oscilloscopes and photodetector (e.g., $2f_3 \sim 64$ GHz). In general, AM is also generated at lower frequencies (e.g, $f_3 - f_2 \sim 10$ GHz), but a photodetection system with insufficient bandwidth might lead to a significant underestimate of the physical modulation, particularly in the presence of cubic phase.

Conclusions

The spectral and temporal properties of optical signals generated by multiple sinusoidal phase modulations of a monochromatic source have been studied. A formalism for the statistical prediction of the optical spectrum of these signals has been developed based on the central limit theorem, showing the convergence of the spectrum of a signal with multiple phase modulations to a Gaussian spectrum with identical rms bandwidth, which can be calculated analytically from the modulation parameters, and the associated convergence of their cumulative density functions. The comparison between the directly simulated spectrum and predicted Gaussian spectrum for a finite number of frequencies confirmed the asymptotic result and showed that in most conditions, the frequency interval containing 98% of the energy can be predicted from the modulation parameters, although there is significant variation when the number of frequencies is low. FM-to-AM conversion on signals with multiple phase modulations has been analytically described for typical spectral impairments to extend the results known for signals modulated at a single frequency. An excellent agreement with direct simulations has been observed. These results are useful in understanding the current limitations of the laser systems using phase modulation along with the associated subsystems and diagnostics, and in optimizing the engineering of existing and future systems.

REFERENCES

1. J. D. Lindl *et al.*, Phys. Plasmas **11**, 339 (2004).

2. R. L. McCrory, D. D. Meyerhofer, R. Betti, R. S. Craxton, J. A. Delettrez, D. H. Edgell, V. Yu Glebov, V. N. Goncharov, D. R. Harding, D. W. Jacobs-Perkins, J. P. Knauer, F. J. Marshall, P. W. McKenty, P. B. Radha, S. P. Regan, T. C. Sangster, W. Seka, R. W. Short, S. Skupsky, V. A. Smalyuk, J. M. Soures, C. Stoeckl, B. Yaakobi, D. Shvarts, J. A. Frenje, C. K. Li, R. D. Petrasso, and F. H. Séguin, Phys. Plasmas **15**, 055503 (2008).

3. C. A. Haynam *et al.*, Appl. Opt. **46**, 3276 (2007).

4. N. Fleurot, C. Cavailler, and J. L. Bourgade, Fusion Eng. Des. **74**, 147 (2005).

5. J. R. Murray *et al.*, J. Opt. Soc. Am. B **6**, 2402 (1989).

6. P. J. Wisoff *et al.*, in *Optical Engineering at the Lawrence Livermore National Laboratory II: The National Ignition Facility*, edited by M. A. Lane and C. R. Wuest (SPIE, Bellingham, WA, 2004), Vol. 5341, pp. 146–155.

7. S. Hocquet *et al.*, Appl. Opt. **47**, 3338 (2008).

8. J. D. Kilkenny, S. G. Glendinning, S. W. Haan, B. A. Hammel, J. D. Lindl, D. Munro, B. A. Remington, S. V. Weber, J. P. Knauer, and C. P. Verdon, Phys. Plasmas **1**, 1379 (1994).

9. S. Skupsky, R. W. Short, T. Kessler, R. S. Craxton, S. Letzring, and J. M. Soures, J. Appl. Phys. **66**, 3456 (1989).

10. J. E. Rothenberg, J. Opt. Soc. Am. B **14**, 1664 (1997).

11. *LLE Review Quarterly Report* **114**, 73, Laboratory for Laser Energetics, University of Rochester, Rochester, NY, LLE Document No. DOE/NA/28302-826, OSTI ID 935224 (2008).

12. Y. Lin, T. J. Kessler, and G. N. Lawrence, Opt. Lett. **20**, 764 (1995).

13. T. J. B. Collins, J. A. Marozas, K. S. Anderson, R. Betti, R. S. Craxton, J. A. Delettrez, V. N. Goncharov, D. R. Harding, F. J. Marshall, R. L. McCrory, D. D. Meyerhofer, P. W. McKenty, P. B. Radha, A. Shvydky, S. Skupsky, and J. D. Zuegel, Phys. Plasmas **19**, 056308 (2012).

14. J. H. Kelly, A. Shvydky, J. A. Marozas, M. J. Guardalben, B. E. Kruschwitz, L. J. Waxer, C. Dorrer, E. Hill, A. V. Okishev, and J.-M. Di Nicola, in *High Power Lasers for Fusion Research II*, edited by A. A. S. Awwal (SPIE, Bellingham, WA, 2013), Vol. 8602, Paper 86020D.

15. B. E. Kruschwitz, J. H. Kelly, C. Dorrer, A. V. Okishev, L. J. Waxer, G. Balonek, I. A. Begishev, W. Bittle, A. Consentino, R. Cuffney,

E. Hill, J. A. Marozas, M. Moore, R. G. Roides, and J. D. Zuegel, in *High Power Lasers for Fusion Research II*, edited by A. A. S. Awwal (SPIE, Bellingham, WA, 2013), Vol. 8602, Paper 86020E.

16. C. Dorrer, R. Roides, R. Cuffney, A. V. Okishev, W. A. Bittle, G. Balonek, A. Consentino, E. Hill, and J. D. Zuegel, IEEE J. Sel. Top. Quantum Electron. **19**, 3500112 (2013).

17. J. E. Rothenberg, D. F. Browning, and R. B. Wilcox, in *Third International Conference on Solid State Lasers for Application to Inertial Confinement Fusion*, edited by W. H. Lowdermilk (SPIE, Bellingham, WA, 1999), Vol. 3492, pp. 51–61.

18. H. Cao *et al*., Appl. Opt. **50**, 3609 (2011).

19. S. Hocquet, G. Lacroix, and D. Penninckx, Appl. Opt. **48**, 2515 (2009).

20. L. W. Couch III, *Digital and Analog Communication Systems*, 3rd ed. (Macmillan Publishing Company, New York, 1990).

21. S. Vidal, J. Luce, and D. Penninckx, Opt. Lett. **36**, 3494 (2011).

22. D. Penninckx *et al*., J. Lightwave Technol. **24**, 4197 (2006).

23. S. Hocquet *et al*., Appl. Opt. **49**, 1104 (2010).

24. J. W. Goodman, *Statistical Optics* (Wiley, New York, 2000).

25. D. Collett, *Modelling Binary Data*, 2nd ed. (Chapman & Hall/CRC, Boca Raton, FL, 2003).

The Fifth Omega Laser Facility Users Group Workshop

Introduction

A capacity gathering of over 100 researchers from 25 universities and laboratories met at the Laboratory for Laser Energetics (LLE) for the Fifth Omega Laser Facility Users Group (OLUG) workshop. The purpose of the 2.5-day workshop was to facilitate communications and exchanges among individual Omega users and between users and the LLE management; to present ongoing and proposed research; to encourage research opportunities and collaborations that could be undertaken at the Omega Laser Facility and in a complementary fashion at other facilities [such as the National Ignition Facility (NIF) or the Laboratoire pour l'Utilisation des Lasers Intenses (LULI)]; to provide an opportunity for students, postdoctoral fellows, and young researchers to present their research in an informal setting; and to provide feedback to LLE management from the users about ways to improve the facility and future experimental campaigns. The interactions were wide-ranging and lively, as illustrated in the accompanying photographs.

OLUG consists of over 300 members from 35 universities and many centers and national laboratories. Names and affiliations can be found at **http://www.lle.rochester.edu/media/about/documents/OLUGMEMBERS.pdf**. OLUG is by far the largest users group in the world in the field of high-energy-density physics and is also one of the most active.

The first two mornings of the workshop were comprised of seven science and facility presentations. The facility talks proved especially useful for those unfamiliar with the art and complexities of performing experiments at the Omega Laser Facility. But since the facility is constantly evolving and improving, even experienced users benefited significantly from these updates. The overview science talks, given by leading world authorities, described the breadth and excitement of high-energy-density (HED) science either being undertaken at the Omega Laser Facility or well within the reach of the facility with improvements or upgrades.

U1627JR

Figure 136.31
A capacity gathering of 100 researchers from 25 universities and laboratories around the world participated in this year's workshop. The users group itself has well over 300 members from 35 universities and 25 laboratories, making it by far the largest users group in the world in high-energy-density physics. The next annual OLUG Workshop will occur 23–25 April 2014.

Forty students and postdoctoral fellows participated in the workshop, and 36 were supported by travel grants from the National Nuclear Security Administration (NNSA). The content of their presentations encompassed the spectrum from target fabrication to simulating aspects of supernovae; the presentations generated spirited discussions, probing questions, and friendly suggestions. In total, there were 68 contributed posters, including eight that focused on the Omega Laser Facility.

U1606JR

Figure 136.32
Nearly all the 40 students and postdoctoral fellows who attended made poster presentations; 36 received travel assistance from an NNSA grant. The workshop emphasized the participation and involvement of young researchers.

An important function of the workshop was to develop a set of **Findings and Recommendations** to help set and define future priorities for the Omega Laser Facility. These were grouped into three areas: 60-beam OMEGA, OMEGA EP, and general facility improvements and accessibility of OMEGA operational information. LLE management uses these recommendations as a guide for making decisions about Omega Laser Facility operations, priorities, and future changes. In addition, the status of these OLUG **Findings and Recommendations** will be updated and reviewed at a satellite evening meeting during the 2013 APS-DPP Conference. They will also form the grist for the forthcoming workshop. The widely discussed **Findings and Recommendations** are listed below.

One highlight of the workshop, as in past workshops, was a panel of students and postdoctoral fellows who discussed their experiences at the Omega Laser Facility and their thoughts and recommendations on facility improvements. Engaging discussions were sparked by this forum, which resulted in the student/postdoctoral recommendations for the facility.

For the first time, three posters were presented by students in LLE's Summer High School Research Program. We plan to expand the number of these excellent presentations in the 2014 April Workshop.

U1607JR

Figure 136.33
A total of 68 posters, the majority by young researchers, were presented during three poster sessions.

Another important event at the end of the workshop was a panel of experts who gave an overview of the HED opportunities at national laboratories. These discussions are very useful for young researchers who may not know all the capabilities and HED research occurring at these various institutions.

Finally, it was decided to hold the next workshop on 23–25 April 2014. Plans are already well underway for this event.

**Principal Findings and Recommendations
of the 2013 Workshop**
1. Wednesday Evening Session for Young Researchers
The young researchers would like to have a Wednesday evening session (on the first day of the workshop), where they could discuss topics and concerns that most directly impact their research, especially as it relates to the Omega Laser Facility. From their discussions, this would be used as important input to the Findings and Recommendations for the 2014 workshop.

2. Tritium-Filling Capability
While notable and important capabilities have occurred in tritium filling of capsules with different gas mixtures (such as with ^{3}He for D^{3}He shots), and as well with reasonable high-T purity (for TT shots, where an ~1.5% D contamination level was achieved), we look forward, with implementation of the isotope separator, to even higher-purity-T experiments (0.2% D).

This will lead to very important advances in plasma nuclear science (D. McNabb, M. Gatu Johnson, D. Casey, J. Caggiano, H. Herrmann, L. Bernstein, and J. Frenje).

3. OMEGA EP to Full Specifications

While very significant improvements in the last year have occurred in bringing OMEGA EP closer to full performance specifications, for which we applaud the Omega Laser Facility, we look forward to continued improvement in its capabilities (L. Willingale, M.-S. Wei, R. Mancini, P. Norreys, and P. Drake).

4. OMEGA EP Long-UV-Pulse Operations

Long-pulse operation, in the 10- to 100-ns interval, would enable new and unique science to be performed. These include shock, photoionization-relaxation and nonequilibrium, late-time instabilities, and, in general, larger time-scale laboratory astrophysical experiments (R. Mancini, C. Kuranz, R. Heeter, D. Martinez, J. Kave, P. Drake, P. Keiter, M.-S. Wei, and H.-S. Park).

5. Opposing UV Beams on OMEGA EP

While OLUG recognizes this is a long-term, substantial project requiring considerable resources, it also felt that such a project would be an important new capability of the facility (M.-S. Wei, L. Willingale, C. Kuranz, H. Chen, P. Drake, C. Huntington, and H.-S. Park).

6. Independent, or Semi-Independent, Legs for OMEGA-60's Three Legs

While OLUG recognizes this as a major undertaking, this would bring with it significant new capabilities for exciting frontier science (C. Kuranz, R. Mancini, L. Willingale, R. Rygg, and P. Norreys). Related to this is the possible decoupling of Beam 25 for Thomson scattering (C. Huntington).

7. Foreground Target Illumination on OMEGA-60

Improvement in the foreground target illumination is recommended (J. Cobble and C. Kuranz).

8. Updating the Omega Users' Guide

This document is extremely useful to all users and would benefit from being updated (many users).

9. Low-Energy Neutron Spectroscopy.

Extending spectroscopy in the ~1- to ~2-MeV regime, as well as from ~0.1 to ~1 MeV, would be an outstanding new diagnostic to add to the existing OMEGA 60-beam neutron diagnostics. In addition to giving a new window for basic capsule-implosion performance, it would almost certainly significantly advance the frontier field of plasma nuclear science, which has been pioneered at the Omega Laser Facility. It is important to note that very significant work has taken place in the past year in this regard (C. Forrest, M. Gatu Johnson, D. McNabb, C. Sangster, J. Frenje, L. Bernstein, J. Caggiano, H. Herrmann, and Y. Kim).

10. High-Resolution X-Ray Imaging Spectrometer

This current project, initiated in 2013 by colleagues from Princeton and the University of Rochester, is an outstanding diagnostic that we applaud, bringing additional unique capabilities to the OMEGA 60-beam laser (K. Hill, P. Nilson, H.-S. Park, N. Landen, and J. Frenje).

11. Super GCD-3 Gamma Spectrometer

Extending gamma spectroscopy to study low-probability reactions would be highly desirable from both the point of view of implosions physics and for enabling innovative plasma nuclear science/nucleosynthesis such as the H–D fusion line at 5.5 MeV (Y. Kim, H. Herrmann, D. McNabb, A. Zylstra, J. Frenje, and L. Bernstein).

12. Differential Burn-Time Diagnostic of D–D and D^{3}He

There is a very strong likelihood that for capsules filled with D^{3}He, the bang times of D–D and D^{3}He may differ by an order of ~30 ps or more. Such a differential could be an indication of either two-ion-fluid effects or kinetic effects, neither of which have been deeply explored, although there is strong evidence that such effects should be present. This is a project that was initiated in 2013 and is well underway, with the first system tests and experiments to be conducted on 20 November 2013 (H. Sio, C. Bellei, R. Mancini, P. Amendt, P. Norreys, N. Hoffmann, S. Wilks, S. Atzeni, J. Frenje, C. Stoeckl, V. Glebov, R. Betti, and D. Shvarts).

13. Implementing a Two-Ion Fluid Capability in *LILAC*

LILAC and all other standard hydrocodes in existence—*LASNEX*, *HYDRA*, *DUED*, *HYADES*—are all single-ion-fluid codes. Having a capability to probe differences in bang time for the two-ion species would be a timely development, as noted above for the differential burn-time diagnostic (H. Sio, C. Bellei, J. Frenje, S. Wilks, P. Amendt, N. Hoffmann, G. Kagan, R. Betti, S. Atzeni, K. Molvig, and D. Shvarts).

14. Improvement in SOP/ASBO

Several recommendations were made in this regard. For the active shock breakout (ASBO): a faster comb (4 GHz) is needed along with the ability to image spatial-distortion data

at full sweep speed; alignment and *Q*-switching procedures should be updated; new etalons should be acquired. For the streaked optical pyrometer (SOP): improvements are needed in background and noise mitigation along with absolute calibration and imaging spatial-distortion data at full sweep speed (M. Millot, P. Celliers, and T. Boehley).

15. Compact High-Resolution, 14.1-MeV Neutron Spectrometers

Since kinetic-flow effects are very likely to have a significant impact on furthering our fundamental understanding of cryo and non-cryo capsule implosions, this new diagnostic would extend and nicely complement OMEGA-60's present capabilities. The compactness of the design would allow, for the first time, comprehensive views of the implosions, therefore enabling blue and red shifts to be simultaneously observed. This project is well underway, with some excellent preliminary data already obtained (A. Zylstra, J. Frenje, V. Glebov, V. Goncharov, J. Caggiano, and J. Kilkenny).

16. 4ω Thomson Scattering on OMEGA EP

This would be an extremely valuable capability and may not be too resource intensive (W. Fox, C. Kuranz, L. Willingale, H.-S. Park, and C. Hungtington).

The photographs on the following pages provide a representative sampling of the workshop's talks, interactions, and ambience.

(a)   (b)   (c)
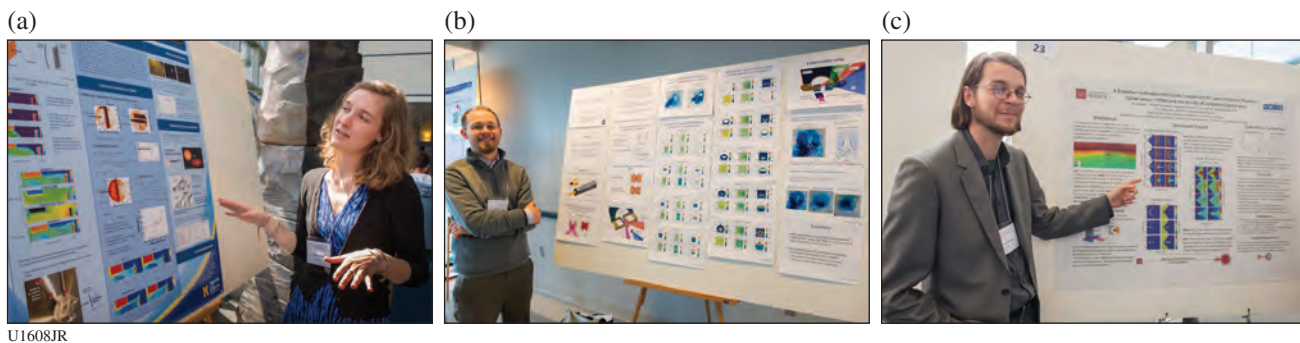
U1608JR

Figure 136.34
The posters ran the gamut from (a) laboratory astrophysics (Christine Krauland from the University of Michigan), to (b) reconnection in high-β plasmas (Will Fox, from the University of New Hampshire), to (c) high-end simulations utilizing FLASH (Chris Orban from Ohio State University).
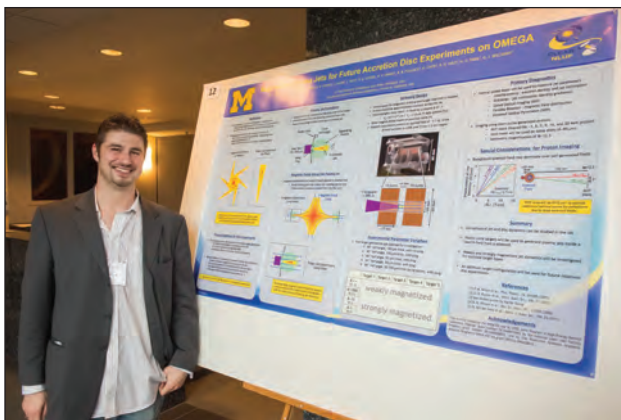
U1609JR

Figure 13.35
NASA's Einstien postdoctoral fellow Mario Manuel presented his continuing OMEGA research plans. Mario, now at the University of Michigan, is the first NLUF/NNSA-sponsored Ph.D. to receive this prestigious Einstein Fellowship. Congratulations to Mario and the Omega Laser Facility, where Mario's Ph.D. research was conducted.

U1610JR

Figure 136.36
Presentations included superb posters given by three researchers in LLE's 2012 Summer High School Research Program. Shown from left are Emily Armstrong, Christa Caggiano, and Raz Rivlis. We plan to expand the number of these high school LLE summer participants in the 2014 workshop.
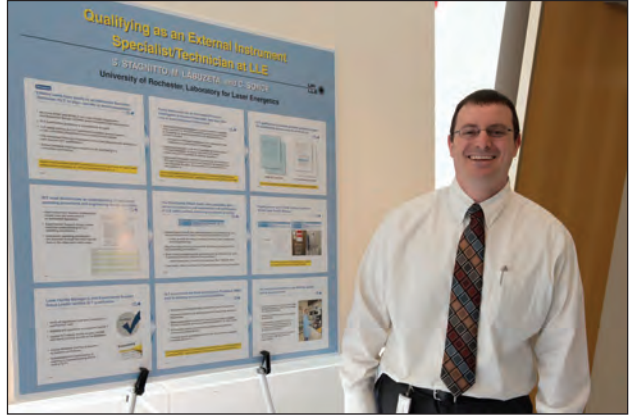
(a)

(b)

U1611JR

Figure 136.37
(a) Engineers Mark Labuzeta and Chuck Sorce and (b) engineer Steve Stagnitto. The eight "Facility" posters, many addressing Findings and Recommendations of OLUG, were widely lauded by the users; "tremendously useful and informative" was the universal sentiment for this session. The 2014 workshop will continue this tradition since it has proved so valuable to the workshop attendees.

U1614JR

Figure 136.38
The young researcher's panel and town meeting is one of OLUG's most important sessions, highlighting many of the challenges faced by young researchers at the Omega Laser Facility and elsewhere. Next year's chair of the young researcher's panel is MIT's Alex Zylstra (far left).

U1613JR

Figure 136.39
Tours of the facility are a critical part of the workshop and bring home the complexity, coordination, and long-range planning needed for implementing a successful campaign. Here OMEGA EP Senior Engineer and Laser Facility Manager Dave Canning describes OMEGA EP's hardware, layout of the principal components in the Laser Bay, and the planning needed for a successful OMEGA EP campaign.

U1617JR

Figure 136.40
One of the Finding and Recommendations, discussed here by MIT Ph.D. student Hong Sio, was to use a novel diagnostic to measure, with high accuracy, the differential nuclear bang time of D–D and D^3He in D^3He–filled implosions. Such work should illuminate two-fluid-ion effects and/or kinetic plasma effects. The first full-on test of this diagnostic will take place 20 November 2013.

(a)

(c)

(b)

U1612JR

Figure 136.41
World-class physicists described cutting-edge research either ongoing at the Omega Laser Facility, or those tantilizing possibilities "just around the corner:" (a) Don Lamb from the University of Chicago, (b) Mark Koepke from West Virginia University, and (c) Valeri Goncharov from LLE.

U1620JR

Figure 136.42
The workshop banquet at the Meliora, on the University of Rochester's campus, offered a wonderful time for old and new friends to mingle in a congenial ambiance.

LLE's Summer High School Research Program

During the summer of 2013, 15 students from Rochester-area high schools participated in the Laboratory for Laser Energetics' Summer High School Research Program. The goal of this program is to excite a group of high school students about careers in the areas of science and technology by exposing them to research in a state-of-the-art environment. Too often, students are exposed to "research" only through classroom laboratories, which have prescribed procedures and predictable results. In LLE's summer program, the students experience many of the trials, tribulations, and rewards of scientific research. By participating in research in a real environment, the students often become more excited about careers in science and technology. In addition, LLE gains from the contributions of the many highly talented students who are attracted to the program.

The students spent most of their time working on their individual research projects with members of LLE's technical staff. The projects were related to current research activities at LLE and covered a broad range of areas of interest including laser physics, computational modeling of implosion physics, experimental diagnostic development, spectroscopy, cryogenic deuterium properties, liquid crystal devices, tritium detection and capture, ballistic deflection transistors, positioning systems, and 3-D virtual modeling (see Table 136.IV).

The students attended weekly seminars on technical topics associated with LLE's research. Topics this year included laser physics, fusion, holography, nonlinear optics, atomic force microscopy, electronic paper, and scientific ethics. The students also received safety training, learned how to give scientific presentations, and were introduced to LLE's resources, especially the computational facilities.

The program culminated on 28 August with the "High School Student Summer Research Symposium," at which the students presented the results of their research to an audience including parents, teachers, and LLE staff. The students' written reports will be made available on the LLE Website and bound into a permanent record of their work that can be cited in scientific publications.

Three hundred and twelve high school students have now participated in the program since it began in 1989. This year's students were selected from nearly 80 applicants.

At the symposium LLE presented its 17th annual William D. Ryan Inspirational Teacher Award. The recipient this year was Mrs. Eugenie Foster, a mathematics teacher from Brighton High School. This award is presented to a teacher who motivated one of the participants in LLE's Summer High School Research Program to study science, mathematics, or technology and includes a $1000 cash prize. Teachers are nominated by alumni of the summer program. Mrs. Foster was nominated by Mitch Perry, Julia Tucker, and Jack Valinsky, participants in the 2012 program. They wrote, "Not only is Mrs. Foster a smart and capable teacher, she also has a knack for making math fun and cares about her students … She allows her students to develop an intuition for the material on their own and encourages them to further their exploration of math outside of the classroom." They credit Mrs. Foster with developing a discrete math course to showcase mathematical topics outside of the core curriculum for students who "have that extra thirst which only mathematics can quench." They also credit Mrs. Foster with developing an Intro to College Math course "to reach out to students who do not perceive themselves pursuing math-related fields in college or those to whom math does not come easily." They go on to say, "Her popularity among her students is due not only to her superb teaching and love of math, but also the personal connections she makes with her students…Past students still come into her classes years after they have graduated to say hello, showing her lasting impact on each and every one of her students." Mrs. Foster also received strong support from Dr. Thomas Hall, principal of Brighton High School, who described her as "a phenomenal teacher, dedicated and passionate, someone who makes herself available to students 24/7."

Table 136.IV: High School Students and Projects—Summer 2013.

Name	High School	Supervisor	Project Title
Aaron Appelle	Brighton	R. Sobolewski and Y. Akbas	Drift-to-Ballistic Electron Transport in Conducting Nanochannels for the Operation of Ballistic Deflection Transistors
Alexander Frenett	Allendale Columbia	F. J. Marshall	Integration of X-Ray Microscope Elements to a High-Speed Framing Camera Format
Sara Gnolek	Webster Thomas	W. T. Shmayda	Catalytic Oxidation of Hydrogen in Air Streams
Samuel Goodman	Pittsford Mendon	W. T. Shmayda	Detecting Hydrogen in Helium Streams
Michael Hartman	Pittsford Sutherland	R. Kidder	Creating a Virtual Research Environment Through Collaborative Networking
Eric Hwang	Penfield	R. Boni and W. R. Donaldson	The Development and Testing of a Signal Processing Algorithm to Improve OMEGA Beam Timing
Katherine James	Honeoye Falls-Lima	K. L. Marshall	Rewriteable Photoalignment of Liquid Crystals as a Route to High-Laser-Damage-Threshold Active Beam Shapers
John Jamieson	Allendale Columbia	M. J. Guardalben	Modeling the Effects of Deformable Mirror Location in the OMEGA EP Pulse Compression System
Yifan Kong	Webster Schroeder	R. S. Craxton	Beam-Pointing Optimization for Proton Backlighting on the National Ignition Facility
Nathaniel Rogalskyj	McQuaid	G. Brent and D. Lonobile	A Cryogenic and Radiation Tolerant Encoder
Benjamin Saltzman	Brighton	P. M. Nilson	Understanding K-Line Shifts in Rapidly Heated Matter
Adeeb Sheikh	Pittsford Sutherland	R. Epstein	Controlling Laser Beam Speckle with Optimized Illumination of Zooming Phase Plates
Logan Toops	Webster Thomas	R. Sobolewski and Y. Akbas	Modeling and Controlling Electron Movement in a Ballistic Deflection Transistor
Erin Wang	Brighton	D. R. Harding	Thermodynamics of the Solid–Liquid Phase Boundary of Deuterium
Cameron Ziegler	Canandaigua Academy	S.-W. Bahk	Alignment of an Offner Triplet Radial Group Delay Compensator

FY13 Laser Facility Report

During FY13, the Omega Laser Facility conducted 1408 target shots on the 60-beam OMEGA laser and 576 target shots on the four-beam OMEGA EP laser for a total of 1984 target shots (see Tables 136.V and 136.VI). OMEGA averaged 11.5 target shots per operating day with Availability and Experimental Effectiveness averages of 93.9% and 96.6%, respectively.

OMEGA EP was operated extensively in FY13 for a variety of internal and external users. Of the 576 total shots, 507 target shots were taken into the OMEGA EP target chamber and 69 joint target shots were delivered to the OMEGA target

chamber. OMEGA EP averaged 6.7 target shots per operating day with Availability and Experimental Effectiveness averages of 93.8% and 93.7%, respectively.

Highlights of Achievements in FY13

1. Joint Cryo Backlighting

A new platform has been developed for backlighting 60-beam cryogenic target implosions on OMEGA using the OMEGA EP beam. A ten-inch manipulator (TIM)–based fast positioner has been developed that can place a backlighter target 10 mm from the cryogenic target after the cryogenic shroud

Table 136.V: OMEGA Laser Facility Target Shot Summary for FY13.

Laboratory/ Program	Planned Number of Target Shots	Actual Number of Target Shots	ICF	Shots in Support of ICF	Non- ICF
CEA	40	53	0	0	53
LANL	170	206	21	0	185
LBS	155	163	0	0	163
LLE	390	428	0	416	12
LLNL	295	350	108	0	242
NLUF	150	183	0	0	183
UMich	10	10	0	0	10
Other	0	15	0	15	0
Total	1210	1408	129	431	848

Table 136.VI: OMEGA EP Laser Facility Target Shot Summary for FY13.

Laboratory/ Program	Planned Number of Target Shots	Actual Number of Target Shots	ICF	Shots in Support of ICF	Non- ICF
LANL	0	0	0	0	0
LBS	65	106	0	0	106
LLE	110	165	0	129	36
LLNL	110	158	58	0	100
NLUF	65	91	0	0	91
Other	0	56	0	56	0
Total	350	576	58	185	333

has been retracted. The target is inserted 80 mm in 70 ms with a position accuracy of 25 μm. This fast positioner is being utilized in concert with the spherical crystal imager to capture stop-action images of the cryogenic target during implosions.

2. 4ω Probe Diagnostics

Following the successful installation of the 4ω probe laser in the OMEGA EP Target Bay, the optical diagnostic infrastructure was commissioned in FY13. The first diagnostic leg that was activated can capture shadowgraphs or schlieren images of the laser–plasma interaction. A novel improvement to the schlieren diagnostic placed an angular filter at the Fourier plane to map the refraction of the beam at the target plane to contours in the image plane. The diagnostic also has additional ports available; a polarimetry diagnostic has been designed and will be completed in early FY14.

3. Neutron Temporal Diagnostic Replaced

The neutron temporal diagnostic (NTD) is the primary diagnostic for characterization of the reaction rate history of neutron emission for a DT or D$_2$ target experiment. The original NTD, in use for 15 years on OMEGA and ~10 years prior to that on NOVA at LLNL was decommissioned after the controls and mechanics became obsolete. The improved design increases the service access, shielding, and operability and modernizes the control electronics and streak camera.

4. Tritium Fill Station Cryo Permeator

The yield on cryogenic target shots has been improved by a factor of ~2 following the addition of a permeator. A Pd/Ag permeator removes organic impurities and decay helium from the DT fuel as the tritium is transported from the storage beds to the high-pressure fill system. This additional fuel purification step was added to the fill procedures and has been in use on all fills since 1 January 2013.

5. Sydor Framing Camera

In a joint development venture with Sydor Instruments LLC, a new gated x-ray detector has been fielded on OMEGA. The Sydor framing cameras can be paired with all unimount-compatible front ends including pinhole imagers and crystal spectrometers. It is compatible with film packs and also with a Sydor vacuum charge-coupled–device (CCD) camera design. Two units have been deployed, one "fast" and one "slow" camera.

6. Solid-State Pockels Cell Drivers

LLE has developed a custom solid-state Pockels cell driver to replace discontinued commercially available high-voltage power supplies. The large-aperture ring amplifiers in OMEGA utilize a pulsed Pockels cell in a configuration where thyratron high-voltage switching electronics were used reliably for the past 20+ years. These supplies were the only available technology that could achieve the required long-duration pulse and failsafe requirements to prevent laser damage. The replacement LLE device uses readily available metal–oxide–semiconductor field-effect transistor (MOSFET) solid-state electronics in an inductive–adder configuration to reliably produce pulses with improved rise times, fall times, and uniformity. Five of the LLE-designed power supplies were fabricated in FY13.

Experimental Operations and Diagnostics

Twenty-five new target diagnostics were commissioned in FY13 on OMEGA and seven on OMEGA EP. The OMEGA additions included the neutron temporal diagnostic (NTD) and framing camera projects described above. The two new Sydor x-ray framing cameras (SFC's) were commissioned on both OMEGA and OMEGA EP. Updates to the diagnostic inventory on OMEGA EP included the commissioning of the 4ω probe laser and diagnostic table, the slit imager for the ultrafast x-ray streak camera (UFXRSC), and the LLNL specular frequency-resolved optical gating (SpecFROG) diagnostic. Also on OMEGA, reflective spectrometer channels were added to the TIM-based μDMX x-ray diode array. As in previous years, many of the new instruments were developed by or in collaboration with other laboratories, including LLNL, LANL, and CEA.

Facility improvements on OMEGA included the Sydor CCD x-ray framing camera readout system, the FASTPOS target positioning system for cryogenic target backlighting, and the Port-2 neutron diagnostic inserter (NDI) system. Two additional OMEGA TIM's were retrofitted with new electromagnetic interference (EMI)–resistant control systems; four are now complete and the remaining two will be completed in FY14. Minor changes to the OMEGA target chamber and diagnostics improved the typical operating vacuum pressure by nearly an order of magnitude. On OMEGA EP, Target Viewing System (TVS) distortion correction was implemented.

National Laser Users' Facility and External Users' Programs

Under the facility governance plan that was implemented in FY08 to formalize the scheduling of the Omega Laser Facility as a National Nuclear Security Administration (NNSA) User Facility, Omega Facility shots are allocated by campaign. The majority (68.3%) of the FY13 target shots were allocated to the Inertial Confinement Fusion (ICF) campaign conducted by integrated teams from the national laboratories and LLE and the high-energy-density campaigns conducted by teams led by scientists from the national laboratories.

The fundamental science campaigns were allocated 28.3% of the shots taken in FY13. Half of these were dedicated to university fundamental science under the National Laser Users' Facility (NLUF) Program, and the remaining shots were allotted to the Laboratory Basic Science (LBS) Program, comprising peer-reviewed fundamental science experiments conducted by the national laboratories and by LLE, including the Fusion Science Center (FSC).

The Omega Laser Facility is also being used for several campaigns by teams from the Commissariat à l'Énergie Atomique (CEA) of France and the Atomic Weapons Establishment (AWE) of the United Kingdom. These programs are conducted at the facility on the basis of special agreements put in place by DOE/NNSA and participating institutions.

The facility users during this year included 11 collaborative teams participating in the NLUF Program; 16 teams led by Lawrence Livermore National Laboratory (LLNL) and LLE scientists participating in the LBS Program; many collaborative teams from the national laboratories conducting ICF experiments; investigators from LLNL and Los Alamos National Laboratory (LANL) conducting experiments for high-energy-density-physics programs; and scientists and engineers from CEA, AWE, and the Center for Radiative Shock Hydrodynamics (CRASH) of the University of Michigan.

In this section, we briefly review all the external user activity on OMEGA during FY13.

FY13 NLUF Program

FY13 was the first of a two-year period of performance for the NLUF projects approved for the FY13–FY14 funding and OMEGA shots. Eleven NLUF projects (see Table 136.VII) were allotted Omega Laser Facility shot time and conducted a total of 274 target shots at the facility. This NLUF work is summarized in this section.

Systematic Study of Fast-Electron Energy Deposition in Imploded Plasmas with Enhanced OMEGA EP Laser Contrast and Intensity

Principal Investigators: F. N. Beg (University of California, San Diego) and M.S. Wei (General Atomics)
Co-investigators: C. McGuffey and B. Qiao (University of California, San Diego); R. B Stephens (General Atomics); A. A. Solodov, W. Theobald, C. Stoeckl, J. A. Delettrez, and R. Betti (LLE); C. D. Chen, M. H. Key, P. Patel, and H. McLean (LLNL); and T. Yabuuchi and H. Habara (Institute of Laser Engineering, Japan)
Lead Graduate Student: L.C. Jarrott (University of California, San Diego)

Understanding fast-electron transport and spatial energy deposition in high-density plasmas is extremely important for fast-ignition (FI) inertial confinement fusion. The goal of the University of California San Diego NLUF project is to characterize fast-electron spatial energy deposition in integrated cone-guided FI experiments by measuring fast-electron–induced Cu K-shell fluorescence emission using Cu-doped CD shells attached to a Au cone. This target design facilitates the knowledge of the crucial parameters that can affect the coupling, so that coupling to the core can be improved. In this FY13 experiment, the laser energy contrast on the OMEGA EP laser had been improved by nearly two orders of magnitude compared with the FY12 NLUF campaign (from ~80 mJ to <1 mJ in the nanosecond prepulse). With this, a comparison of fast-electron coupling efficiency and spatial distribution as a function of laser contrast was made.

Table 136.VII: NLUF proposals approved for shots at the Omega Laser Facility for FY13–FY14.

Principal Investigator	Institution	Project Title
F. N. Beg	University of California, San Diego	Systematic Study of Fast-Electron Energy Deposition in Imploded Plasmas with Enhanced OMEGA EP Laser Contrast and Intensity
R. P. Drake	University of Michigan	Experimental Astrophysics on the OMEGA Laser
T. Duffy	Princeton University	Dynamic Compression of Earth and Planetary Materials Using OMEGA
W. Fox	University of New Hampshire	Dynamics and Instabilities of Magnetic Reconnection Current Sheets in High-Energy-Density Plasmas
P. Hartigan	Rice University	Astrophysical Dynamics in the Laboratory: Mach Stems and Magnetized Shocks
R. Jeanloz	University of California, Berkeley	Journey to the Center of Jupiter, Recreating Jupiter's Core on OMEGA
H. Ji	Princeton University	Study of Particle Acceleration and Fine-Scale Structures of Collisionless Magnetic Reconnection Driven by High-Energy Petawatt Lasers
R. D. Petrasso	Massachusetts Institute of Technology	Studies of Laboratory Astrophysics, Inertial Confinement Fusion, and High-Energy-Density Physics with Nuclear Diagnostics
B. Qiao	University of California, San Diego	Dynamics of High-Energy Proton Beam Focusing and Transition into Solid Targets of Different Materials
A. Spitkovsky	Princeton University	Generation of Collisionless Shocks in Laser-Produced Plasmas
R. B. Stephens	General Atomics	Investigation of the Dependence of Fast-Electron Generation and Transport on Laser Pulse Length and Plasma Materials

This work used the OMEGA laser for fuel assembly and an OMEGA EP beam focused onto the inner cone tip to produce fast electrons. A spherical crystal imager (SCI) was used to image the K_α radiation from the Cu dopant atoms. Emission was observed in the imploding plasma initiated by suprathermal electrons from the OMEGA beams as well as the fast electrons produced from the OMEGA EP beam. A calibrated zinc Von Hamos (ZVH) x-ray spectrometer, tuned to measure Cu K-shell and ionic line emission, recorded yield measurements. Several other diagnostics, including broadband x-ray imaging pinhole cameras and Kirkpatrick–Baez (KB) microscopes, neutron time-of-flight detectors, and magnetic electron spectrometers (one multichannel spectrometer along the OMEGA EP beam axis and one single-channel spectrometer at the side), were employed.

With improvements to our FY12 demonstration experiment, the dopant level in the CD shells was increased from 0.9% to 1.3% as a means to increase Cu K_α photon statistics, and the SCI beam block was modified to reduce background. The filtration level on the neutron detectors was also adjusted from previous campaigns, resulting in observed neutron yields for the first time in this series of experiments.

Figure 136.43 compares integrated Cu K_α yield for FY12 and FY13 NLUF campaigns measured with the ZVH spectrometer. Differences in dopant level have been taken into account. With the improved OMEGA EP contrast, up to ~50% enhancement in fast-electron–produced Cu K_α was measured. Further, the scaling of Cu K_α with OMEGA EP energy was steeper, indicating better coupling of laser energy into fast electrons at high (kJ) laser energies. Fusion neutron yield was also found to increase by roughly a factor of 3 when increasing the OMEGA EP energy from 0 J (OMEGA-only implosion) to full energy (1.2 kJ) as seen in Fig. 134.44.

A major component of the project has been the development and benchmarking of our modeling capabilities through experimental results. Three parallel studies are underway using three different codes to model the experimental results. In each study, simulations of the implosion using the radiation–hydrodynamic code *DRACO* are used as input to model the fast-electron transport through the imploded plasma. In addition the laser–plasma interaction from the OMEGA EP beam with the inner Au cone is simulated using the particle-in-cell code *LSP*. With this, a more-accurate electron source can be used while simultaneously validating the electron source simulations via
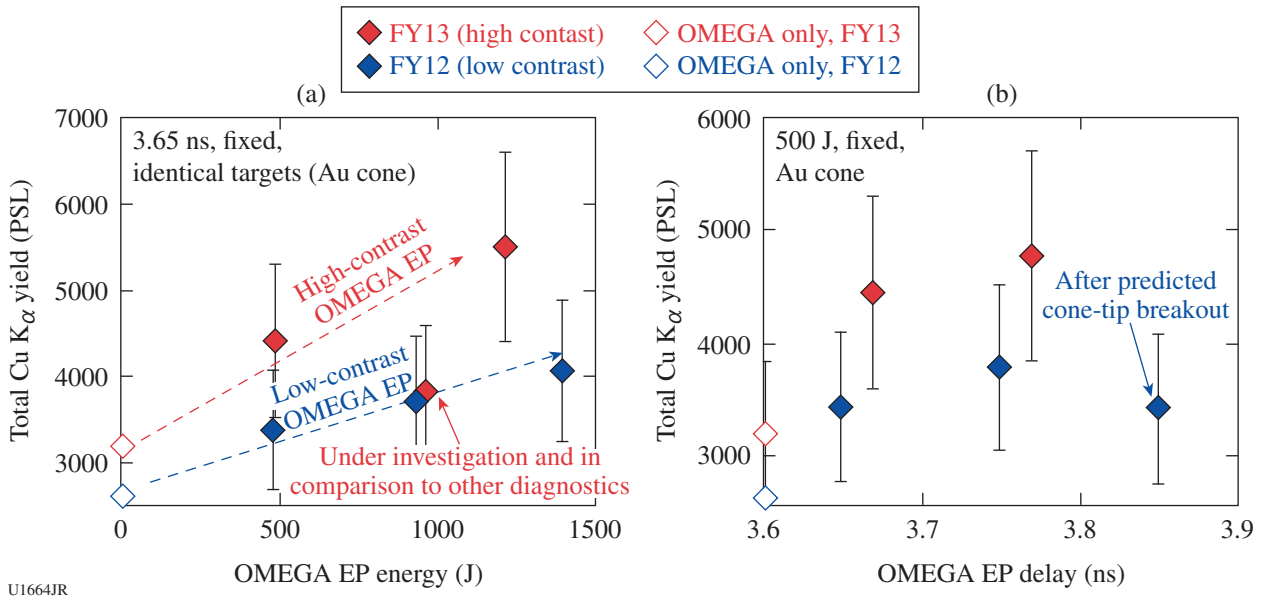
Figure 136.43
Comparison of Cu K_α yield enhancement caused by fast electrons measured by zinc Von Hamos (ZVH) as a function of (a) OMEGA EP beam energy and (b) OMEGA EP timing delay using high- and low-contrast OMEGA EP pulses. The 1-kJ shot had anomalously low K_α and continuum on the ZVH diagnostic only, which is under further scrutiny.
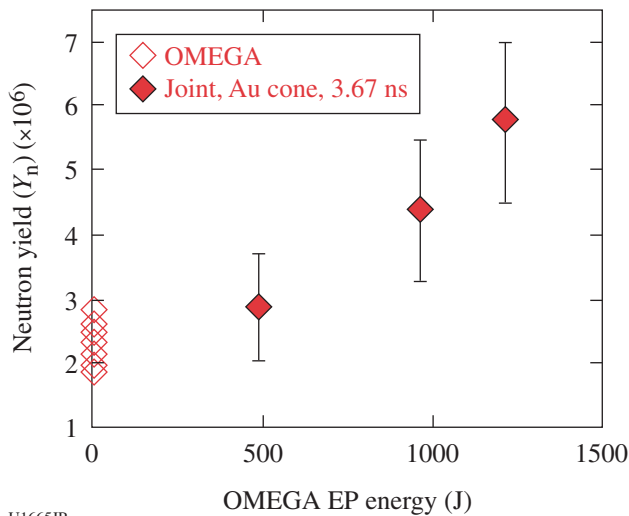
Figure 136.44
FY13 data set showing D–D neutron yield for the first time from the Cu-doped targets. Yield increased as a function of laser energy.

a backward analysis of the transport codes. Diagnostics have been implemented in the codes to emulate the projected Cu K_α profile for direct comparison to the experimental images.

In summary, the NLUF fast-electron transport experiment using a cone-in-shell (with Cu doping) target has been success-

fully performed on the OMEGA laser with a comprehensive suite of x-ray, particle, and, for the first time, neutron diagnostics. The platform for complex electron-transport physics experiments has been established and will be pursued for >kJ short-pulse laser energies.

Richtmyer–Meshkov Mode Coupling on OMEGA EP
Principal Investigators: R. P. Drake, P. Keiter, and C. Kuranz (University of Michigan)
Co-investigators: S. Lebedev (Imperial College); D. Shvarts and Y. Elbaz (Negev Research Center); G. Gregori (Oxford); M. Koenig (École Polytechnique); B. van der Holst, B. Torralva, and M. Grosskopf (University of Michigan); E. Blackman (University of Rochester); J. P. Knauer, T. R. Boehly, G. Fiksel, and D. H. Froula (LLE); C. Michaut (Observatoire de Paris); and B. Loupias (CEA)

Shock-wave–related interface phenomena play important roles in many diverse high-energy-density (HED) processes, such as the cooling of fusion fuel capsules or mixing of layers in supernova remnants. Recently, the unique laser and diagnostic capabilities of OMEGA EP has enabled us to develop a novel series of experiments exploring HED hydrodynamics driven by steady shock waves. Here, we describe an experiment observing, for the first time, well-characterized multimode Richtmyer–Meshkov (RM) physics under these conditions.

RM occurs when a shock wave crosses the interface between two materials of differing densities. If a region of such an interface is not perfectly smooth, the shock will cross the interface at different times in adjacent locations and will briefly have different velocities in the two locations. This results in the deposition of vorticity at this interface perturbation, and the vorticity in turn causes the perturbation to grow in time. This experiment seeks to study RM behavior at late times, when the growth has become nonlinear, and in particular to observe the interaction between perturbation modes.

The initial conditions for this experiment involve a layer of carbon foam of 0.4-g/cm^3 density pressed against a layer of plastic of 1.4-g/cm^3 density. On the surface of the plastic, at its interface with the foam, a two-mode (wavelengths of 50 and 100 μm) sinusoidal seed perturbation has been machined. The materials are ordered such that the shock passes from the lower-density foam into the higher-density plastic, making the configuration Rayleigh–Taylor stable. A plastic ablator, of 1.2-g/cm^3 density, is placed before the foam in order to avoid direct irradiation of the foam by the laser. A sketch of this system is shown in Fig. 136.45. Two (a third can also be used) OMEGA EP beams, operating in UV mode with 10-ns pulse durations and fired sequentially to create an effective 20-ns-long pulse, are used to drive a shock wave into this system. The beams have an energy of roughly 4 kJ each and are smoothed by 1100-μm-diam phase plates, resulting in an irradiance of roughly 4×10^{13} W/cm^2. Following passage of the shock wave, a RM structure develops over time at the foam/plastic interface. The interface is then diagnosed using the OMEGA EP spherical crystal imager to perform side-on radiography. Examples of data are shown in Fig. 136.46.

Figure 136.46
Examples of radiographs from shots (a) with and (b) without the machined seed perturbation, respectively. Both images were taken roughly 13 ns after the shock crossed the foam/plastic interface. (c) The Fourier transform of the foam/plastic interface contour, demonstrating the growth of the initial modes of wave number $k = 4$ and $k = 8$, corresponding to 100-μm and 50-μm wavelengths, respectively, as well as the appearance of harmonic modes $k = 4 + 8 = 12$ and $k = 12 + 4 = 16$, corresponding to 33-μm and 25-μm wavelengths, respectively.

X-Ray Diffraction Study of the Structure and Equation of State of Molybdenum to 9 Mbar
Principal Investigator: T. Duffy (Princeton)

The goal of this campaign was to study the structure of solid molybdenum (Mo) using x-ray diffraction under both ramp and shock-wave loading. Experiments were performed using the powder x-ray diffraction image plate (PXRDIP) diagnostic (Fig. 136.47). Four OMEGA beams were focused on the main target to drive and compress the Mo powder (sandwiched between two diamonds) and up to ten beams were focused on a Cu backlighter to generate quasi-monochromatic x-ray emission for diffraction measurements. We used a 3.5-ns ramp (rm3501) followed by a 1-ns square pulse (sg1018) to drive
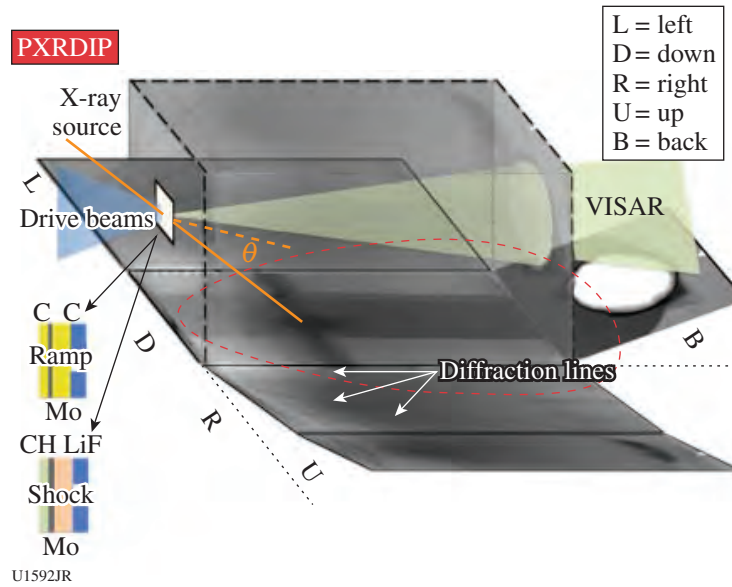

Figure 136.45
Experimental schematic. The laser irradiates the left edge of the ablator, driving a rightward-propagating shock into the system.

Figure 136.47
Powder x-ray diffraction image plate (PXRDIP) experimental setup. Thin Mo pellets (~4 μm) or foils (~10 μm) were placed between two diamond plates (ramp) or a CH ablator and LiF window (shock) and attached to a 300-μm-diam Ta pinhole. The target package was ramp compressed or shock compressed by the OMEGA laser drive. The pressure was determined from the velocity interferometer system for any reflector (VISAR) record of the interface of Mo and window material. X rays generated from a Cu foil were collimated through the pinhole and produced diffraction from the sample. The unfolded image plates show the diffraction lines of the sample and pinhole material.

the main target and a 1-ns square to drive the backlighter. The active shock breakout (ASBO) [velocity interferometer system for any reflector (VISAR)] was used to measure the free-surface velocity of the diamond, and backward integration was used to determine the pressure at the interface of the diamond and sample.

The Mo was ramp and shock compressed to approximately 900 GPa and 350 GPa, respectively. The x-ray diffraction patterns were recorded on image plates attached to the inner wall of the PXRDIP diagnostic. Diffraction peaks obtained from ramp-compressed Mo are consistent with the body-centered-cubic (bcc) structure up to 900 GPa, and we found no evidence of solid–solid phase transition as predicted by theoretical studies using the density functional theory. Under shock loading, the bcc phase of Mo also remained stable along the Hugoniot to at least 350 GPa, and no evidence was obsered for the solid–solid phase transformation around 210 GPa as reported in previous gas-gun experiments. Figure 136.48 shows the pressure–density relationship obtained from the diffraction data combined with applied stress from the VISAR record. Since ramp compression avoids large heating compared with shock loading, our data are intermediate between previous shock (gray triangles) and static (red symbols) compression data (Fig. 136.48).
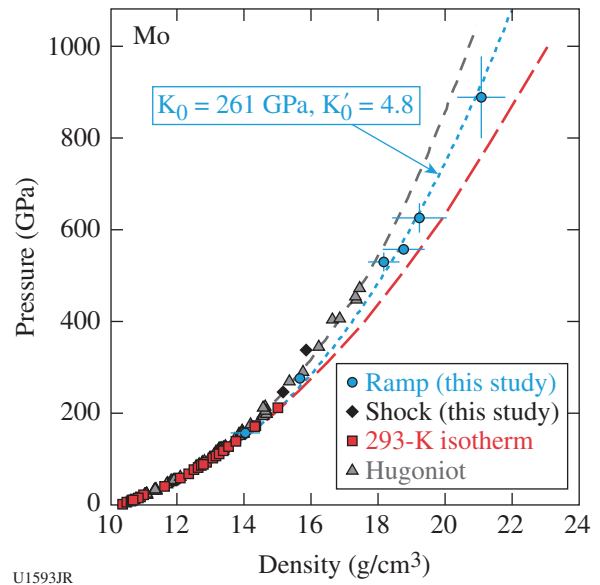
Figure 136.48
Compression behavior of molybdenum under both ramp and shock loading up to 900 GPa. The blue circles represent the data from ramp compression fit with the body-centered-cubic (bcc) structure. The black diamonds show the data along Hugoniot curve also fit with the bcc structure. The blue dashed line is an equation-of-state fit to the ramp-compression data with the bulk modulus K_0 fixed to 261 GPa and a fit pressure derivative of the bulk modulus $K_0' = 4.8$. Also plotted in this figure for comparison are the results of previous shock and static compression studies.

Dynamics of Magnetic Reconnection Current Sheet in High-Energy-Density Plasmas

Principal Investigator: W. Fox (University of New Hampshire)
Co-investigators: A. Bhattacharjee (Princeton); and G. Fiksel, P. M. Nilson, and S. X. Hu (LLE)

We have developed and conducted experiments on OMEGA EP to study the phenomenon of magnetic reconnection. Magnetic reconnection occurs when regions of opposite directed magnetic fields in a plasma can interact and relax to a lower-energy state; it is an essential plasma physics process in many systems that governs the storage and explosive release of magnetic energy in systems such as the earth's magnetosphere, the solar corona, and magnetic fusion devices. The energy thereby liberated can produce heat and flows and can enable the acceleration of a large number of particles to high energies.

These experiments on OMEGA EP used an externally applied magnetic field of the order of 12 T as the seed field for reconnection. With an externally applied field, the fields undergoing reconnection are under experimental control, so it is possible to conduct experiments with variable fields and topologies; for example, we have already conducted the "zero field" null experiment. We have successfully magnetized and collided the counterpropagating plasmas. Figure 136.49 shows
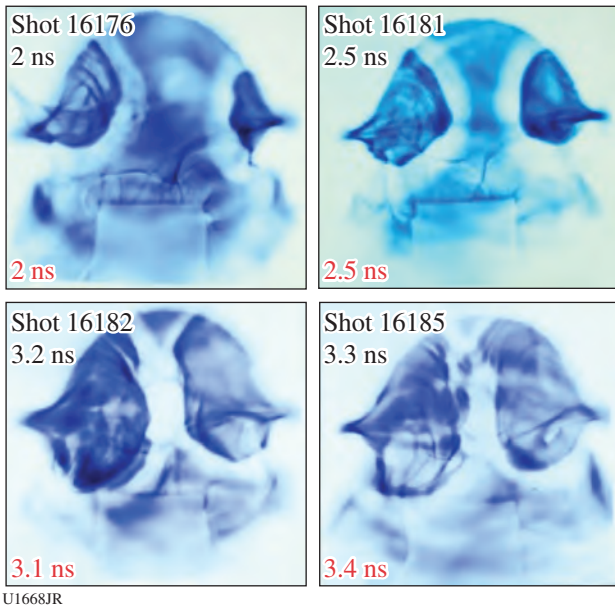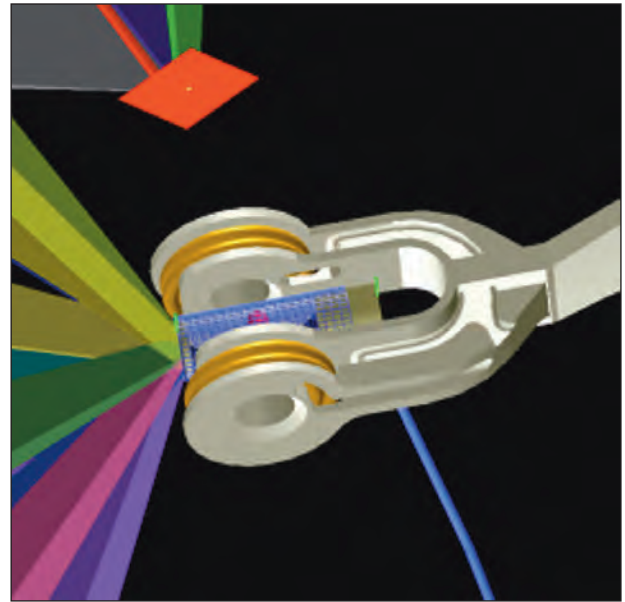

Figure 136.49
Time-sequenced proton radiography images of the collision and interaction of two counter-propagating plasmas (left and right, respectively, on each shot). The two white zones (magnetized ribbons) propagating toward each other represent a reduction in proton flux.

a sequence of proton radiography images of the collision and interaction of the magnetized plasmas. The results are qualitatively different than the unmagnetized case and show the formation of a pair of magnetized "ribbons" propagating toward one another. These ribbons are regions of a deficit of protons to the film and indicate regions of strong magnetic field—magnetized plasma—that have steered the diagnostic proton beam off-film. The successful formation of these pairs of ribbons is non-trivial—it was found that it was essential to add a third "background" plasma source, triggered before the blowoff plasma forms the two primary targets, to fill the experimental volume with a diffuse low-density plasma. The image sequence shows the ribbons propagating toward one another and colliding at the midplane, generating bubble-like structures as the regions of oppositely magnetized plasmas interact and drive reconnection of the magnetic fields. The results are presently being analyzed and compared with particle-in-cell simulations.

Shock Waves and Clumpy Environments in Astrophysical Flows

Principal Investigator: P. Hartigan (Rice University)
Co-investigators: A. Liao (Rice University); J. Foster, P. Graham, and P. Rosen (AWE); G. Fiksel (LLE); G. Gregori and J. Cross (Oxford); K. Yirak and B. Wilde (LANL); A. Frank and S. Li (University of Rochester); and B. Blue (General Atomics)

During FY13, we continued our investigation of irregular (Mach) shock-reflection phenomena that was partly reported last year; we have tested a laser-driven gas-cell target for the study of shock-interaction phenomena in radiative shocks; and we have begun a new series of experiments by developing a platform to study hydrodynamic flow in clumpy media in the presence of an imposed magnetic field. The now-complete set of data from our Mach-reflection experiment (Mach-stem growth rate and hysteresis for various angles of incidence of a warm-dense-plasma shock at a reflecting boundary) was reported at the most-recent High-Energy-Density Laboratory Astrophysics (HEDLA) meeting.[1] In the present report, we concentrate on our work to develop a platform for a magnetized-plasma laboratory analogue of the wind–cloud interaction.

Magnetic fields are ubiquitous in astrophysical environments, and yet the hydrodynamics of magnetized plasmas has been largely neglected in many laser-driven laboratory astrophysics studies. This omission arises from the difficulty of establishing an environment in which the magnetic pressure is sufficiently large, compared to the thermodynamic and
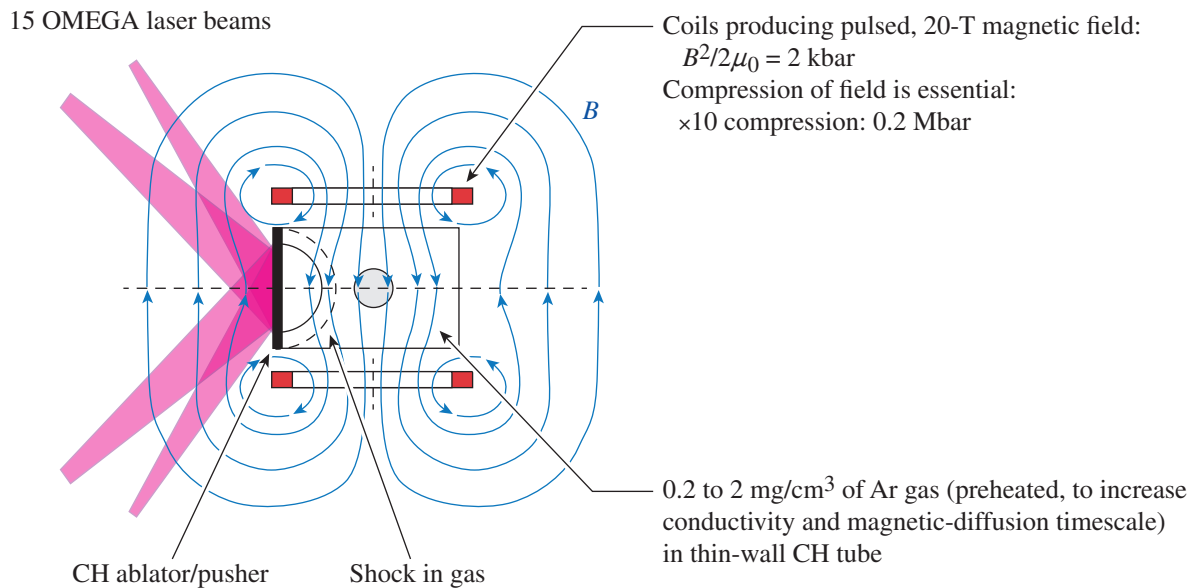
ram pressures, to affect some measurable quantity such as the overall hydrodynamic flow or the growth of instabilities. The recent availability on OMEGA of the magneto-inertial fusion electrical discharge system (MIFEDS) compact magnetic-field generator has led us to attempt a laboratory analogue of the interaction between a magnetized wind and embedded denser cloud in relative supersonic motion. Gregori *et al.*[2,3] present results from three-dimensional magnetohydrodynamic (MHD) simulations investigating such wind–cloud interactions. In their model, the cloud is treated as initially spherical, while the magnetic field is uniform and transverse to the direction of relative motion of the cloud and ambient, magnetized medium. Stretching the magnetic field lines leads to a strong enhancement of the field at the leading edge of the cloud and a significant modification of the hydrodynamics. Even for a surprisingly large initial ratio of the ram and magnetic pressures ($\beta = 100$), a clear difference is found from a simulation without magnetic field ($\beta = \infty$) because of compression enhancement of the magnetic field at the pole of the cloud. A laboratory analogue of Gregori's model astrophysical simulation seems to be accessible only on OMEGA—given an imposed magnetic field from MIFEDS of the order of 20 T, supersonic flow in a low-density ($\ll$1-mg/cm^3) gas, and an adequately long magnetic diffusion time scale ($>$200 ns) in the (radiatively preheated and therefore conducting) ambient gas.

Figures 136.50 and 136.51 show our experimental setup. Fifteen OMEGA laser beams directly drive (2×10^{14} W/cm^2 incident intensity) a thin (few-μm–thickness) CH ablator that

U1670JR

Figure 136.51
VISRAD rendering of the experiment, showing the MIFEDS magnetic-field coils and x-ray backlighting target.

15 OMEGA laser beams

Coils producing pulsed, 20-T magnetic field:
$B^2/2\mu_0 = 2$ kbar
Compression of field is essential:
$\times$10 compression: 0.2 Mbar

B

0.2 to 2 mg/cm^3 of Ar gas (preheated, to increase conductivity and magnetic-diffusion timescale) in thin-wall CH tube

CH ablator/pusher   Shock in gas

U1669JR

Figure 136.50
Schematic of an OMEGA experiment to study the flow of a low-density, magnetized plasma over an embedded particle—a laboratory analogue of the astrophysical wind–cloud interaction.

closes one end of a cylindrical gas-cell laser target (typically 3 mm in diameter, several mm in length). The gas cell is filled with, for example, argon gas at atmospheric or subatmospheric pressure (0.2- to 2-mg/cm^3 density) and contains a low-density aerogel sphere or cylinder, or a gas-filled, thin-wall capsule. This assembly is placed at the center of the MIFEDS pulsed magnetic-field generator that provides an initial magnetic field transverse to the axis of the experiment of 10 to 20 T. Direct laser drive at the thin end wall of the gas cell results in an ablatively driven shock that reaches and sweeps over the embedded object in a time scale of 20 to 50 ns, and radiative preheat ahead of the shock results in a radiation precursor, raising the ambient gas temperature to 20 to 50 eV over a distance of the order of 1 mm. This radiative preheat results in sufficient electrical conductivity for the magnetic-diffusion time (~200 ns) to adequately exceed the hydrodynamic time scale of the experiment, allowing (at least in principle) significant enhancement of the field. The hydrodynamic flow of the embedded particle is diagnosed by x-ray point-projection backlighting radiography, and comparison is made of experiments with and without magnetization of the ambient-gas plasma.

We concluded our FY13 NLUF allocated time on OMEGA by starting this experiment. In developing the experimental platform, we used a relatively simple (although not ideal) laser target (1 atm–pressure argon gas, 50-mg/cm^3 embedded silica-aerogel cylinder) and modest magnetic-field strength (7 T), resulting in conditions that fall somewhat short of our required plasma $\beta = 100$. Nevertheless, the excellent experimental data that we obtained have been used to verify pre-shot, 2-D, non-MHD simulations of the hydrodynamics. Our pre-shot calculations of shock positions in the gas and embedded particle (spherical particle in the case of the 2-D simulation) agree well with those observed experimentally and provide confidence in modeling our design of a lower gas density, $\beta = 100$, experiment planned for FY14.

Figure 136.52 shows typical radiographic data from the experiment, at the time of approximately half-crushing the embedded aerogel cylinder. Further modeling of the experiment, including both ideal- and resistive-MHD simulations, is in progress.

In addition to our experimental work on OMEGA, one of the authors (P. Hartigan) has acted as editor of the proceedings of the recent HEDLA laboratory-astrophysics meeting and has published a paper[4] on irradiated interfaces that is also of direct relevance to our experiments on OMEGA.
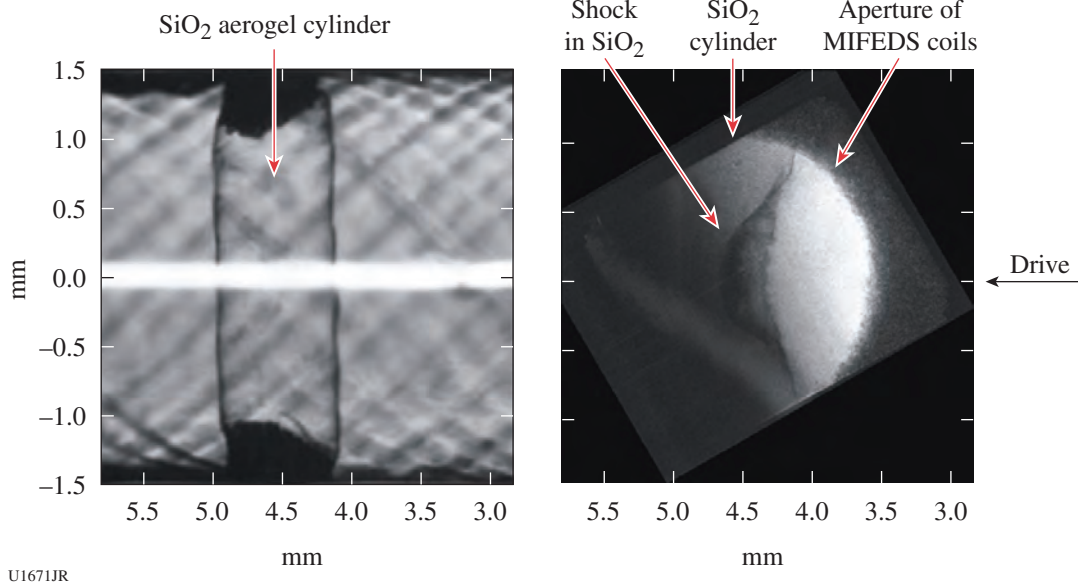
Figure 136.52
(a) Pre-shot optical image of the silica-aerogel cylinder within the gas-cell target and (b) experimental radiograph of the shock in the aerogel cylinder, observed at approximately one-half crushing time and 50 ns after the onset of the laser drive. The dimensions of the space scale are in millimeters, and the spatial resolution is 15 μm. MIFEDS imposed a magnetic field of 7 T.

Journey to the Center of Jupiter: Recreating Jupiter's Core at Omega

Principal Investigator: R. Jeanloz (University of California, Berkeley)

Co-investigators: S. Brygoo and P. Loubeyre (CEA); M. Millot (University of California, Berkeley); P. M. Celliers, J. H. Eggert, S. Hamel, J. R. Rygg, and G. W. Collins (LLNL); and T. R. Boehly (LLE)

During FY13, the PlanetCore University of California, Berkeley/CEA/LLNL/LLE collaboration conducted four very successful campaigns at the Omega facility with 28 shots. We continued our long-term effort to document the physics of warm dense hydrogen and helium under the extreme conditions of pressure and temperature that exist deep within giant planets like Jupiter, Saturn, and extra-solar objects. We used ultrafast Doppler velocimetry (VISAR) and streaked optical pyrometry (SOP) to measure the equation of state and optical properties of H_2 and He along the Hugoniot, starting from highly precompressed states.

We recently managed (see Fig. 136.53) to significantly extend the precompression domain in hydrogen and helium

(a)

0.4 GPa   2.0 GPa   4.0 GPa

(b)
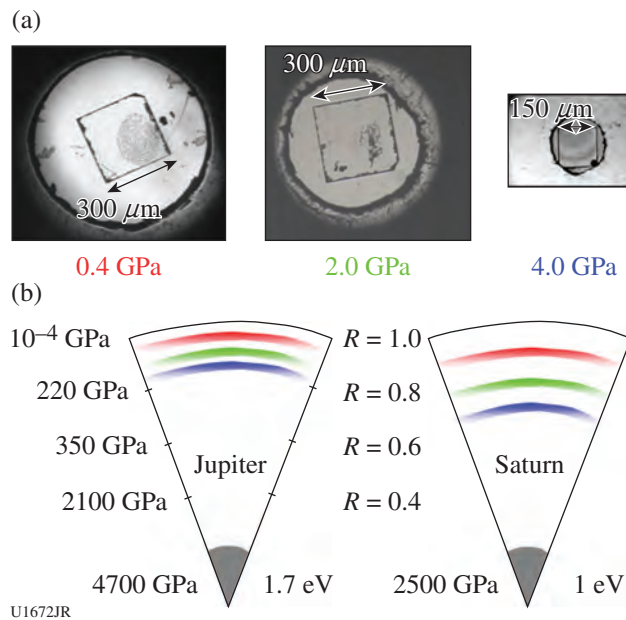
Figure 136.53
(a) Change in pressure-chamber dimensions within the diamond-anvil cell targets, documenting how design improvements over the past years have allowed the PlanetCore team to achieve higher precompressions than ever. (b) Achieving higher precompression allowed us to study hydrogen, helium, and hydrogen–helium mixtures at pressure–density–temperature conditions relevant for deeper regions inside Jupiter and Saturn: the color scale links the initial pressure and the depth within the planets that we were able to *recreate* at the Omega Laser Facility.

samples to an initial pressure larger than 5 GPa. The new equation-of-state data in very dense plasmas of hydrogen (Fig. 136.54) now approach the degeneracy and correlation conditions of the DT plasma along the ICF compression path. Preliminary analysis provides new constraints on the temperature–pressure–density localization of the metallization of warm dense fluid hydrogen. However, no density discontinuity was found along the Hugoniot, in contrast with previous explosive-driven compression radiographic measurements in a cylindrical geometry.[5] The nature and magnitude of a density jump on metallization are of particular importance for comparisons with theory.
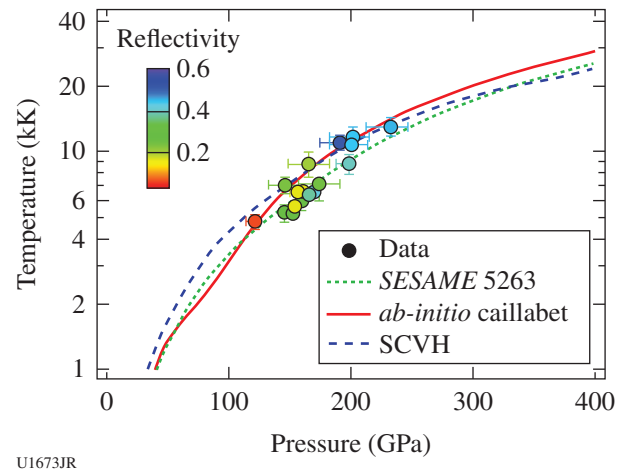
Figure 136.54
During FY13 the PlanetCore team measured the equation of state and optical reflectivity of shock-compressed deuterium, starting from solid D_2 precompressed to 6 GPa and reaching final pressures above 250 GPa. The initial density is 1.7× the highest initial density previously reported [precompression of 1.5 GPa (Ref. 7)]. Preliminary analysis suggests that the new data provide an important benchmark in temperature–pressure–density space for characterizing the metallization of warm dense fluid hydrogen. No density discontinuity is found along the Hugoniot, in contrast with previous explosive-driven compression radiographic measurements in a cylindrical geometry.[5] Shock temperatures are in good agreement with recent *ab-initio* simulations (solid red line). SCVH: Saumon–Chabrier–Van Horn EOS model.

In our previous measurement of the He Hugoniot with precompressed data to 1.5 GPa, the reflectivity was measured versus density and temperature. A fit to the data suggested that (1) the electronic mobility gap closes with density and (2) hot dense helium should become metallic around 1.9 g/cm^3, i.e., at much lower density than predicted by first-principles calculations. We have now measured the reflectivity of shock-compressed helium up to a final density of 2 g/cm^3 along the Hugoniot starting at 5 GPa (Fig. 136.55). Preliminary analysis of the new data set suggests that the metallization density,
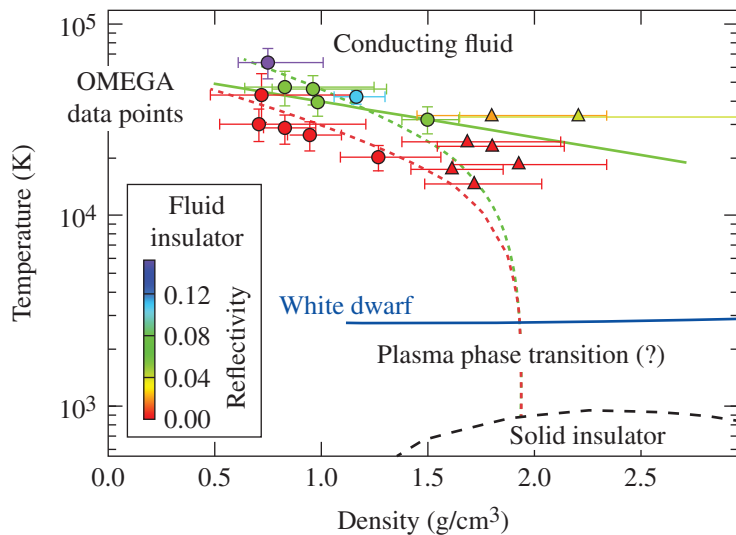
Figure 136.55
Evolution of the optical reflectivity (representative of metallization, color scale) of warm dense helium as a function of temperature and density. During FY13, the PlanetCore team measured the reflectivity of shock-compressed helium up to a final density of 2 g/cm³ along the Hugoniot, starting at 5 GPa (solid triangles). In 2008, a set of helium data points (solid circles) were obtained on OMEGA with a maximum precompression of 1.1 GPa, covering a density from 0.7 g/cm³ to 1.5 g/cm³ (Ref. 8). A Drude model fit of the 2008 data predicted metallization (closure of the band gap) ~2 g/cm³ at moderate temperature (dotted lines). The new data set indicates that the metallization density was previously underestimated. The new determination of gap closure as a function of density and temperature (solid green line, preliminary analysis) is in fair agreement with a recent *ab-initio* prediction of gap closure above 5 g/cm³ (Ref. 6).

obtained by extrapolation over a more-limited density range, was previously underestimated. The new experimental estimate for the gap closure as a function of density and temperature is found to be in fair agreement with the recent *ab-initio* prediction of a gap closure above 5 g/cm³ (Ref. 6).

Particle Acceleration from Collisionless Magnetic Reconnection Using the Short-Pulse OMEGA EP Laser
Principal Investigator: H. Ji (Princeton)

Magnetic reconnection is a ubiquitous astrophysical phenomenon in which magnetic-field energy is rapidly converted into plasma kinetic energy, in the form of flow energy and thermal energy, as well as nonthermal energetic particles. Despite its long history, little laboratory work in this area has focused on the particle acceleration. The experiments performed on OMEGA EP were the first of this kind using short-pulse (10-ps), high-energy petawatt (10^{18}-W/cm²) lasers, in contrast to many previous experiments using long-pulse (1-ns) and low-energy (10^{15}-W/cm²) lasers.

Experiments during the first shot day were performed using two short-pulse OMEGA EP lasers, successfully demonstrating the timing and pointing capabilities necessary for the proposed studies; an initial assessment of particle acceleration and jet formation was also made. Cu foils were used as the target with two laser foci separated by about 100 μm. Each laser was 20 ps long in duration, but timing of these two lasers was controlled to also about 20 ps in accuracy, resulting in only about half of the shots being useful for this study. Three radiochromic film detector packs were used to measure high-energy particles in different angles with respect to the target plane, and an

energetic beam was detected in one of the co-timed shots in the direction consistent with the expectations from the reconnection processes. The next step will be to perform relevant numerical simulations to guide the choices of experimental parameters and to develop new magnetic and particle diagnostics for the proposed shot day in FY14.

Studies of High-Energy-Density Plasmas, Inertial Confinement Fusion Implosions, and Nuclear Science for Astrophysics
Principal Investigators: R. D. Petrasso and C. K. Li (MIT)
Co-investigators: F. H. Séguin and J. A. Frenje (MIT); T. C. Sangster, V. Yu. Glebov, D. D. Meyerhofer, and R. Betti (LLE); and O. L. Landen (LLNL)

MIT work in FY13 included a wide range of experiments that applied proton radiography, charged-particle spectrometry, and neutron spectrometry methods developed by MIT and collaborators to the study of high-energy-density physics (HEDP) and inertial confinement fusion (ICF) plasmas. Seven papers[9–15] and two MIT Ph.D. theses[16,17] about NLUF-related research were published in FY13; also many invited and contributed talks were presented at conferences. Our NLUF experiments provided unique research opportunities in HEDP for seven MIT graduate students, and much of the current NLUF data will appear in major parts of upcoming theses. Several MIT undergraduates also participated.

The success and relevance of MIT's NLUF work during the last decade are reflected in the fact that Principal Investigator R. D. Petrasso received this year's Edward Teller Medal (see Fig. 136.56) for his MIT Division's work in ICF and HEDP.

Figure 136.56
Principal Investigator R. D. Petrasso accepting the Edward Teller Medal at the International Inertial Fusion Science and Applications Conference (IFSA) in Nara, Japan, in September 2013. The medal was awarded by the Fusion Energy Division of the American Nuclear Society "for pioneering the use of nuclear diagnostics for understanding inertial confinement fusion implosions and high-energy-density physics." Much of his work and that of his MIT Division was supported by the NLUF Program.

A large fraction of that work was done at the Omega Laser Facility, and much of that was directly sponsored by NLUF.

Topics studied this year on the OMEGA[18] and OMEGA EP[19] Laser Systems and already published include imaging, identifying, and measuring electric and magnetic fields generated in direct- and indirect-drive ICF plasmas[9–12,14,17] and other laser-generated plasmas,[15–17] and measuring ICF performance and fusion products.[13] Data acquired in FY13 and currently under analysis bear on a range of topics including magnetic reconnection, plasma kinetic effects in ICF implosions, the behavior of plasma jets, the stopping of ions in plasmas, cross sections of nuclear reactions relevant to stellar nucleosynthesis, and developing new diagnostics. This work successfully addresses basic physics issues and issues directly relevant to the future success of ignition experiments at the National Ignition Facility (NIF) as well as general issues of importance to HEDP and the physics of fields generated by laser–plasma interactions. A few highlights are discussed below.

Previous MIT NLUF work developed the tool of proton radiography[20] and then used it to provide the first images of coronal filamentation in direct-drive ICF implosions.[21,22] New NLUF work utilized proton imaging of self-generated electric and magnetic-field structures on laser-driven planar foils to investigate the possible roles of different instabilities in generating the filamentation seen in ICF experiments. Planar foils were used because they allow for direct observation in a direction perpen-

dicular to the laser-driven surface, which cannot be accomplished when studying ICF capsules with thick shells; x-ray images were used to study areal-density perturbations in the foil so their effects on proton radiographs could be separated from the effects of fields. The radiographic data were compared with the mathematical characteristics of a wide range of plasma instabilities (including collisionless Weibel, magnetothermal, laser–plasma, collisional Weibel, electrothermal, and Rayleigh–Taylor), and it was determined that the instability most likely to be causing the observed filamentation was the magnetothermal instability.[23]

Other recent NLUF work[15] utilized local, time-resolved Thomson-scattering measurements of electron and ion temperatures in combination with proton radiography measurements of magnetic fields to comprehensively characterize experiments with a single laser beam incident on a foil and with two laser beams incident on a foil (see Figs. 136.57 and 136.58). Each laser beam generated a plasma bubble and, in the
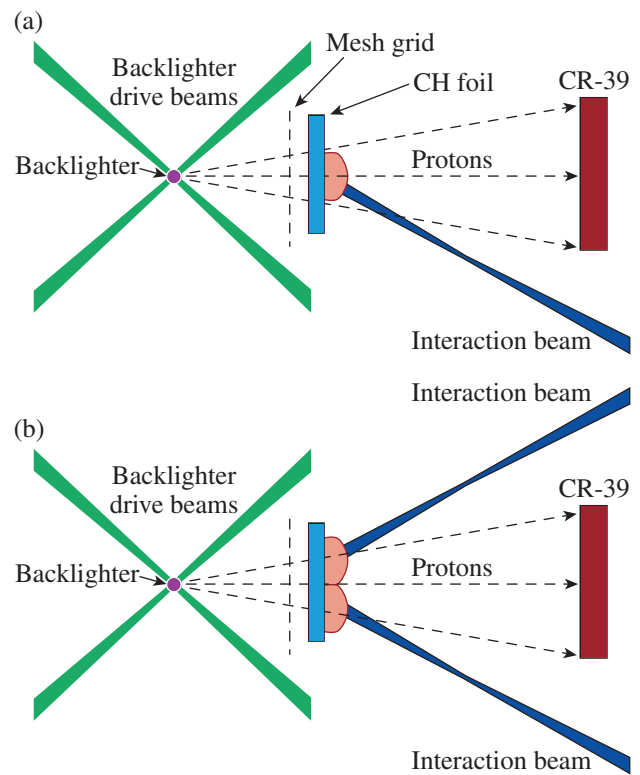
Figure 136.57
Proton radiography setups for imaging (a) one plasma bubble, generated on a CH foil by a single laser interaction beam, and for imaging (b) a pair of plasma bubbles, generated by two beams that collide and produce magnetic reconnection. The backlighter[20] is an imploding pusher implosion of a capsule with D^3He fill, which produces 14.7-MeV protons, and the imaging detector is CR-39.
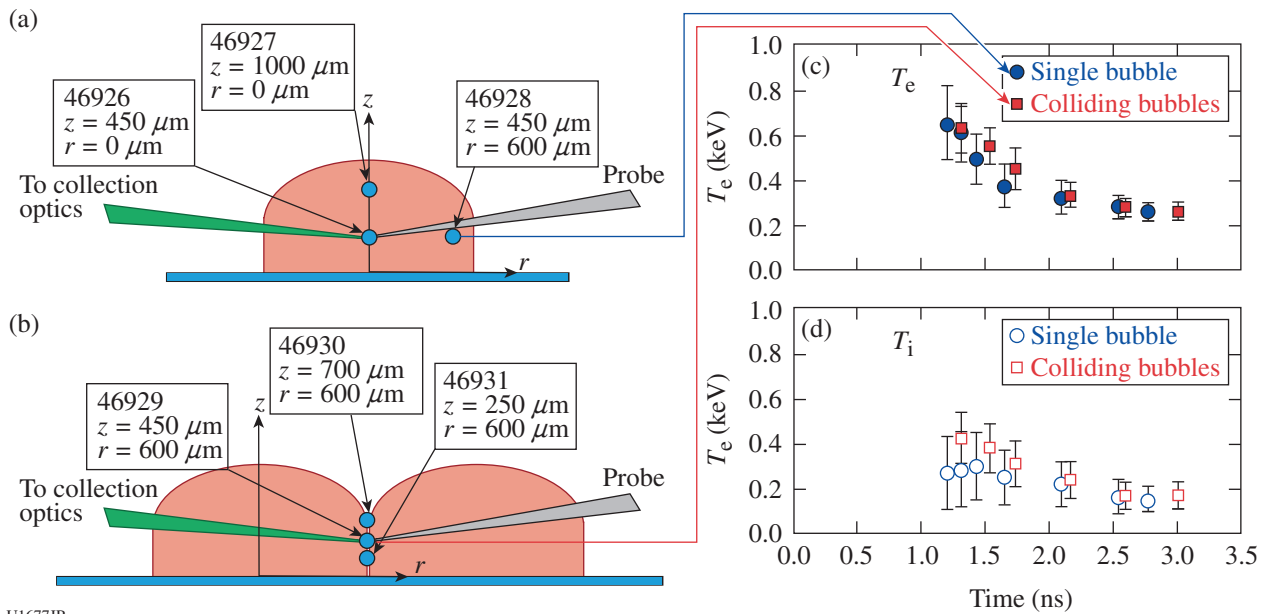
U1677JR

Figure 136.58

[(a) and (b)] Thomson-scattering setup for experiments shown in Fig. 136.57. In different experiments, measurements were made in three different locations in each type of experiment. (c) Electron temperatures and (d) ion temperatures were found to be approximately equal in single-bubble and colliding-bubbles experiments, suggesting that thermal enhancement caused by magnetic reconnection is minimal in these experiments. This experimental conclusion is consistent with the fact that the β of the plasma is high. (For details, see Ref. 15.)

case with two bubbles, their collision produced reconnection of ~0.5-MG magnetic fields. The temperature evolution in a single laser-produced plasma bubble was well captured by 2-D radiation–hydrodynamics models, predicting a gradual decay after laser shutoff. It was found that there is minimal difference in either the electron or ion temperature between the perimeter of a single plasma bubble and in the interaction region of two colliding bubbles. This result confirms the expectation of negligible enhancement of thermal energy caused by the annihilation of magnetic fields in the two-bubble reconnection experiments since the plasma β (ratio of thermal to magnetic energy) is ~8 and the initial magnetic energy is comparably small.

Dynamics of High-Energy Proton-Beam Focusing and Transition into Solid Targets of Different Materials

Principal Investigators: B. Qiao (University of California, San Diego)
Co-investigators: C. McGuffey (University of California, San Diego); M. E. Foord (LLNL); J. Fuchs and S. N. Chen (LULI); R. B. Stephens and M. S. Wei (General Atomics); and P. M. Nilson (LLE)

Intense, focused proton beams have applications ranging from isochoric heating of plasma to imaging shock wave and magnetic fields. Beam production and use involve a constantly evolving target/plasma topology and hot-electron flow as the protons are accelerated from a shaped surface into vacuum and then transition into target plasmas for heating or probing. The dynamics involved are expected to become more complex as the laser energy and resulting beam current increase, and as a beam's pulse length increases. The goal of this project is to extend our physics understanding of the phenomena into this range, facilitating optimal source designs for various applications and eventually experiments like NIF-integrated proton fast-ignition experiments with the advanced radiographic capability (ARC) beam. Data from this study will be used to benchmark simulation codes including 3-D explicit particle-in-cell (PIC) and hybrid PIC codes. The results will have a significant impact in the field of HED physics.

In this FY13 experiment, we used the OMEGA EP dual short-pulse configuration to study focusing of the proton beam created by the interaction of the OMEGA EP backlighter (BL) beam (1250 J in 10 ps) with a spherically curved ($R_c = 300 \mu$m) diamond (C) target. Three target-mounting configurations were investigated: (1) on a stalk, (2) with an open-sided wedge structure surrounding the focusing beam, and (3) with a conical structure [see Fig. 136.59(a)]. A 10-μm Cu foil was placed at the expected beam focus position (on the back of the structures or stalk mounted at the same distance). Cu K-shell

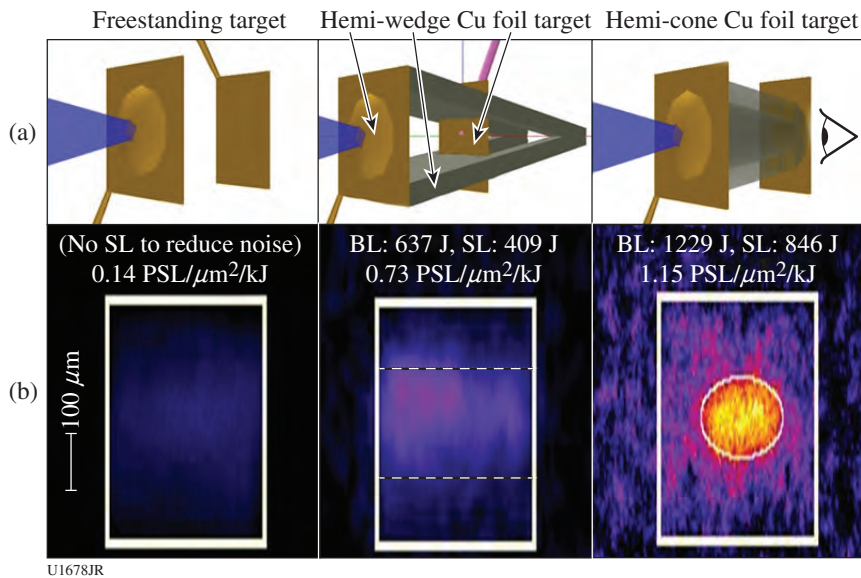Freestanding target   Hemi-wedge Cu foil target   Hemi-cone Cu foil target

(a)

(b) |—100 μm

(No SL to reduce noise)
0.14 PSL/μm²/kJ

BL: 637 J, SL: 409 J
0.73 PSL/μm²/kJ

BL: 1229 J, SL: 846 J
1.15 PSL/μm²/kJ

U1678JR

Figure 136.59
(a) Schematic of the three target configurations used in the experiment. (b) Cu K$_\alpha$ images were obtained with the spherical crystal imager for the corresponding target configuration. BL: back-lighter; SL: sidelighter.

x-ray fluorescence was caused by collisions of the beam protons and electrons (to a lesser extent) with Cu atoms. The emission profile was imaged with the spherical crystal imager (SCI) giving an indication of the beam profile and total energy. The spectrum of transmitted protons was measured in the forward direction using a stack of radiochromic films.

The OMEGA EP sidelighter (SL) (850 J in 10 ps) was used to sidelight the target, structure, and Cu foil via proton radiography. The SL irradiated a Au foil, producing protons with a broad spectrum. The protons probed the interaction and were recorded on a stack of radiochromic films.

This was the first measurement of a proton-induced copper K profile on OMEGA EP and high-quality data were obtained, as shown in Fig. 136.59 (b). The white overlays show the foil dimensions and approximate positions of the structure edges. For the stalk-mounted target, the beam was not obscured by any structure and emission was observed from the majority of the foil. For the targets with wedge and cone structures, the emission from the unblocked region was brighter than the stalk-mounted case by factors of 5 and 8, respectively. In the cone structure case, smooth, bright emission is observed in a circle with the exact size of the cone bore. The enhanced emission is presumably due to focusing caused by charging of the structures as hot electrons from the diamond target escape into the structure, forming an electrostatic sheath along the structure walls. This effect has been documented in our previous experimental[24] and PIC simulation[25] work at much lower laser energy.

Forty-four proton radiograph frames were captured on a single shot, showing the evolution of the target and surrounding plasma features throughout a span of 163 ps. Example radiographs are shown in Fig. 136.60, displaying some of the interesting features observed near the time of BL laser arrival from the right side of the images [Figs. 136.60(a)–136.60(c)] and a closeup at later times [Fig. 136.60(d)]. Of particular interest is

(a) $t = 0\pm0.4$ ps

(b) $t = +1.6$ ps

(c) $t = +3.5$ ps

(d) $t = +56$ ps

U1679JR
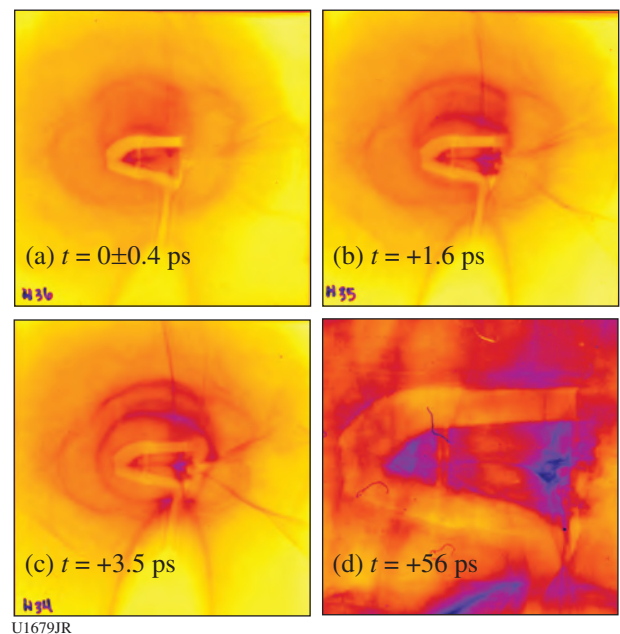
Figure 136.60
Time-sequenced proton radiographs showing the evolution of the target and surrounding plasma features throughout a span of ~52 ps.

the horizontal dark feature on the wedge structure axis of symmetry during the interaction. Darkness indicates an additional dose, i.e., focusing of probe electrons toward the axis. This may be a measurement of the electrostatic structure charging field implicated in the discussion above. At late time a dark line is observed centered on the Cu foil [Fig. 136.60(d), left vertical feature], suggesting opposing fields on the foil surfaces.

In the upcoming FY14 experiment, we will use the stalk-mounted and conical structure targets to focus protons into various transport materials coated in front of the Cu foil to study material-dependent transport effects that were observed in an experiment with lower beam current using the Trident laser.

Generation of Collisionless Shocks in Laser-Produced Plasmas
Principal Investigator: A. Spitkovsky (Princeton, for the ACSEL Collaboration)

This NLUF program studies the creation of collisionless shocks in counter-propagating laser-produced plasmas. Collisionless shocks are of great importance in astrophysical and space plasmas and occur when the mean free path to Coulomb collisions is large compared to the size of the shock transition. The shock is then mediated by collective plasma effects related to the interaction between plasma particles and the self-generated electromagnetic fields. Collisionless plasma conditions can now be created on OMEGA and OMEGA EP, where the laser-driven plasmas propagate at speeds of ~1000 km/s and densities of ~10^{18} to 10^{19} cm^{-3}. The experiments in this program collide two streams of high-speed plasma and study the formation of shocks as a function of externally applied magnetic field that is generated by a set of Helmholz coils at the interaction region (Fig. 136.61). The theoretical expectation is that at low external fields, the shock is mediated by the filamentation (Weibel) instability, while at higher fields, magnetic reflection of ions will form the shock. These regimes are representative of the conditions encountered in a range of astrophysical environments, including supernova remnant shocks and solar wind shocks. The experiments on OMEGA and OMEGA EP are testing these shock-formation mechanisms and addressing the open questions of astrophysical collisionless shock physics such as the presence of particle acceleration and the mechanisms of magnetic-field amplification in shocks.

In FY13, we had two shot days: an OMEGA EP–only experiment, EP-MagShock-13a, on 28 February 2013, and a joint shot day, MagShock-J-13a, on 21 May 2013. In these experiments the lasers (OMEGA and/or OMEGA EP) were used to initiate
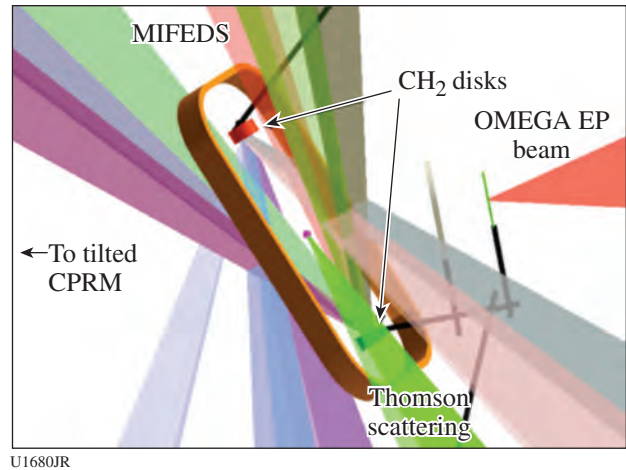
Figure 136.61
Diagram of the experimental setup for NLUF MagShock-12a. CPRM: tilted circular proton radiography module.

two ablated plasma flows from CH or Be foils. An OMEGA EP short pulse was then used to provide proton radiography of the interaction region. On the joint shot day, the Thomson-scattering diagnostic was also used. A new design of a magnetic coil together with upgraded the magneto-inertial fusion electrical discharge system (MIFEDS) energy resulted in higher B fields of 6.5 T at target chamber center (TCC). For the first time we used MIFEDS on both OMEGA EP and joint days. We monitored the interaction of the flows with and without magnetic fields. One of the main goals was to reconcile the features seen in radiography on OMEGA EP and in previous joint shots. Prominent "line" features orthogonal to the flow direction were previously observed on OMEGA EP shots,[26] yet in our previous joint campaign in 2011–2012, they were not clearly seen.

We now understand that these features are due to advected Biermann battery fields that were created during target ablation. When we changed the proton radiography impact angle to be 90° to the flow as on OMEGA EP (previously it was 60° on joint shots because of experimental constraints), we recovered the Biermann features, as illustrated in Fig. 136.62. Now that it has been confirmed that the results on the two laser systems are consistent, we can proceed with more confidence to study the collisionless physics of the interaction. In particular, on joint shots we begin to see the filamentation instability of the two counter-streaming flows [vertical striations on Fig 136.62(b)]. This major result, recently confirmed in the ACSEL July experiment using D^{3}He probing, has recently been submitted to Nature by the ASCEL collaboration.

We continued to model the experiment using particle-in-cell (PIC) simulations and simulated proton radiography, where
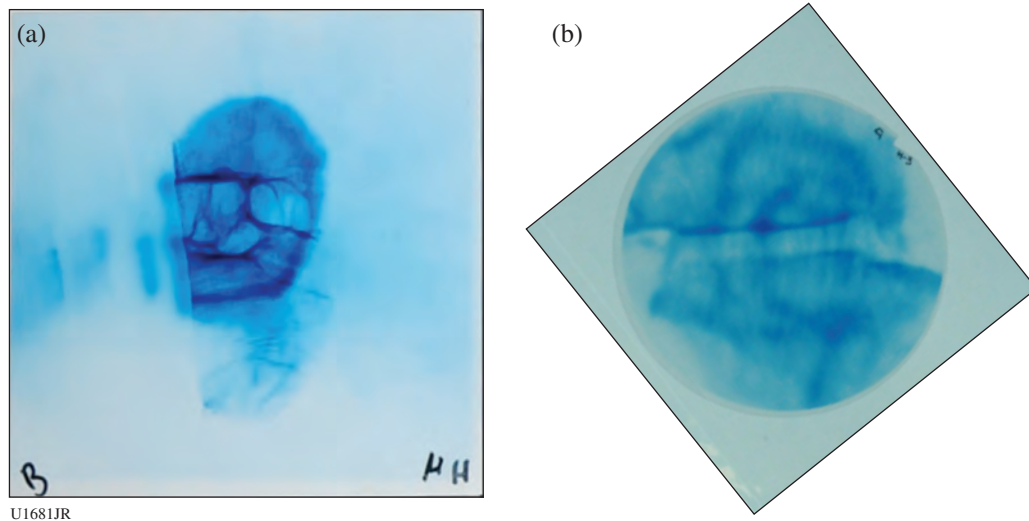
Figure 136.62
Proton images 3 ns after the lasers were fired. (a) Example of "horizontal line" features in proton radiography of counter-streaming flows on OMEGA EP. (b) The same features appear on joint shots with an appropriate radiography angle. Flows collide along the vertical direction.

test protons are traced through the output of a PIC simulation. We are now including Biermann fields and multitemperature species (hot electrons, cold ions) to self-consistently model the creation and advection of the magnetic fields and their interaction with the superimposed fields. We also produced a number of 3-D simulations with predictions for NIF conditions. On the NIF, larger effective separation of the targets will result in the creation of a full shock.

Study of Fast-Electron–Beam Dynamics and Resistive Magnetic Collimation Using the High-Contrast OMEGA EP Laser at a 10-ps Pulse Duration
Principal Investigators: M. S. Wei and R. B. Stephens (General Atomics)
Co-investigators: F. N. Beg, C. McGuffey, and B. Qiao (University of California, San Diego); H. McLean and P. Patel (LLNL); W. Theobald (LLE); and R. Mishra and Y. Sentoku (University of Nevada, Reno)
Lead graduate students: A. Sorokovikova and J. Peebles (University of California, San Diego)

Efficient conversion of high-intensity laser energy to fast electrons and their subsequent transport is fundamental to high-energy-density (HED) science, which has many potential applications such as initiating fusion using the fast-ignition (FI) technique, producing warm dense matter by isochoric heating, and creating x-ray emission for use as a backlighter source. The energy coupling is controlled by laser–plasma interaction (LPI) dynamics, which strongly depends on laser-

intensity distribution and the plasma density scale length at the LPI interface, as well as the dynamic response of the transport material. Using the high-intensity, high-energy (up to 1.5 kJ) OMEGA EP laser with low-contrast pulses in our previous experiments, we observed that electron beams dynamically evolve from a single diffuse spot in a subpicosecond interaction into multiple angularly separated electron filaments over a 10-ps interaction.[27] Collisional particle-in-cell simulations suggest that the high-intensity laser beam undergoes filamentation, hole-boring, and hosing instabilities, which have time to grow during the multiple-picosecond interaction in the preformed plasma created by the intrinsic nanosecond pedestal prepulse, leading to the observed electron filaments. The objectives of this General Atomics NLUF project are to further investigate the LPI dynamics and fast-electron transport dependence on pre-plasma, pulse duration, and target material using the OMEGA EP laser with the newly available high-contrast pulse.

In the FY13 NLUF experiment, we first studied the LPI-produced electron-beam characteristics using the high-contrast laser pulse to understand time evolution of the LPI dynamics from 0.7 ps to 10 ps and the role of pre-plasma (by comparing with previous data taken with the low-contrast pulse). For this study, we used identical multilayered planar-foil targets consisting of an Al substrate with a Cu x-ray tracer layer (20 μm thick) buried ~100 μm below the front surface and a large (5-mm × 5-mm, 1-mm-thick) conductive carbon layer at the back to minimize refluxing, similar to that used in previous experiments with the low-contrast pulse. The high-contrast OMEGA EP backlighter

beam (0.7- and 10-ps pulse durations with energies of 150 J and 1500 J, respectively) was normally incident onto the front target surface. The beam was tightly focused with a spot radius of ~15 μm that contained 80% of the laser energy, resulting in a peak laser intensity of 4×10^{19} W/cm^2. The measured nanoscecond prepulse energy was ≤1 mJ, which is 100× smaller than in the case of the low-contrast pulse. Fast electrons were characterized by measuring their induced Cu K$_\alpha$ fluorescence spot using a spherical crystal imager (SCI), and the total K$_\alpha$ yield was characterized by a calibrated x-ray spectrometer using a curved highly oriented pyrolytic graphite (HOPG) crystal [zinc von Hamos (ZVH) spectrometer]. A fast-electron–induced high-energy bremsstrahlung spectrum was monitored at two angles behind the targets with two fixed-port bremsstrahlung MeV x-ray spectrometers (BMXS's). The measured bremsstrahlung data showed that fast electrons produced from the 10-ps LPI have a hotter spectrum than in the subpicosecond case, consistent with particle-in-cell (PIC) simulation results.[28,29] Detailed bremsstrahlung data analysis including field effects via the hybrid transport modeling is underway.

As shown in Fig. 136.63, K$_\alpha$ image data showed a more-confined electron beam produced from the clean interaction with a steep density gradient in the 10-ps LPI case using the high-contrast OMEGA EP pulse. Also noted is the higher signal level in the K$_\alpha$ intensity in the confined electron beam, compared to that in the spreading multiple electron filaments in the

LPI in the low-contrast case [Fig. 136.63(c)]. This verified that the multiple angularly separated electron filaments observed in the low-contrast pulse experiment were indeed caused by nonlinear instabilities during LPI over multiple picoseconds with the presence of a large pre-plasma. These new findings emphasize the requirement of a high-contrast capability of the high-energy, high-intensity laser pulse needed to avoid the unnecessary LPI instability for efficient energy coupling.

Using the high-contrast OMEGA EP pulse, we have also extended our previous work on resistive collimation with laser pulses at subpicosecond[27,30] to a 10-ps pulse duration using a high-Z transport target that has a thin (a few-μm) Au layer embedded about 10 μm beneath the Al substrate [Fig. 136.64(a)]. Two-dimensional K$_\alpha$ images [Figs. 136.64(b) and 136.64(c)] clearly show a better confined and stable electron beam compared to that with the pure Al transport target [Fig. 136.64(b)]. A remarkably collimated electron beam, with a spot size as small as 50 μm after a >100-μm propagation distance, has been demonstrated for the first time for fast-ignition–relevant 10-ps pulses. The achieved electron-beam size is comparable to the required spot size (~40 μm) for FI. In addition, the sensitivity of magnetic collimation of fast-electron transport on the Z-layer thickness has also been examined. As shown in Figs. 136.64(c) and 136.64(d), both 9-μm and 3-μm Au layers showed collimation effects compared to the Al transport target case.

(a) High-contrast OMEGA EP
Shot 13520, 10 ps/1573 J,
$R_{80} = 18$ μm

(b) High-contrast OMEGA EP
Shot 13521, 10 ps/1524 J,
$R_{80} = 15.4$ μm

(c) Low-contrast OMEGA EP
Shot 11998, 10 ps/1450 J,
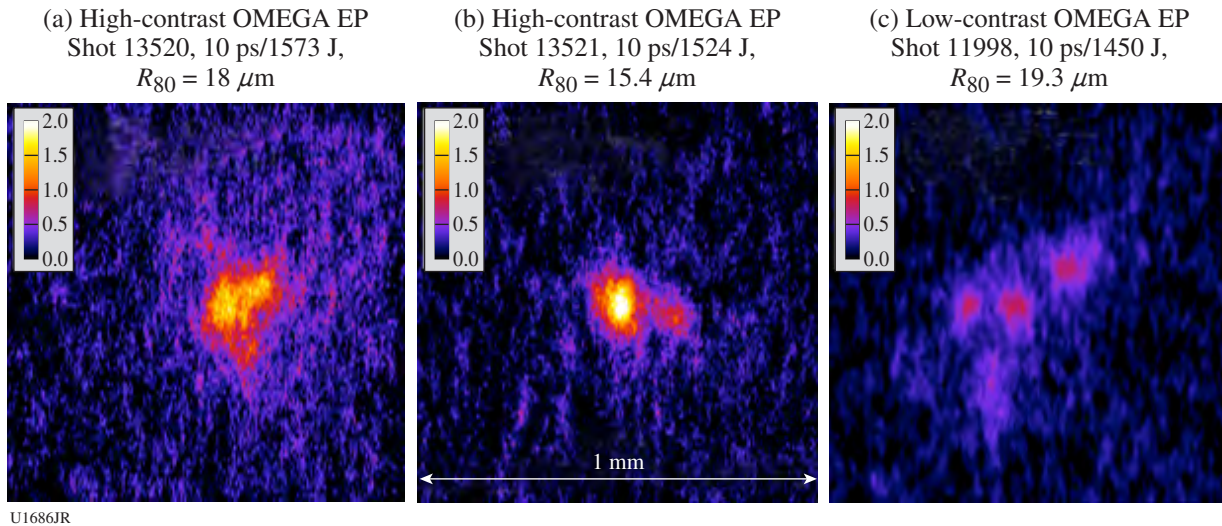$R_{80} = 19.3$ μm

U1686JR

Figure 136.63
Two-dimensional K$_\alpha$ images observed in a 10-ps laser–plasma interaction (LPI) with identical Al transport targets [(a) and (b)] using the high-contrast OMEGA EP pulse (nanosecond prepulse energy ~1 mJ) and (c) with the low-contrast (prepulse energy ~110 mJ) OMEGA EP laser beam. Images (view angle corrected) are on the same spatial and color scale. Although shape varied shot-to-shot, high-contrast, laser-produced electron beams are more confined with brighter peak signals compared to the spreading filaments in the low-contrast case.
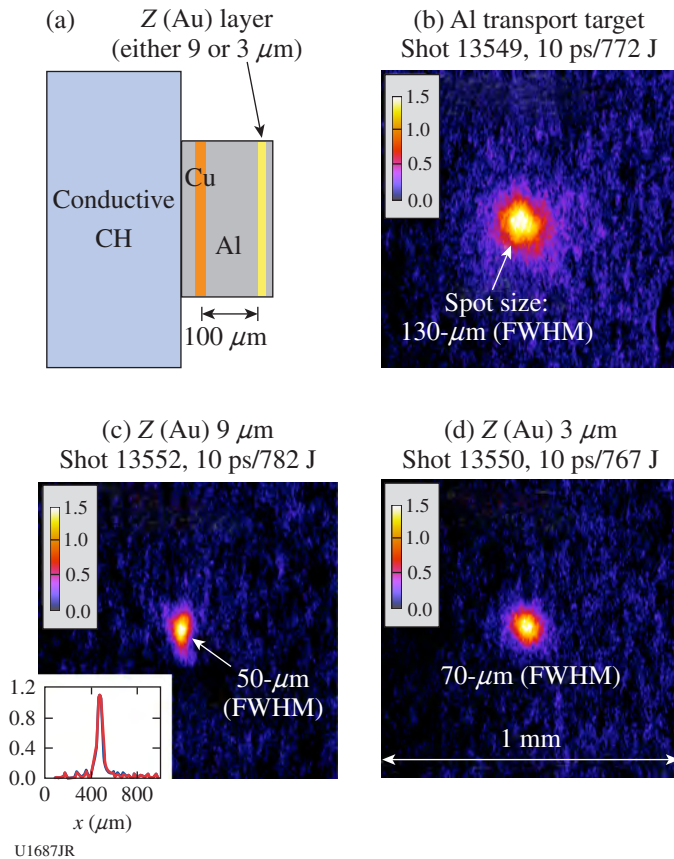
U1687JR

Figure 136.64
(a) Multilayered planar-foil target with a Z (Au) transport layer and the measured K_α images (view angle corrected) from the 10-ps interactions using the high-contrast OMEGA EP pulse; (b) from the Al transport target without the high-Z Au layer and [(c) and (d)] from the Z (Au) transport targets with a 9-μm and 3-μm Au layer, respectively. Inset in (c) is the horizontal lineout of the image data (blue) and the Lorentzian fit (red) showing the spot size of 50 μm [full width at half maximum (FWHM)].

In summary, the FY13 GA-led NLUF experiment was successfully performed and demonstrated that high-contrast pulses improve energy coupling and facilitate strong electron-beam collimation in high-Z transport targets by self-generated resistive magnetic fields in a 10-ps interaction. The experimental data will be used to benchmark various PIC and hybrid PIC codes for developing a predictive modeling capability.

FY13 Laboratory Basic Science (LBS) Program

In FY13, LLE issued a solicitation for LBS proposals to be conducted in FY14. A total of 38 proposals were submitted. An independent review committee reviewed the proposals and recommended that 17 proposals receive 28 shot days at the Omega Laser Facility in FY14. Table 136.VIII lists the successful LBS proposals.

Sixteen LBS projects were allotted Omega Facility shot time and conducted a total of 269 target shots at the facility in FY13 (see Table 136.IX). This work is summarized in this section.

Equation of State and Optical Properties of Dense Silica: Shock Study of Stishovite
Principal Investigator: P. Celliers (LLNL)
Co-investigators: M. Millot and R. Jeanloz (University of California, Berkeley); N. Dubrovinskaia, A. Cernok, S. Blaha, and L. Dubrovinsky (Bayreuth University, Germany); S. Hamel, J. H. Eggert, and G. W. Collins (LLNL); and T. R. Boehly (LLE)

The equation of state and optical properties of silica (SiO_2) were investigated in an unexplored regime of warm dense matter, with pressure above 20 Mbar (2 TPa) and density in excess of 10 g/cm^3. Such conditions were achieved by laser-induced shock loading of stishovite, a high-pressure polymorph of SiO_2. Because of its high initial density ($\rho_0 = 4.3$ g/cm^3), the Hugoniot of stishovite explores a much denser and cooler path than the shock Hugoniot of α quartz ($\rho_0 = 2.65$ g/cm^3) and fused silica ($\rho_0 = 2.2$ g/cm^3) (see Fig. 136.65).

U1684JR
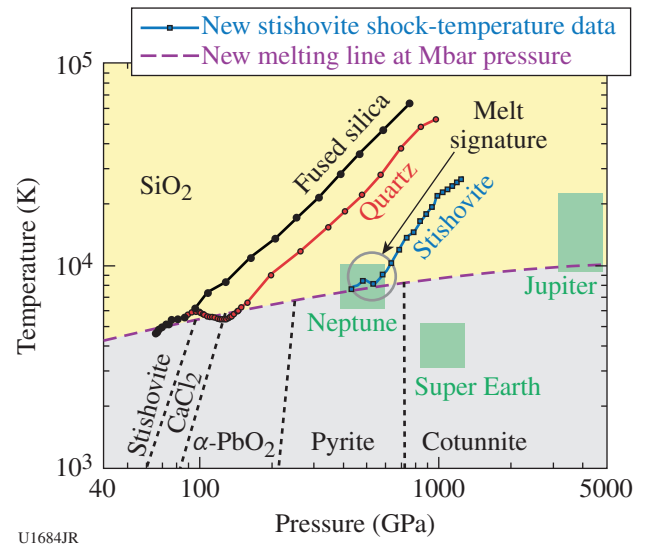
Figure 136.65
Phase diagram for warm dense SiO_2, including previous shock-temperature data for fused silica (black) and α quartz (red) as well as representative new data for stishovite (blue, preliminary analysis). We interpret a temperature anomaly along the stishovite Hugoniot, indicated by the gray circle, as a signature of melting similar to that observed for the fused silica and α quartz at lower pressures. This allows us to pinpoint the melting line for SiO_2 at 5 Mbar and 8000 K. This measurement is directly relevant to models of planetary formation (e.g., late-stage giant impacts) and interior evolution (green squares show typical planetary core conditions).

Knowledge of the physical properties of highly compressed silica is critical for astrophysical applications, particularly for modeling the origins and interior structures of terrestrial ("rocky") planets, as well as the cores of giant and supergiant gaseous planets. Silica is a prototypical constituent of rock and abundant in the planet Earth and many exoplanets because it is a strongly bonded form of oxygen, the most-abundant chemical element after the light elements hydrogen and helium. The behavior of silica at high pressures is vastly different from its well-known properties at ambient conditions, and, as a rela-

Table 136.VIII: LBS proposals approved for shots in FY14.

Principal Investigator	Title	Institution	Facility required	OMEGA shot days allocated	OMEGA EP shot days allocated
A. Bernstein	Nuclear Excitation by Electron Capture in a Reduced-Scale Hohlraum	LLNL	OMEGA	1	0
P. M. Celliers	Measurement of the Viscosity of Shock-Compressed Fluids of Water and Silica	LLNL	OMEGA	2	0
H. Chen	Exploring Pair Plasmas and Their Applications Using the OMEGA EP and OMEGA Lasers	LLNL	OMEGA EP	0	2
G. Fiksel	Magnetized ICF Implosions on OMEGA	LLE	OMEGA (1) and joint (1)	2	1
R. F. Heeter	Gattling Gun Long-Duration Radiation Sources on OMEGA EP for Sustained-Drive Hydrodynamics and Low Density at Atomic Physics Applications on OMEGA EP and the NIF	LLNL	OMEGA EP	0	1
S. Ivancic	Channeling Through Long-Scale-Length Plasmas	LLE	OMEGA EP	0	1
M. Lafon	Gigabar Shocks for Shock-Ignition and High-Energy-Density-Physics Studies	LLE	OMEGA	1	0
T. Ma	Creation and Measurements of Novel High-Pressure Electride States of Matter	LLNL	OMEGA	1	0
D. Martinez	Imprint-Driven Richtmyer–Meshkov Instability in Thick Planar Targets	LLNL	OMEGA	2	0
D. McNabb	Thermonuclear Reactions in Stellar Plasmas	LLNL	OMEGA (2 half days, 1 full day)	2	0
S. Nagel	Measuring Charged-Particle Stopping Powers Using Short-Pulse Lasers	LLNL	OMEGA EP	0	1
P. M. Nilson	Radiation Hydrodynamics of Double-Ablation Fronts	LLE	OMEGA EP	0	1
H.-S. Park	Astrophysical Collisionless Shocks and Magnetic Fields in Laser-Produced Plasmas	LLNL	OMEGA EP	0	2
P. K. Patel	Fast-Electron Focusing Using Ellipsoidal-Tip Cone Targets for Fast Ignition	LLNL	OMEGA (1) and joint (1)	1	2
J. R. Rygg	Structure and Equation of State of Solid and Super-Ionic Warm Dense Matter	LLNL	OMEGA	2	0
R. Smith	Understanding Strength Effects in Diamond Ablators Used for Ramp Compression	LLNL	OMEGA EP	0	1
C. Stoeckl	Spectroscopy of Neutrons Generated Through Nuclear Reactions with Light Ions in Short-Pulse Laser Interaction Experiments	LLE	OMEGA EP	0	2

tively simple covalent material, it is an excellent test case for understanding changes in bonding and electronic properties in the warm-dense-matter regime.

Multiple synthesis runs led by the Bayreuth University team produced optically transparent stishovite, including large single crystals, using large-volume press techniques at high-pressure/ temperature conditions (see Fig. 136.66). The samples were characterized by powder and single-crystal x-ray diffraction, Raman spectroscopy, scanning electron microscopy, and wavelength-dispersive x-ray spectroscopy. Their phase and chemical purity was confirmed by appropriate analytical methods. Finally the crystals were oriented and polished into thin plates suitable for the envisioned laser-shock experiments.

We collected ultrafast Doppler velocity interferometry (VISAR) and streaked optical pyrometry (SOP) data during direct-drive shock compression of stishovite single and poly-

crystals using up to 6 kJ of UV light at the Omega Laser Facility (see Fig. 136.67). This provided pressure/density/temperature equation-of-state (EOS) data, as well as information on the optical reflectivity (therefore electron conductivity) of warm dense SiO_2 along the stishovite Hugoniot.

U1685JR
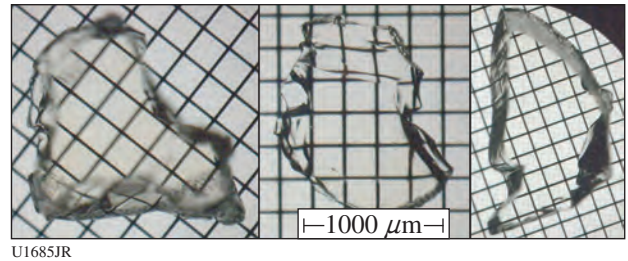
Figure 136.66
Representative single crystals of stishovite as polished into thin plates. Lateral dimensions in excess of 1 mm allow planar laser-shock compression studies.

Table 136.IX: Approved FY13 LBS proposals.

Principal Investigator	Affiliation	Project Title
P. M. Celliers	LLNL	Equation of State and Optical Properties of Dense Silica: Shock Study of Coesite and Stishovite
H. Chen	LLNL	Exploring Pair Plasmas and Their Applications Using OMEGA EP
J. R. Davies	LLE	Fast-Electron Control with a Magnetic Field in a Hohlraum
J. H. Eggert	LLNL	HED Condensed Matter: Magnesium and Aluminum
G. Fiksel	LLE	Magnetized ICF Implosions in OMEGA
G. Fiksel	LLE	Magnetic Reconnection and Particle Energization in High-Energy-Density Plasmas and the Presence of an External Magnetic Field
R. F. Heeter	LLNL	"Gattling Gun" Long-Duration Radiation Sources on OMEGA EP for Sustained-Drive Hydrodynamics and Low-Density Atomic Physics Applications on OMEGA EP and the NIF
B. R. Maddox	LLNL	Direct Measurements of Dislocation-Based Plastic Flow in Quasi-Isentropically Compressed bcc Metals
H.-S. Park	LLNL	Astrophysical Collisionless Shock Generation by Laser-Driven Experiments
P. K. Patel	LLNL	Areal-Density Measurements of Cone-in-Shell Implosions Using Compton Radiography for Fast Ignition
Y. Ping	LLNL	Long-Term Dynamics of Hole Boring and Target Heating at Fast-Ignition–Relevant Conditions
S. P. Regan	LLE	Collective X-Ray Scattering from Shocked Liquid Deuterium
J. R. Rygg	LLNL	Extreme Chemistry, Equation of State, and Optical Properties of Dense Water at Terapascal Pressure
A. A. Solodov	LLE	Fast-Ignition Integrated Experiments with Low-Z Cone-Tip Targets
C. Stoeckl	LLE	Spectroscopy of Neutrons Generated Through Nuclear Reactions with Light Ions in Short-Pulse Laser-Interaction Experiments
W. Theobald	LLE	Laser Channeling in Long-Scale-Length, Overdense Plasmas
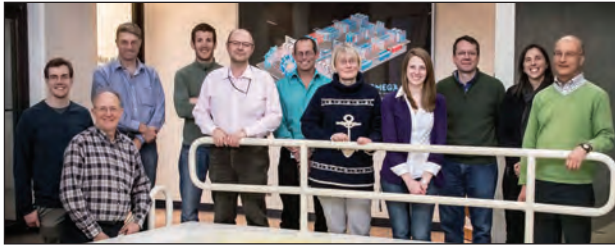
Figure 136.67
LLNL/University of California, Berkeley/Bayreuth University/LLE experimental team at the Omega Laser Facility for the first laser-shock campaign on stishovite.

Preliminary analysis suggests that we were not only able to document the onset of metallic reflectivity but also to pinpoint melting along the Hugoniot of stishovite, near 5 Mbar and 8000 K. This is the first experimental measurement of the melting temperature for silica above 2 Mbar.

These data serve as a valuable complement to existing shock studies on α quartz and fused silica, and we plan to include our data in an updated EOS table. This fundamental study will serve as an important experimental benchmark for advanced condensed matter theories, planetary modeling, and a more-complete understanding of the evolution of chemical bonding at extreme pressure and temperature conditions.

Exploring Pair Plasmas and Their Applications Using OMEGA EP
Principal Investigator: H. Chen (LLNL)

In FY13, three successful Laboratory Basic Science (LBS) experiments on OMEGA EP were performed by an LLNL/LLE team on the subject of "exploring pair plasmas and their applications." The experiments focused on the pair-jet collimation using both an electrical and a magnetic field. Very effective pair-jet collimation was observed using an externally applied magnetic field.

Previous LBS experiments by this team have shown that quasi-monoenergetic relativistic positron jets are formed during high-intensity interactions with thick gold targets.[31] The beam divergence was 30° (Ref. 32). The current experiments were designed to collimate the positron jet with an external magnetic lens. Using the new magneto-inertial fusion electrical discharge system (MIFEDS),[33] strong collimation of both positrons and electrons was observed. This resulted in a near pencil beam with an equivalent beam divergence angle of 5°.

The charge imbalance was reduced from ~100 (no collimation) to ~2.5 (with collimation)—a significant step toward making a charge-neutral electron–positron pair plasma in the laboratory.

The experiments were performed using the OMEGA EP short-pulse beams at ~1 kJ at 10 ps. The targets were made of 1-mm-thick gold. A jet of positrons and electrons was emitted from the rear side of the target. Between the target and the detector, MIFEDS coils produced a peak magnetic field of about 7 T (Fig. 136.68). The collimated beams were measured with a magnetic electron–positron spectrometer. Without the external magnetic field, the peak densities were about 10^{13} and 10^{15} cm^{-3} for positrons and electrons, respectively.[32] With the external B field applied, a factor of ~40 increase in the peak positron and electron signal was observed.
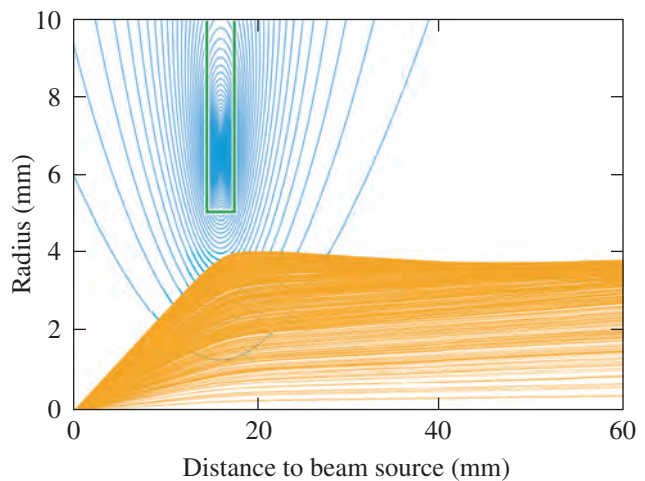
Figure 136.68
Simulation of the B fields (blue) from the MIFEDS coil (green box) and their effect on the positron jets (golden).

The next step is to confine the particles to make a pair plasma.[34] The ultimate goal will be to confine the particles to make a relativistic charge neutral electron–positron pair plasma. If successfully confined, an electron–positron plasma would offer a novel system that would enable us to conduct a detailed study of some of the most-exotic and energetic systems in the universe.[35]

Fast-Electron Control with Magnetic Field in Hohlraums
Principal Investigator: J. R. Davies (LLE)

The objectives of this experiment were to demonstrate control of fast-electron transport and suppression of stimulated

Raman scattering (SRS) in gas-filled hohlraums using a magnetic field, generated by MIFEDS—two potential benefits of magnetized inertial confinement fusion (ICF) specific to indirect drive that had not been studied before. The experimental setup is shown in Fig. 136.69.

TC11059JR

Figure 136.69
View of a hohlraum and MIFEDS coils in the target chamber. In this setup a peak magnetic field of 10 T is generated along the hohlraum axis to inhibit electron transport into the walls. The hohlraum is filled with gas but does not contain a capsule.

The basic mechanism is quite simple: the magnetic field prevents charged particles from moving across field lines. Fast electrons, generated by SRS, can therefore be prevented from reaching the walls, where they would produce hard x rays, and the capsule, where they would cause preheat. Similarly, electron thermal transport across the field is reduced, leading to a higher gas temperature, thereby reducing the SRS growth rate. A further benefit is a lower gas density sufficient enough to prevent hohlraum wall expansion from affecting the capsule, further reducing SRS growth rate.

Unfortunately, leakage of the hohlraums led to a wide range of gas densities with no repeat shots; therefore, only tentative conclusions can be drawn from these initial experiments. The results indicate that (1) SRS was negligible at fill densities of 0.03 n_c or less, where n_c is critical density; (2) at densities around 0.04 n_c—the density in a National Ignition Campaign (NIC) hohlraum—a 10-T axial magnetic field reduced SRS light and hard x-ray emission by a factor of 10; and (3) at densities of 0.09 n_c and greater, the magnetic field had no significant effect since, as expected, the collision frequency exceeded the electron cyclotron frequency. These results provide a strong motivation to further study magnetic-field suppression of SRS in gas-filled hohlraums.

Magnetized ICF Implosions on OMEGA
Principal Investigators: G. Fiksel, P.-Y. Chang, J. R. Davies, D. Barnak, and R. Betti (LLE)

The objective of this OMEGA experiment was to measure fusion enhancement (increase in neutron yield and ion temperature) in spherically imploded targets embedded in an externally generated seed field. The experiment was conducted in April 2013.

The experimental setup is shown in Fig. 136.70. A spherical CH plastic shell with a diameter of 860 μm and a thickness of 22 μm was irradiated by 40 OMEGA laser beams with a beam energy of 450 J. The beams were arranged in the polar-drive (PD) configuration. The targets were filled with D_2 gas at a pressure of 10 atm. A seed magnetic field of 7 T was created by a four-turn coil with an internal diameter of 4.5 mm powered by MIFEDS.
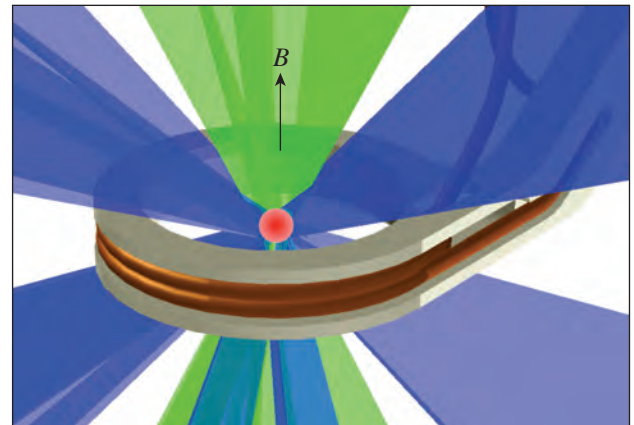
E22666JR

Figure 136.70
Setup for the fusion enhancement experiment.

The neutron yield and ion temperature for shots with and without a magnetic field are compared in Fig. 136.71. For this plot, the shots were grouped in pairs with target and laser parameters as similar as possible. On average, we observed a 23% increase in the neutron yield and an 11% increase in the ion temperature. The results are close to that obtained with *LILAC* simulations (20% and 10%, respectively). A surprisingly high jump in both neutron yield and ion temperature for shot pair #2 is not understood at this time.
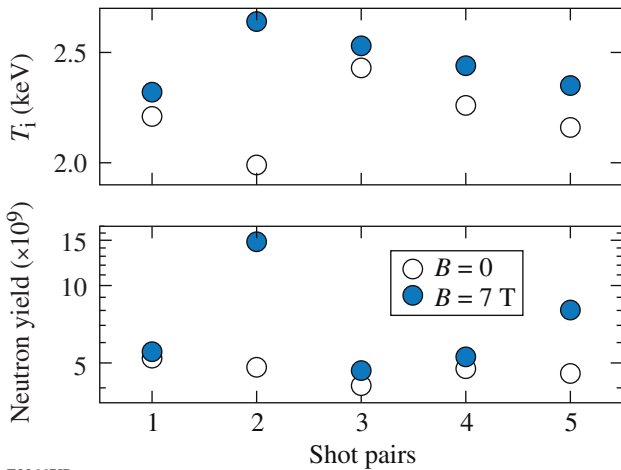
E22667JR

Figure 136.71

Comparison of neutron yield and ion temperature for shots with and without a magnetic field.

The objective of the joint experiment was to measure the compressed magnetic field in spherically imploded targets embedded in an externally generated seed field. To improve the quality and the accuracy of that measurement we (a) significantly increased the proton fluency by using OMEGA EP–generated fast protons and (b) used radiochromic film (RCF) as a proton detector for prompt image visualization. The experiment was conducted in February 2013.

The experimental setup is shown in Fig. 136.72. A spherical CH plastic shell with a diameter of 860 μm and a thickness of 22 μm was irradiated by 40 OMEGA laser beams with a 1-ns square pulse and beam energy of 450 J. The beams were arranged in the polar-drive–like configuration and laser-beam rings 1 and 1*, 2 and 2*, and 4 and 4* (top and bottom) were used. Rings 3 and 3* were blocked by the magnetic-field coils

and were not used in this experiment. In addition, the energy in the polar-most Rings 1 and 1* was reduced by 25% to improve the compression symmetry [as indicated by the *DRACO*–magnetohydrodynamic (MHD) code]. The targets were filled with D_2 gas at a pressure of 20 atm. The seed magnetic field was created by a pair of Helmholtz coils powered by MIFEDS.

To diagnose the field compression, the imploding plasma was imaged by fast protons generated with a short-pulse IR beam (1.053 μm, 800 J, 10 ps) irradiating a thin Cu disk with a focal spot of about 25 μm. The protons were imaged with a stack of radiographic film interleaved with Al filters of varying thickness, with proton energies resolved by their varying Bragg peak. The Cu proton source disk was located 7 mm from target chamber center (TCC), while the film pack was placed ~26.5 cm from TCC. A collimating Ta slit with a thickness of 0.5 mm and a width of 0.35 mm was placed in front of the proton source to prevent the background protons from striking the RCF area, where protons deflected by the compressed magnetic field are expected to land. The magnetic field was evaluated from

$$\int B dr = (d/eL)(2m_p E_p)^{1/2},$$

where d is the proton linear deflection, L is the distance to the detector, and m_p and E_p are the proton mass and energy.

The proton radiography image (shot 68758) for a proton energy of E_p = 16.7 MeV and a corresponding synthetic ion-tracing simulation are shown in Fig. 136.73. For this shot, a magnetic seed field of 6 T was applied and the OMEGA EP beam was fired at a "bang time" of 2.2 ns after the drive beams
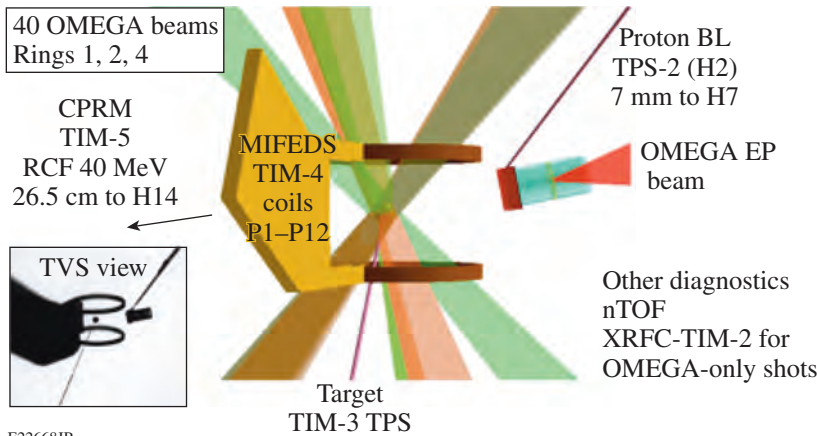
E22668JR

Figure 136.72

The experimental setup for the magnetic compression experiment.

E_p = 16.7-MeV simulations

Collimator edge

Hot-spot proton void

Shot 68758

3.7 cm

Coil shadow

Deflected protons

Filaments around shell

−1 0 1 2 3

x (cm)

E22669JR
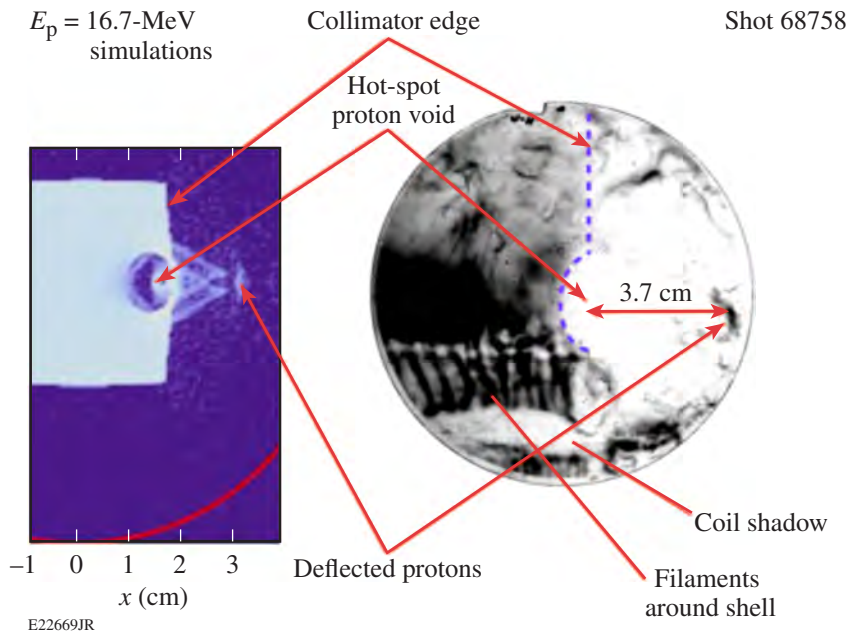
Figure 136.73
Comparison of a proton deflectometry image (right) for 16.7-MeV protons and simulation results (left). For this shot, the target was magnetized with a seed magnetic field of 6 T. E_p: proton energy.

were turned on. The most-notable features of the image are the following:

- A boundary separates the left part (where undeflected protons strike the RCF) from the right, "clean" part (where the protons deflected by the compressed magnetic field are expected to land).

- A half-circle–shaped proton void at the center of the film could be an indication of a strong magnetic field deflecting the protons away from the area.

- A dark spot at 3.7 cm from the hot-spot center could be an imprint of the deflected fast protons. The direction of the deflection agrees with the polarity of the applied seed magnetic field, and the amount of deflection corresponds to the field integral of 0.08 Tm, which is close to a value of 0.06 Tm expected from *DRACO*–MHD simulations.

Magnetic Reconnection and Particle Energization in High-Energy-Density Plasmas in the Presence of an External Magnetic Field
Principal Investigators: G. Fiksel, P. M. Nilson, and S. X. Hu (LLE); W. Fox (University of New Hampshire); and A. Bhattacharjee (Princeton)

We have been developing and conducting counter-propagating plasma interaction experiments on the OMEGA EP laser, including experiments with and without magnetic fields. Experiments with applied magnetic fields can study the inter-

action and collision of magnetized plasmas and phenomena such as magnetic reconnection. We first conducted a simpler experiment with zero applied field, leading to collision and interaction of unmagnetized plasmas. A pair of opposing CH targets separated by 4.5 mm were irradiated by 1.8-kJ laser pulses on OMEGA EP, driving a pair of ablative flows toward the collision region at the midplane between the two foils. As a result of the long mean free path between ions in opposing streams, the streams are initially free to interpenetrate, establishing supersonic counter-streaming conditions in the ion populations.

These first unmagnetized experiments found an unexpected and very interesting result: observation of the growth of an ion-driven Weibel instability generated as the two plumes interpenetrate. This instability is interesting because it has been predicted to be a key ingredient in astrophysical collisionless shocks. These astrophysical shocks must be mediated by collective electromagnetic fields since coulomb collisions alone are too weak to sustain shocks in such high-temperature astrophysical plasmas. The Weibel instability has been proposed to generate a turbulent magnetic field in the shock front and thereby mediate shock formation in cosmological shocks and blast-wave shocks in gamma ray bursts and supernova remnants. This is the first experimental observation of this instability in the shock-relevant case of interpenetrating supersonic flows.

Figure 136.74 shows radiochromic film images of the development of a striated instability as the two plumes interact. Qualitatively, the observations bear many expected features

E22670JR
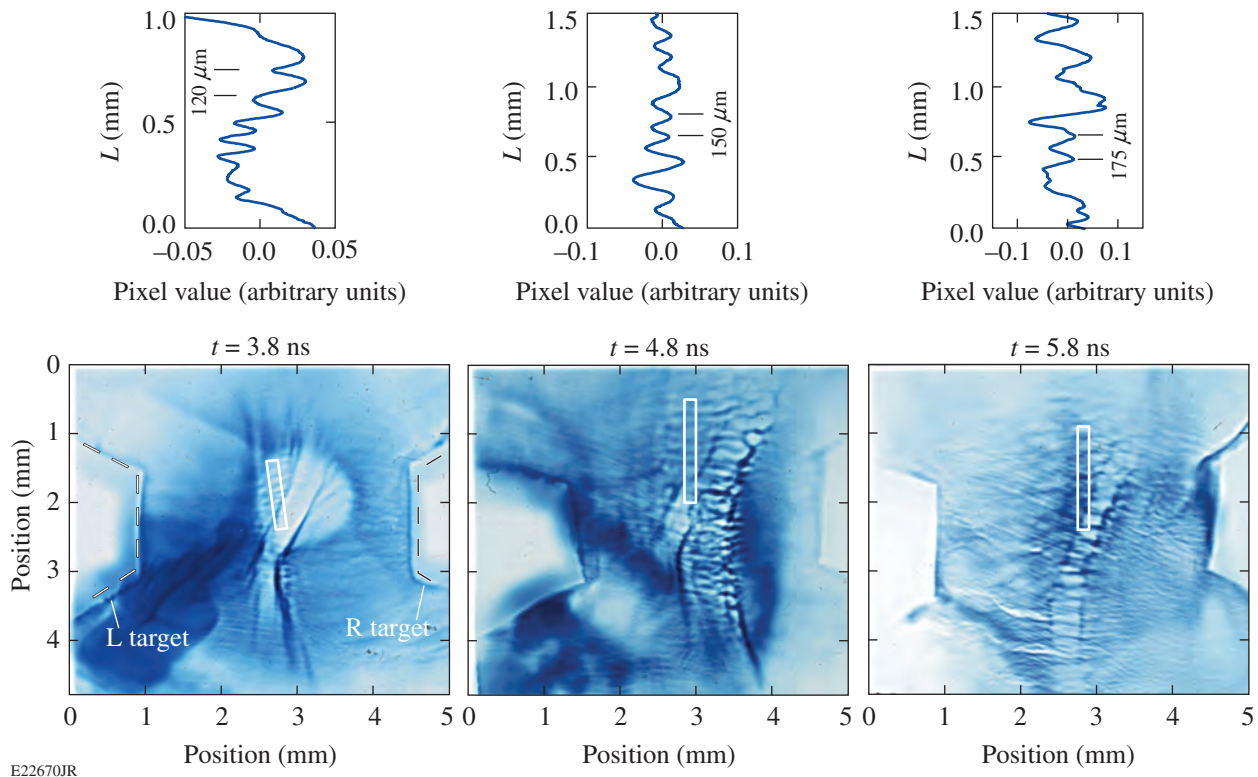
Figure 136.74
Sequence of proton radiography images taken on radiochromic film of the interaction of two plasma plumes. The insets show 1-D traces of the proton intensity along the long axis of the regions denoted in the film. L: left; R: right.

of this instability, including localization to the overlap region and formation of elongated filaments parallel to the ablation flows. The insets show 1-D traces of proton intensity along the long axis of the regions denoted in the film. Typical filament wavelengths of 100 to 150 μm at 3.8 and 4.8 ns expand to wavelengths near 250 μm at 5.8 ns. The growth rate and typical filament size compare favorably to predictions from the Weibel-instability linear theory and to particle-in-cell simulations. These results are presently under review at Physical Review Letters.

Laser Channeling in Long-Scale-Length, Overdense Plasmas
Principal Investigators: S. Ivancic and W. Theobald (LLE)
Co-investigators: D. Haberberger, D. D. Meyerhofer, D. H. Froula, S. X. Hu, K. S. Anderson, C. Stoeckl, and J. R. Davies (LLE); and H. Habara, T. Iwawaki, and K. A. Tanaka (Osaka University, Japan)

Laser-beam propagation at relativistic intensities (>10^{18} W/cm^2) is important for the field of highly nonlinear laser–plasma interactions in both under- and overdense plasmas with a long density scale length. The purpose of this LBS experiment was to study the physics of guiding a high-intensity IR laser pulse along the density gradient of large surrounding plasma to the vicinity of high densities. This study has potential applications for the fast-ignition scheme[36] without using a re-entrant cone target. The experiment was performed with the OMEGA EP laser using one of the short-pulse IR beams (1.2 kJ, 10 ps) to form a channel in a large blowoff plasma with an electron temperature of ~1.8 keV that was generated by 2-ns, 1-kJ UV laser beams. The plasma was diagnosed using a 10-ps, 263-nm probe laser[37] to simultaneously measure the background plasma density and image the channel. The phase gradients were discriminated by a novel technique using an angular spectral filter that is placed in a Fourier plane behind the collection optics of the probe beam. The details of the technique are described in Ref. 38.

Figure 136.75 shows measured images of the plasma at various delay times of the probe beam with respect to the channeling beam. Figure 136.75(a) shows an image of the unperturbed plasma taken 45 ps prior to the channeling pulse. The expanding plume is made visible by the alternating light and dark

270
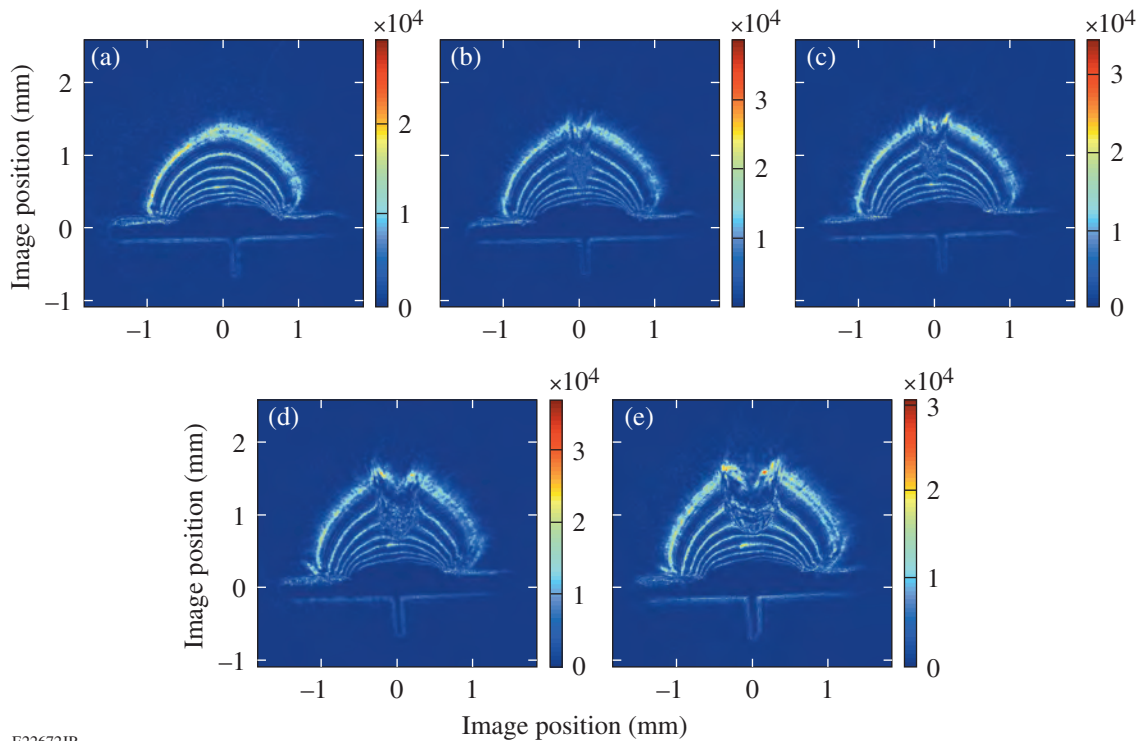
E22672JR

Figure 136.75
Probe image of the plasma taken at various delay times of the probe beam (–45 ps, 6 ps, 15 ps, 78 ps, and 200 ps) with respect to the channeling beam. Image (a) was taken prior to the channeling beam while images (b)–(e) show the channel formation in the plasma and the subsequent hydrodynamic evolution. The edge of the channel steepens to a shock wave moving at a velocity of ~1 μm/ps measured by the radial expansion of the outer limb as a function of time. The lower sharp contour shows the back surface of the foil target and the alignment fiber.

bands. Counting from the outside toward the initial target surface, the plasma density increases, as does the refracted angle of the probe beam. The band structures correspond to contours of constant refracted angle through the plasma. By relating the angle of refraction to density scale length in the plasma, a quantitative measure of plasma density and scale length is obtained. The outermost contour corresponds to roughly 2×10^{19} cm^{-3} and the innermost corresponds to the critical density for IR light. An average density scale length of 275 μm is inferred from the image. Two-dimensional hydrodynamic simulations are in good agreement with the measured plasma density profile. Figure 136.75(b) was taken during the interaction of the channeling beam showing that a channel was formed that reached up to half the IR critical density with a channel width of ~200 μm. Individual filaments were observed at the critical surfaces, indicating that the laser became unstable and broke up into multiple filaments. Images taken at later times in Figs. 136.75(c)– 136.75(e) show the radial evolution of a strong blast wave from the channel walls.

"Gatling Gun" Long-Duration Radiation Sources on OMEGA EP for Sustained-Drive Hydrodynamics and Low-Density Atomic Physics Applications on OMEGA EP and the NIF

Principal Investigators: D. Martinez, J. O. Kane, and R. Heeter (LLNL); A. Casner (CEA); and R. C. Mancini (University of Nevada, Reno)

The High Energy Density Laboratory Physics (HEDLP)–funded Eagle nebula project, in collaboration with the LLNL/ University of Nevada Photoionization/Black Hole Physics effort, has successfully executed the first day of Laboratory Basic Science (LBS) long-duration radiator shots, performed on OMEGA EP. This experiment employed a novel technique using a copper multihohlraum target with three hohlraums filled with a 4-mg/cm^3 poly(4-methyl-1-pentene) (TPX) foam fill to act as a gas surrogate. Each hohlraum was driven with an OMEGA EP UV beam with either a 6-ns pulse with 3.3 kJ of energy or a 10-ns pulse with 4.3 kJ. Each hohlraum was

heated in succession to generate an 18-ns or 30-ns, 100-eV x-ray source for future laboratory astrophysics studies. The x-ray source was characterized with the CEA μDMX diagnostic and velocity interferometer system for any reflector (VISAR) using a quartz shock sample with a CH ablator over a single hohlraum. The shot day was successful with six hohlraum shots on OMEGA EP with two 30-ns x-ray drive shots. The data indicated that the novel foam-filled multihohlraum ("Gatling gun"), long-duration source performed as designed with all three hohlraums lighting up without significant interhohlraum interference (Fig. 136.76). In addition, the x-ray drive source was able to illuminate a Ti photoionization demonstration physics package with a 90- to 100-eV x-ray drive, generating Ti L-shell band radiation as expected. This source will next be applied to study ablation-driven hydrodynamic experiments relevant to the Eagle nebula and to further develop the photoionization studies with a controlled 30-ns x-ray source.
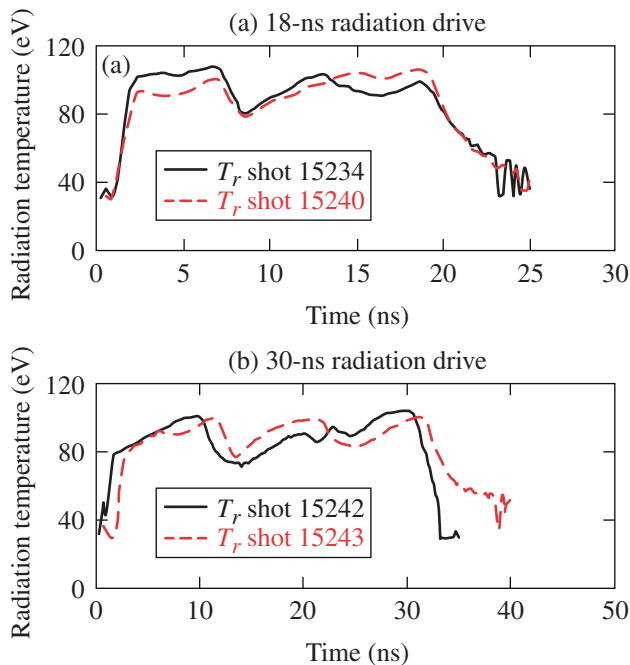
Figure 136.76
Radiation temperature generated from the Gatling gun target measured with μDMX.

Astrophysical Collisionless Shock Experiments with Lasers (ACSEL)

Principal Investigator: H.-S. Park, S. Ross, and C. Huntington (LLNL)

The ACSEL collaboration had three shot days in FY13, with two shot days on OMEGA EP and one on OMEGA. These experiments expanded on the collisionless shock platform common to ACSEL (LBS) and MagShock (NLUF), the former concentrating exclusively on nonmagnetized (no external applied magnetic field) plasmas. Irradiating a pair of opposing planar targets with 2.2 kJ (OMEGA EP) or 4 kJ (OMEGA) of laser light, counter-propagating flows are created, each with bulk velocity near 1000 km/s (Ref. 39). The flows interact near the midplane between the targets, where the interpenetrating plasma is susceptible to a range of instabilities, including the two-stream and Weibel instabilities. Study of these phenomena is essential to understanding a range of astrophysical systems, including gamma-ray bursts, supernovae remnants, and young stellar objects.

Experiments conducted this year included several new diagnostics, including x-ray spectroscopy (MSPEC on OMEGA EP), 4ω imaging (optical suite on OMEGA EP), neutronics (wedge-range filters on OMEGA), and proton probing at 14.7 MeV using D^3He (OMEGA). In the D^3He experiments, filamentation of the plasma was observed along the direction of the flow, consistent in size and growth rate with Weibel instability (see Fig. 136.77).[40] Weibel is notoriously difficult to diagnose in an experiment, making this an important laboratory astrophysics result. In additional to ongoing efforts to analyze data from the many new diagnostics, ACSEL experiments in FY13 also employed various single- and multispecies targets
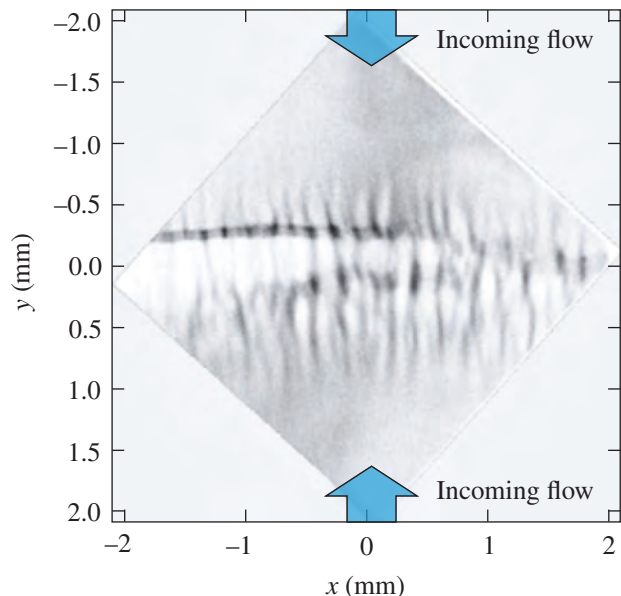
Figure 136.77
Proton radiography image of the interaction of two counter-streaming plasmas showing filaments produced by the Weibel instability.

to create plasma flows. Observations from a range of target material increase our understanding of the stabilizing effect of light ions (H in CH targets versus pure C or Be targets) in the instabilities that shape these counter-streaming plasmas.

Protons from a D^3He capsule are detected using a CR-39 detector at an ~30× magnification. Incoming plasma flows from the top and bottom of the frame interact, coalescing into filaments along the plasma-flow direction. Additionally, horizontal magnetic plate structures are observed, consistent with previous experiments in similar geometries.[41] These are the result of Biermann battery fields produced at the target surface that are entrained in the flow and lead to large-scale features at the midplane.

Areal-Density Measurement of Fast-Ignition Targets
Principal Investigators: F. Pérez (LLNL) and H. Sawada (University of California, San Diego)
Co-investigators: W. Theobald, A. A. Solodov, J. A. Delettrez, V. Yu. Glebov, and C. Stoeckl (LLE); L. C. Jarrott and F. N. Beg (University of California, San Diego); M. S. Wei and R. B. Stephens (General Atomics); and H. S. McLean, M. H. Key, and P. Patel (LLNL)

The fast-ignition (FI) approach to inertial fusion has a potential to achieve a higher energy gain compared to a central-hot-spot–ignition scheme. It requires a moderate fuel assembly and an injection of a high-energy, short laser pulse near the peak compression to locally heat the fuel core, initiating thermonuclear ignition and burn wave. In the cone-guided FI scheme, a re-entrant Au cone embedded in a capsule clears the path of the ignition laser. Since the presence of the cone in the shell breaks symmetry, it is important to measure an evolution of the fuel assembly of the cone-in-shell target and to benchmark the 2-D radiation–hydrodynamics code with the experimental result. Based on the results of our FY12 Compton radiograph campaign and the success of the recent K_α radiograph campaign by W. Theobald *et al.* for cone in shell with Al disk targets, a joint experiment to measure areal density of a cone-in-shell target was conducted using 54 18-kJ OMEGA beams for implosion and a 10-ps, 1.25-kJ OMEGA EP laser beam to generate Cu K_α backlighter x rays. The radiograph images were recorded using the OMEGA spherical crystal imager (SCI). Figure 136.78 shows a schematic of a cone-in-shell target and four snapshots of the radiograph images at 3.68, 3.85, 4.02, and 4.22 ns after the beginning of the implosion drive. Each image clearly shows the shadow of the cone as well as the formation of the dense core. Preliminary comparisons of the experimental optical depth and post-processed 2-D *DRACO* simulations show a
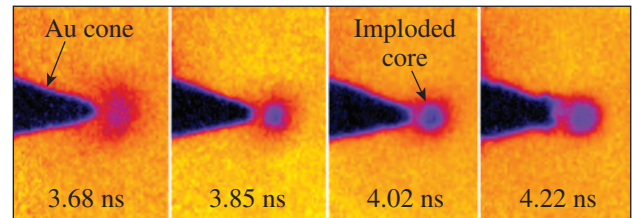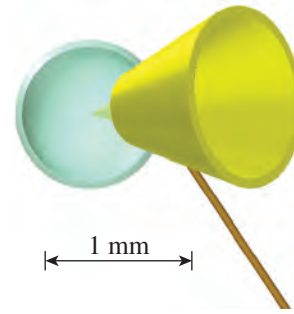
Figure 136.78
Schematic of the cone-in-shell target and four sequential snapshots of the K_α x-ray radiography of the implosion.

very good agreement (<5% discrepancy of areal density) for early times; i.e., when the knowledge of the implosion is most important for future FI studies such as integrated FI simulations for core heating. For later times, the comparison shows a deviation of up to 30%. These high-quality, radiograph images will provide a solid basis for benchmarking the 2-D *DRACO* code and advancing integrated FI core-heating simulations to compare OMEGA integrated FI experiments.

Simultaneous X-Ray Diffraction and EXAFS Measurements of Al and Mg
Principal Investigators: Y. Ping, F. Coppari, J. Hawreliak, J. Emig, R. Heeter, J. H. Eggert, and G. W. Collins (LLNL); and B. Yaakobi (LLE)

Our paper on extended x-ray absorption fine structure (EXAFS) measurements of dynamically compressed iron up to 560 GPa has been published in Physical Review Letters.[42] During FY13 we extended this platform to study Al and Mg. Both materials have new phases at high pressures that have been predicted but not previously observed. In addition to EXAFS, the setup on OMEGA with an implosion backlighter allowed us to perform simultaneous diffraction measurements, providing complimentary phase information to EXAFS on the compressed material. We have obtained undriven EXAFS data of Al [Fig. 136.79(a)] that is in good agreement with calculations. A few issues have been identified from the two half-day campaigns. First, because of the low x-ray energy of Al and
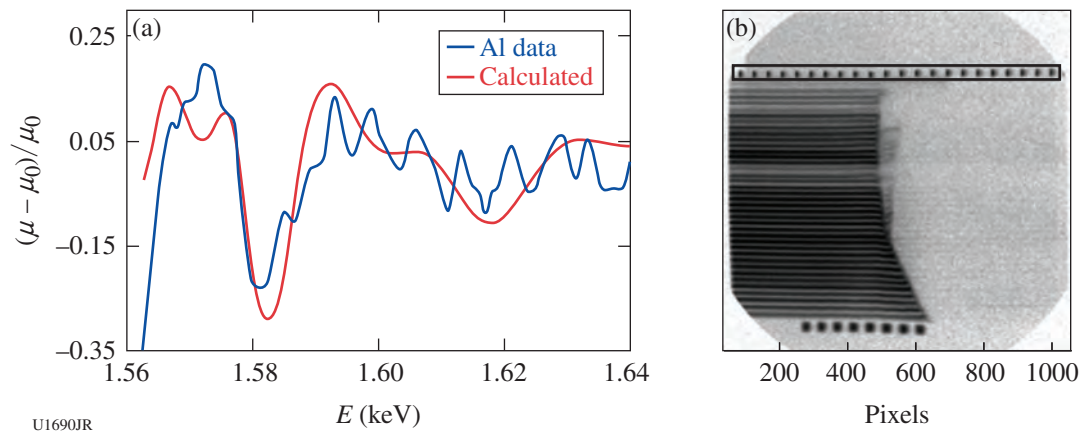
Figure 136.79
(a) Measured EXAFS spectrum of undriven Al, showing good agreement with calculations. (b) ABSO data during multishock compression. The loss of reflectivity of Be causes the signal to diminish when the shock breaks out.

Mg K edges, the blast shield of the x-ray spectrometer must be minimized, resulting in some damage to the crystal during shots. Second, the target material was sandwiched in Be foils and the active shock breakout (ASBO) beam was reflected from a polished Be surface. The ASBO signal was blanked out when the shock broke out because of loss of reflectivity of Be, as shown in Fig. 136.79(b). Third, the diffraction angle and dispersion angle were coupled in the diffraction geometry, making it difficult to exactly match for any diffraction peaks. We are working on potential improvements to mitigate these issues.

Hole-Boring Dynamics and Electron Focusing Under Fast-Ignition–Relevant Conditions
Principal Investigators: Y. Ping, T. Link, E. Kemp, N. Whiting, M. S. Wei, and P. Patel (LLNL)

During FY13 we designed and installed SpecFROG—a new diagnostic for OMEGA EP. This diagnostic, based on a scheme of frequency-resolved optical gating (FROG), measures time-resolved spectral shift with a high temporal resolution of ~200 fs. We used it to measure the Doppler shift induced by the competition between the light pressure and the plasma thermal pressure at the laser–plasma interface. Initial testing of SpecFROG was complicated by electromagnetic interference (EMI) noise that prevented the data-acquisition system from operating properly. This issue was finally resolved after the seventh shot. The 2ω light reaching SpecFROG was lower than expected, so we plan to operate SpecFROG at 1ω for FY14 LBS shots that have been awarded. The second goal of this OMEGA EP campaign was to focus relativistic electrons by an ellipsoidal magnetic field using a novel target with buried ellipsoids or wires. The target geometry and results are shown in Fig. 136.80. Three types of targets have been used: flat foil, buried ellipsoid, and buried wire. The Cu layer at the back serves as a fluor layer to show the distribution of hot electrons. The spot size in ellipsoid/wire targets is clearly reduced in comparison to the flat target, indicating focusing or collimation of relativistic electrons. These promising results provide a pathway to eventually solving the electron divergence problem, which is the current bottleneck for the fast-ignition scheme.

Collective X-Ray Scattering from Shocked Liquid Deuterium
Principal Investigators: S. P. Regan, T. R. Boehly, S. X. Hu, and P. B. Radha (LLE)
Co-investigators: G. Gregori and P. Kozlowski (Oxford)

The experimental platform to measure inelastic x-ray scattering from shocked liquid deuterium on OMEGA was extended from the noncollective regime[43] to the collective regime by changing the scattering angle from 90° to 40°. Two shot days on OMEGA for Laboratory Basic Science were used to demonstrate the planar cryogenic target having a 40° scattering geometry. A photograph of the new target is shown in Fig. 136.81. On the first shot day, a weak signature of elastic scattering was observed; however, the target produced too much debris, which punctured the blast shield of the primary diagnostic that recorded the scattered spectra. The target was redesigned for the second shot date to mitigate the target debris problem and to increase the amount of x rays incident on the shocked liquid deuterium. The debris mitigation strategy was successful on the second shot date at the end of FY13. Increasing the photon throughput from the backlighter to the scattering sight was also successful. Preliminary analysis of the measured spectra

indicates evidence of elastic scattering from the shocked liquid deuterium as well as plasmon features. A flat fielding shot to calibrate the Bragg crystal spectrometer used to record the spec-

trum will be taken as a ride-along experimental objective for an upcoming diagnostic development day on OMEGA. Once the flat-field response is determined, the collective x-ray scat-
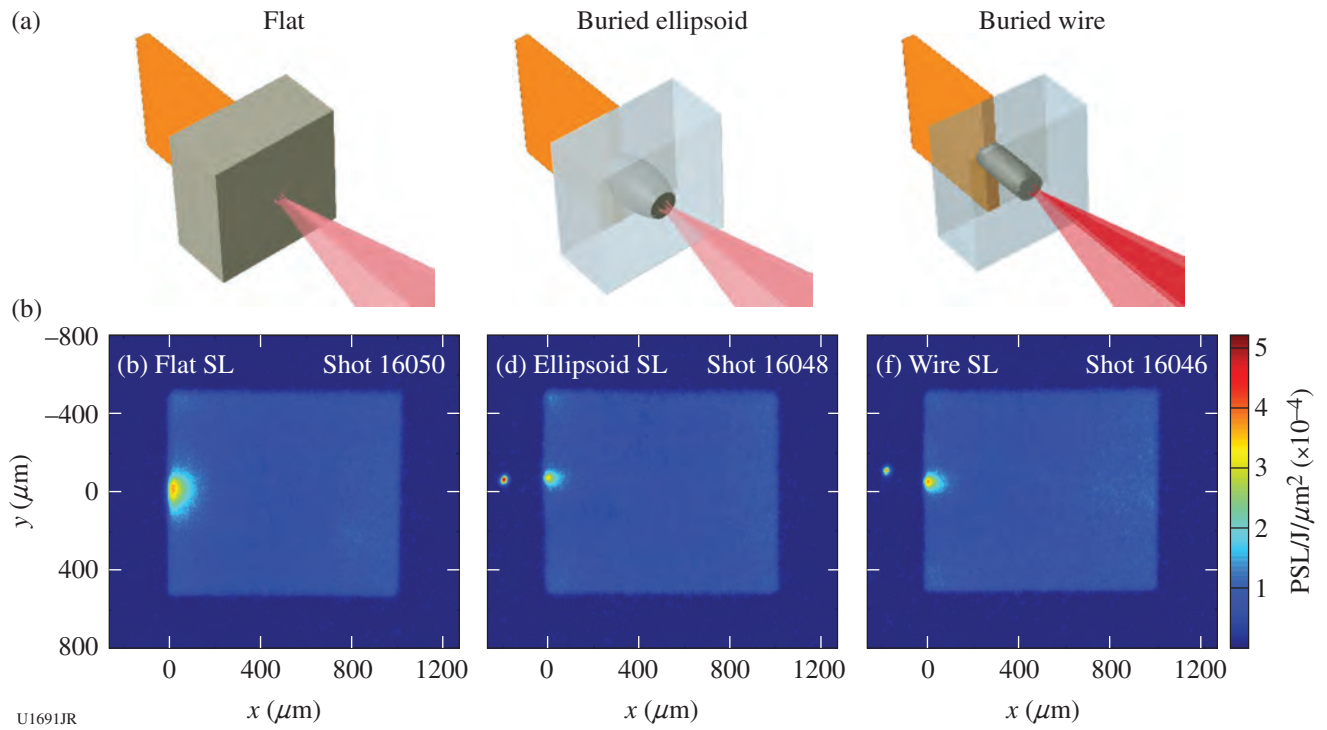

Figure 136.80
(a) Schematic of three types of targets: flat foil, buried ellipsoid, and buried wire. The Cu layer at the back serves as a fluor layer to show the distribution of hot electrons. (b) Cu K_α images from the three targets. The spot size in the ellipsoid/wire targets is clearly reduced in comparison to the flat target.
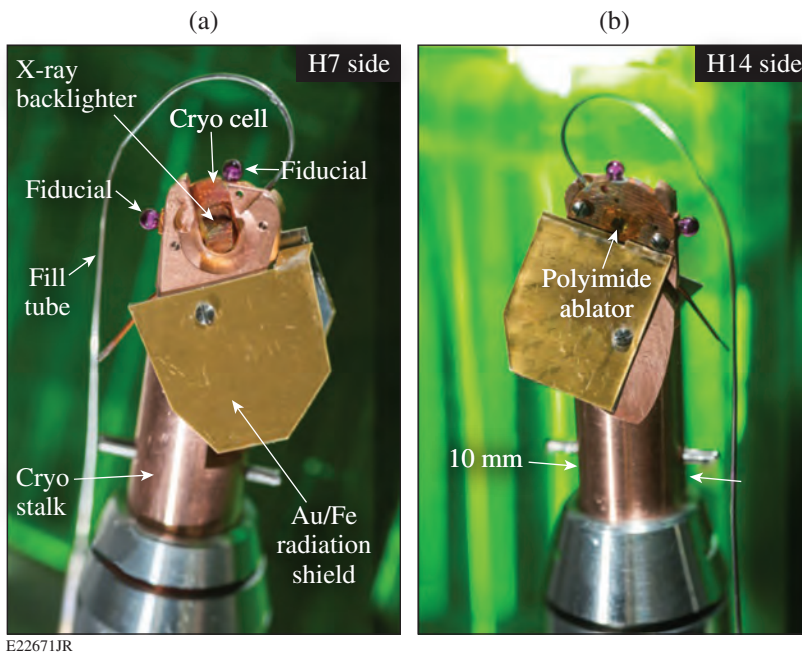
Figure 136.81
Photographs of the planar cryogenic liquid deuterium target for a 40° x-ray scattering experiment. Deuterium is delivered to the cryo cell via the fill tube. The cryo cell, containing ~5 mm³ of liquid deuterium, is aligned using the mechanical fiducials. The Au/Fe radiation shields block a direct line of sight between the x-ray emission sources and the detector (not shown). (a) The H7 side of the target highlights the x-ray backlighter and (b) the H14 side of the target highlights the 8-μm-thick polyimide ablator.

tering spectrum will be analyzed to infer the electron density of the shocked liquid deuterium from the downshifted photon energy of the plasmon feature. To lowest order, the position of the energy-downshifted plasmon feature is related to the electron plasma frequency $\omega_{pe} = \left(e^2 n_e \big/ 4\pi\varepsilon_0 m_e\right)^{1/2}$, providing an electron density diagnostic.

Extreme Chemistry, Equation of State, and Optical Properties of Dense Water at Terapascal Pressure

Principal Investigator: J. R. Rygg (LLNL)
Co-investigators: M. Millot and R. Jeanloz (University of California, Berkeley); and S. Hamel and G. W. Collins (LLNL)

We investigated the bonding of dense water at extreme conditions, achieving terapascal (TPa) pressures by shock loading precompressed samples. Our LLNL/UC Berkeley team conducted four half-day campaigns, obtaining 27 shots on the OMEGA Laser System.

Improving our knowledge of dense water is of paramount importance for modeling *icy* planets, such as Neptune and Uranus, and numerous exoplanets. However, our knowledge of the physical and chemical properties of water at the conditions existing in the deep interiors of these objects is limited. A better understanding of the equation of state of hot dense water is needed to constrain the mass distribution within the planets, model their internal energy fluxes, and determine how the planets formed and evolved. In addition, improving our knowledge of the transport coefficients, such as the electrical conductivity,

is crucial for correlating the gravitational and particular magnetic properties of these planets. A unique superionic phase with a solid lattice of oxygen ions and mobile protons could play a key role in the thermal and electric-charge fluxes.

Using diamond anvil cells to precompress water up to 1.6 g/cm^3 and ultrafast Doppler velocity interferometry (VISAR) coupled with streaked optical pyrometry (SOP), we obtained a set of equation-of-state (EOS) and optical conductivity data for warm dense water (see Fig. 136.82). These measurements were taken at unprecedented conditions of pressure and temperature, so they provide an important experimental benchmark for advanced condensed matter theories and planetary modeling and for a more-complete understanding of chemical bonding at extreme pressure and temperature conditions. Preliminary analysis suggests that the most-recent first-principle–based molecular dynamics simulations capture most of the behavior of water at these conditions.

Furthermore, we obtained clear experimental evidence of a sharp transition in the optical properties of dense water around 2 Mbar and 4000 K along the Hugoniot of solid ice VII (initial pressure and density of $p_0 \sim 2.4$ GPa and $\rho_0 \sim 1.6$ g/cm^3, respectively) (see Fig. 136.83). In this region, SOP data exhibit a dramatic change from a semiconducting, absorbing state to a metallic, reflecting state, while shock pressure is only slightly increased (see Fig. 136.83). We interpret this transition as the *melting* of the superionic solid into the dense plasma fluid state that has been predicted. Further analysis will allow us to pre-
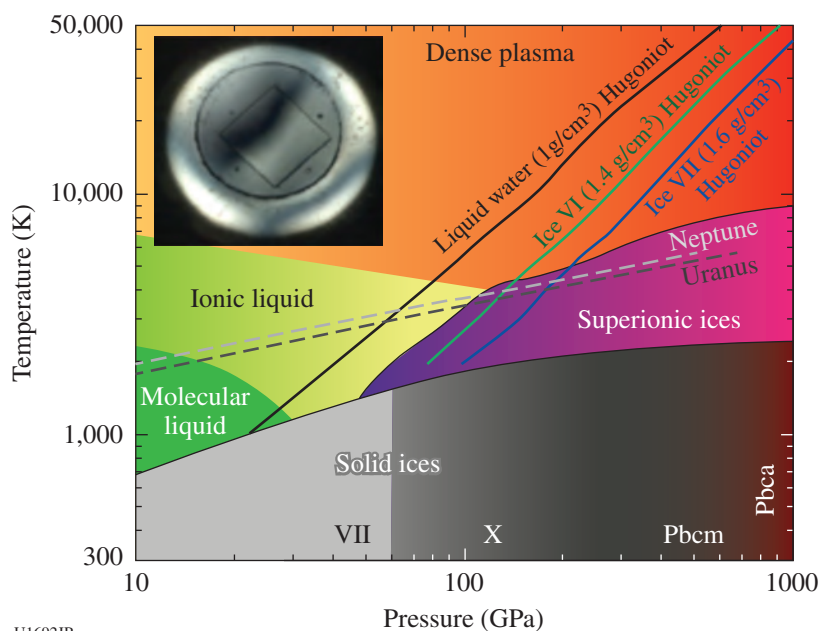
Figure 136.82
Theoretical water pressure/temperature phase diagram including the molecular liquid, the ionic liquid, the solid and superionic high-pressure ices, and warm dense metallic plasma. State-of-the-art theoretical interior isentropes for Neptune and Uranus (dashed lines) suggest that superionic ices may exist deep within these planets. The shock Hugoniot from water ice VI (green) and ice VII (light blue) were investigated during this campaign, from the vicinity of the predicted transition from superionic to metallic plasma around 1 to 2 Mbar up to pressure in excess of 7 Mbar (0.7 TPa). Inset: Microscope image of the diamond-anvil cell pressure chamber at 2.5 GPa containing ice VII water and a 400-μm-sq quartz witness plate ready for a laser-shock compression experiment on the OMEGA laser.

U1692JR

cisely locate the pressure–density–temperature conditions of this transition, as well as the first experimental measurements of the electronic conductivity in the superionic phase.
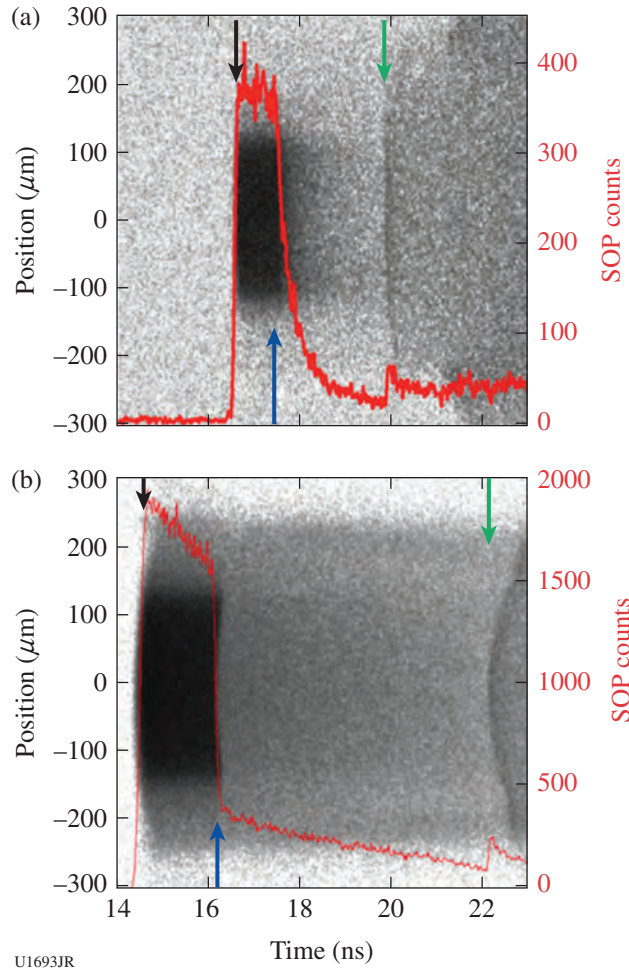

Figure 136.83
Representative raw streaked optical pyrometry (SOP) images acquired during laser-shock compression of water ice VII in the vicinity of the predicted transition from superionic to metallic plasma around 2 Mbar. Lineouts (red) are overlaid. Strong optical emission is recorded as the shock travels through the quartz plate (from the black to the blue arrows), but a striking difference in the temporal behavior of the SOP signal as the shock transits the water layer (from the blue to the green arrows) is indicative of a qualitative difference in the optical properties of water at these different pressures. (a) At lower pressures, the SOP intensity exhibits an exponential decay with time, interpreted as the quartz emission transmitted through an increasing thickness of semiconducting, partially optically absorbing water as the shock transits the water layer. (b) At slightly higher pressure, the SOP intensity drops sharply upon breakout from the quartz into the water (blue arrow) and decays nearly linearly as the slightly decaying shock transits the water layer. This, together with the VISAR data (not shown), provides a clear signature of the metallic-like reflecting state.

Fast-Ignition Integrated Experiments with Low-Z Cone-Tip Targets

Principal Investigators: A. A. Solodov and W. Theobald (LLE)
Co-investigators: C. Stoeckl (LLE); F. N. Beg (University of California, San Diego); E. Giraldez, R. B. Stephens, and M. S. Wei (General Atomics); H. McLean (LLNL); H. Sawada (University of Nevada, Reno); and H. Habara (Institute of Laser Engineering, Japan)

Integrated fast-ignition experiments on OMEGA with cone-in-shell targets have demonstrated ~3.5% coupling efficiency of short-pulse laser energy into the compressed target.[44] The goal of this LBS experiment was to study the short-pulse–laser/fast-electron coupling efficiency using an improved OMEGA EP laser and to compare the coupling of a new aluminum cone tip target to the previous Au cone-tip design.[44] The hydrodynamics of the new target design has been modeled with simulations using the code *DRACO*.[45] The modeling predictions were validated in an FY12 LBS backlighter experiment[46] that showed excellent agreement between measured and simulated fuel assemblies. The radiographs showed how the implosion destroys and pushes back the cone tip. The measured time of peak compression (~4.10±0.05 ns) compared well to the predicted time (4.06 ns), and the measured peak areal density of 270±50 mg/cm^3 was close to the predicted peak value of 320 mg/cm^3.

The fast-electron coupling was studied for the two target types. The OMEGA EP laser was significantly improved with a smaller focus ($R_{80} = 15 \ \mu$m), a higher energy (1.2 kJ), and a higher contrast (~0.5 mJ of prepulse energy). Compared to the previous experiment,[44] the average intensity increased about 4× to ~2 × 10^{19} W/cm^2. The laser contrast was sufficiently high so that no significant pre-plasma formation was expected. Figure 136.84 shows the measured neutron yield versus OMEGA EP laser energy for (a) the LBS experiment using the two cone types with regular plastic shells and (b) the same cone designs with Cu-doped plastic shells. The later data were obtained in an FY13 NLUF experiment led by F. Beg from the University of California, San Diego. The blue lines mark the neutron yield from the implosion alone without OMEGA EP. The measured neutron yield increase in (a) is marginal and smaller than in (b) with Cu-doped shell targets. The neutron yield from the target with the Al tip was similar to the implosion yield in (a) and a factor of ~2 higher in (b) for 500-J short-pulse energy. A clear trend of an increased yield with laser energy is observed in (b) for the standard targets with Au tips. The data show that the ~1% atomic Cu doping in the plastic shell increased the energy deposition

of the fast electrons in the compressed shell. Compared to previous measurements with higher prepulse and a lower OMEGA EP laser intensity, the neutron yield was lower and the fast-electron coupling did not improve. This was probably due to the higher laser intensity, which resulted in a more-energetic fast-electron population that did not couple as well in the compressed plasma as a colder distribution. This was supported by the measured slope temperature of the distribution of escaped fast electrons, which increased from ~2.5 to ~5 MeV with higher intensity.
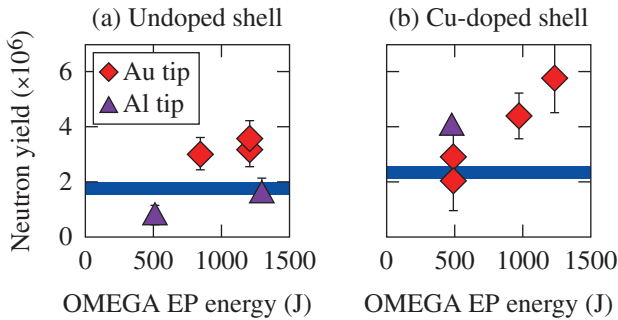
Figure 136.84
Measured neutron yield from integrated experiments using standard Au tip targets (red diamonds) and Al tip targets (purple triangles) using (a) regular plastic shells and (b) Cu-doped plastic shells. The series in (b) was obtained from an NLUF experiment in FY13 led by F. Beg from the University of California, San Diego.

Spectroscopy of Neutrons Generated Through Nuclear Reactions with Light Ions in Short-Pulse Laser Interaction Experiments
Principal Investigators: C. Stoeckl, V. Yu. Glebov, and U. Schroeder (LLE)

The experimental objective of this project is to study nuclear reactions in light ions by measuring the spectrum of neutrons generated in short-pulse laser interaction experiments and comparing it with simulated spectra based on the published cross sections.

Planar targets are irradiated with one short-pulse beam focused at the target's front surface. Charged particles from the back side of the target create neutrons and charged particles through nuclear reactions in a second converter target placed closely behind the primary interaction target. The spectrum of the neutrons generated in the converter target is measured using a three-channel scintillator photomultiplier–based neutron

time-of-flight detector system. Charged-particle detectors are used to measure the spectra of the primary particles.

The previous experiments in FY12 with copper primary and LiD secondary targets resulted in neutron spectra dominated by background from p–n reactions in the targets and the target chamber. No specific spectral features like DT fusion neutrons were visible in the recorded data.

Two shot days were available for experiments in FY13. On the first shot day a larger LiD container with 10× more LiD compared to the FY12 experiments was used to increase the expected signal. Even with the increased mass of the LiD in the secondary target, no DT fusion neutrons were observed; the neutron spectrum was still dominated by background. Two different strategies were used on the second shot day in an effort to reduce the background. A CH shield tube was placed around the primary target (see Fig. 136.85), which stops or slows protons below the threshold of (p,n) reactions. Since carbon has a high threshold for (p,n) reactions of >20 MeV, placing a CH shield to intercept all protons that would not interact with the secondary target could significantly reduce the background, provided that the proton spectrum not contain a large number of protons above 20 MeV. Additionally a pre-plasma was created on the front side of the primary target using a 100-J, 100-ps UV laser pulse, which was fired 1 ns before the main IR short pulse. Previous experiments have shown that the presence of plasma can significantly reduce the number of charged particles generated on a surface. The
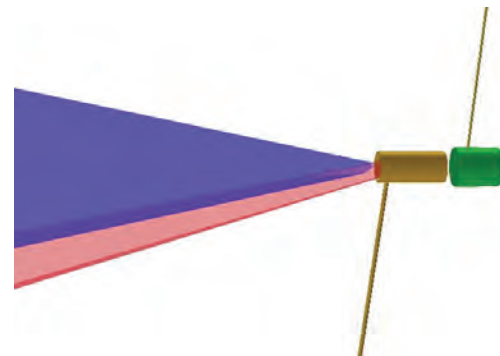
Figure 136.85
Schematic of the target setup for the background-reduction experiments. The primary target (not visible) is contained in a CH shield tube (brown). It is irradiated by a 100-J, 100-ps UV laser pulse (purple), 1 ns before the main IR short pulse (red) arrives, to create a pre-plasma. The secondary converter target (green) is placed as close as possible to the end of the shield tube.

UV laser energy and timing were chosen such that a plasma was generated only on the front side of the primary target and not on the back side of the target from the laser-generated shock reaching the back surface at the time the short-pulse laser was fired.

CD foils were used for primary and secondary targets in the background reduction study since the D–D fusion cross section is higher (of the order of 1 barn) than the Li breakup cross section (<100 mb) and very well known.

Figure 136.86 shows two neutron time-of-flight signals from the background reduction experiments, (a) with UV prepulse and (b) without prepulse. The neutron background is reduced substantially with the prepulse, and a clean D–D fusion neutron peak can be seen at the expected time of 750 ns. Without a prepulse, the background signal is very high and masks any D–D peak that might be present. A detailed analysis of the experimental data is in progress.
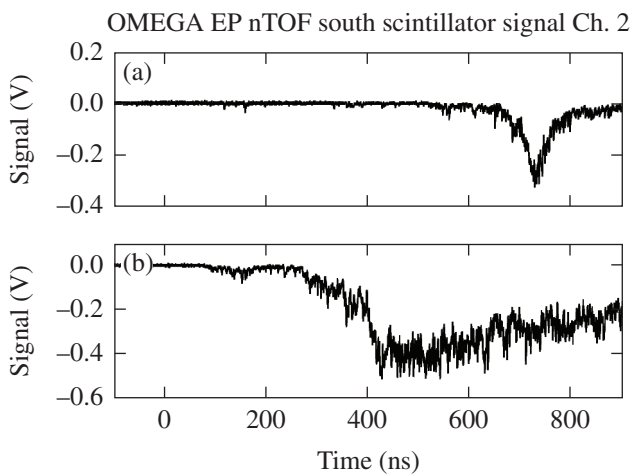
Figure 136.86
Neutron time-of-flight (nTOF) signals from the background-reduction experiments. (a) When the UV prepulse is used, the background is reduced substantially and a clean D–D fusion neutron peak is visible at the expected time of 750 ns. (b) Without a prepulse, the data are dominated by background and no D–D peak is seen.

Direct Measurement of Dislocation-Based Plastic Flows in Quasi-Isentropically Compressed bcc Metals
Principal Investigator: C. Wehrenberg (LLNL)

Our goal was to record a time series of Laue diffraction patterns in shock-compressed single-crystal Ta at a range of shock pressures near the expected homogeneous nucleation threshold. With these results we would be able to study the strain relaxation process in Ta. For these shots, an imploding CH capsule driven by 29 beams provided a broadband x-ray source, and a Ta sample with a high-density–carbon (HDC) ablator was driven by a single beam. High-quality diffraction data were recorded for shock pressures of 0.4 to 0.8 Mbar. Data at 0.4 Mbar show the strain at first extending out to a maximum that matches theoretical predictions for unaxial compression and then relaxes to a final strain state over the course of ~1 ns. Above 0.7 Mbar, the Ta relaxes to a final strain state faster than the resolution of the experiment (~0.2 ns). This behavior is consistent with the predicted homogenous nucleation threshold occurring at 0.65 Mbar.

In addition, simultaneous recovery experiments designed to measure the average dislocation velocity during shock loading of Ta were performed. In these experiments a high dislocation density region was seeded by nano-indenting single-crystal Ta samples and grown by driving a shock wave with a single beam. Movement of the dislocation region was measured pre- and post-mortem by transmission electron microscopy (TEM). Several samples with a range of single crystal orientations and indents were recovered and the TEM analysis is ongoing.

FY13 LLNL OMEGA Experimental Programs
Principal Investigators: R. Heeter, K. Fournier, K. Baker, G. V. Brown, D. T. Casey, P. M. Celliers, L. Fletcher, D. E. Fratanduono, J. Hawreliak, C. Huntington, A. Lazicki, T. Ma, D. Martinez, M. May, A. Moore, A. Pak, H.-S. Park, R. Patterson, F. Perez, Y. Ping, C. Plechaty, J. S. Ross, J. R. Rygg, M. Schneider, V. A. Smalyuk, R. Tommasini, C. Wehrenberg, G. W. Collins, O. L. Landen, A. Wan, and W. Hsing (LLNL); H. Rinderknecht and A. Zylstra (MIT)

In FY13, LLNL's high-energy-density (HED) physics and indirect-drive inertial confinement fusion (ICF-ID) programs conducted several campaigns on the OMEGA and OMEGA EP Laser Systems, as well as campaigns that jointly used the OMEGA and OMEGA EP beams. Overall LLNL led 448 target shots (290 target shots involving OMEGA and 158 target shots involving OMEGA EP). (These shots do not include the target shots taken under the LBS program.) Approximately 34% of the total number of shots (93 OMEGA shots, 58 OMEGA EP shots) supported the ICF-ID Program. The remaining 66% (197 OMEGA shots and 100 OMEGA EP shots) were dedicated to experiments for HED physics.

Indirect-Drive Inertial Confinement Fusion Experiments

A New Platform for Absolute Equation-of-State Measurements
Principal Investigator: D. E. Fratanduono

Using OMEGA EP, a radiographic equation-of-state (EOS) platform was developed for use at the National Ignition Facility (NIF). The concern regarding traditional velocity interferometer system for any reflector (VISAR)–based EOS platforms is that at high pressures (>5000 GPa), optical windows (i.e., quartz and LiF) would become opaque because of x-ray preheat or radiative shock fronts. As a result, at such extreme pressures, the VISAR diagnostic would no longer be useful in performing EOS measurements. In addition, VISAR EOS measurements at the NIF and OMEGA are not absolute since they rely on a standard reference. Therefore, a new experimental platform is required to perform high-pressure absolute Hugoniot measurements.

Radiography experiments have been conducted to measure the shock density and shock velocity at high pressure. The purpose of these experiments was to radiograph a shock front in a low-Z sample (CH) as shown in Fig. 136.87. The radiographs were used to determine the shock velocity and the shock density of the compressed materials. ABSEOS-13A-EP was successful in demonstrating the platform. We were able to determine the EOS of the CH sample. Measurements are in agreement with previous experiments performed by M. A. Barrios using VISAR as shown in Fig. 136.88. The platform design was improved for a second campaign, ABSEOS-13B-EP, to reduce high background levels in the emission and to resolve parallax issues. Both issues were resolved in ABSEOS-13B-EP, producing better-quality data. Future platform development would be to conduct experiments on OMEGA using halfraum drives since the OMEGA EP experiments use direct drive.

VISAR Measurements of the EOS of Boron Carbide
Principal Investigator: D. E. Fratanduono

The ICF campaign has begun to investigate alternate ablators (i.e., diamond, B_4C, and SiC). As a result, a campaign to measure the Hugoniot of B_4C was conducted. Previous Hugoniot measurements of B_4C were limited to ~200 GPa because of the limiting pressure range using a two-stage gas

$$U_s = \frac{X_D}{t}$$

$$\rho = \rho_0 \frac{X_D}{x_p - x_{U_p}}$$

U1628JR
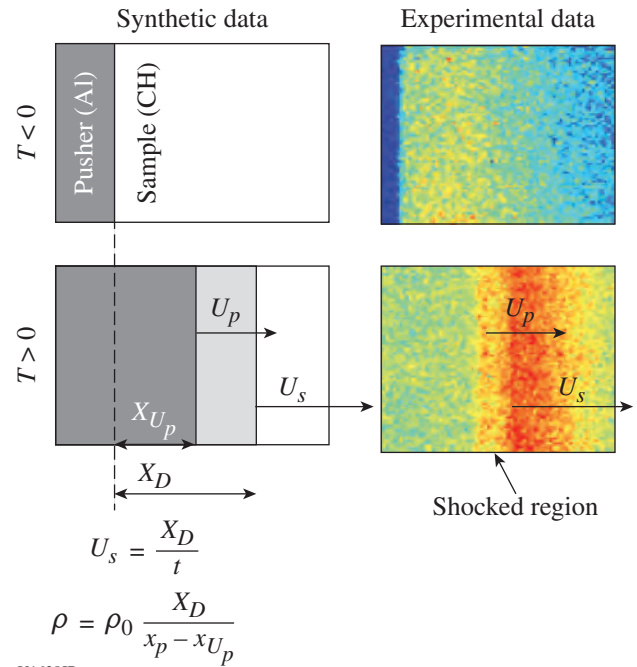
Figure 136.87
Synthetic and experimental data illustrating the radiography technique to perform Hugoniot experiments.

U1629JR
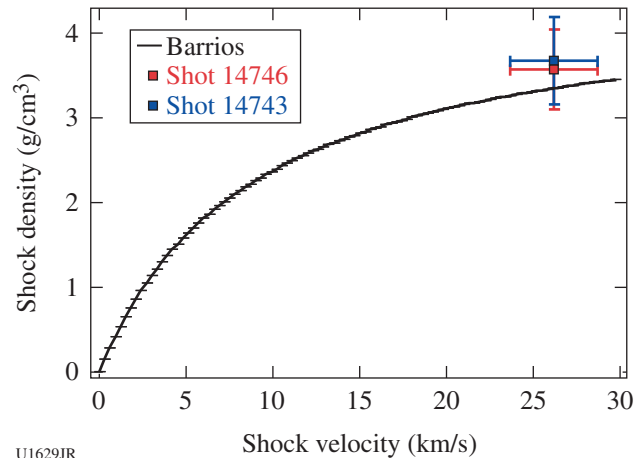
Figure 136.88
Comparison of radiography measurements with experimental fit to CH data from the thesis of M. A. Barrios.

gun. Experiments were conducted on OMEGA to extend the pressure range to 800 GPa; 12 experiments measured the Hugoniot from ~250 GPa to ~800 GPa. Experimental data are shown in Fig. 136.89. Measurements are consistent with lower-pressure data. A slight disagreement with LEOS table
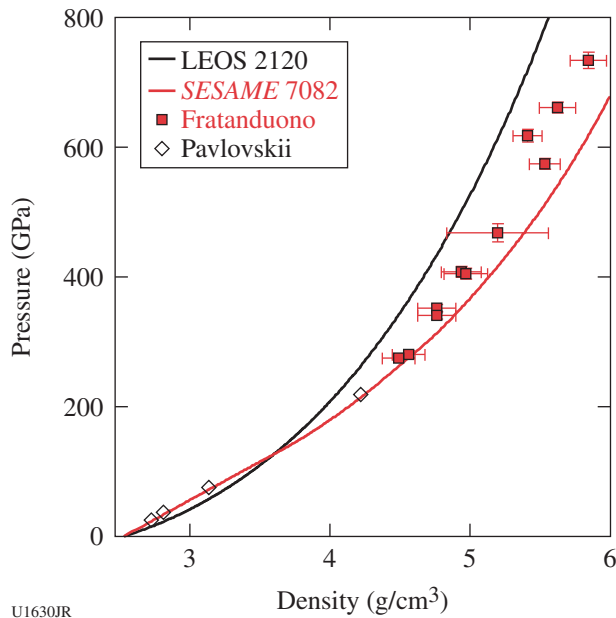
Figure 136.89

B_4C Hugoniot measurements (red squares) from the B4C-EOS-13A campaign. Measurements are compared with low-pressure Pavlovskii data, LEOS table 2120, and *SESAME* table 7082.

2120 and *SESAME* table 7082 is observed. These data will be used to generate a new EOS model that will assist in hydrocode simulations and future experimental design for ICF.

Shock Release Isentrope Measurements of ICF-Relevant Materials
Principal Investigator: D. E. Fratanduono

The goal of this campaign was to demonstrate the feasibility of previous experimental designs using thin silicon-nitride films (150 nm) with a low-density methane gas (0.6 mg/cm^3) present on both sides of the film simulating the D_2 vapor that would be present on a NIF capsule experiment. Previously, the thin films acted as a boundary between methane and vacuum. The concern was that the methane gas behind the silicon nitride would become opaque to the VISAR when the shock passed through the silicon-nitride film. Experimental results indicated that the methane gas is transparent to the VISAR probe and the silicon-nitride velocity was observed. Results also indicated that the presence of gas on both sides of the film helped to tamp the nitride and prevent it from breaking during the experiment. Results continue to indicate that the LEOS tables overpredict the velocity of the release isentropes (see Fig. 136.90).
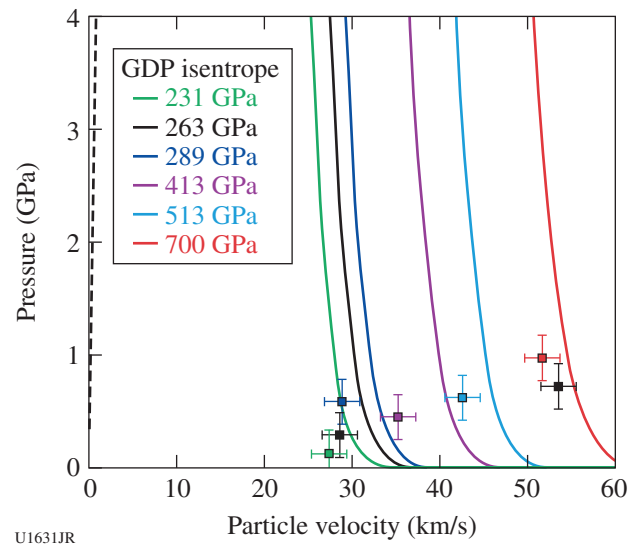
Figure 136.90

Experimental measurements are shown as squares and are color coded with release isentropes from the LEOS table for CH. Measurements indicate that the LEOS models overpredict the release velocity.

Thomson-Scattering Measurements from Au Spheres
Principal Investigator: J. S. Ross
Co-investigators: E. L. Dewald and M. D. Rosen (LLNL); and D. H. Froula (LLE)

During the AuSphere-13A campaign we performed high-Z sphere experiments illuminated in direct-drive geometry to investigate atomic physics models and radiative properties of the laser-spot plasma relevant to ICF indirect-drive–ignition hohlraum plasmas. Using SG4 laser phase plates, 1-mm Au spheres were uniformly irradiated with 3 to 30 kJ of laser energy at intensities of 0.1, 0.5, and 1×10^{15} W/cm^2, similar to the intensities found in National Ignition Campaign (NIC) hohlraums. The 4ω Thomson-scattering probe beam was aligned at various radial locations ranging from 100 to 300 μm from the target surface and used to characterize the low-density plasma blowoff. All of the laser beams used a 1-ns square laser pulse. An example of the Thomson-scattering ion feature data is shown in Fig. 136.91, taken 200 μm from the target surface.

The electron temperature and density, the plasma-flow velocity, and the average ionization state were measured by fitting the theoretical Thomson-scattering form factor to the observed data. The measured data were then compared to post-shot simulations with different atomic physic and elec-
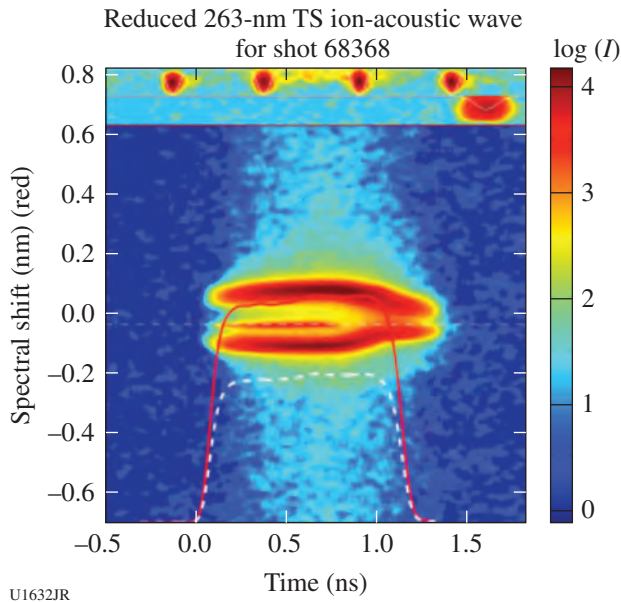
Figure 136.91
Thomson-scattering (TS) data from 200 μm off the surface of the Au sphere irradiated at an intensity of 5×10^{14} W/cm^2.

tron transport models. The different models predict different electron temperatures for the experimental conditions (see Fig. 136.92).

The simulation with the detailed-configuration accounting (DCA) nonlocal model most closely reproduces the tempera-

tures measured during the experiment. The LLNL atomic physics model XSN with a flux-limited transport model using a flux limiter of 0.05, previously used to simulate high-Z hohlraums, predicts an electron temperature significantly higher than measured. Additional measurements at different radial locations and different intensities appear most consistent with an intermediate model with a temperature between that predicted by the XSN and DCA models. Further data analysis is underway to compare Thomson-scattering data, Dante absolute x-ray flux measurements, and x-ray spectroscopy to simulations in our effort to validate atomic physics models employed in simulations.

Measuring the Adiabatic Index of Polystyrene Using Counter-Propagating Shocks and X-Ray Thomson Scattering

Principal Investigator: A. Pak
Co-investigators: T. Ma, L. Fletcher, T. Döppner, S. H. Glenzer, and O. L. Landen

Understanding the EOS and opacity of polystyrene—a material similar to the NIF ablator—at densities of a few g/cm^3 and temperatures of several eV is of interest since it can inform the design and performance of current implosion experiments. In the CH-HeatCap campaign on OMEGA EP, the electron density, temperature, and charge state of shocked polystyrene (CH) were directly measured with x-ray Thomson scattering (XRTS). The goal of these campaigns was to test the hypothesis
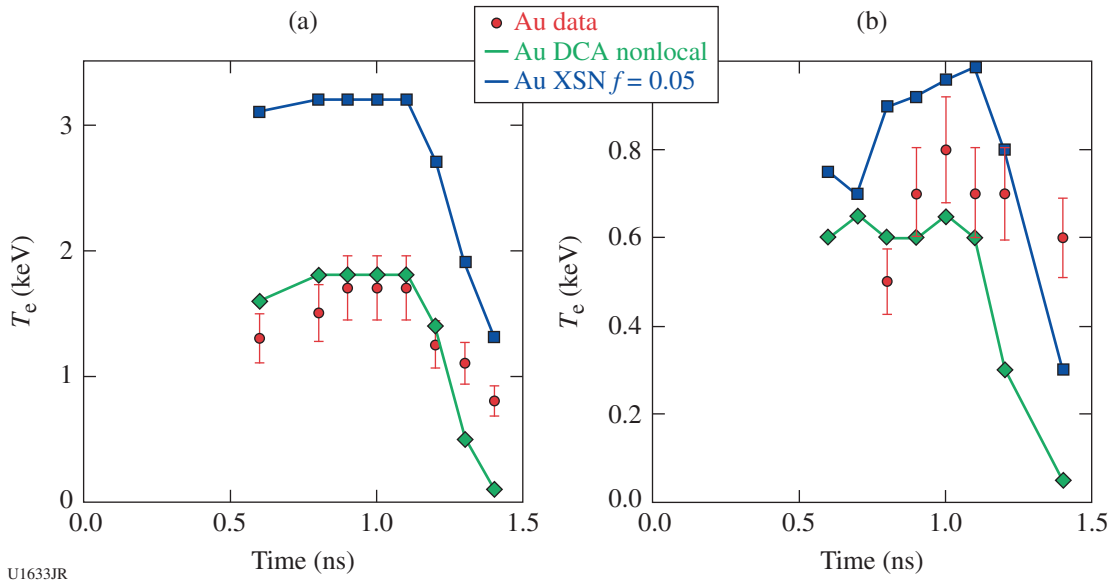
Figure 136.92
The measured electron temperature (red dots) compared to post-shot simulations using the detailed-configuration accounting (DCA) nonlocal model (green line) and the XSN flux-limited model (blue line) for intensities of (a) 5×10^{14} W/cm^2 and (b) 1×10^{14} W/cm^2 at a radial location of 200 μm.

that the continuum lowering effect would increase the charge state of CH as the compression of the material was increased. Understanding in detail the charge state of CH could improve opacity models that are used to calculate the ablation dynamics of NIF implosions.

In the experimental setup [Fig. 136.93(a)], Beams 2 and 3 were used to drive a shock in the CH sample. The strength of the shock, and therefore the expected post-shock density, was varied from shot to shot by using three different drive intensities of 5×10^{12}, 1.5×10^{13}, and 2×10^{14} W/cm^2. The shocked state was probed using the zinc He$_\alpha$ line at an energy of 9 keV. This line was produced by irradiating a zinc foil placed 1.6 mm away from the CH sample with Beams 1 and 4 at an intensity of ~1×10^{15} W/cm^2. X rays that were scattered at an angle of 154° with respect to the incident angle were collected by a curved highly oriented pyrolytic graphite (HOPG) crystal placed in the ZSPEC spectrometer. The HOPG crystal spectrally dispersed the transversely focused scattered signal onto a framing camera detector that has a integration time of 250 to 300 ps.

Figure 136.93(b) compares the measured spectral intensity for three different shots: undriven, driven at $I = 5 \times 10^{12}$ W/cm^2, and driven at $I = 2 \times 10^{14}$ W/cm^2. Detailed fits of the scattered spectrum using the current description of the bound-free scattering component have been unable to accurately model the data. A revised code that incorporates a more-accurate model of the bound-free spectrum has been developed and will be applied to this data in the future. Qualitatively, the increase in charge state as the density of the shock state is increased is believed to have been

observed. This is shown in Fig. 136.93(c), where the inelastic components of the three spectra have been overlaid. As the drive intensity is increased, the spectral width of the inelastic feature is observed to increase on the higher-energy side, while decreasing on the lower-energy side. It is believed that the decrease in spectral width on the low-energy side is due to the decreased L-shell contribution in the bound-free spectra, while the broadening on the high-energy side is due to an increase in the electron density.

The initial results of the heat capacity campaign appear of sufficient quality to determine if continuum lowering is occurring and how the final charge state, density, and temperature vary with the magnitude of the drive intensity.

Angularly Resolved X-Ray Thomson-Scattering Measurements of Shock-Compressed Aluminum

Principal Investigator: L. Fletcher (University of California, Berkeley)
Co-investigators: T. Ma, A. Pak, H. J. Lee, T. Döppner, C. Fortmann, O. L. Landen, and S. H. Glenzer (LLNL); and R. Falcone (University of California, Berkeley)

We have directly demonstrated the ability to measure the ion–ion correlation peak using simultaneous angularly, temporally, and spectrally resolved x-ray scattering measurements in laser-driven shock-compressed aluminum. Molybdenum He$_\alpha$ (17.9-keV) x rays have been used to probe Al foils that are compressed using both single and double (counter-propagating) shocks in a forward, small-angle scattering platform with very high angular precision (Fig. 136.94).
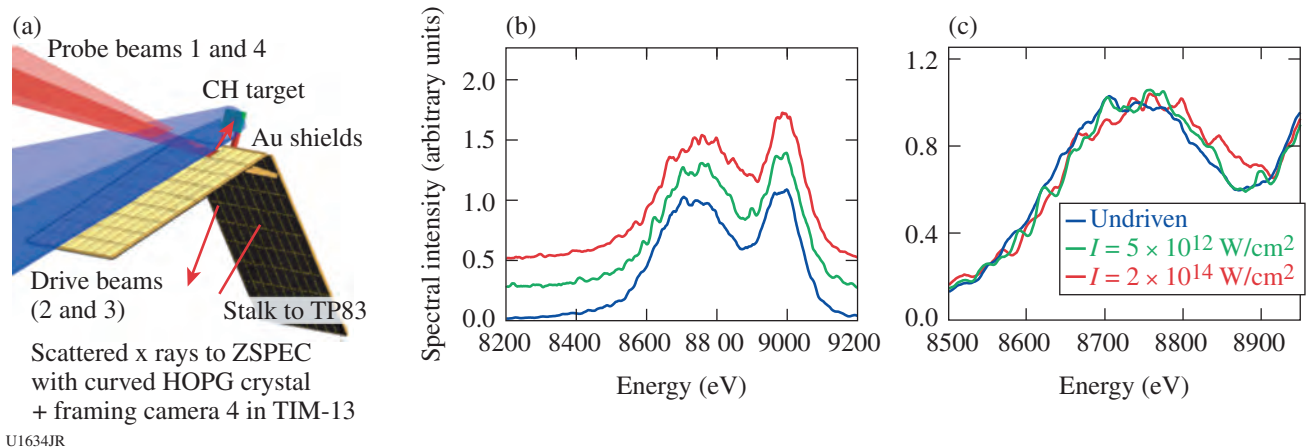

Figure 136.93
(a) Experimental setup. (b) Scattered spectrum observed at three different drive conditions. Here the signals have been normalized and offset from each other. (c) Overlay of the normalized inelastic scattered feature where the decrease in the width on the low-energy side as the drive intensity is increased may be an indication of continuum lowering.
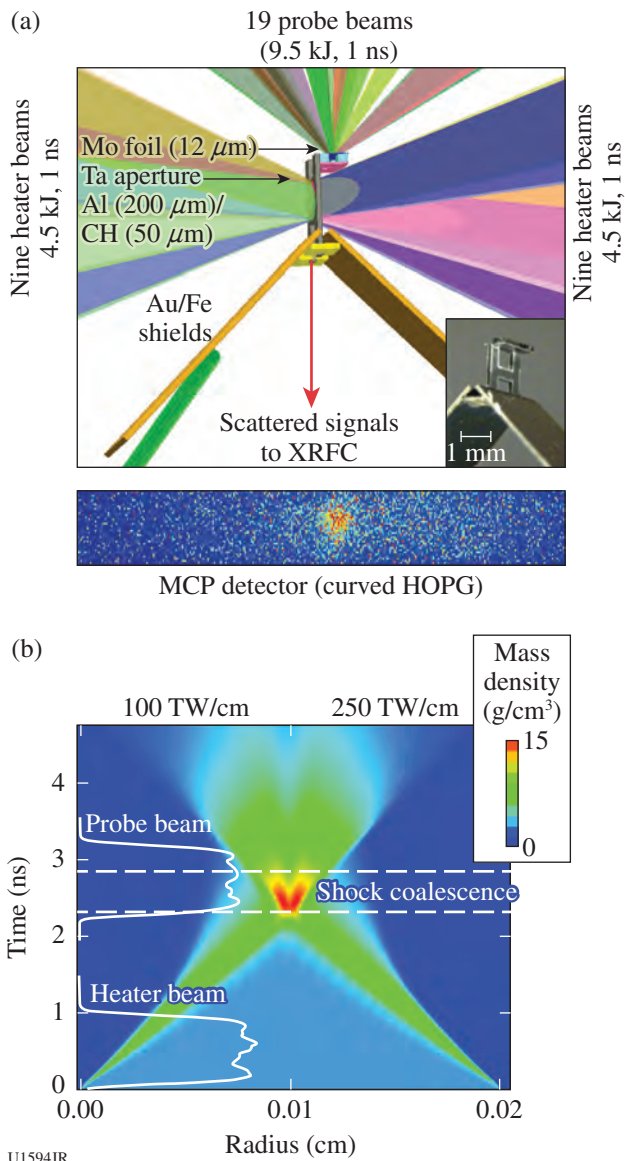
Figure 136.94
The experimental setup for HiZShk-13A: (a) 200-μm-thick Al target (double-shock configuration) and beam configuration, along with a photo of the Al scattering target, and gated x-ray framing-camera–multichannel plate (XRFC–MCP) detector data; (b) 2-D Helios simulation of the mass density as a function of Al foil radius, and input pulse shape dimensions (TW and time duration).

a well-pronounced peak in the static structure factor at wave numbers of $k = 3.5$ Å^{-1} and 4.5 Å^{-1}, corresponding to higher-compression material states.

The magnitude of this correlation peak is in good agreement with calculations that use a potential with strong short-range
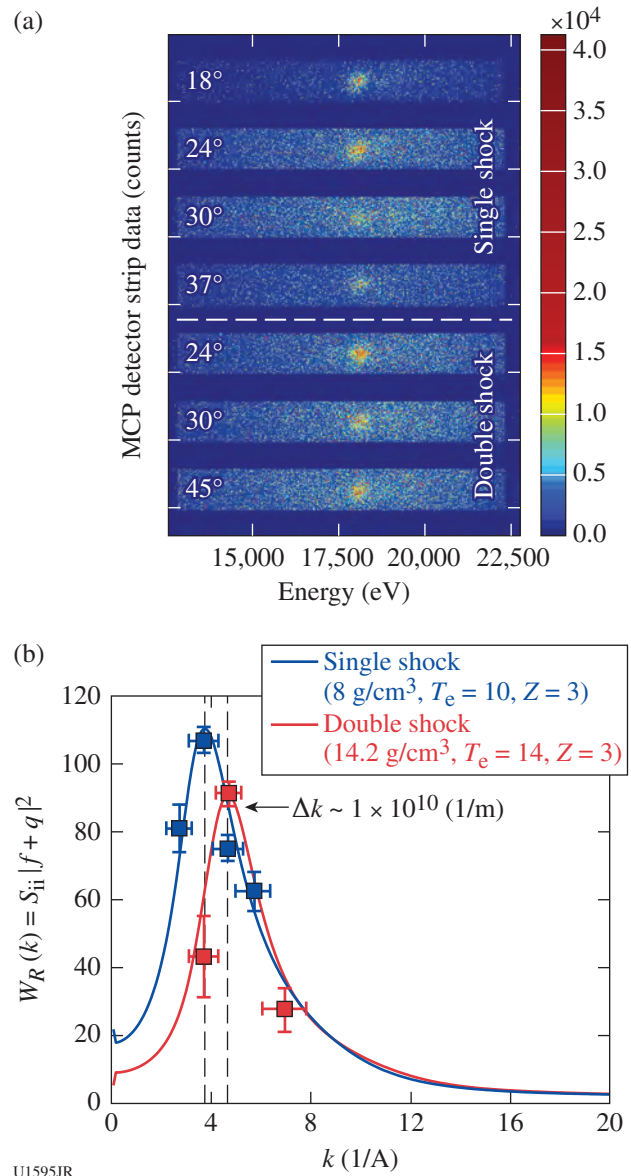
Figure 136.95
(a) Raw data of scattered spectrally resolved x-ray Thomson-scattering (XRTS) signals for single- and double-shock configurations. (b) Preliminary data analysis shows the total integrated signal (corrected for experimental geometry) of the scattering data as a function of k follows the trends predicted by the split-ring resonator (SRR) models using the frequency-integrated, quasi-elastic contribution to the dynamic structure factor of single-shocked ($\rho = 8$ g/cm^3) and double-shocked ($\rho = 14$ g/cm^3) aluminum.

In our study, 125-μm-thick and 200-μm-thick Al targets were compressed 3× and 6× the solid density using 1-ns pulses with a total laser energy of 4.5 kJ and 9 kJ, respectively. A total drive intensity of 3×10^{14} W/cm^2 on each irradiated aluminum surface was used to drive shocks into the sample, while 7×10^{14} W/cm^2, incident on a thin Mo foil, was used to generate Mo He$_\alpha$ x rays at 17.9 keV, in order to probe the compressed targets. Figure 136.95(b) demonstrates a shift in

repulsion (SRR). The results will show that the elastic x-ray scattering amplitude, angularly resolved, shifts to a higher wave number of approximately $\Delta k = 1 \times 10^{-10}$ m^{-1} with increasing density. This presents a new scattering diagnostic to fully characterize states of matter at densities and temperatures that have not been previously accessible.

Enhanced Bremsstrahlung Backlighters
Principal Investigator: R. Tommasini

The motivation of the UV–CR-BL-13A campaign was to test and characterize enhanced broadband x-ray sources emitting around and above 75 keV, to be used in the Compton radiography of ICF targets on the NIF. In FY09 we characterized Au microwire backlighters irradiated by 10-ps-long OMEGA EP pulses. In FY10 we characterized Au microwire backlighters irradiated by 100-ps-long OMEGA EP pulses (1ω) and OMEGA pulses (3ω), with the primary goal of measuring the effect of a longer-pulse–generated backlighter with respect to the source size. In FY13 we characterized Au microwire backlighters irradiated by 1-ns OMEGA pulses (3ω) and compared the performance of wires with and without CH wedges (see Fig. 136.96).

(a)

(b)
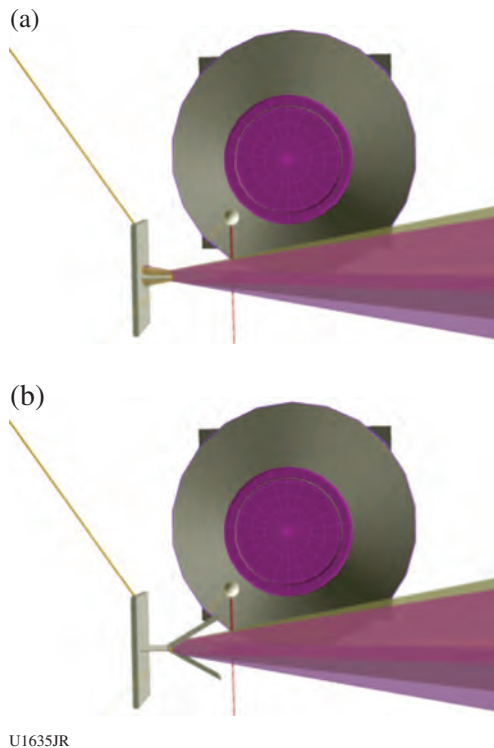
U1635JR

Figure 136.96
Backlighter geometry used for the experiments: (a) bare Au wire; (b) Au wire inside a CH wedge.

The 30-μm Au microwires were arranged in a point-projection end-on geometry and were ~500 μm long. They were mounted on a CH slab, and, in about half of the performed shots, they were sitting inside a CH wedge with a 30° half-angle. The bremsstrahlung radiation was generated by irradiating the Au wires with 1-ns square pulses. The energy on target was changed between 500 J and 2500 J by changing the number of incident beams from one to five. Solid W spheres with diameters of 200 μm located at a distance of 10 mm from the backlighters were used as radiography samples.

A Compton radiography snout (CRS) was used to record the radiographs and measure the time-integrated backlighter spectra. A combination of high- and low-Z filters inside the snout restricted the backlit photon energies to about and above 75 keV. A Fuji BAS imaging plate was used as a detector 400 mm from the backlighter. The neutron temporal diagnostic (NTD) recorded the time-resolved emission from the backlighter. The data show an increase in the peak of the time-resolved backlighter signal by ~4× and in the total time-integrated signal by ~2× when using wire in the CH wedge. These values are very close to those predicted by simulations. The analysis of the radiographs of the W sphere allowed us to reconstruct the source size of the backlights. We measured ~30 μm for the Au wire in the CH wedge versus ~45 μm for the bare Au wire, which we ascribe to plasma confinement generated by the CH wedge.

Hohlraum Drive Spectroscopy
Principal Investigator: G. V. Brown and M. Schneider
Co-investigators: K. Widmann, R. Heeter, and J. Emig

The objective of the DriveSpec-13A campaign was three-fold: (1) to assess what is necessary to field on the NIF a fully calibrated, high-resolution crystal spectrometer whose spectra can be used to refine data from the Dante diode array drive diagnostic; (2) to assess the atomic physics taking place in a hohlraum's non-LTE (local thermodynamic equilibrium) drive radiation field; and (3) to use the high-resolution spectra to aid in the deconvolution of the Dante spectra.

To provide benchmark high-resolution spectra for models of the drive radiation for ICF, three target types were fielded. The first was a 2.25-mm-long, 1.2-mm-diam, 100%-open laser entrance holes (LEH's), 25-μm-wall gold hohlraum; the second was a gold hohlraum of the same dimensions but with interior surfaces coated with 4 to 11 μm of uranium; and the third was a gold halfraum with a single 0.8-mm, 100%-open LEH, a length of 0.75 mm, and closed on the side opposite the

LEH. Eight of the 1.2-mm LEH gold targets, one 1.2-mm LEH uranium target, and two 0.8-mm LEH gold targets were shot.

Radiation from each shot was detected with several spectrometers. The main diagnostics were three high-resolution "MSpec" elliptical spectrometers, each covering a continuous bandwidth form of ~1.7 to 3 keV. Two of the Mspecs recorded time-integrated spectra using an image plate and were on nearly the same sightline at the Dante temperature diagnostic: one at 42° relative to the LEH on the H10 side of the hohlraum, i.e., on the opposite side as Dante, and one at 37° on the H11 side of the hohlraum, i.e., on the opposite side of Dante. A third MSpec recorded time-resolved spectra. A variable line spaced grating spectrometer (VSG) covering the ~0.2 to 1.5 keV band was also used to record time-resolved spectra.

Spectra from this campaign have already provided new insight as to the deconvolution of the Dante spectra, especially regarding the distribution of the M-band emission from highly charged gold ions. High-resolution spectra of the gold M-band emission is also being compared to models used to predict the drive radiation field in NIF ICF hohlraums. Calibration measurements of the full instrument response, including filter x-ray transmission efficiencies and Bragg crystal reflectivities, have been completed. These results demonstrate technical readiness to field a fully calibrated drive spectrometer on the central channel of the NIF Dante.

Ablator Opacity Measurements
Principal Investigator: R. Heeter
Co-investigators: A. Graf, G. V. Brown, C. Mauche,
R. E. Marrs, and B. Wilson

In a follow-up to earlier ablator opacity measurements, improved experiments were performed to measure the transmission opacity of hot Si-doped glow-discharge polymer (GDP) (using OMEGA 60) and pure Si (using OMEGA EP) at $T \approx 100$ eV, $\rho \approx 0.1$ g/cm^3. The OMEGA platform used a Be-tamped, Si-doped GDP sample heated indirectly in a hohlraum. The OMEGA EP platform used a CH-tamped, embedded Si dot heated by 100-ps UV impulses. Both platforms used dual-axis backlighting, both face-on and edge-on, simultaneously to obtain density via sample expansion radiography, Si ionization balance data, and GDP and/or Si transmission opacities via absorption spectroscopy. The GDP measurements used a high-Z backlighter to record the transmission spectrum for x rays rang-

ing from 250 to 1600 eV, as well as from 1600 to 3000 eV. The Si measurements span the x-ray band from 1600 to 3000 eV.

Compared to prior measurements using similar opacity platforms on OMEGA, the sample density was increased about fourfold, and the sample uniformity was also improved, particularly for the Si on OMEGA EP by using a thicker tamper on the laser-heated side. In addition, backlighter and spectrometer performances were also improved on both platforms, yielding $2\times$ to $3\times$ improvements in signal-to-noise of absorption and transmission measurements. The resulting data can provide constraints on opacities in conditions approaching those where capsule performance (via the Atwood number) may depend strongly on the Si and C opacities (Fig. 136.97).
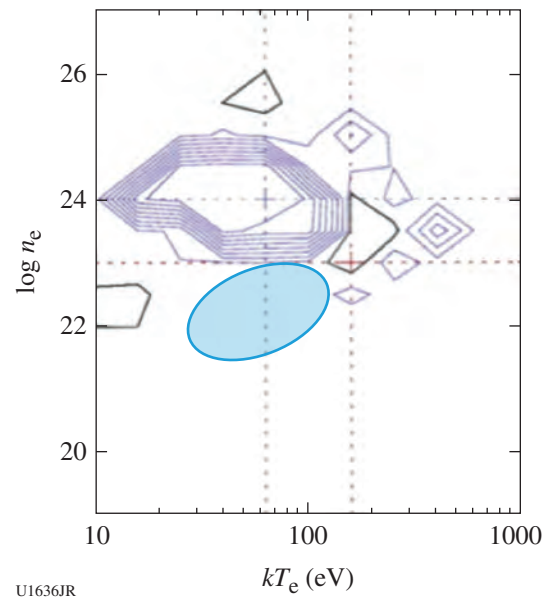

U1636JR

Figure 136.97
Using 1-D ignition capsule simulations, and varying the assumed opacity of the Si dopant in localized regions of density/temperature space by 30%, it was found that the Atwood number varies by up to 37%. The sensitivity is localized for near-solid density plasmas at temperatures from 30 to 100 eV. The Atwood number is also sensitive to the opacity of carbon, although the specific processes and region in parameter space are different.

The Si measurements illustrated in Fig. 136.98 can be brought into agreement with simulations for the $n = 1$ to $n = 2$ absorption features, but they require a wider charge-state distribution than expected in LTE, suggesting non-LTE physics or sample nonuniformities. Data for the higher-n transitions
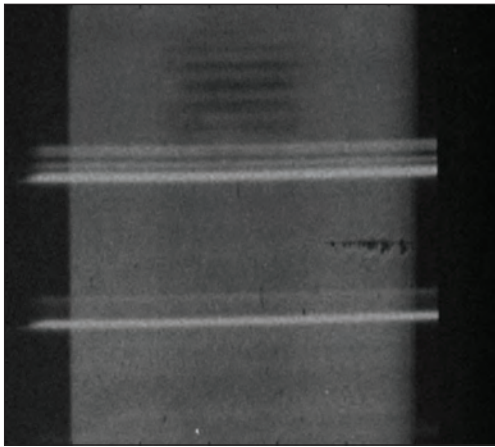
U1637JR

Figure 136.98
X-ray absorption spectrum of silicon from ~1.7 to ~2.1 keV, from a plasma at $T \approx 70$ eV, $\rho \approx 0.2$ g/cm^3. Photon energy runs from top to bottom; the horizontal direction includes regions of background, sample self-emission, backlighter-only and backlit sample transmission spectra. Absorption features including $n = 1$ to $n = 2$ transitions, higher-n features, and continuum absorption appear as a dark band running down the center of the image from top to bottom. The absorption features from multiple L-shell ion stages of Si (Be, B, C-like…) are seen as dark horizontal bands in the top center. Emission features from H-like and He-like ions of the hotter, denser Si produced prior to the short-pulse absorption measurement are also observed (horizontal white features).

are not in especially good agreement with the opacity models. Additional Si measurements are planned for FY14.

Hohlraum Wall-Plasma Emissivity Measurements
Principal Investigator: R. Heeter
Co-investigators: A. Graf, G. V. Brown, M. E. Foord, C. Mauche, R. E. Marrs, J. S. Ross, and B. Wilson

Motivated by discrepancies observed in NIF hohlraum experiments, new benchmark data for the x-ray emissivity of hot gold plasmas were sought. Of particular interest were the inferred "drive deficits" on ignition capsule implosions and observed differences in drive spectra and x-ray emission images on ViewFactor shots. The NIF data indicate a substantially different distribution of mass and temperature in the ablated gold "wall plasma" than predicted by simulations. One concern that arises is that the complex modeling of the gold itself may need better validation. This requires precision spectroscopy of uniform, near-steady-state plasmas at the relevant conditions. Prior benchmark data[47] were obtained at $n_e = 10^{21}$/cm^3, but on the NIF the gas- and capsule-plasma filling holds back the expanding gold plasma ablated off the walls, such that the

density of interest is an order of magnitude greater. In addition, alternate NIF ICF hohlraum designs incorporate a mid-Z coating (Ni or Cu) to suppress the Au M-band emission, so measurements of Ni or Cu are timely as well.

In the experiment fielded late in Q4 FY13, Be-tamped samples of Au, Ni, or co-mixed Au:Ni were directly heated for 3 ns using a train of OMEGA beams. To obtain the sample density and temperature, a combination of expansion imaging, Ni K-shell spectroscopy, and 4ω Thomson-scattering diagnostics were applied. A sample of the Thomson data is shown in Fig. 136.99. Using thicker tampers and lower laser drive, and

U1638JR
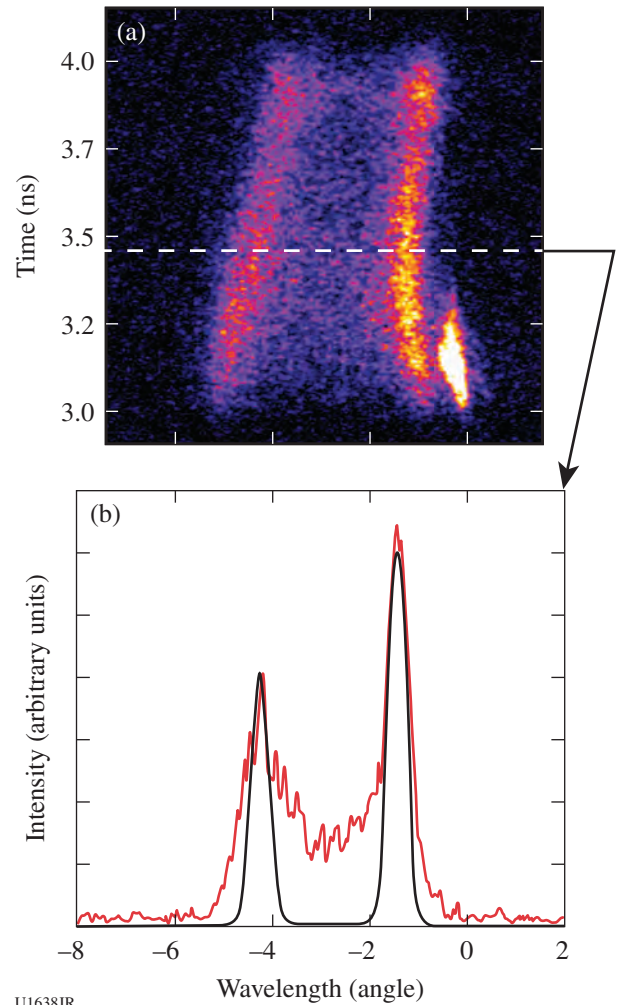
Figure 136.99
Ion feature data from fourth-harmonic Thomson-scattering diagnostic, with fit by J. S. Ross for nickel plasma at $T_e = 850$ eV.

imaging the sample expansion with 15- to 20-μm resolution, plasmas with $n_e > 2 \times 10^{22}$/cm^3 were studied. Samples at two temperatures were produced by varying the laser intensity on different shots. Benchmark-quality, absolute- and relatively calibrated sample emission spectra were obtained from 250 to 3000 eV using gated, space-resolved grating and crystal spectrometers and the Dante multichannel filtered diode array.

D–D and D–^{3}He Yield Anomalies Versus D:^{3}He Fuel Ratio in Indirect-Drive Exploding Pushers
Principal Investigator: H. Rinderknecht (MIT)
Co-investigators: C. K. Li (MIT) and P. A. Amendt (LLNL)

Anomalous nuclear yield reduction as a function of D:^{3}He fuel ratio was observed in a study of D^{3}He-filled indirect-drive implosions performed on 7 May 2013 using the OMEGA laser. Previous experiments in directly driven implosions of CH capsules demonstrated anomalous reduction of the compression yield in D^{3}He mixtures, relative to implosions filled with hydroequivalent fills of D$_2$ (Ref. 48). A similar yield anomaly has also been observed in shock yield from directly driven thin glass targets.[49] This study was designed to investigate whether these yield trends were also observed in indirectly driven SiO$_2$ shells filled with D^{3}He mixtures.

Targets were 600-μm-diam SiO$_2$ shells with 24.4-μm-thick walls, fielded inside 2-mm-long vacuum hohlraums with a 1.6-mm outer diameter (OD) and a 50% LEH. These targets were filled with mixtures of D$_2$ and ^{3}He with an initial mass density of 4.6 mg/cm^3, with a deuterium ion fraction of 0.2, 0.5, 0.8, and 1. Resulting compression yields demonstrated a trend of reduction in the DD-neutron and D^{3}He-proton yield-over-clean (YOC) as the deuterium ion fraction was decreased from pure D$_2$ fill (see Fig. 136.100) [simulations were performed by P. A. Amendt (LLNL)]. The observed trend is comparable with direct-drive studies between the deuterium fractions of 0.5 and 1; however, unlike previous studies, the observed yield continues to decrease relative to hydro-equivalent D$_2$ as the deuterium fraction drops below 0.5. A similar trend is also observed in D^{3}He proton yields for targets with initial gas fill between the deuterium fractions of 0.2 and 0.8 (see Fig. 136.101). Implosions of targets with 50:50 mixtures of D^{3}He and mass density of 2.9 and 1.5 mg/cm^3 demonstrated a reduction in the observed DD-neutron YOC as pressure was reduced. These results confirm the anomalous reduction of compression yield in indirect-drive implosions of D^{3}He fuel mixtures, supporting the hypothesis that multiple-ion plasma effects are significantly perturbing the evolution of indirect-drive implosions.
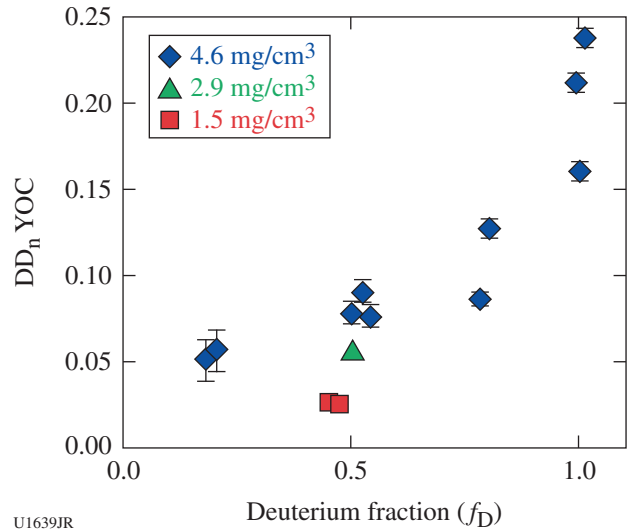
Figure 136.100
DD-neutron YOC versus deuterium fraction in indirect-drive hydro-equivalent D^{3}He fuel mixtures. Initial mass density is given for each set of implosions.
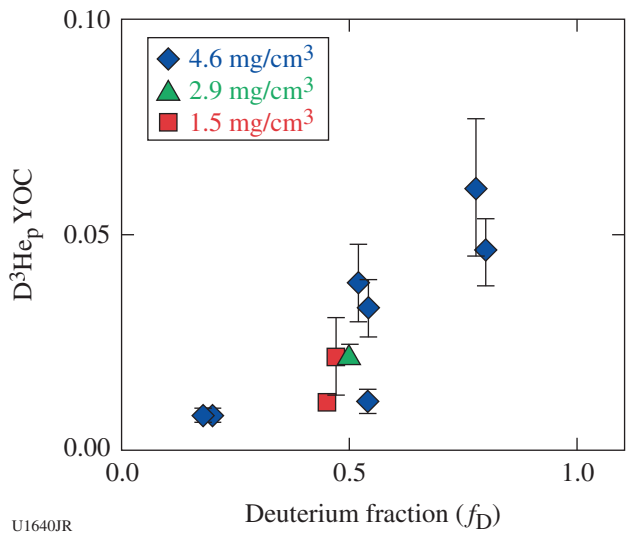

Figure 136.101
D^{3}He-proton YOC versus deuterium fraction in indirect-drive hydro-equivalent D^{3}He fuel mixtures.
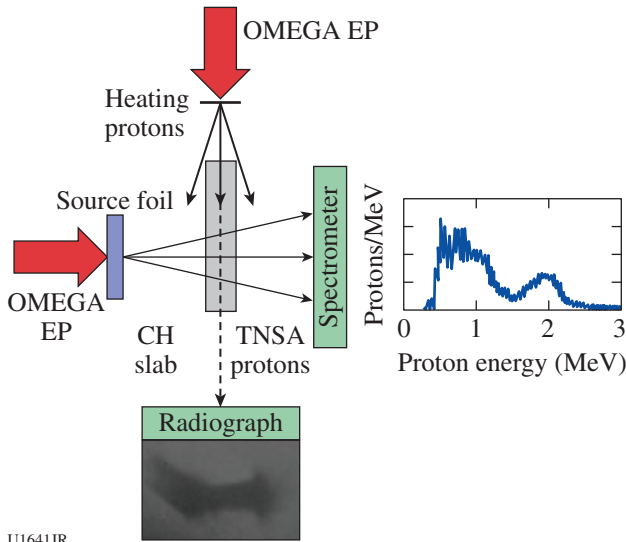
Platform Development for Measuring Charged-Particle Stopping in Warm Dense Plasmas
Principal Investigator: A. Zylstra (MIT)
Co-investigator: J. R. Rygg (LLNL)

Charged-particle stopping power is a critical transport process for ignition and burn, and calculating DT-α stopping in relevant plasma conditions depends on untested theories. To address the need to validate these theories, a platform is being developed on OMEGA EP to measure charged-particle energy

loss. The experimental schematic is shown in Fig. 136.102, where the two short-pulse beams are used to generate energetic protons via the target normal sheath acceleration (TNSA) mechanism that heats and then probes a sample plasma. The FY13 experiments characterized the heating and probing protons separately via x-ray radiography and charged-particle spectroscopy (shown in Fig. 136.102). Future experiments will combine these techniques to measure the stopping power.

Figure 136.102
Experimental schematic. One OMEGA EP short-pulse laser beam is used to heat a sample via proton isochoric heating; the second beam creates probing protons. The FY13 campaign characterized the isochoric heating with x-ray radiography (bottom) and studied proton source candidates for the stopping experiment (right).

High-Energy-Density Experiments
1. Material Dynamics and Strength

Tantalum Rayleigh–Taylor Experiments
Principal Investigator: C. Plechaty

The focus of the ICETaRT campaign was to study Ta material strength at high pressure (>1 Mbar) and high strain rates (10^6 to 10^8 s^{-1}). To achieve these conditions in an experiment while keeping the temperature of the Ta sample well below melting, a reservoir and vacuum gap[50] configuration was employed to produce a quasi-isentropic pressure drive (Fig. 136.103). In the experiment, the plasma drive was produced by using 40 OMEGA beams to deposit 20 kJ of laser energy into a hohlraum. The x rays produced in this process interact with the reservoir to produce a plasma. The plasma then crosses the gap and stagnates onto the physics package.
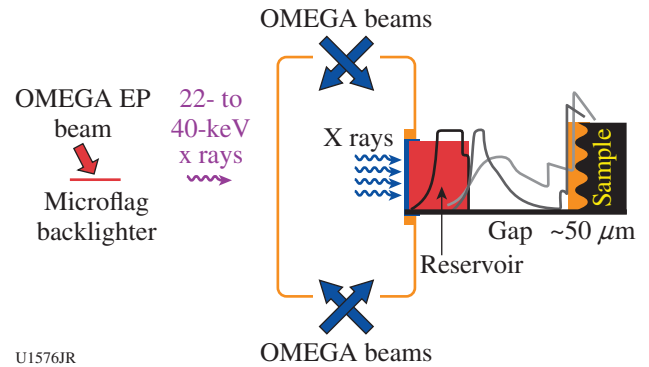
Figure 136.103
Experimental configuration employed for OMEGA EP joint shots. OMEGA beams deposited energy into the hohlraum, producing a plasma drive. Face-on, high-energy radiography was employed on the rippled Ta sample by using a short-pulse OMEGA EP beam to ablate an Ag backlighter. For OMEGA shots, the rippled Ta sample was replaced by a VISAR witness sample to characterize the plasma drive.

The physics package employed for these experiments consisted of a Ta sample, coated with a polyethylene (CH) heat shield (to protect the Ta sample from the hot plasma). Imposed on the surface of the Ta were sinusoidal perturbations with a 50-μm wavelength and an amplitude of 1.7 μm or 2.0 μm. In the experiment, as the plasma from the reservoir crosses the gap and stagnates on the sample package, the Ta ripples undergo an effective acceleration from the stagnating plasma drive. This acceleration actuates Rayleigh–Taylor (RT) growth of the pre-imposed sinusoidal pattern. Since the Ta material strength acts to suppress the amount of RT growth, measuring the RT ripple amplitude gives a measure of the material strength.[50–52] To measure the perturbation amplitude, face-on, high-energy x-ray radiography (22-keV Ag K$_\alpha$) was employed using the OMEGA EP short-pulse beam. The OMEGA EP beam was required in order to employ a high-energy backlighter (22 keV) to probe the high-Z tantalum material. To characterize the plasma drive, separate shots were taken using VISAR, where the physics package was replaced with a witness package.

The FY13 ICETaRT campaign (ICETaRT-13A) focused on studying the effect of crystal orientation on the material strength. In the multiscale model,[53] crystal orientation can affect material strength via a parameter known as the "Taylor factor." To understand the effect of crystal orientation on the material strength, we placed [100] and [111] oriented samples side by side and compared the ripple growth between these samples for the same shot and under the same drive conditions. Initial results from these shots suggest that the difference in the growth factor between these two crystal orientations is

too small to be measured within our error bars of ~25%. The implications of this are currently under investigation.

Iron Rayleigh–Taylor Experiments
Principal Investigator: C. Huntington

The solid–solid phase transition between the bcc (α) and hcp (ε) lattice structures in iron is known to occur as the material is compressed. When kept below its melting point, an effective increase in the macroscopic strength of the material accompanies this phase transition. Understanding the material strength of iron throughout the deformation process presents a significant computational challenge, but it is important for improving models of planetary structure, including interpretation of seismic measurements taken through Earth's core.

The IronRT OMEGA campaign used an indirect-drive platform to produce pressures of ~1 Mbar on a thin Fe disk with a sinusoidal ripple pattern machined on its face. These ripples seed the growth of the Rayleigh–Taylor (RT) instability, the magnitude of which is suppressed by the material strength of the sample. The amplitude of the ripples was diagnosed with high-energy x-ray radiography, using Ag micro-flags as the x-ray source (see Fig. 136.104). In addition to radiography, the VISAR diagnostic was essential to characterizing the drive profile on the iron sample. On this IronRT shot day, five radiography shots measured the Fe growth factors between 1 and 2.
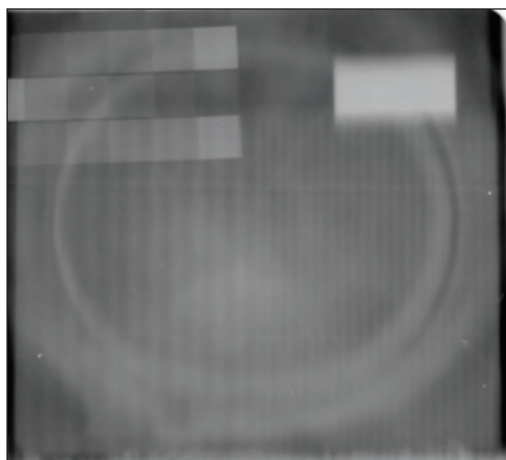
U1642JR

Figure 136.104
Example radiography data from the IronRT-13A campaign. The step features in the upper left allow for calibration of the detected x-ray signal with the material areal density (ρR) traversed by the x rays. The opaque region in the upper right is a gold knife edge for calculating the modulation transfer function (MTF), with the remainder of the sample dedicated to the ripple measurement at two wavelengths (side-by-side 100- and 50-μm wavelengths).

Comparison of these measured iron growth factors to a range of models for material strength in iron is ongoing. More important, the ability to reach ~1 Mbar on OMEGA extends the accessible parameter space for this work, when combined with previous experiments conducted at 0.1- to 0.3-Mbar pressures.[54]

Long-Pulse Silver Backlighter Development
Principal Investigator: C. Huntington

The LPAgBL campaign was a half-day effort to quantify the spatial resolution achievable from a range of micro-flag x-ray source (backlighter) designs. Crucial for experiments in the material strength campaigns on the NIF and OMEGA, the small (300×300-μm) silver foils produce a quasi-1-D x-ray source when heated by the laser and viewed edge on, allowing for radiography of ripple growth in the strength experiments. On this shot day, each of the five designs was irradiated with 18 beams, producing a total on-target intensity of 8×10^{16} W/cm^2 and generating Ag K$_\alpha$ x rays (near ~22-keV photon energy). From knife-edge radiography, the modulation transfer function (MTF) of each backlighter was measured. From this work it was determined that the MTF at a spatial frequency of 100 μm from a 3-μm-thick foil was twice that from a 10-μm-thick foil. The results of this experiment have been incorporated into several recent NIF target designs exploring the material strength of Ta.

Material Recovery Experiment
Principal Investigator: M. May

The FY13 material recovery shots tested a prototype target recovery system that enables us to perform post-shot target analysis of material samples (see Fig. 136.105). A new recovery tube platform was qualified for use on OMEGA for these experiments. Five hohlraum target shots were performed. OMEGA was used to deliver 20 kJ of energy with 40 beams in a 1-ns pulse to heat these targets. Four hohlraum targets were used to drive samples into the recovery tubes. Two of the samples were driven into recovery tubes at a lower pressure (~1 Mbar) and two were driven at a higher pressure (~2 Mbar). One drive characterization target was shot to measure the high-pressure drive using the VISAR. Analysis of the VISAR indicated that this pressure was ~1.8 Mbar. Platinum was used as the driven sample material since it is uncommon in laser-produced plasma experiments and can be easily extracted chemically from the recovery tubes. To catch and hold the driven Pt, the recovery tubes were filled with two layers of increasing-density (50- and 500-mg/cm^3) dicyclopentadiene with a final layer of solid-density CH. The photographs show (a) the pre-shot target mounted to the

recovery tube and (b) the post-shot recovery tube. The post-shot photo shows material residue on the recovery tube and a small gap between the target mount and the recovery tube. Post-shot analysis of the recovered samples indicated that <10% of the Pt from the targets was collected in the recovery tubes. Valuable insight was gained regarding the participating physics and changes needed for future catcher designs involving a hohlraum.
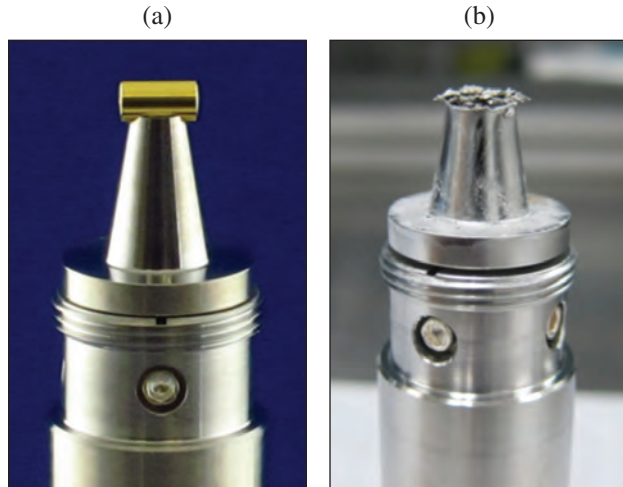
(a)   (b)

Figure 136.105
Photographs of (a) the pre-shot target and recovery tube and (b) the post-shot recovery tube.

Diffraction Studies on Shocked Tantalum
Principal Investigator: C. Wehrenberg

Two distinct diffraction experiments were conducted to study the behavior of shocked tantalum. The first experiment sought to make strength measurements of single-crystal Ta samples that were shock compressed in the low-pressure (<0.6-Mbar) regime. Previous campaigns (FY11, FY12) have explored up-to-2-Mbar shocks in Ta and successfully matched multiscale model predictions; however, ~0.6 Mbar is expected to be a threshold for homogeneous nucleation of dislocations, which should alter the material's behavior. In two half-day campaigns on OMEGA, 12 shots were performed in which an imploding CH capsule driven by 29 beams provided a broadband x-ray source. A single beam drove a thick CH ablator, with the shock wave attenuating as it propagated through the ablator to lower the shock pressure into the desired range. A time series of Laue patterns were recorded in the 0.2- to 0.8-Mbar range. Figure 136.106 shows a series of Laue patterns for a 0.4-Mbar shock pressure. This series shows the strain evolving from uniaxial compression to an ultimate flow stress. These lattice level measurements are directly comparable to multiscale model predictions.
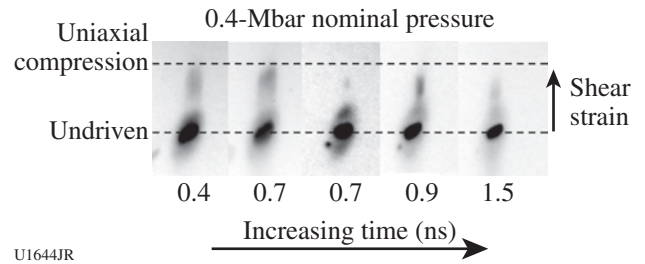
Figure 136.106
A time series of Laue images of single-crystal Ta loaded along the (001) direction by a 0.4-Mbar shock wave. Shear strain is indicated by a shift in the diffraction spot from the undriven position. The time series shows the strain relaxing with time.

In parallel, a second class of experiments developed methods for recording diffraction patterns from polycrystalline samples using high-energy backlighters. In one shot day, a single short-pulse (100-ps) beam drove the Zr backlighter foil. In a second shot day, three UV beams were used to drive a Zr foil backlighter with a 2-ns pulse. A separate UV beam was used to drive a target consisting of a high-density-carbon (HDC) ablator, a Ta foil sample, and a HDC window attached to a heavimet pinhole mounted on the broadband x-ray diffraction (BBXRD) diagnostic. No diffraction lines were recorded with the short-pulse beam because of a very high background. The long-pulse shot day recorded up to seven diffraction lines from the Ta sample, using backlighter laser intensities of 3 to 9 × 10^{15} W/cm^2. Figure 136.107 shows a static shot (no Ta drive
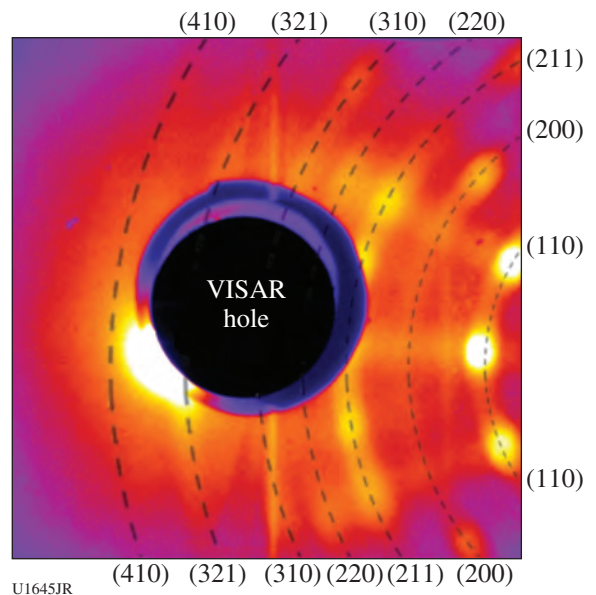

Figure 136.107
Static diffraction image from a Ta foil sample using a Zr backlighter (2-ns pulse) and a 1-mm pinhole.

beam) using a 1-mm pinhole. Additional shots used a 0.5-mm pinhole to achieve greater angular resolution, but with a lower signal-to-noise ratio. These shots represent the first high-quality diffraction data recorded using high-energy, laser-driven x-ray sources. Driven diffraction data were recorded at ~2 Mbar; however, due to difficulties in timing the arrival of the shock wave, the diffraction was taken while the Ta was in the process of releasing to ambient pressure. Despite essentially splitting the signal between two strain states, two driven diffraction lines and four ambient lines were recorded.

Classical Rayleigh–Taylor Experiments
Principal Investigator: H.-S. Park

The classical Rayleigh–Taylor campaign is part of a continuing effort aimed at assessing the strength of various metals (primarily Ta and Fe) at high strain rates. Central to all of these experiments is a planar sample with a pre-imposed sinusoidal ripple on one surface (Fig. 136.108). Under load

generated by the laser drive, the rippled surface is unstable to Rayleigh–Taylor (RT) instability and will grow in time to a perturbation that can be measured using face-on radiography. In the metal samples, strength of the material resists deformation and suppresses RT. To properly characterize the degree of resistance in metals, however, the classical RT platform was developed to measure purely plastic RT evolution (that is, instability growth in the absence of material strength). On this shot day the rippled sample was made of brominated plastic (BrCH), which is able to deform without any resistance from an underlying lattice structure. The VISAR and face-on x-ray radiography were the primary diagnostics, and the laser drive was generated via direct irradiation of a plastic ablator. Good data were collected using both primary diagnostics, and growth factors of ~10 have been calculated for the plastic sample. This experiment provided important "no-strength" data for the materials strength effort, and the remainder of the plastic dispersion curve will be measured in an upcoming FY14 shot day.

U1646JR
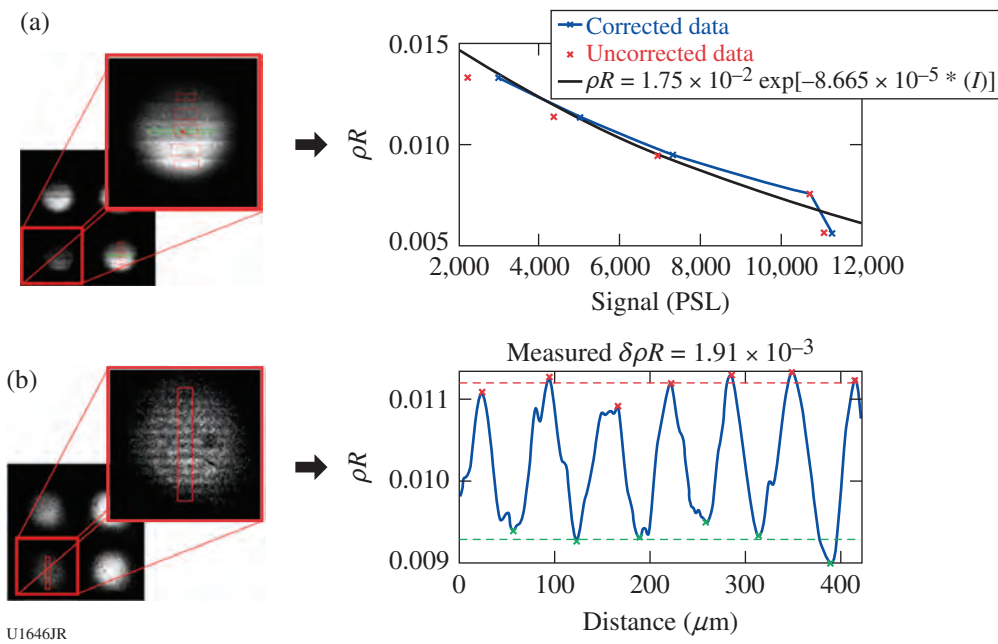
Figure 136.108
Classical RT is an experimental campaign that evaluates the Raylegh–Taylor (RT) strength platform on a material without strength. Our test material for this campaign was brominated plastic (12.5% BrCH). (a) An x-ray framing-camera (XRFC) image of BrCH steps (left panel) for radiometric calibration. The right panel shows the raw data points (red ×'s) and the background corrected data points (blue ×'s). The data are fitted to an exponential function (black line) that converts the raw gray values of the XRFC image into the areal density in g/cm^2. This calibration is used to derive the growth factor from the ripple images. (b) A face-on BrCH ripple growth radiography (left panel) driven by ~1 Mbar ramped pressure at 45 ns after the laser. The initial ripple amplitude was 0.6 μm and the wavelength was 60 μm. The ripple growth is clearly visible as shown in the lineouts on the right panel. The measured growth factor is ~10, which agrees with the post-shot simulation results, demonstrating that the RT platform works for the materials without strength.

2. Material Equation of State

*Demonstration of Single-Shot EXAFS Measurements
on Ramp-Compressed Ta*
Principal Investigator: Y. Ping
Co-investigators: F. Coppari, J. H. Eggert, and G. W. Collins
(LLNL); and B. Yaakobi (LLE)

Experiments in FY13 advanced a recently published extended x-ray absorption fine structure (EXAFS) technique for dynamically compressed materials. The prior work on EXAFS measurements of dynamically compressed iron up to 560 GPa (Ref. 42) has been extended to study ramp-compressed Ta. EXAFS at the Ta L edge is challenging because the signal is very small (of the order of 1% modulation in intensity). We have improved the backlighter brightness by 2× and the spectrometer efficiency by 5×, so that one shot is now equivalent to ten previous shots. A specially designed quintuple-crystal spectrometer [Fig. 136.109(a)] acquires five spectra in a single shot [Fig. 136.109(b)], which can be averaged to improve the signal-to-noise ratio. EXAFS of both undriven and ramp-compressed Ta at 1 to 3 Mbar has been observed in single-shot measurements. A typical EXAFS spectrum is shown in Fig. 136.109(c). The data indicate that Ta undergoes a phase transition above 1 Mbar. A paper summarizing these results has been submitted.[55]

Tin Melting and Recrystallization
Principal Investigator: A. Lazicki

The TinMelt campaign is an effort to detect and map out a recrystallization transition by shock melting a sample and then ramp-compressing it across the solid–liquid phase boundary. The metrics for recrystallization are (1) features in the profile of the ramped velocity history, measured using VISAR, that could indicate a phase transition, and (2) the presence of a solid x-ray diffraction signature after the recrystallization. Two half-day campaigns in FY13 searched for evidence of this transition in tin and also in lead. Lead is isovalent with tin, has a similarly low melting temperature, and is a much-stronger x-ray scatterer. These shots also experimented with new methods for optimizing the signal-to-noise ratio on the image plates in our diffraction diagnostic. Efforts were made to increase the x-ray flux from the backlighter foil by (1) ablating it from both sides, (2) increasing the laser-to-x-ray conversion efficiency by adding a prepulse to the laser drive, and (3) increasing the laser-to-x-ray conversion efficiency by using a new converging cylinder geometry.

The targets for these shots were composed of tin or lead foils placed next to foils of high-melting-temperature tantalum. The two regions were subjected to the same shock-ramp pulse shape to determine if the wave profile features could be associated
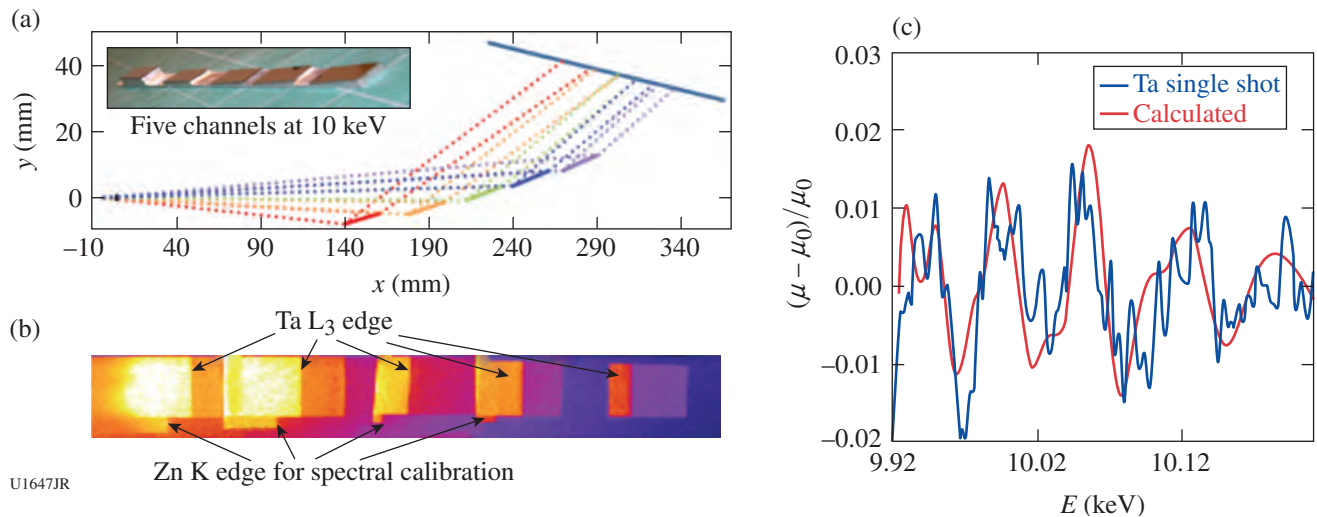

Figure 136.109
(a) Design of the quintuple-crystal spectrometer to record five spectra in one shot. The ray-tracing results of the five channels are represented by different colors. A photo of the actual crystal is displayed at the upper-left corner. (b) A raw image of the detected spectra shows the five channels with Ta L$_3$ edges and Zn K edges as a spectral fiducial. (c) EXAFS data at Ta L$_3$ edge taken by the quintuple-crystal spectrometer in a single shot and averaged over the five channels.

with a solid–liquid transition (expected in the Sn/Pb but not in Ta). Diffraction from the shock-melted, ramp-compressed samples shows a crystalline solid (see Fig. 136.110), indicating that recrystallization occurs over the time scale of the experiment. However, the wave profile results do not definitively show a unique feature that could be associated with this transition.
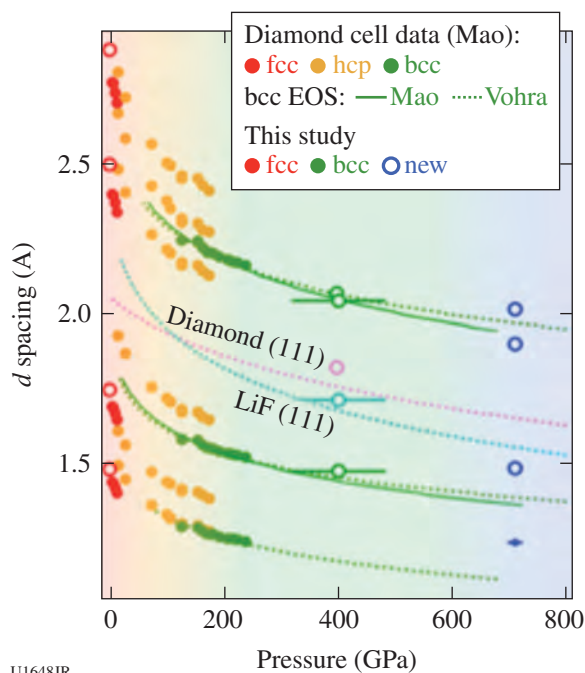

Figure 136.110
X-ray diffraction results from lead ramp compressed from a shock-melted state bcc (body-centered cubic) EOS from Refs. 56 and 57. fcc: face-centered cubic; hcp: hexagonal close packed.

Ta X-Ray Diffraction with Ramp Compression
Principal Investigator: A. Lazicki

The TaDiff-13A/13B campaigns were designed to study a high-pressure phase transition and equation of state in tantalum and to improve methods for performing the diffraction measurements above 10 Mbar. During these campaigns, targets were ramp compressed to pressures as high as 14 Mbar and x-ray diffraction measurements were made using the powder x-ray diffraction image plate (PXRDIP) diagnostic with a copper foil x-ray source. Pressure was determined from VISAR measurements. The 13 successful shots consisted of eight tantalum targets, two tin targets, two lead targets, and one iron target, all sandwiched between diamond plates, with indium or sputter-deposited gold heat shields. The tantalum shots were interspersed with tin, iron, and low-pressure lead shots to

produce information needed to tune the ramp pulse shape and properly time the x-ray source. Diffraction data were obtained from tin between 11 to 13 Mbar (see Fig. 136.111), from lead at 7 Mbar, and from tantalum at 2 Mbar and 7 to 12 Mbar. Successfully tested were a new black kapton filter material, an x-ray preheat shield, and a new x-ray source configuration, all of which contributed to diffraction data that were much improved over previous campaigns. The data on Pb indicate a new high-pressure phase transition, and the results on Sn further support a previously observed transition.
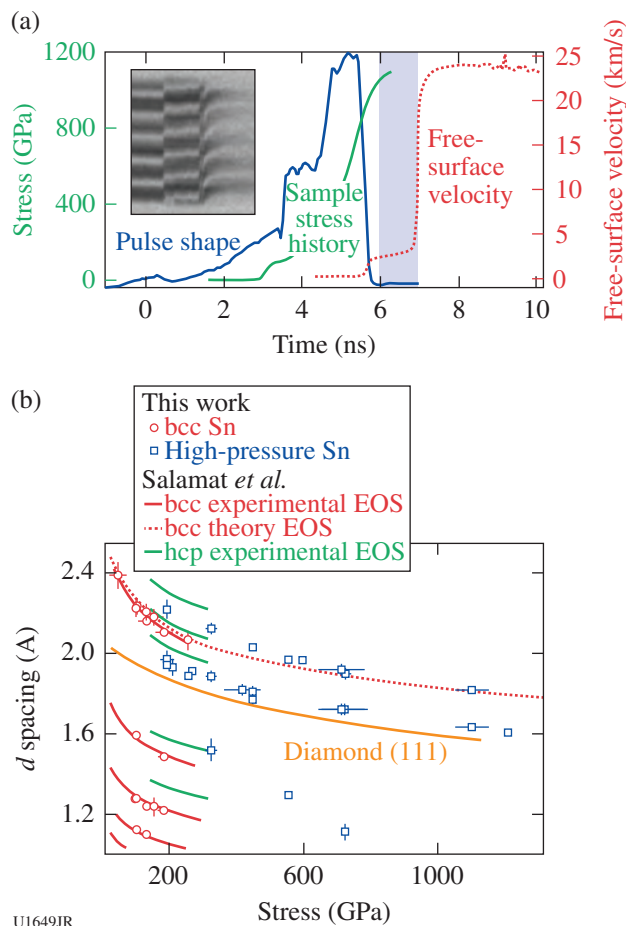
Figure 136.111
(a) VISAR and (b) diffraction data from tin above 10 Mbar collected during the TaDiff-13B campaign.

Development of a Soller-Slit Diagnostic for Dynamic Diffraction Studies
Principal Investigator: J. Hawreliak

The bulk of high-pressure research over the past century has been conducted in a diamond anvil cell (DAC), where pressure

is applied by two opposing anvils. This technique is ultimately limited by the strength of the anvils, and for diamond—the strongest material—it is extremely difficult to achieve and sustain pressures above 300 GPa. Studying material states at higher pressures requires the use of dynamic compression techniques, which are not limited by the ability of an anvil to sustain the pressure, but instead rely on inertial confinement of the material to sustain great pressures temporarily. Dynamic compression is ultimately limited by the energy density, which can be imparted to the sample before it disassembles or the pressure is released. *In-situ* x-ray diffraction has become an important tool for probing the atomic structure of these materials at ultrahigh-pressure states. The most-extreme environments associated with laser-driven dynamic compression experiments require unique diagnostic capabilities, and in FY13 the ADVXRD campaign tested a Soller-slit diffraction diagnostic.

A conventional Soller slit on a synchrotron is a single pair of thin high-Z metal plates (typically tantalum) used to isolate a single line of sight. The direction of the slit is adjusted over a range of angles, and a measurement is made of a static sample. This reduces noise by allowing only the signal that follows a particular path to fall on the detector. For laser-based experiments, one can use an array of Soller collimators to provide a range of angles for a single experimental event. Figure 136.112(a) shows the array of Soller collimators used over the detector, giving an effective pixel size of 400 μm. This reduces the background and makes it possible to record diffraction from a dynamically driven sample without collimating the beam at the target. There are two experimental advantages to this technique over collimating at the target: (1) The target can be simplified because it does not need to include a collima-

tor. (2) Drive noise is reduced because the collimation occurs farther from the x-ray sources, i.e., not at the sample, but at the detector. Figure 136.112(b) shows the diffracted signal from an undriven tantalum sample. The alignment was such that some pixels had direct line of sight of the backlighter and are saturated, but the diffraction ring is visible. These data will be used to benchmark the diagnostic and drive further development to improve the signal-to-noise ratio and angular resolution. Future experiments are envisioned to use this Soller-slit collimator with a hohlraum-driven sample.

Radiographic Equation-of-State Measurements of Shocked Foams
Principal Investigator: J. Hawreliak

Materials in extreme conditions generated by shock compression of aerogel foams are an important area of HED science. LLNL and its partners have developed the capability to engineer low-density foams with the desired properties for a range of programmatic and scientific experiments. The initial density of the foam is used to set the thermodynamic path of the shock Hugoniot. For laboratory astrophysics and other HED experiments, where low-density aerogels are used to model interstellar matter, a detailed understanding of the EOS is important. However, continuum EOS theories make assumptions about bulk behavior of these foams that ignore the underlying fact that foams are fundamentally a heterogeneous material at small scale lengths. Continuum EOS models cannot be scaled simply by density scaling, therefore requiring foam EOS Hugoniot measurements. Furthermore, many low-density carbon and CH-based foams of interest are not transparent, making impedance-matching experiments difficult and less accurate. To avoid these issues, a platform has been developed for *in-situ* radiography of shocked foams, from which the shock speed and density can be measured.

Figure 136.113(a) shows a VISRAD model of the experimental configuration. Two or three beams are used to generate a K-shell area backlighter from a material chosen to deliver sufficient photon flux to the detector with an x-ray energy low enough for the foam sample's absorption cross section to yield good contrast at the shock front. For 50-mg/cm^3 carbon resorcinol formaldehyde (CRF), the Cl He$_\alpha$ x rays from Saran are used as the backlighter. A second set of beams aimed onto a quartz drive plate generates an expanding spherical shock front. The spherical shock front removes parallax issues associated with the different viewing directions of different strips on the framing camera. Figure 136.113(b) shows a single frame from
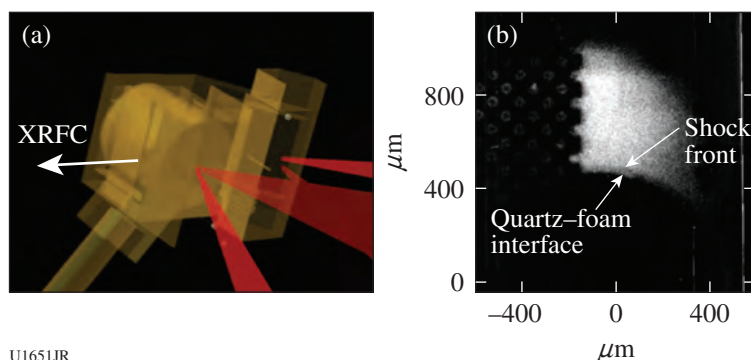

U1650JR

Figure 136.112
(a) The Soller collimators and (b) sample data.

Figure 136.113

(a) VISRAD model of the experiment; (b) single frame from a two-strip framing camera.

the x-ray framing camera identifying the shock front and the opaque quartz pusher.

### High-Energy X-Ray Diffraction Development
Principal Investigator: J. Hawreliak

In-situ x-ray diffraction is a powerful diagnostic technique for probing atomic structure at high pressures. Cutting-edge molecular dynamic simulations show that structure becomes more complex at higher pressures, requiring shorter-wavelength x-ray sources to uniquely determine the phase. K-shell emission short-pulse lasers such as OMEGA EP is a technique for generating high-energy x rays, but it also produces a high-energy bremsstrahlung spectrum that generates background. Although techniques have been developed that use short-pulse x-ray backlighters for radiography, the use of similar backlighters for x-ray line diffraction, in the HighE-Xdiff Campaign, was not successful. To identify the failure mode, one set of Ross-pair filters was used to isolate tungsten L-shell fluorescence, while a second pair isolated >50-keV x rays. The data showed that the predominant source of strong background is from x rays with energies >50 keV. Tungsten was the primary material used for x-ray shielding, and its K-shell fluorescence at 59 keV appears to be the dominant source of background in the BBXRD diffraction diagnostic, rather than direct >50-keV x rays from the backlighter. Figure 136.114 shows the Ross-pair images on the image plate.

Lithium Hydride Equation of State
Principal Investigator: A. Lazicki

The LiHEOS campaigns represent an effort to measure the shock Hugoniot of LiH, for the purpose of constraining theoretical models. Two methods were pursued in FY13: The first used the VISAR velocity diagnostic to track reflecting shock waves in targets composed of single-crystal quartz and LiH, relying upon impedance matching to the quartz standard to determine the Hugoniot data points. The other method used
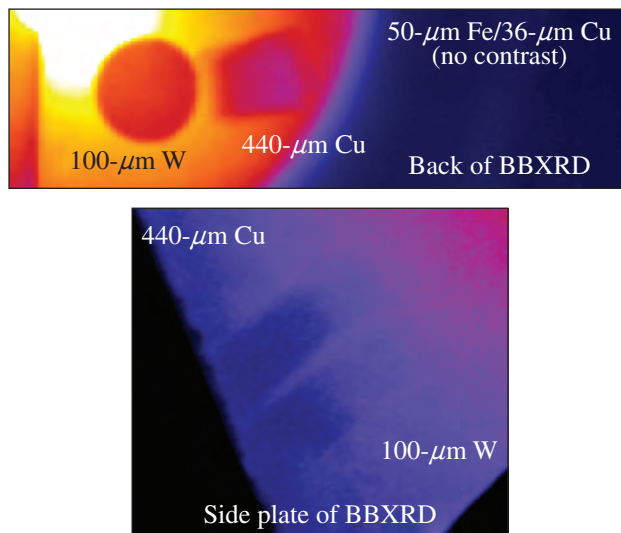
Figure 136.114

Images of the Ross pairs used to study the background spectrum and discriminate between direct x rays from the backlighter and fluorescence from the diagnostic hardware.

radiographic imaging to capture the motion of the shock front in LiH using a framing camera. Several radiography geometries were investigated: imaging through pinholes or slits with an area backlighter and a point-projection configuration.

The VISAR measurements were demonstrated to be successful, and highly valuable data were acquired (see Fig. 136.115), in spite of challenging issues with sample contamination (resulting from LiH's reactivity with moisture) and also with the VISAR technique (because of the large index-of-refraction mismatch between the two materials, which can create spurious reflections off of LiH–quartz interfaces).

Furthermore, after addressing debris, signal strength, and target alignment issues, successful radiographic measurements were demonstrated, using an area backlighter and imaging the shock front through narrow slits.
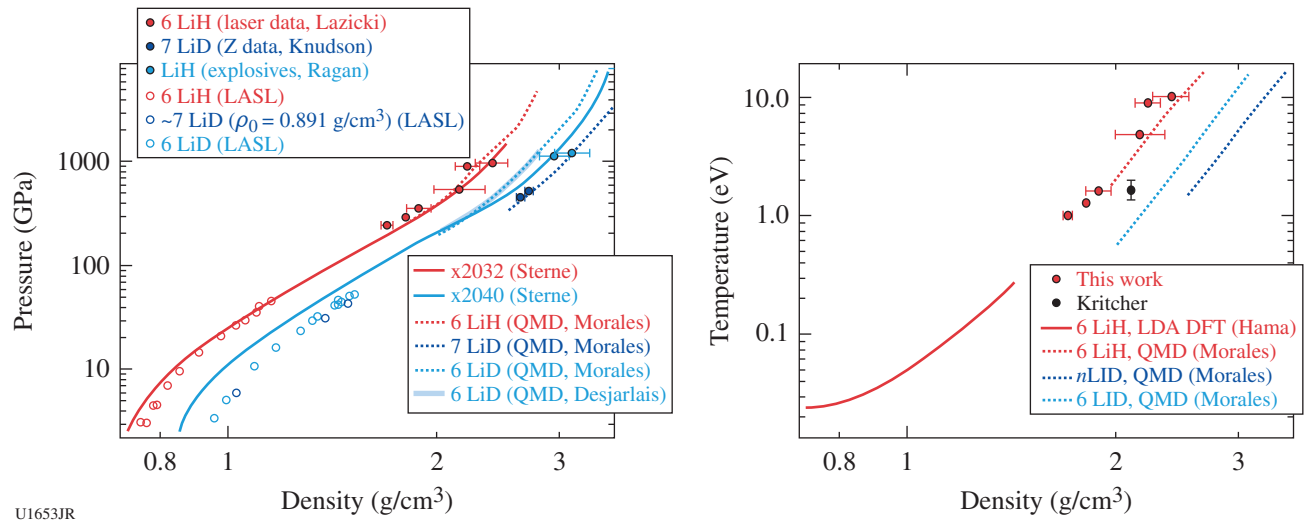
U1653JR

Figure 136.115
Pressure and temperature of LiH along the Hugoniot measured using VISAR and SOP. Previous data from Refs. 58–60.

Ta Equation of State
Principal Investigator: D. E. Fratanduono

Six experimental shots were conducted on OMEGA to measure the shock Hugoniot of Ta. VISAR data were collected.

3. Radiation Transport and Opacity

Heated Wall Radiation Transport
Principal Investigator: K. Baker

A campaign of six shots was carried out on the OMEGA laser to measure radiation transport in a geometry that minimizes wall loss. In these experiments a heat wave was propagated axially down a 30-mg/cm^3 SiO$_2$ foam, 700 μm in diameter $\times$ 1.7 mm in length, whose outer diameter was enclosed by a 70-μm-thick Ta$_2$O$_5$ annular foam. This foam structure was then placed inside a 1.6-mm-diam, 2.9-mm-long hohlraum and radiatively heated by the x-ray flux driven by laser interaction with the hohlraum walls. A supersonic heat wave was driven axially down the length of the SiO$_2$ foam, and a transonic heat wave was driven radially inward through the Ta$_2$O$_5$ foam. The radially propagating transonic heat wave minimized the wall loss for the axially propagating supersonic heat wave, enabling it to propagate over longer distances.

A heat wave was successfully propagated over a distance greater than twice the Rosseland mean free path and more than twice the diameter of the foam cylinder in which the heat wave propagated, as shown in Fig. 136.116(a). A control target was also employed, consisting of an inner SiO$_2$ foam surrounded by 25-μm-thick gold annular walls to prevent a
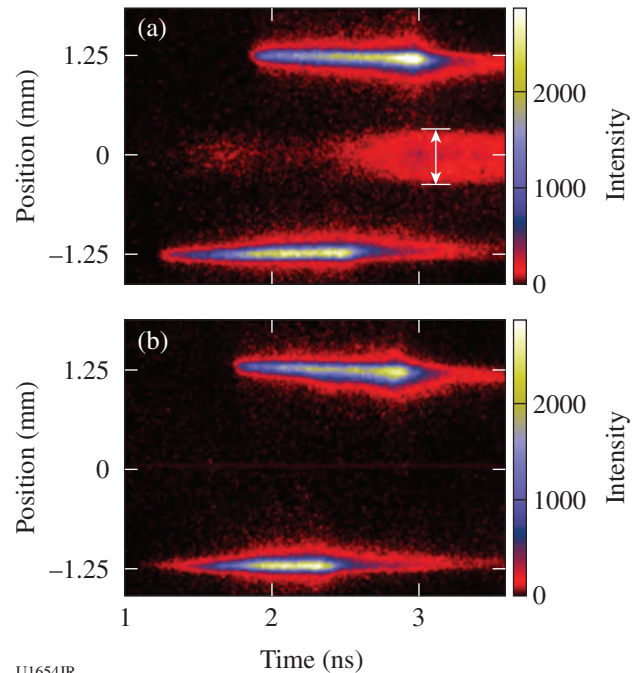
U1654JR

Figure 136.116
Heat-wave signature measured at the end of the SiO$_2$ foam for the case of (a) Ta$_2$O$_5$ and (b) gold walls. The features at the 1.25-mm and –1.25-mm positions represent the two timing lasers, which were incident at 1.75 and 1.25 ns, respectively.

radially propagating heat wave from reaching the inner SiO_2 foam. As seen in Fig. 136.116(b), no heat wave was observed for this control target.

4. Hydrodynamics

Toto—Radiography Development for NIF Hydrodynamics Experiments
Principal Investigator: V. A. Smalyuk

Backlighting experiments were performed on the OMEGA Laser System to study symmetry of foam balls illuminated with hohlraum x rays. Backlighter targets were driven with the OMEGA EP short-pulse IR beam in joint experiments. In the joint configuration, 10-μm-thick Ag wires, mounted on 300 × 300-μm-sq, 10-μm-thick polyimide foils were irradiated with an ~1.2-kJ short-pulse (~100-ps) IR beam at a laser intensity of ~1 × 10^{17} W/cm^2. X-ray radiographs of targets were measured on image plates using the HERIE diagnostic placed ~50 cm from the sample, yielding a magnification of ~50. In addition, tests were performed using the short-pulse backlighting parameters that will be used on future NIF experiments backlit by the short-pulse advanced radiographic capability (ARC) beam. This latter configuration adjusted the OMEGA EP short-pulse beam to deliver 1.0 kJ of IR light with a 50-ps pulse shape and an intensity of ~2 × 10^{17} W/cm^2. The radiograph signal and contrast with the ARC-like beam parameters were consistent with previous experiments and showed increased resolution (13 μm) compared to experiments with the nominal backlighter parameters (19-μm resolution), as shown in Fig. 136.117. These

experiments were very successful, producing high-quality radiographs that created a baseline for future complex hydrodynamics experiments on the NIF.

Copper Foam Shock-Breakout Measurements
Principal Investigator: A. Moore

High-Z metal foams made via a copper ceramic casting process, and with approximately one-tenth solid density (~1 g/cm^3), have been developed at LLNL and are being produced routinely at AWE. These provide a novel target material for use in high-energy-density-physics experiments on the NIF, Orion, and OMEGA, but they must be well characterized with a good understanding of the material opacity and EOS in order for experimental results to be constraining to radiation–hydrodynamics simulation codes. With advances in the manufacturing techniques, it has been possible to produce foam material with an average pore diameter of 1 μm and less. In the five experiments conducted in the CuFmDrive-13A campaign described here, comparisons were made of the shock propagation in two materials, 1.0-μm and 0.5-μm pore foams, as a means to qualify the 0.5-μm foam for use in future experiments.

The Rankine–Hugoniot relations for a single shock demonstrate the simple dependence of the shock velocity on the pressure achieved in the shocked foam, which is in turn dependent on the internal energy of the foam. Given this dependence, measuring the propagation of a single shock through a material sample has been developed as a reliable method to quantitatively validate the EOS model for a given material.
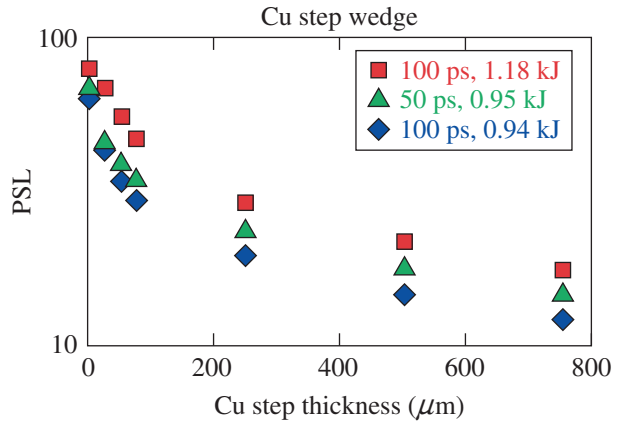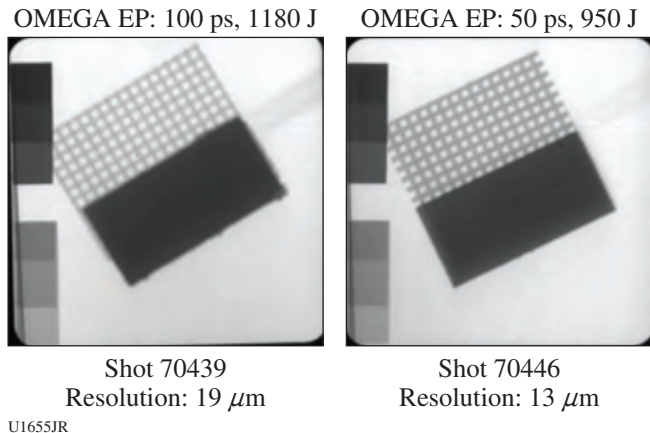

Figure 136.117
Backlighter performance data using a gold foil-grid radiography target and a Cu step wedge.

The platform to measure the shock transit time in Cu foams was developed using a 5.5-kJ laser drive from 15 beams of the 60-beam, 30-kJ, 351-nm OMEGA Laser System. In these experiments the target package consists of a washer containing two foam samples, with a polystyrene ablator and aluminum flashing to improve the VISAR laser reflection. The ablator side faces the drive hohlraum. The copper foam samples are 0.7 mm in diameter and nominally 0.25 mm in thickness with a nominal density of 0.9 g/cm^3. The hohlraum used is 1.6 mm in diameter and 1.0 mm long, with 1.2-mm-diam holes at each end (one for laser-beam entry and one to drive the ablator), and reaches a peak temperature of 208±5 eV. Data using the streaked optical pyrometer (SOP) were obtained on five shots, an example of which is shown in Fig. 136.118(b). The average shock velocity for the 1.0-μm Cu foam was 51.0±3.2 km/s, which is compared to 50.3±3.0 km/s measured with the 0.5-μm foam, indicating

that a reduction in the pore size does not significantly alter the material EOS of the Cu foam.

In general, comparing the results with post-shot simulations are favorable, again indicating that there are no significant differences in EOS. That said, limitations in the pre-shot characterization of the sample led to a large uncertainty in the sample thickness, allowing for a wide range of possible breakout times. A follow-on campaign in FY14 will extend the measurement to include shock velocity using VISAR and will repeat some shots following better characterization of the sample thickness.

Short-Pulse, UV Backlighting Development for the NIF
Principal Investigator: D. Martinez

A series of eight shots were performed on OMEGA EP to optimize, for NIF experiments, a point-projection backlighter technique using a Zn backlighter foil, apertured with a 20-μm pinhole tilted 30° from the normal of a 50-μm-thick, 5-mm × 5-mm-sq Ta plate (see Fig. 136.119). The Zn foil was suspended from the Ta pinhole, with either a 15° or 37° angle between the Zn foil normal and the laser axis, to recreate the designed angle of incidence for the backlighter targets on the NIF. The CH-Zn foil was positioned to create a 500-μm separation distance between the surface of the Zn foil and the pinhole. The intensity was varied between 1×10^{15} and 5×10^{15} W/cm^2 on the Zn foil and was controlled by changing the number of beams on target. The backlighter performance was characterized using a gold foil/grid target and imaged onto a single-strip x-ray framing camera with a magnification of $M = 23$. The Zn spectrum was recorded using the SSC-A SXS streaked spectrometer with a photon energy range of 7.76 to 12.87 keV. The resolution of the system was measured to be 20-μm mode, which corresponds to a 20% transmission in the modulation transfer function (MTF) for all shots. From the spectrometer, the x-ray signal was primarily monochromatic in the observed photon-energy range for all tested intensities; however, there was reduced contrast in the x-ray framing camera (XRFC) images for intensities above 4×10^{15} W/cm^2. Peak contrast recorded for the experiment was at intensities around 2.5×10^{15} W/cm^2. From the streaked spectrometer, the He$_\alpha$ lines scaled well with the intensity of the beam. The angle of incidence did not have a noticeable effect on the peak Zn He$_\alpha$ signal or the resolution of the backlighter. The results from this data were used to confirm the backlighter design for NIF experiments and have led to high-quality images on the NIF.

(a)   (b)

1.0-μm
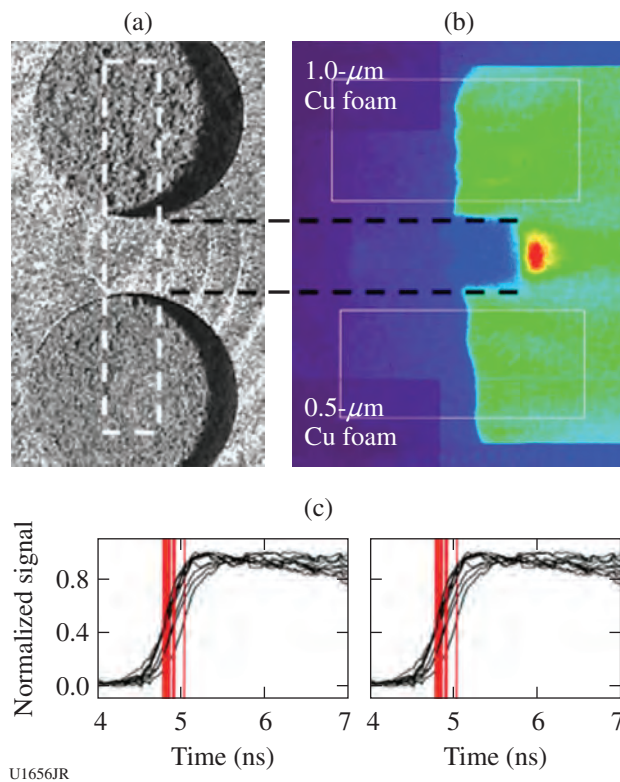Cu foam

0.5-μm
Cu foam

(c)

U1656JR

Figure 136.118
Streaked optical pyrometer (SOP) data from shot 68018. (a) Pre-shot images of the Cu foam surface viewed by the SOP. The thickness of the 1.0-μm foam sample was 248 μm and the 0.5-μm foam was 276 μm. (b) Raw SOP image data and (c) optical emission caused by shock breakout show that the shock in the 1.0-μm Cu foam arrived at 4.86±0.06 ns; in the 0.5-μm foam the shock arrived at 5.49±0.14 ns.
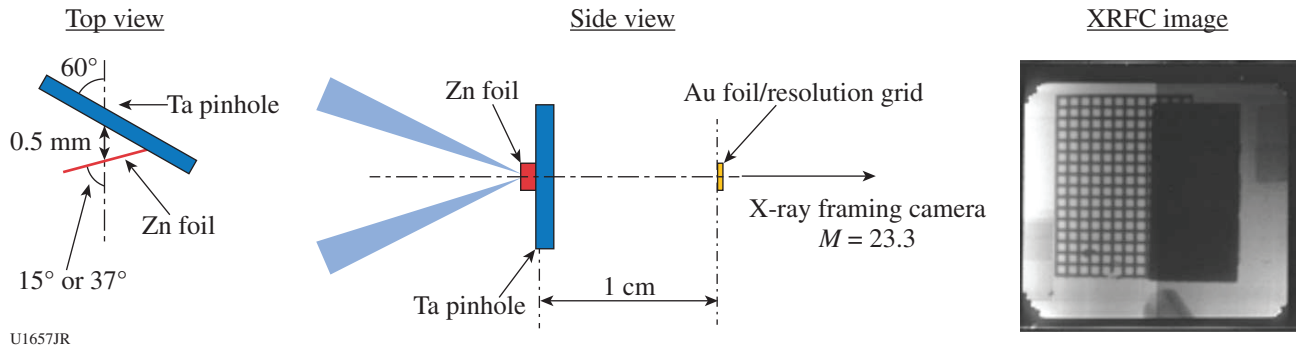
Figure 136.119
The experimental setup, showing angles of the Ta pinhole substrate and Zn foil with respect to the laser/imaging axis. Shown on the right is a sample x-ray framing camera (XRFC) image of the Au Grid and Au foil. A Zn filter covered half the image and two sets of 4- and 8-Cu filter steps are also present in the corners.

X-Ray Area Backlighter Development
Principal Investigator: K. Baker

A campaign of six shots was carried out on the OMEGA laser to measure the conversion efficiency and uniformity of zinc backlighters. A common platform was used to evaluate the conversion efficiency from Zn foils with and without a 2.8-ns prepulse, ZnO-coated aerogels, and ZnO foams. The common platform consisted of a 2-mm-diam, 2-mm-long tube that was filled with either a low-density foam or had two foils glued on the ends of an empty tube. As shown in Fig. 136.120, the highest overall conversion efficiency came from a 5-μm-thick Zn foil target driven with a 2.8-ns prepulse that was ~3× brighter than the same Zn foil without a prepulse. The second-most-efficient target was a pure ZnO foam, followed by ZnO-coated SiO_2 aerogels. The foam targets, which underwent volume ionization, exhibited more-uniform radial emission above 1 keV than the foil targets, with or without prepulse (see Fig. 136.121).

The thinnest Zn exploding foil target, which was 1 μm thick, stagnated in the middle of the tube, producing a temporally longer He_α emission than the other targets.
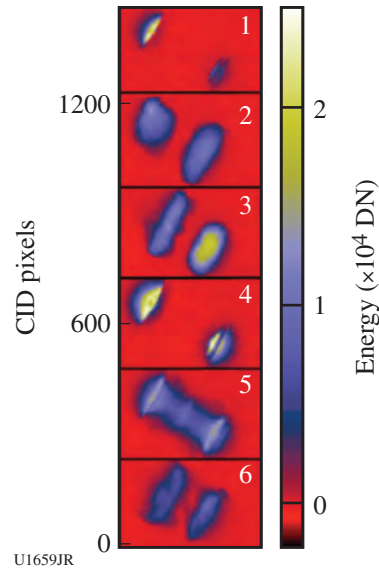

Figure 136.121
Time-integrated x-ray pinhole images of the various targets showing the increased fluence from the foil targets with prepulse (4) and the greatly increased uniformity with the low-density foams (2, 3, and 6).

5. Burn Physics

High-Resolution Measurements of Velocity Nonuniformities in an Alternative Ignition Capsule Ablator Material, Boron Carbide
Principal Investigator: P. M. Celliers

Two days of CAPSEED campaigns took place in FY13. These campaigns began our initial evaluations of boron carbide

Figure 136.120
Relative energy conversion efficiency for the various zinc targets.

(B$_4$C) as an alternate ablator material for NIF ignition target designs. The large fraction of boron in this material makes it a particularly efficient ablator, similar to others such as CH and C. B$_4$C undergoes brittle failure, however, when stresses exceed the yield stress; therefore, it is anticipated that it may have a complicated shock response, similar to diamond. Two CAPSEED campaigns this year provided the initial evaluations of ablator nonuniformities produced in B$_4$C under shock.

For the CAPSEED-13A campaign, the B$_4$C samples were obtained from a commercial source using a sintering process. Characterization of the sample revealed carbon inclusions and voids, and the polished samples incurred large (micron-sized) defects on the surfaces owing to these issues. Attempts to mitigate these problems were made, but the resulting shock quality was severely compromised. The second campaign, CAPSEED-13B, investigated samples that were also created through a sintering process developed at LLNL, but with much lower levels of nonuniformity and voids. Results from the later samples showed a clear improvement; however, the shock-front nonuniformities in these samples were still clearly evident in the data as shown in Fig. 136.122. The velocity spectra of the current B$_4$C samples (Fig. 136.123), when compared with high-quality Be and GDP ablator samples, are too nonuniform for use

in a NIF capsule. Improvements in the fabrication processes to control these nonuniformities are required for further progress with this material.
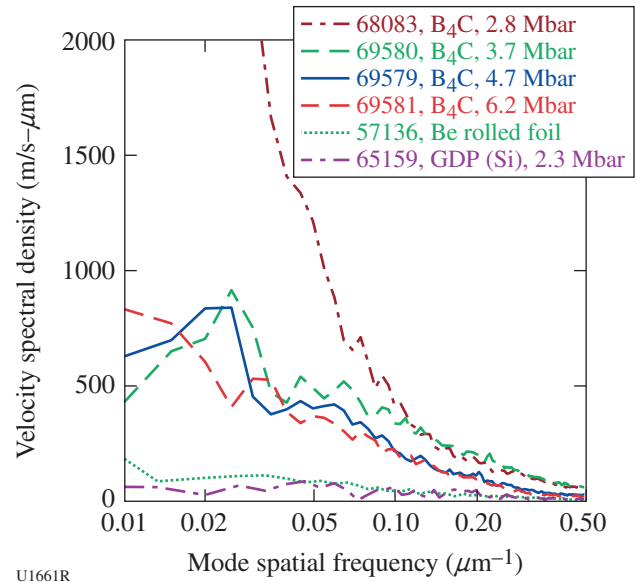

Figure 136.123
Velocity fluctuation spectra measured for B$_4$C from CAPSEED-13A (low-quality sample, shot 68083) and with improved samples CAPSEED-13B (shots 69580, 69579, 69581). Fluctuation levels are still a factor of 5× to 10× too high for use as a NIF ablator. For comparison, results from a NIF-quality Be foil (57136) and silicon-doped glow discharge polymer (GDP) sample (65159) show much lower fluctuation levels.
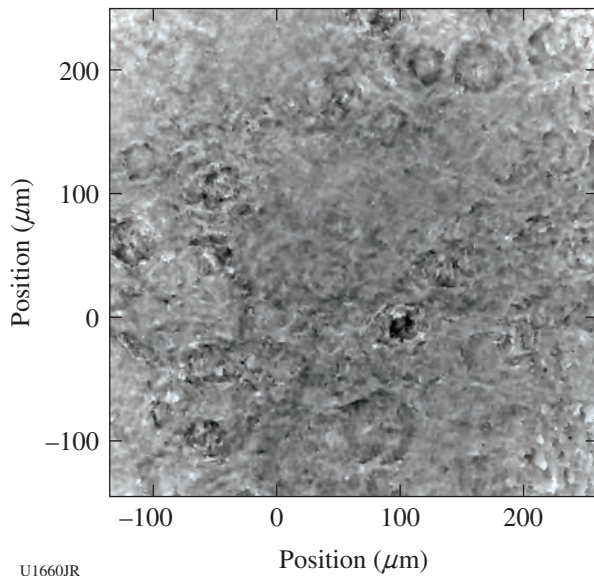
Ablator Physics: Tests of Beryllium Capsules
Principal Investigator: D. T. Casey

The goal of the AblatPhys-J-13A OMEGA/OMEGA EP joint shot day was to demonstrate Be as a high-performance ablator for indirect-drive–ignition experiments on the NIF. These experiments were diagnosed with the OMEGA neutronics suite and also used OMEGA EP–driven Cu K$_\alpha$ backlighting observed with the spherical crystal imager. This was the first use of the spherical crystal imager in indirect drive at the Omega Laser Facility; the excellent data we obtained resulted in high-quality radiographs and neutronics data. The capsules were 600 μm in diameter with 30-μm-thick Be walls (where the inner 7.5 μm was doped with 4% Cu) and were filled with deuterium gas. General Atomics, who manufactured the capsules, tackled a number of complex target fabrication issues, including deuterium gas retention, Be polishing, Cu diffusion, and residual glue from the gas-fill hole. Several targets also included thin 0.1-μm W layers on the inner capsule surface to provide radiographic contrast. The capsules were driven using

Figure 136.122
Gray-scale representation of the shock-front velocity as measured on shot 69581, a B$_4$C sample shocked to 6.2 Mbar. The presence of voids and carbon inclusions distributed throughout the sample resulted in the circular ripple-like disturbances in the velocity pattern. These disturbances produce most of the spectral power in the 10- to 100-μm-wavelength range (0.01- to 0.1-μm^{-1} spatial frequency range).

1.6-mm-diam, 2.1-mm-long, 50-μm-thick Au hohlraums irradiated by 40 OMEGA laser beams. These targets performed exceptionally well, providing around 80% of the neutron yield expected based on simulations. Figure 136.124 shows (a) the radiograph geometry, (b) a sample radiograph, and (c) the Be target performance (without the W layer) as indicated by the yield divided by the simulated yield (YOS).

6. X-Ray Source Development and Application

Solar Cell Electrostatic Discharge
Principal Investigator: R. Patterson

The solar cell electrostatic discharge campaign is a joint effort of the Naval Research Laboratory, the Defense Threat Reduction Agency, and the X-Ray Source Development team at LLNL. The goal of this campaign is to establish a platform capable of performing x-ray exposure testing on arrays of solar cells,[61] specifically to demonstrate that a sustained arc can be formed between individual cells.

On 11 July 2013, the team successfully fielded the time-of-flight Langmuir probe (XLPD)[62] and active solar cell array (XLPDAC) diagnostics on ten shots, obtaining excellent data indicative of electrostatic discharge over a range of source-to-cassette distances between 60 cm and 96 cm. The improvements in robustness and reproducibility of acquired

data resulted from modifications to the XLPDAC hardware (Fig. 136.125), including electrical insulation of the solar cells from the aluminum cassette and improved shielding of previously exposed contacts.

XLPD measurements confirmed the arrival of the source plasma a few μs after x-ray loading,[63] consistent with prior measurements of plasma velocities, ~15 cm/μs. Figure 136.126 shows the solar cell output signals for several shots. The data
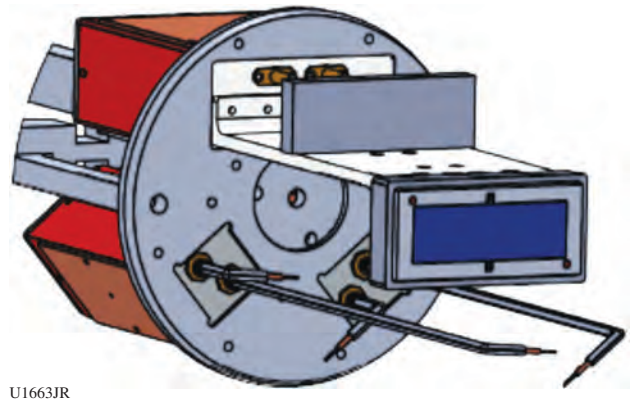

U1663JR

Figure 136.125
A CAD model including the modifications made to the XLPDAC. Mounted from the circular aluminum cassette face are the solar cell support bracket (light gray) with cells (blue) and two pairs of Langmuir probes beneath. The bias and power circuitry housing (red) is attached to the rear of the cassette.
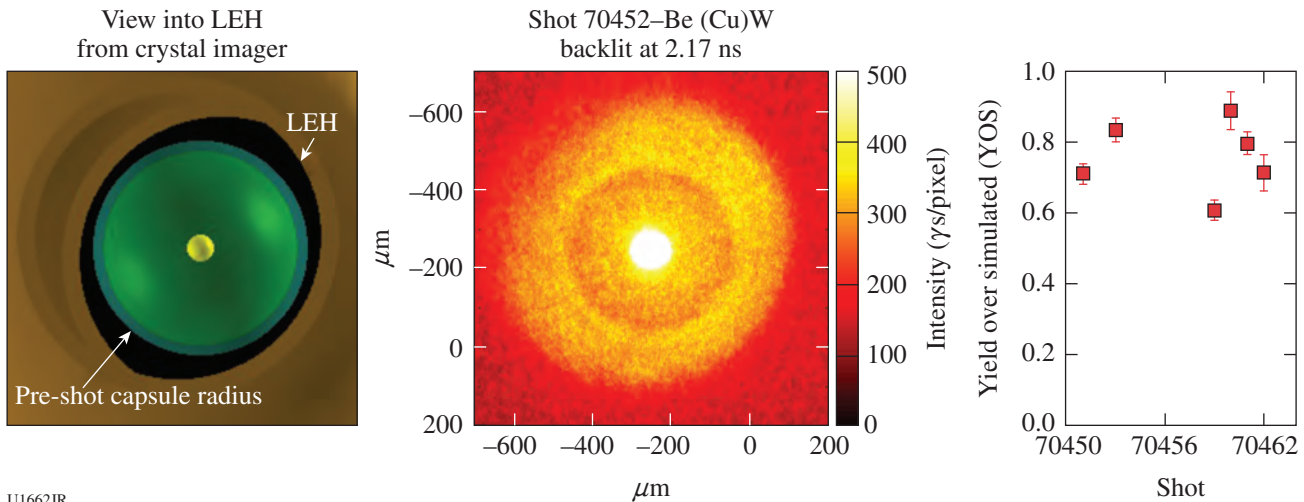

U1662JR

Figure 136.124
(a) A view of the capsule into the hohlraum, as seen by the spherical crystal imager. (b) OMEGA EP–driven Cu K$_\alpha$ backlit radiograph of the imploding shell 2.17 ns after the start of the main OMEGA drive. The radiograph was obtained by the spherical crystal imager. (c) Performance of the Be capsule implosions as indicated by the yield-over-simulated (YOS) neutron yield.

suggest that the arc formation is not between the cells themselves. The cell biased at +100 V and limited to 4-A maximum current behaves similarly to an area Langmuir probe, drawing current from the surrounding plasma. The other cell was grounded and not current limited, showing signals consistent with initial photoionization of the cover glass and a subsequent decrease in amplitude resulting from neutralization with the plasma. Future experiments will include different or no current limits on the cells and cell geometry variations that allow discrimination between arcing and photoionization effects (geometry independent versus scaling with area).
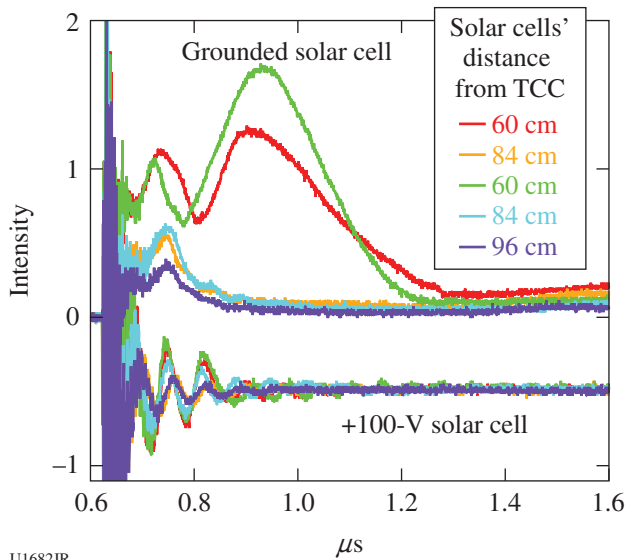
Figure 136.126
Voltages recorded from grounded (upper) and +100 V biased (lower) solar cells. Signals are from shots with Ge-doped SiO_2 aerogel x-ray sources, irradiated with ~20 kJ in a 1-ns square pulse.

X-Ray Source Development with Nanostructured Materials
Principal Investigator: F. Perez

In FY13 the X-Ray Source Development team, funded by the Defense Threat Reduction Agency, created the most-efficient Ti-doped foam for generating bright, ns-class x-ray pulses to date. Two new fabrication techniques achieved record concentrations of Ti emitters (up to 33 at. %) by coating TiO_2 on an aerogel or nano-porous scaffold. These foams now demonstrate laser-to-x-ray conversion efficiencies above 5%, comparable to other types of x-ray-source targets such as metallic cavities and pre-exploded foils. The x rays are generated when 40 beams of the OMEGA laser irradiate a foam sample (see Fig. 136.127).

This year, after obtaining x-ray flux and laser-heating propagation measurements in the targets, the team found that the dynamics of the foam heating were not well reproduced by state-of-the-art computer simulations. This discrepancy, under investigation, could be explained by an unexpected role of foam structure, metal-dopant content, or the presence of absorbed water, or by effects not included in the simulations. Understanding and mitigating these effects may lead to new designs and even-higher x-ray efficiencies.

In parallel, new types of foams are being investigated. The present limitation is that most of the foam is made of elements lighter than Ti (Si and O), which channel energy out of the system. Cu-based foams, containing only trace amounts of light elements, were tested this year for the first time. Being still at an early stage of development, the current results will serve as a reference point for next year's ultralow-density (<10-mg/cm^3), almost-pure Cu foams.
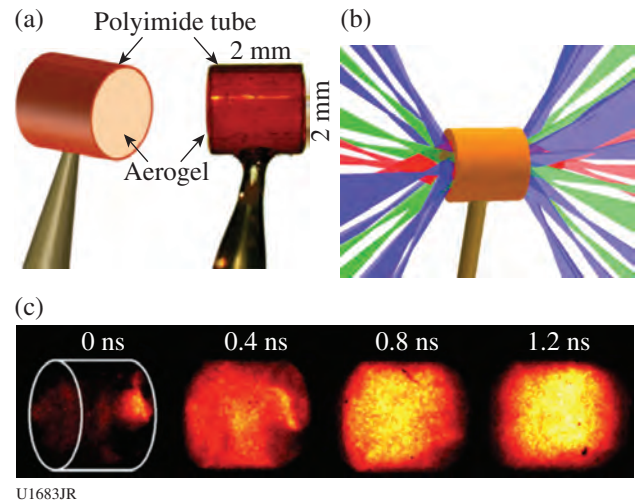

Figure 136.127
(a) Foam sample held in a plastic tube; (b) laser irradiation pattern of the OMEGA laser; (c) x-ray emission images at different times relative to the beginning of the interaction.

FY13 LANL Experimental Campaigns—Overview
In FY13, Los Alamos National Laboratory (LANL) executed 207 total shots on OMEGA. LANL experiments contributed to the National Ignition Campaign (NIC) in the following ways:

- Measured the x-ray ablative Richtmyer–Meshkov growth of isolated defects on beryllium ablators
- Studied branching ratios and species separation (plasma kinetic effects) in DT fusion plasmas
- Continued neutron imaging and gamma-ray scintillator development for the National Ignition Facility (NIF)
- Studied the suppression of hohlraum laser–plasma interaction (LPI) with magnetic fields

High-energy-density (HED) campaigns included

- Study of shear in a counter-propagating flow geometry driving turbulent mixing
- Backlit defect implosion experiments to study polar-drive symmetry control
- Measurement of spatial distribution of mix in gas-filled capsules
- Imaging x-ray Thomson-scattering platform development for dense plasmas and warm-dense-matter equation of state (EOS)
- Measurement of a supersonic radiation wave and foam aerogel EOS

Shear

In FY13 the Shear campaign focused on extending our counter-propagating flow platform for studying shear-driven turbulent mixing to include long-duration streaked imaging of the mix layer. These experiments used beryllium tubes containing low-density polystyrene-foam half-cylinders separated by aluminum tracer layers. The counter-propagating flow is created by inserting gold "plugs" in front of each foam semi-cylinder at opposite ends to hold back the shock in each foam at one end (see Fig. 136.128). With the plugs in place, the beryllium tube ends are irradiated with 10^{15}-W/cm^2 laser intensity to initiate counter-propagating shocks. When the shocks cross, they establish a shear layer in the aluminum, which then grows as a result of Kelvin–Helmoltz followed by turbulent mixing.

During our November 2013 shot day we switched from x-ray-framing-camera (XRFC)–based radiography of the mix layer to a long-duration streaked imager. This required an area backlighter designed to emit x rays over 5 ns or longer that would be recorded with an OMEGA streak camera ($20\times$ magnification). Thin scandium foils sandwiching a thicker beryllium foil allowed us to irradiate both sides of the backlighter with grouped beams staggered in time. The central beryllium foil prevented burnthrough but still allowed a significant number of x rays to transmit from the back scandium foil. Figure 136.129 shows an example of a streaked image, indicating where the laser is turned on along with the mix layer (aluminum tracer foil), which shows the absence of a signal as a result of x-ray
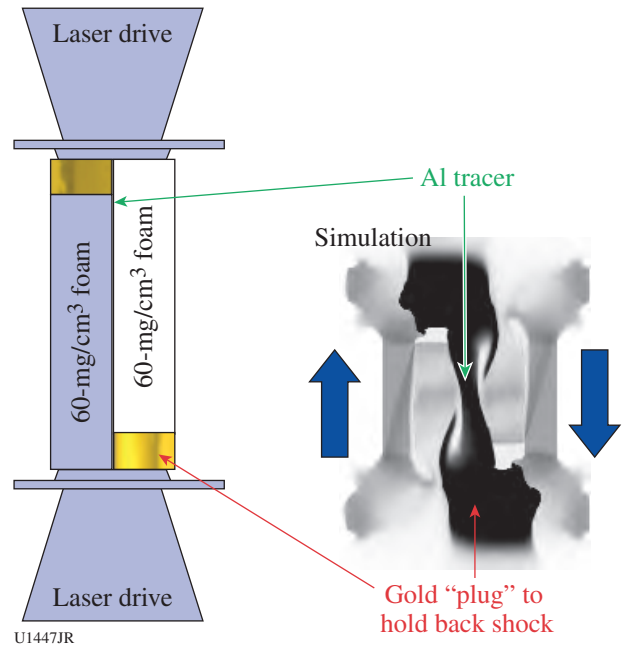
Figure 136.128
Target geometry and simulated radiographs for counter-propagating shear experiments.
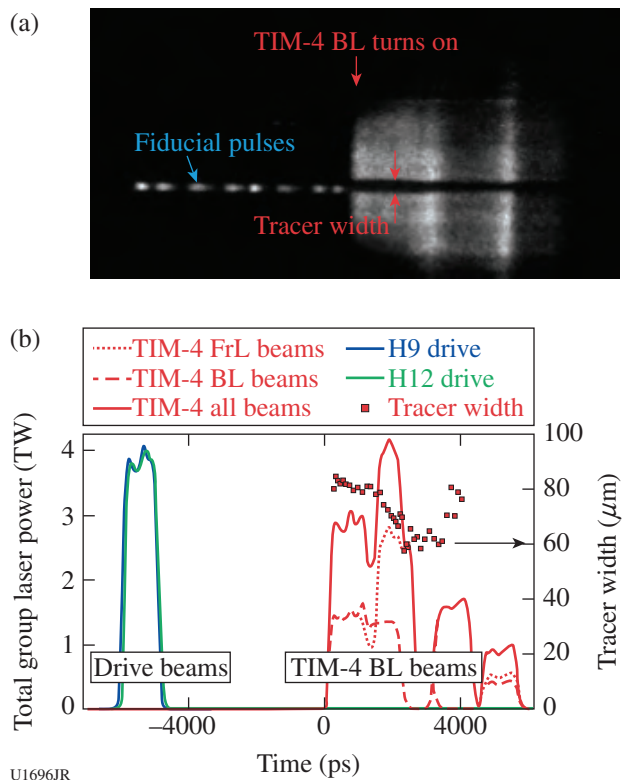
Figure 136.129
(a) Raw and (b) analyzed streak data of mix width from shear experiments. FR: front lit; BL: backlit.

absorption in the aluminum. Figure 136.130 summarizes mix-width data and compares simulations using the Los Alamos Bernard–Harlow–Rauenzahn (BHR) turbulent mix model, streaked imaging, and x-ray-framing-camera data.
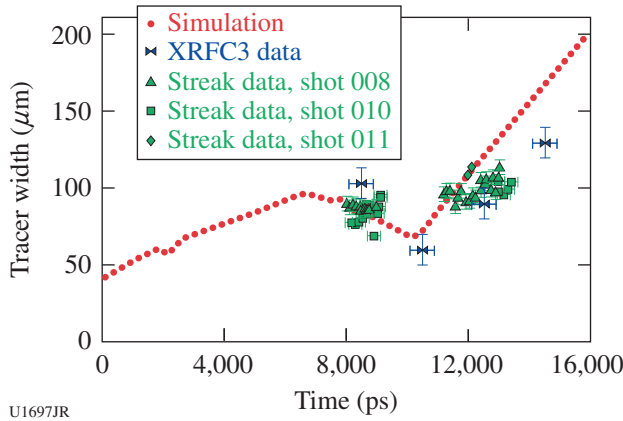

Figure 136.130
Comparison between framing camera, streak camera, and simulated mix-width evolution.

BeARM

The Be ablative Richtmyer–Meshkov (BeARM) campaign had one shot day in January 2013. The overall goal of these experiments was to measure the oscillation frequency of small perturbations on CH and Be ablators driven by the x-ray abla-tion Richtmyer–Meshkov (RM) effect. This knowledge would provide a better understanding of how isolated defects behave during the first shock transit stage of a NIF ignition attempt, which would then provide methods for minimizing perturba-tions at the onset of Rayleigh–Taylor instability.

Our experiments used 15 beams inside large Au half-hohlraums, which were staggered in time to produce a 7.5-ns radiation drive with a radiation temperature of 80 eV (see Fig. 136.131). Targets with 2-D arrays of 5-μm-tall, 17-μm–FWHM Gaussian bumps and 25-μm–wavelength Be sinusoids were attached over the opposite laser entrance hole with the defects facing inside the halfraum. During the experiment the bump arrays were backlit with Y and Ta backlighters (~2.2-keV emission) and imaged at 37× magnification onto an x-ray fram-ing camera. Radiation–hydrodynamics simulations running with equation-of-state (EOS) tables for Be predict these small-amplitude (2.5-μm) sinusoids undergo damped oscillations for our experimental conditions as shown in Fig. 136.132. We measured the ablative RM of the Be sinusoids with four data points extending out to 7 ns as shown in Fig. 136.133. At the
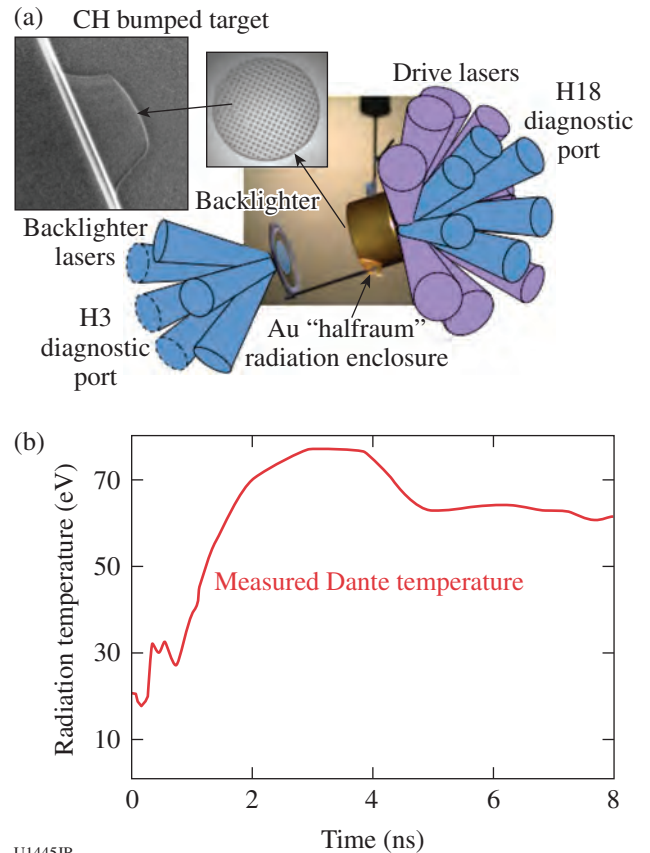

Figure 136.131
Overview of indirect-drive ablative Richtmyer–Meshkov (RM) experiments.

two data points around 3.5 ns, the sinusoids appeared to go through an inversion and then reappear by 7 ns. This appears to be consistent with the 20-μm simulation of Fig. 136.132, where
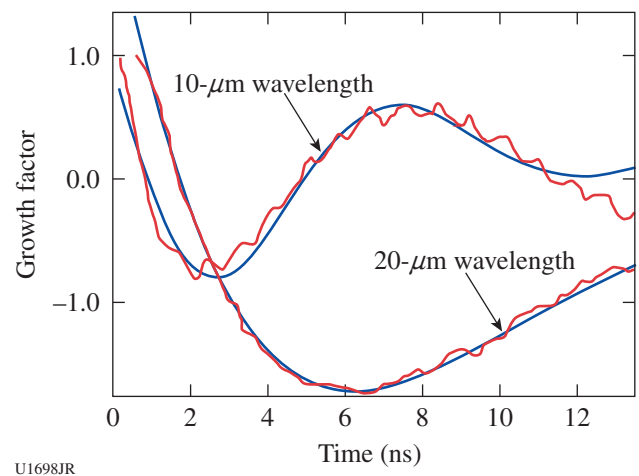

Figure 136.132
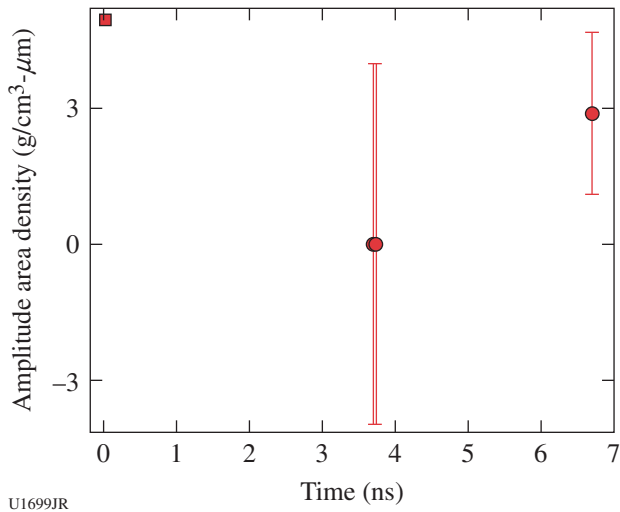Simulated oscillations of ablative RM sinusoids in Be.

Figure 136.133
Measured areal density of Be sinusoids. An apparent inversion is reached near 4 ns. The point at 7 ns is likely an inverted feature (local minimum), which was not apparent directly from the data.

the inversion occurs around 2 ns and then the inverted sinusoid reaches a minimum by 6 ns. With the slightly longer wavelength of our targets (25 μm), the inversion would be delayed slightly along with the time of the minimum of the inverted sinusoid.

Gamma-Ray History

The ICF gamma-ray physics team, led by H. Herrmann and Y. Kim of P-24, completed 24 inertial confinement fusion (ICF) implosions on OMEGA over two days to investigate plasma kinetic effects and turbulent mix. Plastic capsules of four different shell thicknesses were shot at two different fill pressures for each thickness in order to vary the ion temperature and density and, consequently, the ion mean free path. Performance predictions were provided by N. Hoffman and M. Schmitt of XCP-6 prior to the shot day. Hoffman is in the process of developing a reduced ion kinetic transport model for fluid simulations of high-Knudsen-number capsule implosions, where the Knudsen number is simply the ratio of the thermal-ion mean free path to the characteristic system dimension (i.e., approximately the distance from the center of the compressed core to the cold shell). The plasma kinetic terms of ion diffusion, viscosity, and thermal conduction (i.e., conservation of mass, momentum, and energy) as well as reactivity reduction by free-streaming ion loss near the Gamow peak are incorporated into the reduced model. Turbulent mix is also allowed to play a role, although it did not appear to be a dominant factor in these implosions. By employing an extensive suite of diagnostics, we were able to acquire the most highly constrained simulations to date. Measured attributes include laser energy coupling, D–T and

D–D neutron yields and ion temperatures, fusion reaction histories, x-ray imaging, and areal densities of fuel and shell. Preliminary experimental results in terms of yield and ion temperature are reasonably close to predictions from the new model (Fig. 136.134), but there are some remaining discrepancies (by comparison, yield-over-clean was typically in the 5% to 25% range). In particular, simulations tended to slightly overpredict yields at low ion temperature (while remaining within the uncertainty of the prediction) and underpredict at high ion temperature for the 5-atm fills. Notably, the ~7-μm-thick capsules at 2-atm fill pressure did not achieve the high predicted ion temperatures (~12 versus 16 keV) but still achieved the predicted yields. Detailed experimental analysis and post-shot simulations accounting for "as-shot" parameters are in progress.
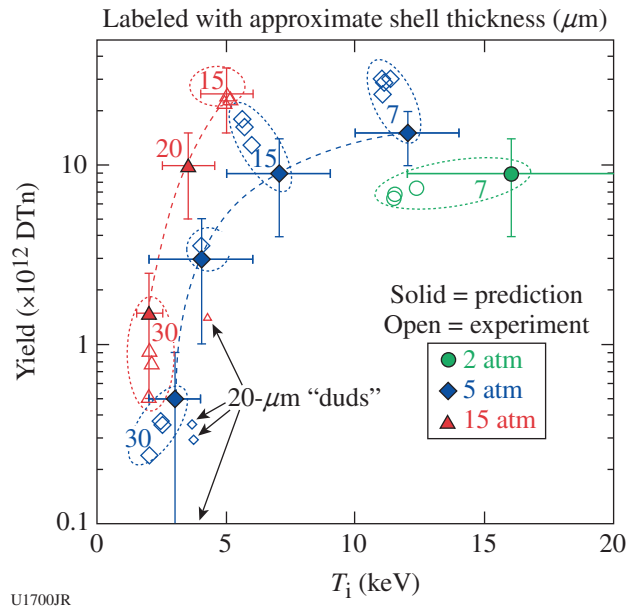

Figure 136.134
Measured and predicted yield at varying fill pressures. Simulations include new models of plasma kinetic effects that better fit the measured yields and ion temperatures.

HED–MMI

1. Spatially Resolving Mix Brings with It Difficulties in Interpretation

An exciting possible method to measure the spatial information of mixing has been doping the inner wall of a plastic shell in conjunction with a relatively new diagnostic that allows one to spectroscopically image the atomic emission. The spectroscopic imager [multiple-monochromatic imager (MMI)] consists of a pinhole array in front of an x-ray crystal. This

produces many dispersed images that can be parsed to provide images over a narrow bandwidth. Alternatively, one may obtain the spectrum emitted from particular zones of the image.

In June 2012 OMEGA experiments, LANL researchers R. Shah and J. Benage (both of P-24), in collaboration with Prof. R. Mancini's University of Nevada-Reno group, obtained images with the MMI imaging spectrometer of such doped targets. To be differentiated from experiments described below, these targets were doped uniformly around the entirety of the spherical shell. Since small-scale features were expected to dominate the mix and create symmetric annular emission, the team was surprised to instead find strongly asymmetric images. Most important, the features cast doubt on the ability to interpret if dopant emission came from central regions or was localized along the shell–fuel interface as predicted.

2. Specialized Targets Provide Insight into Spatial Features of the Mixing

To address the difficulty in interpretation, researchers worked with target fabrication teams at both LANL (Materials Science and Technology) and General Atomics. This collaborative effort resulted in fabricated targets in which only a small patch of the capsule shell was doped. Such a localized doping along the equator of the implosion coupled with imaging down the capsule pole could avoid obfuscation of interior information by surface emission. In February 2013 Shah and Benage, along with a student from the university collaboration,

returned to LLE to test this approach and its relevance to the longstanding absence of images, revealing just how deeply a shell mixes into the imploding cavity. Figure 136.135 shows images obtained at the He_β emission line with such a target using two separate spectral imagers. The two instruments were operated simultaneously and on the same shot but oriented so as to provide different views (as illustrated in the insets). In Fig. 136.135(a) the quasi-polar view very clearly shows that the brightest emission, which in the previous experiment could not be clearly identified as interior or surface, remains near the outside of the capsule. One also notes that a signal—originating from the dopant that was initially in the shell—is present across the image. The more face-on view of Fig. 136.135(b) indicates substantial transverse migration of the dopant.

DIME

For the January 2013 defect-induced mix experiment (DIME) on OMEGA, the primary objective was to demonstrate the ability to manipulate spherical implosion symmetry with 40 beams in the polar-drive (PD) configuration. Typically, with equal-power PD beams and preferred LLE pointing, our capsules compressed with an oblate (pancake) configuration—a major/minor axis ratio increasing in time to >2:1. We explored two modifications of PD: (1) The energy balance was changed for the three sets of PD beam cones as a function of polar angle, $E(\theta)$. We reduced the nominal polar cone power and increased equatorial power to mitigate the oblate effect. As we cooled the poles and provided enhanced heating to the equator, models
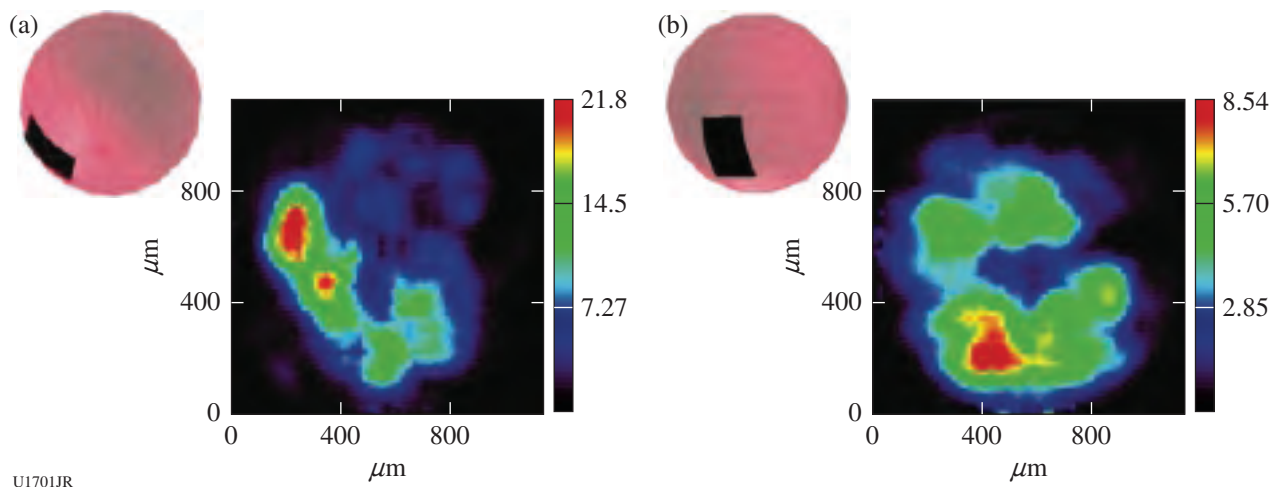

U1701JR

Figure 136.135
Images obtained with modified targets having localized doping of the shell. Spectral images formed at the He_β emission line of dopant for both (a) quasi-polar and (b) quasi-face-on views. Images were obtained using two separate multiple-monochromatic imager (MMI) instruments operating simultaneously on the same shot. Diagrams in each inset show the orientation of the patch.

and experiments showed a capsule transformation away from the oblate shape (Fig. 136.136). (2) The beam pointing was changed on the second shot day with a second $E(\theta)$ scan (see Tables 136.X and 136.XI). As predicted by simulations, the second-order Legendre mode P_2 was reduced (Fig. 136.137),
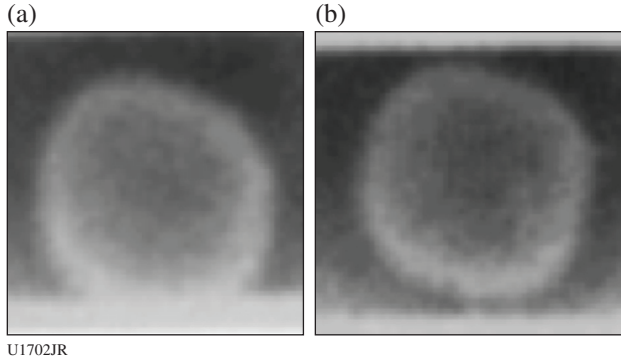

U1702JR

Figure 136.136
Images taken at time when $R \sim 0.5 \, R_0$: (a) shot 68467 and (b) shot 68469.
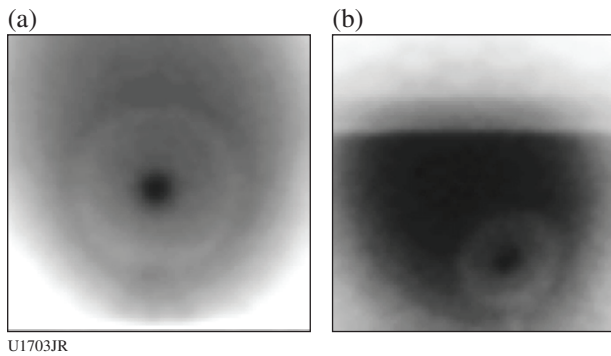

U1703JR

Figure 136.137
(a) Shot 68489 taken at time when $R \sim 0.6 \, R_0$; (b) shot 68486 taken at time when $R \sim 0.4 \, R_0$.

but a fourth-order mode P_4 left the capsules with a "rounded diamond"–like shape. This campaign proved that control of independent PD cone power and pointing can impact capsule symmetry.

DPEOS

The major goal for the dense plasma equation of state (DPEOS) project on OMEGA was to successfully obtain a complete set of EOS measurements on carbon. The technique we are using—laser-driven shock and release combined with imaging x-ray Thomson scattering—should enable us to obtain, for the first time, measurements of density, temperature, and pressure for materials at warm-dense-matter (WDM) conditions. To this end, two experimental days were carried out in FY13: the first on 13 December 2012, where we obtained 13 shots and a near-100% data return, and the second on 29 May 2013, where we completed 15 shots and also obtained a very high data return rate. The emphasis on the first day was to obtain x-ray radiographs for our targets along with improving the Thomson-scattering measurements. The results from that shot day indicated that the WDM conditions in the target were being produced too long after the laser drive was turned off, negating the effectiveness of the pressure measurement. The experimental target and laser drives were reconfigured for the second experimental day with a dramatic improvement in the results.

Our results for the second day have been analyzed, and we can now state with confidence that we have demonstrated that this technique can be used to obtain accurate measurements of density, temperature, and pressure for materials in the WDM regime. An example of our Thomson-scattering results in Fig. 136.138 shows our analyzed scattering results from shot 69918 and fits to these results at various temperatures. These

Table 136.X: DIME cone-energy variation with the usual pointings, 850-μm, 17-μm-thick CH capsule.

Shot	Cone beam energy (J)	Neutron yield	Ti (keV)	Bang time (ns)	P_2 (experiment)	P_2 (simulated)
68467	400/400/400	1.51×10^{10}	3.25	1.85	–11.1%	–16.6%
68469	333/400/433	2.45×10^{10}	3.66	1.88	–3.6%	–8.0%

Table 136.XI: DIME cone-energy variation with new pointings, similar capsules.

Shot	Cone beam energy (J)	Neutron yield	Ti (keV)	Bang time (ns)	P_2 (experiment)	P_2 (simulated)
68486	333/400/433	1.28×10^{10}	3.08	1.88	–7.5%	–6.1%
68489	400/400/400	2.01×10^{10}	3.57	1.87	–3.1%	–7.5%
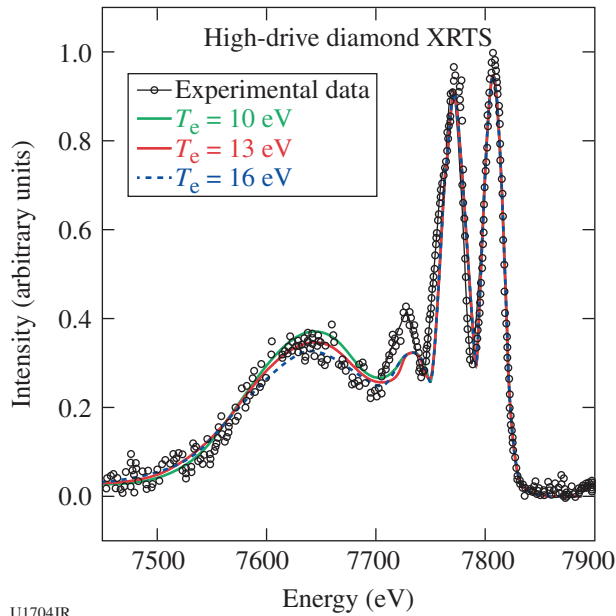
Figure 136.138
X-ray Thomson-scattering data analyzed from OMEGA shot 69918. The fits to the data utilize the known x-ray source spectrum from the Ni backlighter, the scattering angle of 100°, and the density of 2.3 g/cm^3 obtained from the radiograph of this shot.

data, combined with results from the x-ray radiography and the velocity interferometer system for any reflector (VISAR) and streaked optical pyrometer (SOP) measurements, have been used to determine density, temperature, and pressure for carbon at three distinct conditions. We find that our results compare favorably to quantum molecular dynamics (QMD) calculations at these conditions. This is shown in Fig. 136.139 where the

data are compared to QMD and several *SESAME* EOS models. There is also reasonable agreement with several EOS models for carbon, although some models compare better than others.

NIF-5

The major goal for the NIF-5 Project on OMEGA was to successfully obtain temperature measurements from shocked aerogel foams and shocked CH foams using the SOP diagnostic. To accomplish this goal, two experimental days were carried out in FY13: the first on 7 November 2012, where we obtained 15 shots and a high rate of data return, and the second on 1 May 2013, where we also completed 15 shots and obtained a high data-return rate. The emphasis on the first day was to obtain temperature data from our aerogel foam targets at a range of conditions. The second experimental day focused on the CH foams, which had an initial density of 0.15 g/cm^3.

The results for the two days indicate two important things: First, the temperatures measured for the silicon aerogel foams agree with EOS models at low pressures but drop below the models as the pressure is increased. We also find that it is below temperature values obtained using QMD calculations, which we expect to be quite accurate at these low temperatures. This is shown by the graph in Fig. 136.140. We are currently performing highly resolved simulations of the shock process to better understand the physics mechanisms behind this difference. Similar experiments on CH were conducted on the second day. The results were a little surprising because the effective temperatures were quite a bit lower than the aerogel temperatures for a given pressure drive. This is likely because of the higher bond and ionization energies for CH. Further data analysis is ongoing.
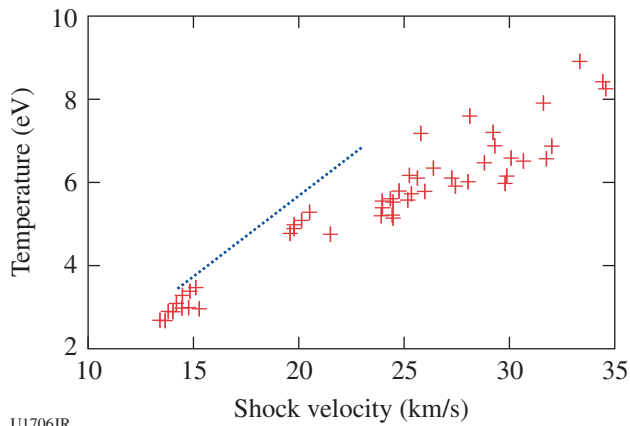

Figure 136.139
Comparison of warm-dense-matter (WDM) carbon measurements to various isochors of equation-of-state (EOS) models of carbon. The data points (marked by inclusion of error bars) represent carbon at 2.8 g/cm^3 and 5.5 eV, 3.1 g/cm^3 and 11 eV, and 2.3 g/cm^3 and 13 eV. The corresponding quantum molecular dynamics (QMD) calculations are color matched and compare very well with the data except for the 11-eV point. For this case we have plotted the QMD results for 3.0 g/cm^3 and several temperatures that fall within the uncertainty of the measurements.

U1706JR

Figure 136.140
Streaked optical pyrometer (SOP) temperature measurements for shocked aerogel foam. The red crosses represent individual data points and the green curve is from QMD calculations for the EOS of the shocked foam.

MagLPI

The goal of the MagLPI campaign at the Omega Laser Facility is to demonstrate laser–plasma instability (LPI) mitigation using magnetic fields. Using a sufficiently strong external magnetic field, thermal heat transport is expected to be reduced across a magnetic field since the transport step size is determined by the electron Larmor radius instead of the electron–ion collisional mean free path. In this regime of "magnetic insulation," the plasma electron temperature is expected to increase compared to the case with no external field. The ability to increase the underdense plasma temperature in a NIF ignition hohlraum is highly desirable since it would reduce inverse bremsstrahlung losses of the NIF inner beams as they propagate through the long-scale-length low-Z plasma. In addition, increasing the plasma temperature would significantly increase Landau damping and help mitigate stimulated Raman scattering (SRS).

Using a magneto-inertial fusion electrical discharge system (MIFEDS)–pulsed magnetic coil, an external field up to $B_z =$ 8 T was applied with the field aligned along the axis of a gas-filled hohlraum on OMEGA (Fig. 136.141). The hohlraum axis was aligned along the P9–P4 ports and 39 beams irradiated the hohlraum in three beam cones. The 4ω Thomson-scattering beam probed the plasma at the center of the hohlraum, as viewed through a diagnostic hole at the hohlraum midplane. The specific deliverables for this campaign were to measure the electron temperature, SRS backscatter, and hard x rays versus B-field strength.

A total of nine target shots were performed on 20 August 2013. Preliminary results indicate an increase in plasma temperature with external B field, and the correlation with LPI and
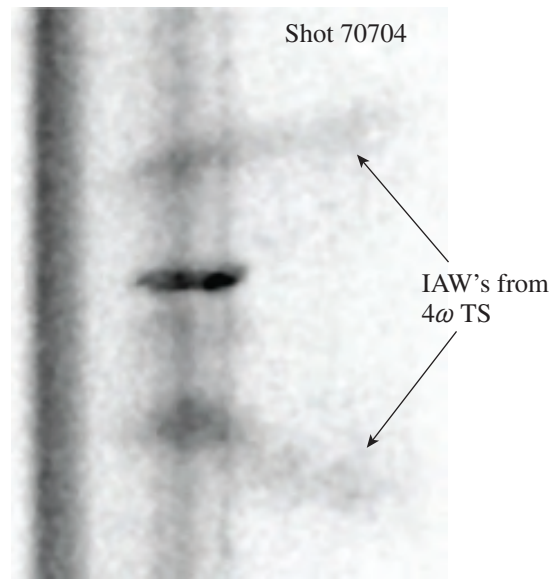
B-field strength is currently being analyzed as seen by data in Fig. 136.142.
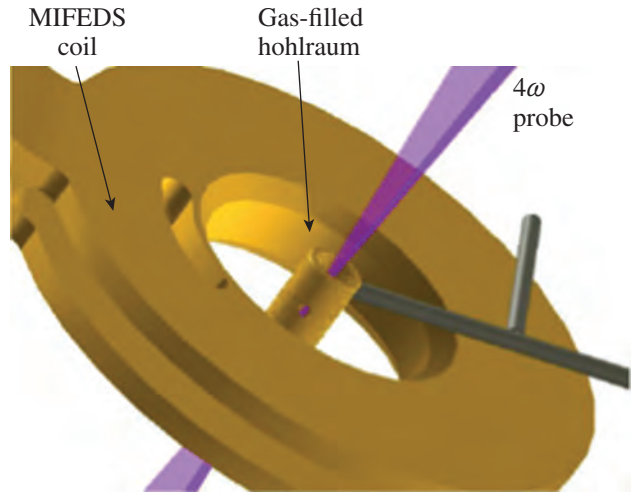
U1707JR

Figure 136.141
Schematic of experimental layout with a magneto-inertial fusion electrical discharge system (MIFEDS) coil, which generates an external magnetic field, and the hohlraum axis aligned along the $4\times$ Thomson probe-beam axis.

U1708JR

Figure 136.142
Thomson-scattering (TS) measurement from thermal levels of ion-acoustic waves (IAW's). Wavelength is in the vertical axis and time increases to the right. The separation between the IAW's increases with increasing plasma temperature.

Gamma-Ray Imaging

On 6 August 2013, LANL successfully executed a full day of shots on OMEGA in support of two experimental science campaigns. Characterization data of a novel gamma-ray imaging camera were collected, as well as hard x-ray aperture images of bremsstrahlung radiation produced by hot electrons traversing the remnant shell material from implosions of plastic capsules. The gamma-ray imaging diagnostic is being developed by LANL in collaboration with the University of Arizona's Center for Gamma Ray Imaging. Additionally, LANL collected data in support of its Turbulent MIX DR project, shooting a variety of separated reactant targets comprised of ^{3}He-filled plastic capsules constructed with 1-μm-thick deuterated layers within the inner regions of a CH shell. In these experiments D–^{3}He fusion reactions are used as the direct signature for atomic mix. Good neutron and proton yield data were collected, as well as gamma images of the implosions, as illustrated in Fig. 136.143.

Neutron Imaging System

Imaging technologies are typically benchmarked with a known system to determine the residual distortions. In radiography a standard static object is imaged in transmission, the analysis techniques are applied, and the result of the analysis is compared to the known object. This allows one to characterize the performance of the image formation and reconstruction algorithms. One of the difficult aspects of neutron imaging has been that no "standard" neutron source is available to perform this type of test. This has resulted in a strong reliance on modeling and simulation to characterize the performance of the image formation and reconstruction algorithms. No neutron source is suitable because the system is designed to image sources that are very bright ($\sim10^{17}$ neutrons/cm^2 at the source surface) and very small (~100 μm in diameter). The system was designed and tested through measurements on OMEGA, but these dynamic sources are not well enough characterized and reproducible to be used as a standard neutron source for benchmarking the full system performance.

A series of experiments have been performed on OMEGA in the last year to overcome this limitation. In the design of these experiments, simulations were used to determine the neutron flux at the detector, which results from a known neutron source after passing through the aperture array. A copper object was designed to generate this same neutron flux at the image plane when located just in front of the image collection system. These known static objects were then placed in front
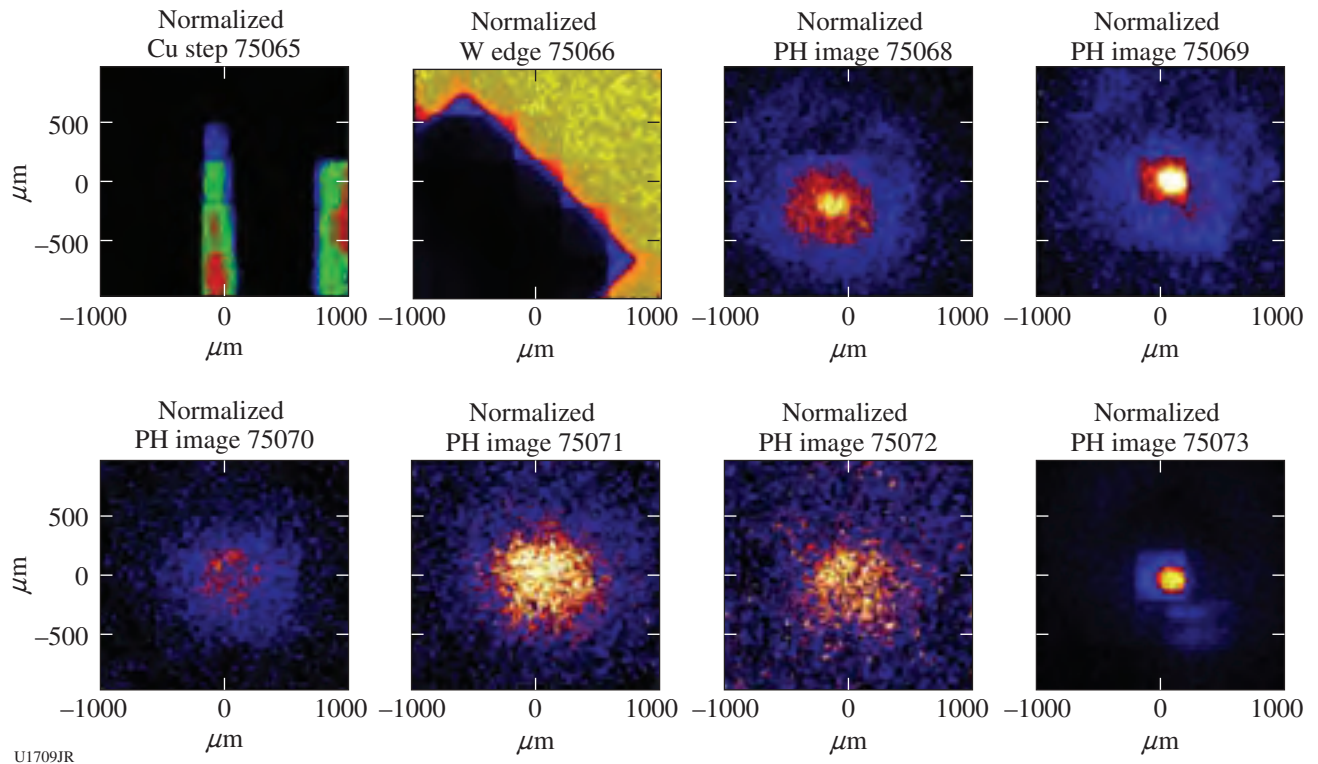

Figure 136.143
Several images taken using the gamma-ray imaging diagnostic.

of the image collection system on OMEGA, and the neutron flux passing through these objects was measured. The standard analysis techniques were used to extract the source information from these images, and this information was compared to the simulated neutron source. These experimental data have allowed us to determine the system performance, including the detector and reconstruction algorithms, and to partially overcome the limitation of not having a standard neutron source for benchmarking our detection and reconstruction algorithms.

Figure 136.144 shows the two images collected from two test objects. Figure 136.144(a) shows the neutron flux after passing through an object designed to simulate a point source of neutrons, while Fig. 136.144(b) shows the flux from a 20-μm-diam neutron source. These test objects were designed to generate the neutron flux that would be expected from the NIF geometry through the mini-penumbra presently being used on the NIF.
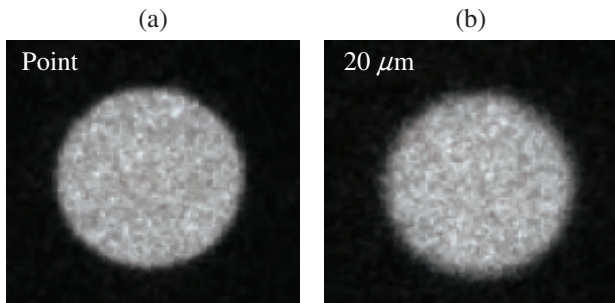

(a)   (b)

Point   20 μm

Figure 136.144
(a) Mini-penumbral image expected from a point source of neutrons through the NIF mini-penumbra; (b) mini-penumbral image expected from a neutron source with a P_0 of 20 μm.

The standard set of reconstruction algorithms, which were developed for NIF data analysis, was used to process and reconstruct these images. The results are shown in Fig. 136.145.

Over the past year a significant effort has been devoted to determining error bars in the reconstructed parameters. These estimates have come directly from simulations. One would expect that these measurements should be consistent, however, with these error bars. To check this, simulations have been performed to determine the error bars in P_0 and P_2 for the extended source shown above to be ±1 μm±5%, respectively. This is in good agreement with the observed reconstruction values.

These measurements have provided a test of our imaging system and analysis scheme using simulation through the aperture array combined with experimental measurements at each
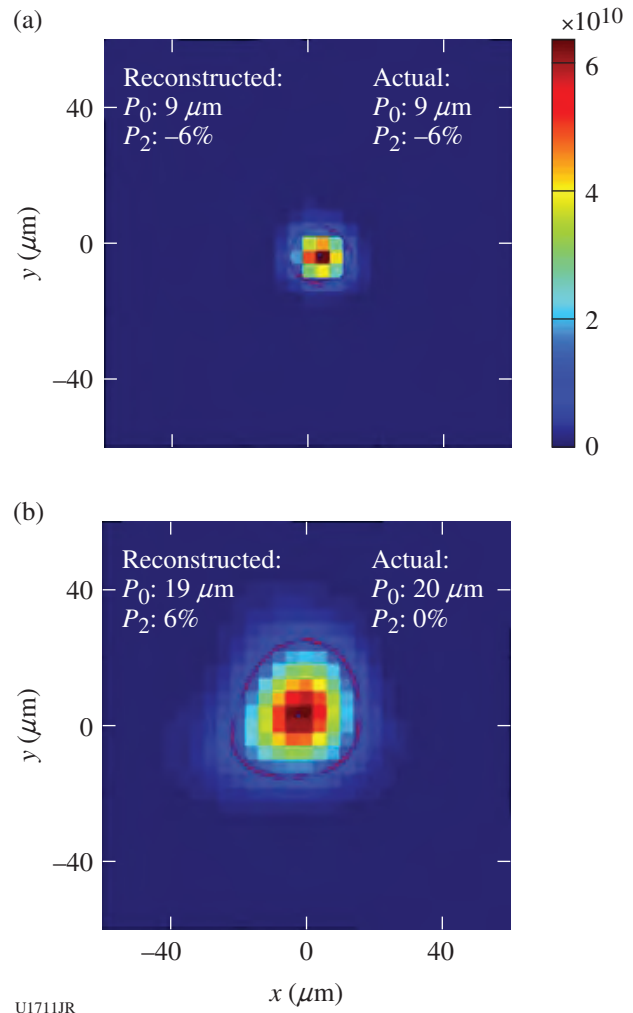

Figure 136.145
Reconstruction of the images in Fig. 136.144. (a) The point source reconstructed to have a radius or P_0 of 9 μm and the source with a P_0 of 20 μm resulted in a reconstructed P_0 of 19 μm. The reconstruction of the point source provides a measure of the reconstructed resolution of this system. The good agreement between the actual and reconstructed P_0 of the extended source demonstrates the performance of the reconstruction algorithms.

level. It has been demonstrated that the reconstructed resolution of the mini-penumbral apertures is ~10 μm and has provided confidence in our determination of error bars.

The DIME series of experiments, which are planned on the NIF in the coming years, will rely on the neutron imaging system for a measure of the extent of mixing in the implosion of separated reactant capsules. This requires the measurement and reconstruction of the neutron source in the shape of a spherical shell. The thickness of this spherical shell provides a measure of the extent of mixing in these experiments. A series of measurements on OMEGA have been performed to test the mini-penumbral aperture being proposed for this

measurement. A test object was constructed, similar to the objects described above, that can generate the flux of neutrons expected in these DIME experiments on the NIF. These measurements were made to test the measurement and reconstruction methods to determine how well these mini-penumbra could be used to reconstruct a spherical shell neutron source. These measurements were collected in August 2013 so the analysis is not complete, but the results are encouraging. The reconstruction of this neutron source (Fig. 136.146) shows that the general characteristics of the spherical shell are recovered in these reconstructions.
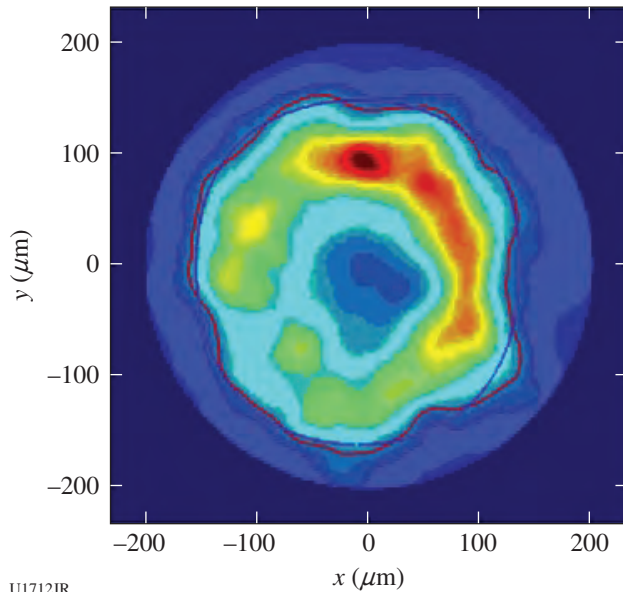

U1712JR

Figure 136.146
Reconstruction of the measured neutron flux from the test object that generates the flux of neutrons expected from the DIME experiments on the NIF (150-mm radius with 50-mm width). This shows a clear spherical source. These data provide an opportunity for comparisons to simulation, ultimately characterizing the error bars associated with this type of measurement.

Neutron-generating experiments on OMEGA continue to provide important data to fully characterize the neutron imaging system at the NIF. These measurements provide a stringent test of our simulations and models as well as providing known sources for the testing of our reconstruction algorithms.

FY13 CEA Experiments at the Omega Laser Facility

CEA Vulnerability Diagnostics on OMEGA
Typical high-yield DT shots at the Omega Laser Facility can deliver up to 10^{14} 14-MeV neutrons. These shots generate an integrated dose in the range of 1 to 10 mrad at 5 m from target chamber center (TCC).

Simulations of 10^{16} neutron-DT shots on megajoule-class facilities such as the National Ignition Facility (NIF) or Laser Mégajoule (LMJ) show that the integrated dose in the immediate surroundings of a diagnostic inserter and in the first 100 ns of the experiment (i.e., time of flight of 14-MeV neutrons from TCC to the target chamber wall) is ~10 mrad. The Omega Laser Facility is therefore an appropriate facility at which to reproduce the dose rates expected during the first 100 ns on megajoule-class laser facilities and can be used to study the survivability of diagnostic elements such as optical relays or optical analyzers.

Continuing FY12 studies, a standard optical-relay system consisting of two Maksutov objectives, a filed lens, a light amplifier, and a cooled charge-coupled–device (CCD) camera, has been exposed to high-neutron-yield shots at a distance of 6 m from TCC (see Fig. 136.147). The level of nuclear background generated on OMEGA leads to visible effects on the recorded image using the CCD camera (see Fig. 136.148), which has been quantified by using masks positioned along the optical path,
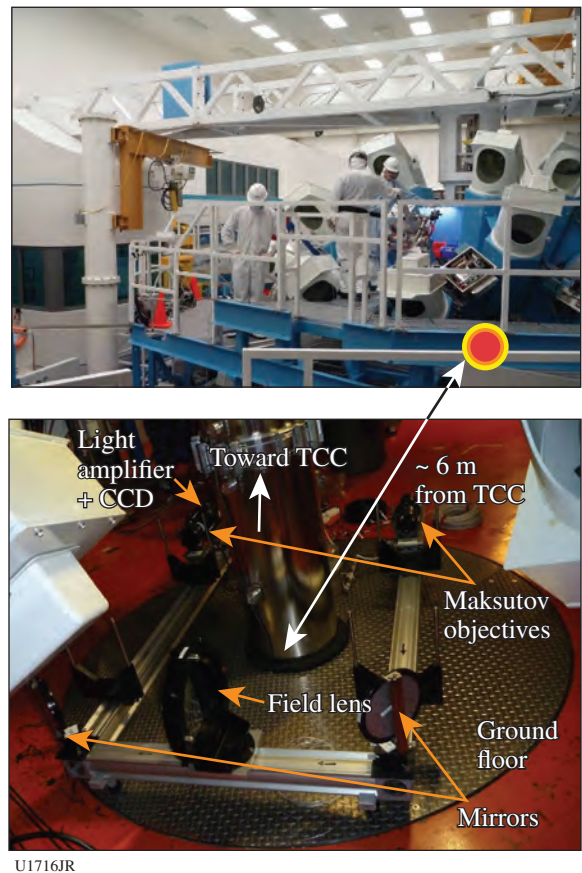

U1716JR

Figure 136.147
Optical-relay benchmark experimental setup.

isolating the contributions of the main components of this optical system. As a result (see Fig. 136.149), the increasing background level of the recording device was clearly proportional to the neutron fluence. In addition, the dynamic loss induced by the optical relay is very low compared to a fiber-optic bundle. The robustness has been checked and extrapolation to NIF or LMJ radiative constraints leads us to expect the diagnostic will be successful. Therefore, such an optical relay presents a hardened architecture and could be used as a diagnostic.

Radiation-tolerance studies of a complementary metal–oxide–semiconductor (CMOS) image sensor used in plasma diagnostics have been performed in a collaboration with CEA, the Institut Supérieur de l'Aéronautique et de l'Espace (ISAE, Toulouse), and the University of Saint-Etienne. Previous experiments performed in April 2012 demonstrated the relevance of the global reset functionality. The CMOS sensor is now part of a basic x-ray imaging diagnostic composed of a pinhole array and a thin layer of P43 (a long-decay-time scintillator) layered on the sensor surface (see Fig. 136.150). This diagnostic was inserted via a ten-inch manipulator (TIM) into the chamber and exposed to neutron yields produced by OMEGA DT shots in an attempt to record an x-ray self-emission image of the imploding target. As expected, the global reset mode significantly reduced the transient perturbation (parasitic white pixels) without degrading the image quality (see Fig. 136.151), but the

x-ray image resolution was very poor due to the bad quality of the scintillator deposition on the sensor.

Nevertheless, this first attempt was successful and improvements in the experiment design will be completed for the next neutron campaign in 2014.
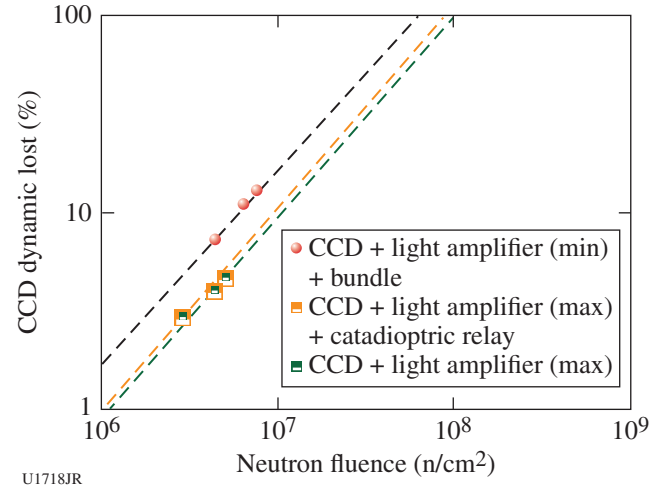

U1718JR

Figure 136.149
Parasitic signal intensity converted into a charge-coupled–device (CCD) dynamic-range loss.
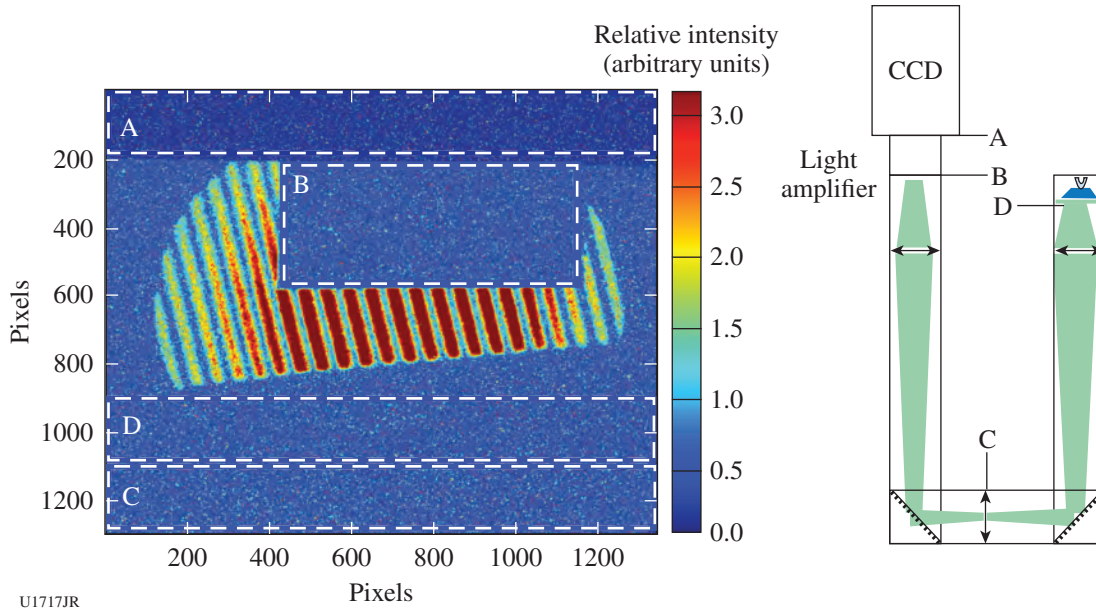

U1717JR

Figure 136.148
Typical image recording on the optical-relay benchmark for neutron yield of 10^{13}. Four masks distributed along the optical path isolate four zones into the image.
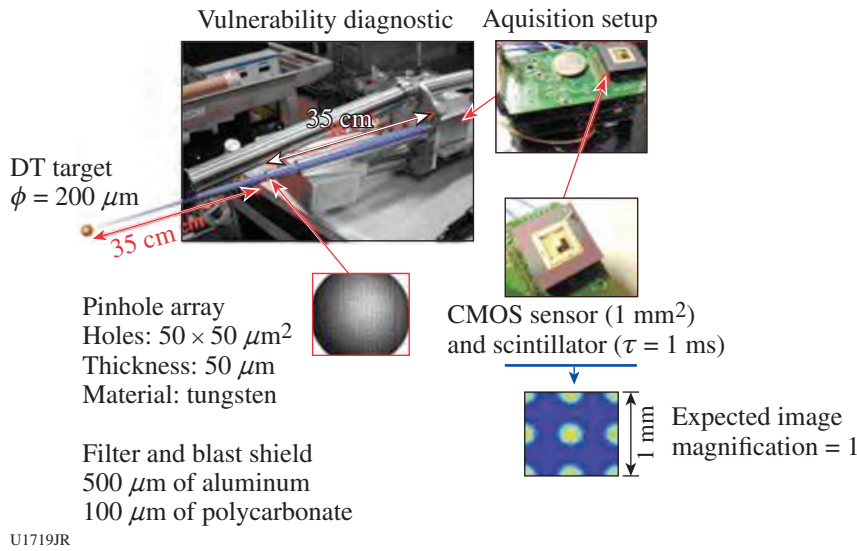
Figure 136.150
Basic x-ray imaging diagnostic experimental setup.

Figure 136.151
Typical image recording for a 10^{13} neutron yield. The global-reset mode proved its efficiency and the CMOS sensor was still operational after 13 shots, even though a slight increase of dark current was observed.

Diagnostic Development

The DEMIN (detector Micromegas for neutrons) neutron spectrometer[64] designed by CEA was successfully qualified and tested on OMEGA in FY13. DEMIN is based on a neutron-to-proton converter (CH foil, 2 mm thick) followed by a thin Micromegas chamber (600 μm thick) (Ref. 65). Neutrons are detected individually on the striped Micromegas anode and neutron energy is measured by the time-of-flight technique. Because of the thin Micromegas chamber dimensions, the signals exhibit good timing properties [~2-ns rise time for a good energy resolution and ~3-ns full width at half maximum (FWHM) to record more than one neutron per strip, important for obtaining enough statistics in the final spectrum]. This original setup makes the diagnostic rather insensitive to gamma rays since the gas-ionization probability for an electron is low, compared to recoil protons (see Fig. 136.152). DEMIN is, therefore, designed to measure the areal density $\langle \rho R \rangle$ in high-neutron-yield implosions by detecting tertiary or secondary neutrons in DT or DD implosions, respectively.
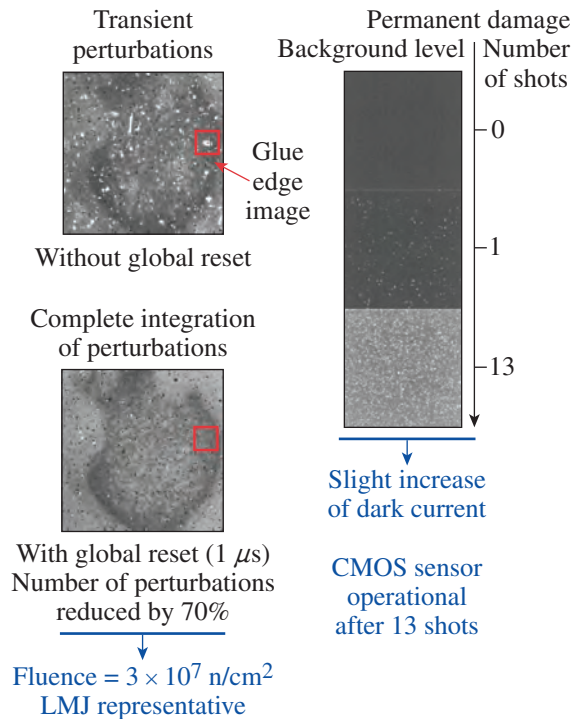
In November 2012 and March 2013, DEMIN was tested on TT (11 shots) and DT (13 shots) gas implosions. Its first use in November was made possible only with the help and involvement of all LLE teams. The aim of these experiments was to test the diagnostic in a harsh environment, to show the capability to measure individual neutrons after the intense 14-MeV peak, and to verify the insensitivity to gamma rays. Prior to the experiments, DEMIN was fully qualified on OMEGA. DEMIN is positioned on the personnel access port (H20), at 2.84 m from TCC (see Fig. 136.153). The aluminum
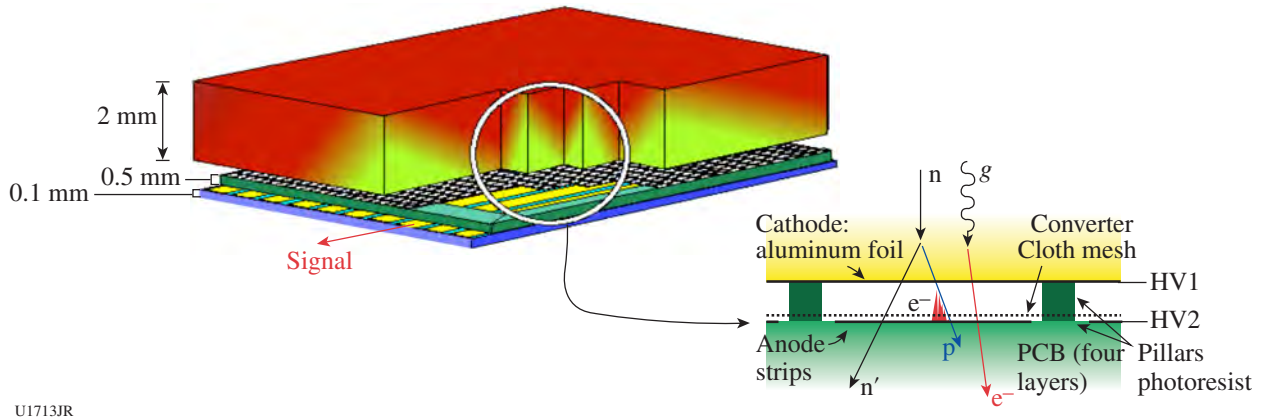
U1713JR

Figure 136.152
Schematic view of the DEMIN concept. Ionization electrons are produced along the path of scattered protons. They drift and are amplified due to the polarizations and are finally detected on the strips. Conversely, electrons produced by γ rays go through the gaps with a low-ionization probability.
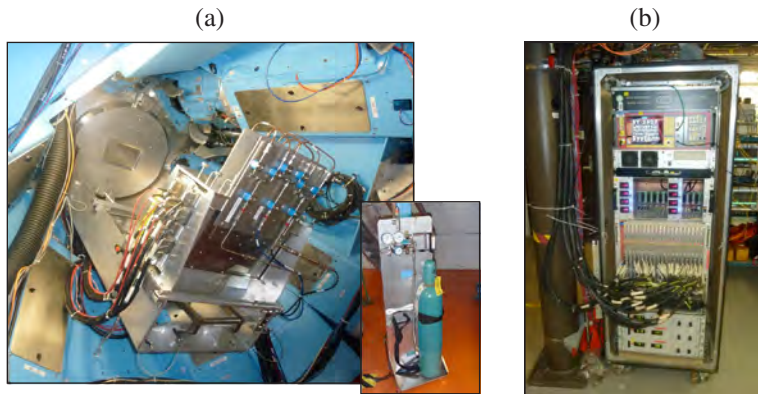
U1714JR

Figure 136.153
DEMIN experimental setup. (a) DEMIN 160-channel prototype positioned on the ManHatch port, viewing the thinned aluminum window. Inset: Part of the gas-distribution system, designed by LLE teams. (b) Electronic bay (acquisition system, HV and LV power supply, etc.) located in La Cave.

window was reduced to a 5-mm thickness by LLE staff to take into account DEMIN constraints. The gas-distribution system (gas bottle, tubing, manifold, pressure gauges, etc.), was designed by LLE's Mechanical Design Group and is fully operational. A gas mixture consisting of He (89%), isobutan (5%), and CF_4 (6%) was used to achieve correct signal shapes. For these experiments, a 160-channel prototype was tested. The data-acquisition system, composed of 20 eight-channel digitizer boards,[66] was located in La Cave. Data-acquisition and Micromegas high voltages were remotely controlled to avoid manual intervention between shots.

Raw DEMIN signals, recorded on a TT implosion (shot 67958, $Y_{14\text{ MeV}} = 3.5 \times 10^{12}$, $Y_{TT} \sim 1.5 \times 10^{12}$) are presented

for three adjacent strips in Fig. 136.154. After a saturated 14-MeV peak, individual neutrons were clearly identified, with decreasing energy according to their time of flight. TT neutrons and sub-MeV neutrons are also detected. The intensity of an individual neutron signal is not proportional to neutron energy, since it depends on the recoil proton-deposited energy in the gas. Therefore, neutron energy can be retrieved only by the neutron arrival time. Before the arrival of 14-MeV neutrons, we observed small signals caused by gamma rays produced by the interaction of 14-MeV neutrons on the aluminum chamber, showing good insensitivity to gamma rays. Nevertheless, a 5-mm lead shielding is necessary to avoid direct gas ionization by an intense x-ray flux. Signals exhibit a good signal-to-noise ratio and no cross-talk between strips was observed.
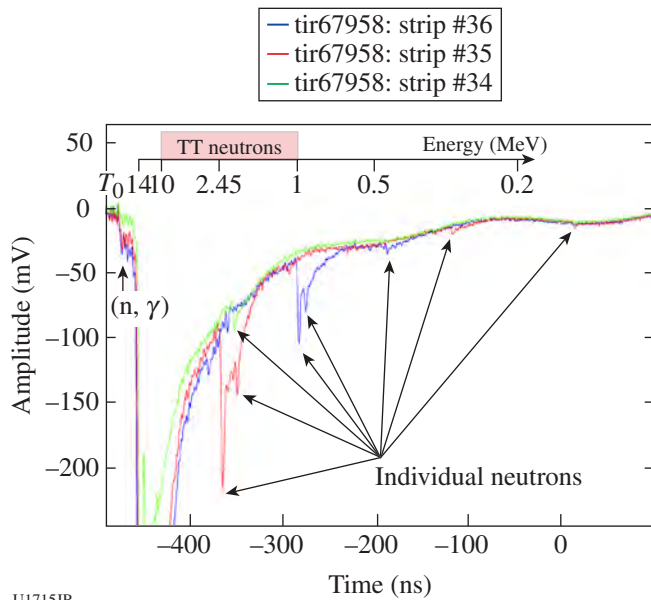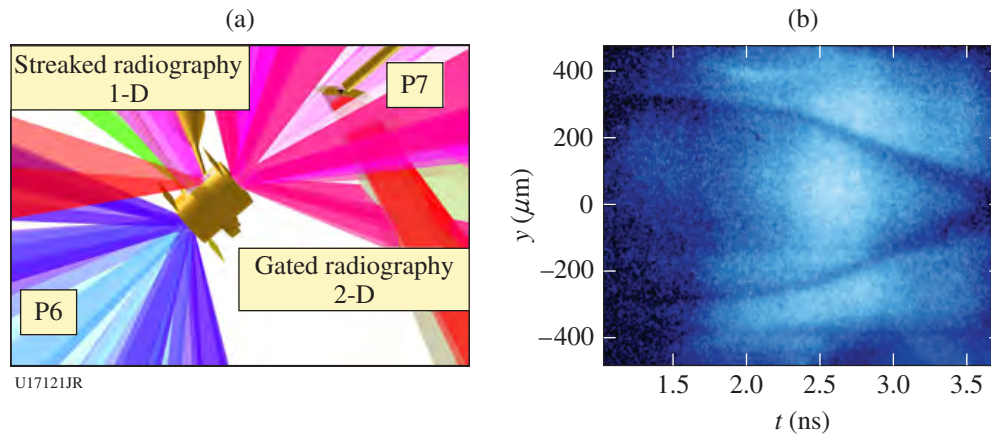
Figure 136.154
Raw DEMIN signals recorded on three adjacent DEMIN strips for a TT implosion (shot 67958, $Y_{14\,MeV} = 3.5 \times 10^{12}$).

Convergent Ablation Measurements Using a Gas-Filled Rugby Hohlraum on OMEGA

The baseline design for implosion experiments on the LMJ relies on a rugby-shaped hohlraum, which presents significant advantages in terms of laser–plasma interaction (LPI) mitigation,[67] coupling efficiency, and symmetry control with energy balance.[68] The increased x-ray flux on capsules in the rugby hohlraum compared to a classical cylindrical hohlraum was subsequently confirmed at the OMEGA scale by enhanced fusion performances.[69] It is, nevertheless, important to acquire convergent ablation measurements[70] to assess the implosion velocity, a key metric for implosion performance. Convergent-ablation experiments with a gas-filled rugby hohlraum were, therefore, performed at the Omega Laser Facility.

A time-resolved 1-D streaked radiography of the capsule implosion [see Fig. 136.155(a)] was acquired in the direction perpendicular to the hohlraum axis, whereas a 2-D gated radiography was acquired on an x-ray framing camera at the same time along the hohlraum axis. The implosion trajectory was measured for various kinds of uniformly doped ablators, including germanium-doped and silicon-doped polymers (CH), at two different doping fractions (2% and 4% by atom). It has, in fact, been demonstrated that Si-doped ablators are more efficient than Ge-doped ones at the NIF scale.[70] A typical backlight implosion is shown in Fig. 136.155(b) for the case of a silicon-doped polymer (4% atomic fraction) with an initial ablator thickness of 55 μm. The position of the external limb of the capsule could easily be extracted by an automatic edge-detection algorithm. The experimental implosion trajectory is compared with an FCI2 post-processed radiograph [see Fig. 136.156(a)]. One should notice that fully integrated 2-D simulations (including hohlraum and capsule) are necessary to describe the dynamics of the implosion. Preliminary post-shot

Figure 136.155
(a) Experimental configuration along P6/P7. The streaked implosion radiography was performed toward H14, perpendicular to the hohlraum axis. (b) Typical streaked radiography on a capsule implosion in a gas-filled rugby hohlraum.

simulations are shown in Fig. 136.156. The general tendency is that the simulated trajectories converge slightly earlier than the experimental radiographs, which is consistent with the late bang times (~200 to 300 ps) measured in rugby implosion experiments on OMEGA.

Figure 136.156(b), however, shows that the final limb velocity does not show an important velocity deficit as observed in NIF implosions. In that case, the final limb velocity is close to 200 μm/ns[1] ($\pm$20 μm/ns[1]) and FCI2 simulations remain in the error bars of the measurements. Final implosion velocities in excess of 300 μm/ns[1] were achieved even in the case of thinner ablators. This rich implosion database will be used to benchmark FCI2 simulations of germanium and silicon-doped ablators and to test the rocket model in the high-ablation regime limit.[71]
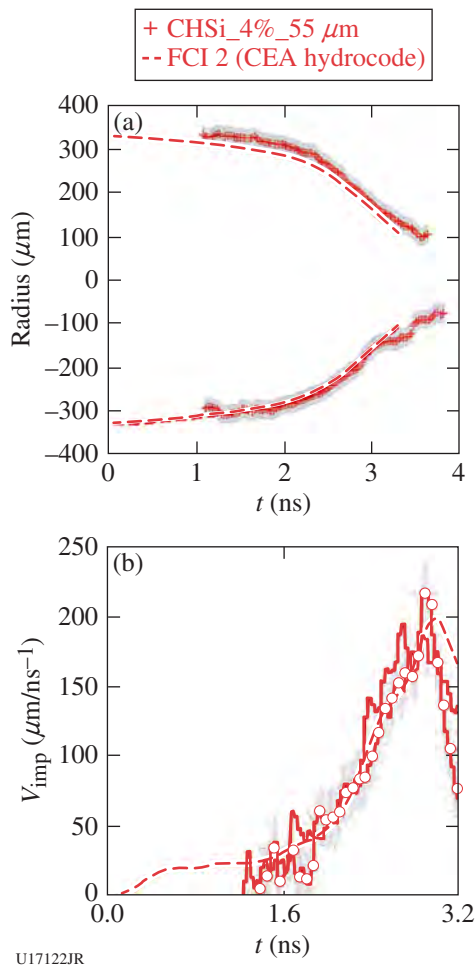

U17122JR

Figure 136.156
(a) Comparison of experimental limb trajectory with FCI2 post-processed simulations. (b) Comparison of experimental and simulated implosion velocities.

Laser-Imprint Mitigation Using Underdense Foams

Laser-beam smoothing by parametric instabilities in low-density foams has been observed in previous experiments.[72] During the ImprintMit-13A campaign on OMEGA, we investigated for the first time the effects of low-density foams on the subsequent Rayleigh–Taylor growth.

The foams used in this campaign—manufactured at Lebedev Institute—were low-density $C_{15}H_{20}O_6$ aerogels with an ~1-μm pore size. They were formed in the center of a Cu washer that was glued to a 15-μm-thick CH foil. A 1-mm-wide slit in the washer side allowed us to measure the self-emission from the ionization wave propagating through the foam and from the accelerated CH foil. The foam was used to mitigate the laser imprint. Indeed, during its propagation through the foam plasma, the laser drive's parametric instabilities, such as forward stimulated Brillouin scattering and filamentation, led to an effective smoothing of the hot-spot pattern. Because of the low density of the foam, the ionization was supersonic and no shock wave was created.

Figure 136.157 shows the experimental configuration. Specific phase plates (M30 and M60) that created 2-D intensity modulations were mounted on one of the drive beams. Imprint conditions were therefore well known and reproducible from shot to shot. The target was either a CH foil alone (to make a reference imprint measurement) or a foil glued to a washer
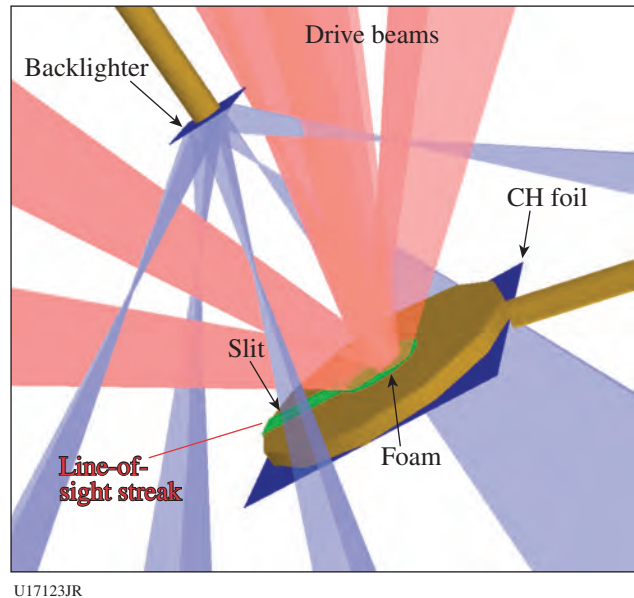

U17123JR

Figure 136.157
Experimental configuration for the ImprintMit-13A campaign. Drive beams (red) illuminating the underdense foam and backlighter beams (blue) are represented.

containing the foam of various densities: 5, 7, or 10 mg/cm^3. The drive pulse was either a 2-ns square pulse at 3×10^{14} W/cm^2 (CH foil alone) or a 2-ns step pulse with a higher intensity during the first nanosecond (target with foam) to balance the energy absorbed in the foam and maintain the laser drive on the CH foil. The growth of target modulations has been measured with x-ray face-on radiography using a uranium backlighter (~1.3 keV) on an x-ray framing camera (XRFC) with 10-μm spatial resolution and 80-ps temporal resolution. The side view self-emission was measured through the slit with a streak camera and showed that trajectories of the foil with and without foam were equivalent [as shown in Figs. 136.158(a) and 136.158(b)].
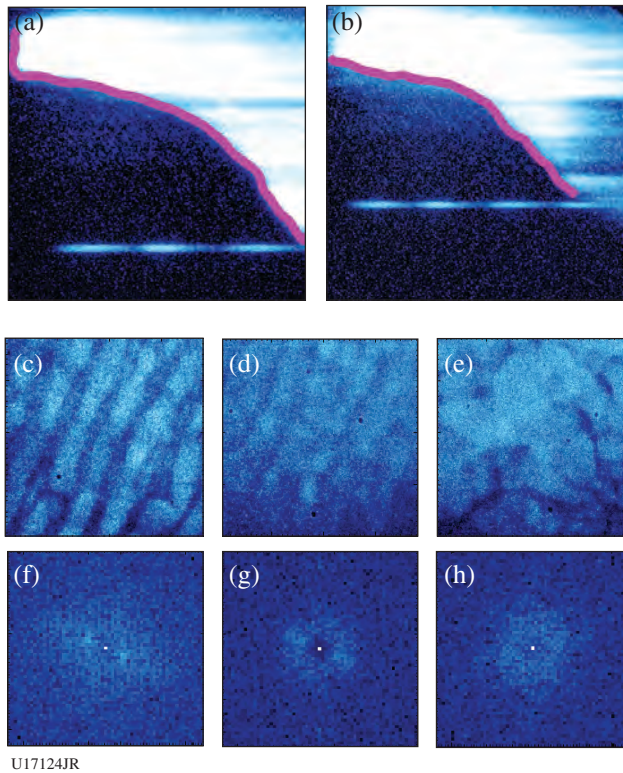

U17124JR

Figure 136.158
Self-emission streak-camera measurements for a foil (a) without and (b) with foam; [(c)–(e)] x-ray framing-camera (XRFC) radiographies and [(f)–(h)] corresponding 2-D Fourier spectra [(c),(f)] imprinted by the M60 phase plate on a CH foil, [(d),(g)] CH foils with 7-mg/cm^3 foam, and [(e),(h)] 5-mg/cm^3 foam 1.41 ns, 1.35 ns, and 1.19 ns, respectively, after the beginning of the acceleration of the ablation front.

Figure 136.158 shows typical experimental XRFC radiographies and the corresponding 2-D Fourier spectra. The imprinting phase plate was the M60, which means that the initial perturbations are 2-D 60-μm–wavelength modulations. These modulations were observed on the first radiography of a target without foam. To summarize the analysis of the images in Fig. 136.158, the initial 2-D pattern imprinted without foam was smoothed in the case of the 7-mg/cm^3 foam and completely disappeared with the 5-mg/cm^3 foam. On the other hand, 3-D modulations appeared with the foams, especially with the one at 5 mg/cm^3. The mechanisms that created those modulations are not completely understood but different options are being investigated: the nonuniformities imprinted by the SG4 beams, the roughness of the CH foil, or an effect of the foam during early laser propagation.

During the experimental campaign ImprintMit-13A on OMEGA, we demonstrated for the first time the effect of low-density foams on the hydrodynamic instability mitigation. A smoothing of the initial pre-imposed perturbation is clearly shown. Several observed features must be investigated further, however, and the interpretation of the experiments is still in progress.

REFERENCES

1. K. Yirak *et al.*, High Energy Density Phys. **9**, 251 (2013).

2. G. Gregori *et al.*, Astrophys. J. **527**, L113 (1999).

3. G. Gregori *et al.*, Astrophys. J. Lett. **543**, 775 (2000).

4. P. Hartigan, J. Palmer, and L. I. Cleeves, High Energy Density Phys. **8**, 313 (2012).

5. V. E. Fortov *et al.*, Phys. Rev. Lett. **99**, 185001 (2007).

6. F. Soubiran *et al.*, Phys. Rev. B **86**, 115102 (2012).

7. P. Loubeyre, S. Brygoo, J. Eggert, P. M. Celliers, D. K. Spaulding, J. R. Rygg, T. R. Boehly, G. W. Collins, and R. Jeanloz, Phys. Rev. B **86**, 144115 (2012).

8. P. M. Celliers, P. Loubeyre, J. H. Eggert, S. Brygoo, R. S. McWilliams, D. G. Hicks, T. R. Boehly, R. Jeanloz, and G. W. Collins, Phys. Rev. Lett. **104**, 184503 (2010).

9. M. J.-E. Manuel, C. K. Li, F. H. Séguin, N. Sinenian, J. A. Frenje, D. T. Casey, R. D. Petrasso, J. D. Hager, R. Betti, S. X. Hu, J. Delettrez, and D. D. Meyerhofer, Phys. Plasmas **20**, 056301 (2013).

10. C. K. Li *et al.*, New J. Phys. **15**, 025040 (2013).

11. C. K. Li, F. H. Séguin, J. A. Frenje, N. Sinenian, M. J. Rosenberg, M. J.-E Manuel, H. G. Rinderknecht, A. B. Zylstra, R. D. Petrasso, P. A. Amendt, O. L. Landen, A. J. Mackinnon, R. P. J. Town, S. C. Wilks, R. Betti, D. D. Meyerhofer, J. M. Soures, J. Hund, J. D. Kilkenny, and A. Nikroo, Nucl. Fusion **53**, 073022 (2013).

12. N. Sinenian *et al.*, Plasma Phys. Control. Fusion **55**, 045001 (2013).

13. D. T. Casey, J. A. Frenje, M. Gatu Johnson, F. H. Séguin, C. K. Li, R. D. Petrasso, V. Yu Glebov, J. Katz, J. Magoon, D. D. Meyerhofer, T. C.

Sangster, M. Shoup, J. Ulreich, R. C. Ashabranner, R. M. Bionta, A. C. Carpenter, B. Felker, H. Y. Khater, S. LePape, A. MacKinnon, M. A. McKernan, M. Moran, J. R. Rygg, M. F. Yeoman, R. Zacharias, R. J. Leeper, K. Fletcher, M. Farrell, D. Jasion, J. Kilkenny, and R. Paguio, Rev. Sci. Instrum. **84**, 043506 (2013).

14. N. Sinenian, W. Theobald, J. A. Frenje, C. Stoeckl, F. H. Séguin, C. K. Li, R. D. Petrasso, and R. B. Stephens, Phys. Plasmas **19**, 112708 (2012).

15. M. J. Rosenberg, J. S. Ross, C. K. Li, R. P. J. Town, F. H. Séguin, J. A. Frenje, D. H. Froula, and R. D. Petrasso, Phys. Rev. E **86**, 056407 (2012).

16. M. J.-E. Manuel, "Rayleigh-Taylor-Induced Electromagnetic Fields in Laser-Produced Plasmas," Ph.D. thesis, Massachusetts Institute of Technology, 2013.

17. N. Sinenian, "Fast-Ion Spectrometry of ICF Implosions and Laser-Foil Experiments at the Omega and MTW Laser Facilities," Ph.D. thesis, Massachusetts Institute of Technology, 2013.

18. T. R. Boehly, D. L. Brown, R. S. Craxton, R. L. Keck, J. P. Knauer, J. H. Kelly, T. J. Kessler, S. A. Kumpan, S. J. Loucks, S. A. Letzring, F. J. Marshall, R. L. McCrory, S. F. B. Morse, W. Seka, J. M. Soures, and C. P. Verdon, Opt. Commun. **133**, 495 (1997).

19. L. J. Waxer, D. N. Maywar, J. H. Kelly, T. J. Kessler, B. E. Kruschwitz, S. J. Loucks, R. L. McCrory, D. D. Meyerhofer, S. F. B. Morse, C. Stoeckl, and J. D. Zuegel, Opt. Photonics News **16**, 30 (2005).

20. C. K. Li, F. H. Séguin, J. A. Frenje, J. R. Rygg, R. D. Petrasso, R. P. J. Town, P. A. Amendt, S. P. Hatchett, O. L. Landen, A. J. Mackinnon, P. K. Patel, V. Smalyuk, J. P. Knauer, T. C. Sangster, and C. Stoeckl, Rev. Sci. Instrum. **77**, 10E725 (2006).

21. J. R. Rygg, F. H. Séguin, C. K. Li, J. A. Frenje, M. J.-E. Manuel, R. D. Petrasso, R. Betti, J. A. Delettrez, O. V. Gotchev, J. P. Knauer, D. D. Meyerhofer, F. J. Marshall, C. Stoeckl, and W. Theobald, Science **319**, 1223 (2008).

22. F. H. Séguin, C. K. Li, M. J.-E. Manuel, H. G. Rinderknecht, N. Sinenian, J. A. Frenje, J. R. Rygg, D. G. Hicks, R. D. Petrasso, J. Delettrez, R. Betti, F. J. Marshall, and V. A. Smalyuk, Phys. Plasmas **19**, 012701 (2012).

23. D. A. Tidman and R. A. Shanny, Phys. Fluids **17**, 1207 (1974).

24. T. Bartal *et al.*, Nat. Phys. **8**, 139 (2012).

25. B. Qiao *et al.*, Phys. Rev. E **87**, 013108 (2013).

26. N. L. Kugland, D. D. Ryutov, P. Y. Chang, R. P. Drake, G. Fiksel, D. H. Froula, S. H. Glenzer, G. Gregori, M. Grosskopf, M. Koenig, Y. Kuramitsu, C. Kuranz, M. C. Levy, E. Liang, J. Meinecke, F. Miniati, T. Morita, A. Pelka, C. Plechaty, R. Presura, A. Ravasio, B. A. Remington, B. Reville, J. S. Ross, Y. Sakawa, A. Spitkovsky, H. Takabe, and H. S. Park, Nat. Phys. **8**, 809 (2012).

27. M. Wei, R. Mishra, S. Chawla, A. Sorokovikova, F. N. Beg, C. Chen, H. Chen, R. Fedosejevs, J. Jaquez, L. C. Jarrott, G. Kemp, M. Key, J. Kim, A. Link, H. McLean, A. Morace, V. M. Ovchinnikov, P. K. Patel, Y. Ping, B. Qiao, H. Sawada, Y. Sentoku, C. Stoeckl, W. Theobald, and R. B. Stephens, in *24th Fusion Energy Conference on CD-ROM* (IAEA, Vienna, 2013), Paper IFE/P6–06.

28. A. Sorokovikova *et al.*, "Intense Laser-Plasma Interaction and Fast Electron Generation in Multi-Picosecond Time Scales," to be submitted to Physical Review Letters.

29. A. J. Kemp and L. Divol, Phys. Rev. Lett. **109**, 195005 (2012).

30. S. Chawla *et al.*, Phys. Rev. Lett. **110**, 025001 (2013).

31. H. Chen, S. C. Wilks, J. D. Bonlie, E. P. Liang, J. Myatt, D. F. Price, D. D. Meyerhofer, and P. Beiersdorfer, Phys. Rev. Lett. **102**, 105001 (2009).

32. H. Chen, S. C. Wilks, D. D. Meyerhofer, J. Bonlie, C. D. Chen, S. N. Chen, C. Courtois, L. Elberson, G. Gregori, W. Kruer, O. Landoas, J. Mithen, J. Myatt, C. D. Murphy, P. Nilson, D. Price, M. Schneider, R. Shepherd, C. Stoeckl, M. Tabak, R. Tommasini, and P. Beiersdorfer, Phys. Rev. Lett. **105**, 015003 (2010).

33. O. V. Gotchev, J. P. Knauer, P. Y. Chang, N. W. Jang, M. J. Shoup III, D. D. Meyerhofer, and R. Betti, Rev. Sci. Instrum. **80**, 043504 (2009).

34. J. Myatt, A. V. Maximov, R. W. Short, and D. D. Meyerhofer, Bull. Am. Phys. Soc. **52**, 66 (2007).

35. H. Chen, D. D. Meyerhofer, S. C. Wilks, R. Cauble, F. Dollar, K. Falk, G. Gregori, A. Hazi, E. I. Moses, C. D. Murphy, J. Myatt, J. Park, J. Seely, R. Shepherd, A. Spitkovsky, C. Stoeckl, C. I. Szabo, R. Tommasini, C. Zulick, and P. Beirsdorfer, High Energy Density Phys. **7**, 225 (2011).

36. M. Tabak *et al.*, Phys. Plasmas **1**, 1626 (1994).

37. D. H. Froula, R. Boni, M. Bedzyk, R. S. Craxton, F. Ehrne, S. Ivancic, R. Jungquist, M. J. Shoup, W. Theobald, D. Weiner, N. L. Kugland, and M. C. Rushford, Rev. Sci. Instrum. **83**, 10E523 (2012).

38. D. Haberberger, presented at the Omega Laser Facility Users Group Workshop, Rochester, NY, 24–26 April 2013.

39. J. S. Ross, S. H. Glenzer, P. Amendt, R. Berger, L. Divol, N. L. Kugland, O. L. Landen, C. Plechaty, B. Remington, D. Ryutov, W. Rozmus, D. H. Froula, G. Fiksel, C. Sorce, Y. Kuramitsu, T. Morita, Y. Sakawa, H. Takabe, R. P. Drake, M. Grosskopf, C. Kuranz, G. Gregori, J. Meinecke, C. D. Murphy, M. Koenig, A. Pelka, A. Ravasio, T. Vinci, E. Liang, R. Presura, A. Spitkovsky, F. Miniati, and H.-S. Park, Phys. Plasmas **19**, 056501 (2012).

40. C. M. Huntington *et al.*, "Direct Observation of Electromagnetic Weibel Filamentation in Counter-Streaming Plasma Flows," to be published in Nature.

41. N. L. Kugland, D. D. Ryutov, P. Y. Chang, R. P. Drake, G. Fiksel, D. H. Froula, S. H. Glenzer, G. Gregori, M. Grosskopf, M. Koenig, Y. Kuramitsu, C. Kuranz, M. C. Levy, E. Liang, J. Meinecke, F. Miniati, T. Morita, A. Pelka, C. Plechaty, R. Presura, A. Ravasio, B. A. Remington, B. Reville, J. S. Ross, Y. Sakawa, A. Spitkovsky, H. Takabe, and H. S. Park, Nat. Phys. **8**, 809 (2012).

42. Y. Ping, D. G. Hicks, B. Yaakobi, F. Coppari, D. Fratanduono, S. Hamel, J. H. Eggert, J. R. Rygg, R. F. Smith, T. R. Boehly, and G. W. Collins, Phys. Rev. Lett. **111**, 065501 (2013).

43. S. P. Regan, K. Falk, G. Gregori, P. B. Radha, S. X. Hu, T. R. Boehly, B. J. B. Crowley, S. H. Glenzer, O. L. Landen, D. O. Gericke,

T. Döppner, D. D. Meyerhofer, C. D. Murphy, T. C. Sangster, and J. Vorberger, Phys. Rev. Lett. **109**, 265003 (2012).

44. W. Theobald, A. A. Solodov, C. Stoeckl, K. S. Anderson, R. Betti, T. R. Boehly, R. S. Craxton, J. A. Delettrez, C. Dorrer, J. A. Frenje, V. Yu. Glebov, H. Habara, K. A. Tanaka, J. P. Knauer, R. Lauck, F. J. Marshall, K. L. Marshall, D. D. Meyerhofer, P. M. Nilson, P. K. Patel, H. Chen, T. C. Sangster, W. Seka, N. Sinenian, T. Ma, F. N. Beg, E. Giraldez, and R. B. Stephens, Phys. Plasmas **18**, 056305 (2011).

45. P. B. Radha, T. J. B. Collins, J. A. Delettrez, Y. Elbaz, R. Epstein, V. Yu. Glebov, V. N. Goncharov, R. L. Keck, J. P. Knauer, J. A. Marozas, F. J. Marshall, R. L. McCrory, P. W. McKenty, D. D. Meyerhofer, S. P. Regan, T. C. Sangster, W. Seka, D. Shvarts, S. Skupsky, Y. Srebro, and C. Stoeckl, Phys. Plasmas **12**, 056307 (2005).

46. W. Theobald, A. A. Solodov, C. Stoeckl, V. Yu. Glebov, S. Ivancic, F. J. Marshall, G. McKiernan, C. Mileham, T. C. Sangster, F. N. Beg, C. Jarrott, E. Giraldez, R. B. Stephens, M. S. Wei, M. H. Key, H. McLean, and J. Santos, Bull. Am. Phys. Soc. **57**, 115 (2012).

47. R. F. Heeter, S. B. Hansen, K. B. Fournier, M. E. Foord, D. H. Froula, A. J. Mackinnon, M. J. May, M. B. Schneider, and B. K. F. Young, Phys. Rev. Lett. **99**, 195001 (2007).

48. J. R. Rygg, J. A. Frenje, C. K. Li, F. H. Séguin, R. D. Petrasso, J. A. Delettrez, V. Yu. Glebov, V. N. Goncharov, D. D. Meyerhofer, S. P. Regan, T. C. Sangster, and C. Stoeckl, Phys. Plasmas **13**, 052702 (2006).

49. H. G. Rinderknecht, H. Sio, C. K. Li, A. B. Zylstra, M. J. Rosenberg, M. Gatu Johnson, J. A. Frenje, F. H. Séguin, R. D. Petrasso, J. Delettrez, V. Yu. Glebov, C. Stoeckl, T. C. Sangster, C. Bellei, P. Amendt, and S. Wilks, "Anomalous Reduction in the Shock Yield of Shock-Driven D^{3}He Implosions at Omega," to be submitted to Physical Review Letters.

50. H.-S. Park *et al.*, Phys. Rev. Lett. **104**, 135504 (2010).

51. J. F. Barnes *et al.*, J. Appl. Phys. **45**, 727 (1974).

52. H.-S. Park *et al.*, Phys. Plasmas **17**, 056314 (2010).

53. N. R. Barton *et al.*, J. Appl. Phys. **109**, 073501 (2011).

54. J. L. Belof *et al.*, AIP Conf. Proc. **1426**, 1521 (2012).

55. Y. Ping, D. G. Hicks, B. Yaakobi, F. Coppari, J. Eggert, and G. W. Collins, "A Platform for XAFS Study of Dynamically Compressed Materials Above 1 Mbar," to be published in Review of Scientific Instruments.

56. Y. K. Vohra and A. L. Ruoff, Phys. Rev. B **42**, 8651 (1990).

57. H. K. Mao *et al.*, Solid State Commun. **74**, 1027 (1990).

58. C. E. Ragan III *et al.*, Los Alamos National Laboratory, Los Alamos, NM, LA-UR-83-2081 (1983).

59. J. Hama, K. Suito, and N. Kawakami, Phys. Rev. B **39**, 3351 (1989).

60. A. L. Kritcher *et al.*, Phys. Plasmas **16**, 056308 (2009).

61. P. P. Jenkins *et al.*, in *35th IEEE Photovoltaic Specialists Conference (PVSC), 2010* (IEEE, New York, 2010), pp. 002550–002553.

62. J. R. Patterson *et al.*, Rev. Sci. Instrum. **83**, 10D725 (2012).

63. K. B. Fournier, J. H. Satcher, M. J. May, J. F. Poco, C. M. Sorce, J. D. Colvin, S. B. Hansen, S. A. MacLaren, S. J. Moon, J. F. Davis, F. Girard, B. Villette, M. Primout, D. Babonneau, C. A. Coverdale, and D. E. Beutler, Phys. Plasmas **16**, 052703 (2009).

64. M. Houry, E. Delagnes, D. Riz, B. Canaud, L. Disdier, F. Garaude, Y. Giomataris, V. Yu. Glebov, Ph. Legou, Ph. Rebourgeard, and C. Sangster, Nucl. Instrum. Methods Phys. Res. A **557**, 648 (2006).

65. Y. Giomataris *et al.*, Nucl. Instrum. Methods Phys. Res. A **376**, 29 (1996).

66. D. Breton, E. Delagnes, and M. Houry, IEEE Trans. Nucl. Sci. **52**, 2853 (2005).

67. S. Laffite and P. Loiseau, Phys. Plasmas **17**, 102704 (2010).

68. M. Vandenboomgaerde *et al.*, Phys. Rev. Lett. **99**, 065004 (2007).

69. F. Philippe, A. Casner, T. Caillaud, O. Landoas, M. C. Monteil, S. Liberatore, H. S. Park, P. Amendt, H. Robey, C. Sorce, C. K. Li, F. Seguin, M. Rosenberg, R. Petrasso, V. Glebov, and C. Stoeckl, Phys. Rev. Lett. **104**, 035004 (2010).

70. D. G. Hicks *et al.*, Phys. Plasmas **19**, 122702 (2012).

71. Y. Saillard, Nucl. Fusion **46**, 1017 (2006).

72. S. Depierreux, C. Labaune, D. T. Michel, C. Stenz, P. Nicholaï, M. Grech, G. Riazuelo, S. Weber, C. Riconda, V. T. Tikhonchuk, P. Loiseau, N. G. Borisenko, W. Nazarov, S. Hüller, D. Pesme, M. Casanova, J. Limpouch, C. Meyer, P. Di-Nicola, R. Wrobel, E. Alozy, P. Romary, G. Thiell, G. Soullié, C. Reverdin, and B. Villette, Phys. Rev. Lett. **102**, 195005 (2009).

Publications and Conference Presentations

Publications

J. R. Davies, R. Betti, P. M. Nilson, and A. A. Solodov, "Copper K-Shell Emission Cross Sections for Laser–Solid Experiments," Phys. Plasmas **20**, 083118 (2013).

K. B. Fournier, M. J. May, J. D. Colvin, M. A. Barrios, J. R. Patterson, and S. P. Regan, "Demonstration of a 13-keV Kr *K*-Shell X-Ray Source at the National Ignition Facility," Phys. Rev. E **88**, 033104 (2013).

D. H. Froula, T. J. Kessler, I. V. Igumenshchev, R. Betti, V. N. Goncharov, H. Huang, S. X. Hu, E. Hill, J. H. Kelly, D. D. Meyerhofer, A. Shvydky, and J. D. Zuegel, "Mitigation of Cross-Beam Energy Transfer: Implication of Two-State Focal Zooming on OMEGA," Phys. Plasmas **20**, 082704 (2013).

S. X. Hu, "Boosting Photoabsorption by Attosecond Control of Electron Correlation," Phys. Rev. Lett. **111**, 123003 (2013).

I. V. Igumenshchev, V. N. Goncharov, W. T. Shmayda, D. R. Harding, T. C. Sangster, and D. D. Meyerhofer, "Effects of Local Defect Growth in Direct-Drive Cryogenic Implosions on OMEGA," Phys. Plasmas **20**, 082703 (2013).

T. Ma, P. K. Patel, N. Izumi, P. T. Springer, M. H. Key, L. J. Atherton, L. R. Benedetti, D. K. Bradley, D. A. Callahan, P. M. Celliers, C. J. Cerjan, D. S. Clark, E. L. Dewald, S. N. Dixit, T. Döppner, D. H. Edgell, R. Epstein, S. Glenn, G. Grim, S. W. Haan, B. A. Hammel, D. Hicks, W. W. Hsing, O. S. Jones, S. F. Khan, J. D. Kilkenny, J. L. Kline, G. A. Kyrala, O. L. Landen, S. Le Pape, B. J. MacGowan, A. J. Mackinnon, A. G. MacPhee, N. B. Meezan, J. D. Moody, A. Pak, T. Parham, H.-S. Park, J. E. Ralph, S. P. Regan, B. A. Remington, H. F. Robey, J. S. Ross, B. K. Spears, V. Smalyuk, L. J. Suter, R. Tommasini, R. P. Town, S. V. Weber, J. D. Lindl, M. J. Edwards, S. H. Glenzer, and E. I. Moses, "Onset of Hydrodynamic Mix in High-Velocity, Highly Compressed Inertial Confinement Fusion Implosions," Phys. Rev. Lett. **111**, 085004 (2013).

R. L. McCrory, R. Betti, T. R. Boehly, D. T. Casey, T. J. B. Collins, R. S. Craxton, J. A. Delettrez, D. H. Edgell, R. Epstein, J. A. Frenje, D. H. Froula, M. Gatu-Johnson, V. Yu. Glebov, V. N. Goncharov, D. R. Harding, M. Hohenberger, S. X. Hu, I. V. Igumenshchev, T. J. Kessler, J. P. Knauer, C. K. Li, J. A. Marozas, F. J. Marshall, P. W. McKenty, D. D. Meyerhofer, D. T. Michel, J. F. Myatt, P. M. Nilson, S. J. Padalino, R. D. Petrasso, P. B. Radha, S. P. Regan, T. C. Sangster, F. H. Séguin, W. Seka, R. W. Short, A. Shvydky, S. Skupsky, J. M. Soures, C. Stoeckl, W. Theobald, B. Yaakobi, and J. D. Zuegel, "Progress Toward Polar-Drive Ignition for the NIF," Nucl. Fusion **53**, 113021 (2013).

S. P. Regan, R. Epstein, B. A. Hammel, L. J. Suter, H. A. Scott, M. A. Barrios, D. K. Bradley, D. A. Callahan, C. Cerjan, G. W. Collins, S. N. Dixit, T. Döppner, M. J. Edwards, D. R. Farley, K. B. Fournier, S. Glenn, S. H. Glenzer, I. E. Golovkin, S. W. Haan, A. Hamza, D. G. Hicks, N. Izumi, O. S. Jones, J. D. Kilkenny, J. L. Kline, G. A. Kyrala, O. L. Landen, T. Ma, J. J. MacFarlane, A. J. MacKinnon, R. C. Mancini, R. L. McCrory, N. B. Meezan, D. D. Meyerhofer, A. Nikroo, H.-S. Park, J. Ralph, B. A. Remington, T. C. Sangster, V. A. Smalyuk, P. T. Springer, and R. P. J. Town, "Hot-Spot Mix in Ignition-Scale Inertial Confinement Fusion Targets," Phys. Rev. Lett. **111**, 045001 (2013).

J. E. Schoenly, W. Seka, G. Romanos, and P. Rechmann, "The Efficacy of Selective Calculus Ablation at 400 nm: Comparison to Conventional Calculus Removal Methods," in *Lasers in Dentistry XIX*, edited by P. Rechmann and D. Fried (SPIE, Bellingham, WA, 2013), Vol. 8566, Paper 85660E.

R. H. H. Scott, E. L. Clark, F. Pérez, M. J. V. Streeter, J. R. Davies, H.-P. Schlenvoigt, J. J. Santos, S. Hulin, K. L. Lancaster, S. D. Baton, S. J. Rose, and P. A. Norreys, "Measuring Fast Electron Spectra and Laser Absorption in Relativistic Laser-Solid Interactions Using Differential Bremsstrahlung Photon Detectors," Rev. Sci. Instrum. **84**, 083505 (2013).

S.-J. Scott and D. R. Harding, "Accelerated Evaporative Drying of RF Foam for ICF Target Fabrication," in *2013 IEEE 25th Symposium on Fusion Engineering (SOFE)* (IEEE, Piscataway, NJ, 2013).

Q. Wang, J. U. Wallace, T. Y.-H. Lee, L. Zeng, J. J. Ou, and S. H. Chen, "Charge Carrier Mobility Through Vacuum–Sublimed Glassy Films of *s*-Triazine- and Carbazole-Based Bipolar Hybrid and Unipolar Compounds," Org. Electron. **14**, 2925 (2013).

B. Yaakobi, A. A. Solodov, J. F. Myatt, J. A. Delettrez, C. Stoeckl, and D. H. Froula, "Measurements of the Divergence of Fast Electrons in Laser-Irradiated Spherical Targets," Phys. Plasmas **20**, 092706 (2013).

Forthcoming Publications

C. Dorrer, R. Roides, R. Cuffney, A. V. Okishev, W. A. Bittle, G. Balonek, A. Consentino, E. Hill, and J. D. Zuegel, "Fiber Front End with Multiple Phase Modulations and High-Bandwidth Pulse Shaping for High-Energy Laser-Beam Smoothing," to be published in IEEE Journal of Selected Topics in Quantum Electronics.

H. P. H. Liddell, K. Mehrotra, J. C. Lambropoulos, and S. D. Jacobs, "Fracture Mechanics of Delamination Defects in Multilayer Dielectric Coatings," to be published in Applied Optics.

M. Storm, B. Eichman, Z. Zhong, W. Theobald, P. Schiebel, C. Mileham, C. Stoeckl, I. A. Begishev, G. Fiksel, R. B. Stephens, R. R. Freeman, and K. U. Akli, "Characterization of a High-Photon-Energy X-Ray Imager," to be published in Review of Scientific Instruments.

Conference Presentations

The following presentations were made at the 43rd Anomalous Absorption Conference, Stevenson, WA, 7–12 July 2013:

D. H. Edgell, T. J. B. Collins, V. N. Goncharov, I. V. Igumenshchev, J. A. Marozas, D. T. Michel, J. F. Myatt, P. B. Radha, W. Seka, and D. H. Froula, "Cross-Beam Energy Transfer in Polar-Drive Implosions on OMEGA and the NIF."

R. K. Follett, D. H. Froula, J. Katz, D. T. Michel, S. X. Hu, J. F. Myatt, and R. J. Henchen, "Observation of Two-Plasmon Decay Produced Electron Plasma Waves Using UV Thomson Scattering."

D. H. Froula, T. J. Kessler, I. V. Igumenshchev, V. N. Goncharov, H. Huang, S. X. Hu, E. Hill, J. H. Kelly, D. D. Meyerhofer, A. Shvydky, and J. D. Zuegel, "Implications of Two-State Focal Zooming on OMEGA to Mitigate Cross-Beam Energy Transfer."

D. Haberberger, D. H. Edgell, S. X. Hu, S. Ivancic, B. Yaakobi, R. Boni, and D. H. Froula, "Measurement of Long-Scale-Length Plasma Density Profiles for Two-Plasmon Decay Studies."

S. X. Hu, D. H. Edgell, D. H. Froula, V. N. Goncharov, D. T. Michel, J. F. Myatt, S. Skupsky, and B. Yaakobi, "Understanding the Creation of NIF-Scale Plasmas on OMEGA EP for Laser−Plasma Instability Studies."

J. A. Marozas, T. J. B. Collins, P. B. Radha, D. H. Edgell, D. H. Froula, M. Hohenberger, F. J. Marshall, D. T. Michel, and W. Seka, "Comparison of the 2-D *DRACO* Cross-Beam Energy Transfer (CBET) Simulations with OMEGA and NIF Experiments."

A. V. Maximov, J. F. Myatt, R. W. Short, I. V. Igumenshchev, and W. Seka, "Nonlinear Interaction Between Multiple Incoherent Laser Beams in the Plasmas of Direct-Drive ICF."

D. T. Michel, V. N. Goncharov, I. V. Igumenshchev, P. B. Radha, S. X. Hu, W. Seka, and D. H. Froula, "Comparison of Implosion Velocities for Be, C, and CH Ablators Measured in Direct-Drive Implosions."

W. Seka, J. F. Myatt, R. W. Short, D. H. Froula, J. Katz, V. N. Goncharov, and I. V. Igumenshchev, "Time-Resolved Electron Temperature Measurements Near $n_c/4$ Reveal Temperature Islands on Imploding Targets."

W. Seka, J. F. Myatt, J. Zhang, R. W. Short, D. H. Froula, D. T. Michel, A. V. Maximov, V. N. Goncharov, I. V. Igumenshchev, D. F. DuBois, D. A. Russell, and H. X. Vu, "The Nonlinear Behavior of the Two-Plasmon–Decay Instability."

R. W. Short, J. F. Myatt, and J. Zhang, "The Effects of Beam Geometry and Polarization on Two-Plasmon Decay Driven by Multiple Laser Beams."

A. A. Solodov, B. Yaakobi, J. F. Myatt, J. A. Delettrez, F. J. Marshall, C. Stoeckl, and D. H. Froula, "Measurements of the Divergence of Fast Electrons in Laser-Irradiated Spherical Targets."

J. Zhang, J. F. Myatt, A. V. Maximov, R. W. Short, D. F. DuBois, D. A. Russell, and H. X. Vu, "Linear Growth and Nonlinear Saturation of Two-Plasmon Decay Driven by Multiple Laser Beams."

———

The following presentations were made at the High-Energy-Density Physics Summer School, Columbus, OH, 15–19 July 2013:

D. D. Meyerhofer, "Diagnostics for High-Energy-Density Physics."

P. B. Radha, "Hydrodynamic Simulations of HED Plasmas."

———

J. D. Zuegel, J. Bromage, S.-W. Bahk, I. A. Begishev, J. Bunkenburg, T. Conley, C. Dorrer, H. Huang, R. K. Jungquist, C. Kellogg, T. J. Kessler, E. Kowaluk, J. R. Marciante, S. F. B. Morse, A. V. Okishev, J. B. Oliver, T. Petersen, C. Stoeckl, D. Haberberger, P. M. Nilson, G. Fiksel, J. F. Myatt, and D. D. Meyerhofer, "Technology Development and Prospects for Exawatt-Class OPCPA Pumped by OMEGA EP," 3rd IZEST Meeting, Livermore, CA, 17–18 July 2013.

———

D. H. Froula, "Direct-Drive Inertial Confinement Fusion: Where We Started (60 kJ), Where We Stand Today (1.5 MJ), and Where We Will be in 50 Years (100 kJ)," Intense Laser and Beam Plasma Interactions Workshop, Los Angeles, CA, 19–20 July 2013.

———

J. Bromage, R. G. Roides, S. -W. Bahk, J. B. Oliver, C. Mileham, C. Dorrer, and J. D. Zuegel, "Noncollinear Optical Parametric Amplifiers for Ultra-Intense Lasers," Nonlinear Optics 2013, Kamuela, HI, 21–26 July 2013.

———

The following presentations were made at Optics and Photonics, San Diego, CA, 25–29 August 2013:

M. Hohenberger, N. E. Palmer, G. LaCaille, E. L. Dewald, L. Divol, E. J. Bond, T. Döppner, J. J. Lee, J. D. Salmonson, C. A. Thomas, D. K. Bradley, C. Stoeckl, and T. C. Sangster, "Measuring the Hot-Electron Population Using Time-Resolved, Hard X-Ray Detectors on the NIF."

K. L. Marshall, D. Saulnier, H. Xianyu, S. Serak, N. Tabiryan, and C. Dorrer, "Liquid Crystal Near-IR Beam Shapers Employing Photoaddressable Alignment Layers for High-Peak-Power Applications."

D. Saulnier, B. Taylor, K. L. Marshall, T. J. Kessler, and S. D. Jacobs, "Liquid Crystal Chiroptical Polarization Rotators for the Near UV Region: Theory, Materials, and Device Applications."

———

The following presentations were made at the University of Alberta ICF Committee, Rochester, NY, 28 August 2013:

K. S. Anderson, R. Betti, P. W. McKenty, T. J. B. Collins, M. Hohenberger, W. Theobald, T. R. Boehly, R. S. Craxton, J. A. Delettrez, D. H. Edgell, S. X. Hu, M. Lafon, J. A. Marozas, D. D. Meyerhofer, R. Nora, T. C. Sangster, W. Seka, S. Skupsky, C. Stoeckl, A. Shvydky, B. Yaakobi, R. Yan, X. Ribeyre, G. Schurtz, A. Casner, L. J. Perkins, M. R. Terry, and D. E. Fratanduono, "Shock-Ignition OMEGA Experiments and Target Design for the NIF."

D. H. Froula, "Experimental Plasma Physics Program."

D. R. Harding, T. B. Jones, D. D. Meyerhofer, S. H. Chen, R. Q. Gram, M. Bobeica, Z. Bei, M. Moynihan, W. Wang, W. T. Shmayda, S.-J. Scott, A. Nikroo, J. Hund, R. Paguio, G. Randall, J. Fooks, D. Goodin, R. Garrell, and A. Tucker-Schwartz, "Mass Production of Targets for Inertial Fusion Energy."

J. F. Myatt, R. W. Short, A. V. Maximov, A. A. Solodov, J. Zhang, C. Ren, R. Yan, I. V. Igumenshchev, S. X. Hu, V. N. Goncharov, W. Seka, D. H. Edgell, D. H. Froula, B. Yaakobi, D. T. Michel, D. F. DuBois, D. A. Russell, and H. X. Vu, "The Theoretical Plasma Physics Program at LLE."

T. C. Sangster, "The Polar-Drive–Ignition Campaign Plan Through FY15."

—————

P. B. Radha, "Overview of Direct-Drive–Implosion Physics: Results from OMEGA and the NIF," 8th International Conference on Inertial Fusion Sciences and Applications, Nara, Japan, 8−13 September 2013.

—————

S. Papernov, A. A. Kozlov, J. B. Oliver, and B. Marozas, "Near-Ultraviolet Absorption Annealing Effects in HfO_2 Thin Films Subjected to Continuous-Wave Laser Irradiation at 355 nm," Laser Damage 2013, Boulder, CO, 22–25 September 2013.

—————

J. Katz, N. Fillion, R. J. Henchen, C. Sorce, D. H. Froula, and J. S. Ross, "A Reflective Image Rotating Periscope of Spatially Resolved Thomson-Scattering Experiments on OMEGA," 16th International Symposium on Laser Aided Plasma Diagnostics, Madison, WI, 22−26 September 2013.